Diss. ETH No. 27684

Gelation, characterization and enhancement of Amyloid networks and modelling of Fibronectin binding towards Growth Factors

A dissertation submitted to attain the degree of

DOCTOR OF SCIENCES of ETH ZURICH

(Dr. sc. ETH Zurich)

presented by

Mattia Usuelli

Laurea Magistrale in Ingegneria Chimica, Politecnico di Milano

born on 4$^{\text{th}}$ September 1991

citizen of Italy

accepted on the recommendation of

Prof. Dr. Raffaele Mezzenga, Examiner

Prof. Dr. Roberto Piazza, Co-Examiner
Dr. Gustav Nyström, Co-Examiner

2021

Gelation, characterization and enhancement of Amyloid networks and modelling of Fibronectin binding towards Growth Factors

Two sorts of truth: profound truths recognized by the fact that the opposite is also a profond truth, in contrast to trivialities where opposites are obviously absurd.

(Niels Bohr)

Felicità

Felicità: finché dietro a lei corri
non sei maturo per essere felice,
pur se quanto è più caro tuo si dice.

Finché tu piangi un tuo bene perduto,
e hai mete, e inquieto t'agiti e pugnace,
tu non sai ancora che cos'è la pace.

Solo quando rinunzi ad ogni cosa,
né più mete conosci né più brami,
né la felicità più a nome chiami,

allora al cuor non più l'onda affannosa
del tempo arriva, e l'anima tua posa.

(Hermann Hesse)

Acknowledgements

David, Sebastian, Katharina, Benito, Ghjulia, Julie, Anna, Sibylle, Jonathan, Hasan, Teo, Kristóf, Christoph, Lena, Moritz and all the other SSC members.

Last, but not least, a huge thank to Michele and to the wonderful PD group. They know for what.

Contents

Summary

Nature is a constant inspiration for us. The mechanisms on which life is based are, at the same time, incredibly complex and surprisingly harmonious; individual macromolecules interact in a seemingly chaotic dance, but which has an order and a melody.

Amyloid fibrils are a class of bio-macromolecules that is being increasingly brought under the spotlight. *In vivo*, amyloids can be both pathological and functional. In fact, they are responsible of severely debilitating diseases, such as Alzheimer's and Parkinson's, but they also assume pivotal roles in key biological functions. *In vitro*, amyloid fibrils synthesized from food sources are more and more used as building blocks of innovative materials, the applications of which range from filtration of water pollutants to drug delivery. Consequently, extensive studies on how amyloid fibrils interact and how they form gels are pivotal, both for finding novel therapeutic approaches for the above-mentioned diseases, and for optimizing the synthesis of materials that meet human needs, while preserving the resilience of our Planet.

Fibronectin is another important biomolecule, which is largely present in the extra-cellular matrix. The heparin-mediated conformational dance of fibronectin tunes its interactions with other key molecules, such as growth factors and, among these, the Vascular Endothelial Growth Factor (VEGF, the role of which is crucial for angiogenesis). A deeper understanding of how fibronectin and VEGF interact would lead to the possibility of synthesizing more effective drugs, the target of which is angiogenesis in pathological conditions (like cancer).

This doctoral thesis contains studies on both the biomolecules mentioned above.

Regarding amyloid fibrils, the aim of the studies we present is to characterize amyloid fibril gels (both over the course of their formation and structurally, when already formed), and to strengthen them through inclusion of polysaccharides. More in details, we show that in amyloid gels, the preparation of which is based on the passage of ions through a semipermeable membrane, the dynamic of the ions is non-diffusive but, instead, advective. This suggests the presence of a force that acts on the ions, that we hypothesize being arising from the Donnan effect. We also show that the ionic strength of the gels has a key role in tuning the entity and the frequency of restructuring phenomena, the role of which is to release the stresses accumulated by the fibrils over the gelation process. From a structural characterisation perspective, we show that the mesh size of amyloid networks can be measured through Dynamic Light Scattering (DLS) experiments, combining the theory of scattering from semi-flexible polymers together with a rigorous approach that takes the nonergodicity of the studied materials into account. Finally, with a more applied focus, we show an approach to strengthen amyloid fibril hydrogels and aerogels through inclusion of polysaccharides. The sugar chains improve the compression resistance of the materials, without interfering with the surface properties of the amyloid fibrils.

In the case of fibronectin, we show how this molecule is able to bind not only with VEGF, but also with an important receptor of this growth factor (VEGFR2). More in detail, heparin has an important role in extending fibronectin molecules, exposing binding sites that can interact with both VEGF and VEGFR2. The interactions are favoured at acidic pH, due to modifications in the protonation state of the binding sites of the ligands: this piece of information deepens the understanding of how hypoxia and low extracellular pH are related to angiogenesis. Moreover, thanks to Surface Plasmon Resonance studies and their modeling, we show that not all the fibronectin molecules interact equally with VEGF and VEGFR2, and can instead be divided into two classes, with different kinetics and affinities.

To resume, the presented studies broaden the actual knowledge on amyloid fibrils and fibronectin, and pave the way for synthesizing new functional materials and for facing severe diseases with novel therapeutic approaches.

Riassunto

La Natura ci è di costante ispirazione. I meccanismi sui quali la vita si basa sono, allo stesso tempo, incredibilmente complessi e sorprendentemente armoniosi; singole macromolecole interagiscono in una danza che sembra caotica, ma che ha un ordine e una melodia.

Le fibrille amiloidi sono una classe di aggregati bio-molecolari che è sempre maggiormente sotto i riflettori. *In vivo*, le fibrille amiloidi possono essere sia patogene che funzionali. Infatti, sono responsabili di patologie gravemente impattanti, come quelle di Alzheimer e di Parkinson, ma possono anche assumere ruoli importanti in meccanismi biologici chiave. *In vitro*, fibrille amiloidi sintetizzate da fonti alimentari sono via via maggiormente utilizzate come elementi costitutivi di materiali funzionali, le cui applicazioni spaziano dalla filtrazione di inquinanti acquosi al trasporto di farmaci. Di conseguenza, studi approfonditi su come le fibrille amiloidi interagiscono e su come formino gel sono di fondamentale importanza, sia per trovare approcci terapeutici per le patologie menzionate sopra, sia per ottimizzare la sintesi di materiali che soddisfino i bisogni umani e che, nel contempo, salvaguardino la resilienza del nostro Pianeta.

Un'altra biomolecola importante è la fibronectina, ampiamente presente nella matrice extracellulare. La danza conformazionale della fibronectina, mediata dall'eparina, regola le sue interazioni con altre molecole chiave, come i fattori di crescita e, nello specifico, il fattore di crescita dell'endotelio vascolare (di importanza cruciale per l'angiogenesi). Una maggiore comprensione dei meccanismi interattivi tra fibronectina e il fattore di crescita menzionato, renderebbe possibile la sintesi di farmaci più efficaci che agiscano sull'angiogenesi in condizioni patologiche (come i tumori).

Questa tesi di dottorato contiene studi su entrambe le biomolecole citate sopra.

Nel caso delle fibrille amilodi, lo scopo degli studi che presentiamo è sia di caratterizzare i gel di fibre amiloidi (durante il corso della loro formazione e strutturalmente, una volta formati), che di rafforzarli mediante l'inclusione di polisaccaridi. Più nello specifico, mostriamo che in gel la cui preparazione è effettuata mediante il passaggio di ioni attraverso una membrana semi-permeabile, la dinamica degli ioni è non-diffusiva ma, piuttosto, avvettiva. Questo suggerisce la presenza di una forza che agisce sugli ioni, che ipotizziamo abbia origine dall'effetto Donnan. Inoltre, mostriamo come la forza ionica dei gel rivesta un contributo determinante nel definire l'entità e la frequenza dei fenomeni di ristrutturazione, il cui ruolo è quello di rilasciare lo stress accumulato dalle fibrille durante il processo di gelazione. Per quanto riguarda la caratterizzazione strutturale, mostriamo che la distanza caratteristica tra le fibrille amiloidi nei gel (in inglese, denominata «mesh size») può essere ricavata da esperimenti di Dynamic Light Scattering (DLS), combinando la teoria di scattering da polimeri semi-flessibili con un rigoroso protocollo per tenere in considerazione la non-ergodicità dei materiali analizzati. Infine, con un risvolto maggiormente applicativo, mostriamo una via per rafforzare i gel di fibrille amiloidi mediante l'inclusione di polisaccaridi. Le catene di zuccheri incrementano la resistenza a compressione del materiale, senza interferire con le proprietà superficiali delle fibrille amiloidi.

Nel campo della fibronectina, mostriamo come questa sia capace di interagire non solamente con il fattore di crescita dell'endotelio vascolare (in inglese, VEGF), ma anche con un suo importante recettore (in inglese, VEGFR2). Maggiormente in dettaglio, l'eparina riveste l'importante ruolo di estendere le molecole di fibronectina, esponendo al contempo siti interattivi che possono interagire con i due ligandi menzionati. L'interazione è favorita a pH acido, che ha il ruolo di modificare la protonazione dei siti interattivi sui ligandi: questa informazione approfondisce come ipossia e basso pH extracellulare siano legate all'angiogenesi. Inoltre, mediante studi di Risonanza Plasmonica di Superficie e opportuna modellizzazione, mostriamo come non tutte le molecole di fibronectina interagiscano ugualmente con VEGF e VEGFR2, e possano invece essere divise in due classi con diverse cinetiche e affinità.

Riassumendo, gli studi presentati incrementano la conoscenza attuale sulle fibrille amiloidi e sulla fibronectina, e mostrano nuove possibilità per sintetizzare materiali funzionali e per fronteggiare malattie debilitanti con approcci terapeutici innovativi.

1. Introduction

The advances of global society over the past century are remarkable. Average life expectancy has been steadily growing, and technological innovations allowed the creation of tools which, if thought about only few decades earlier, would have sounded belonging to the science fiction world. However, the impressive growth we just mentioned came at a cost. While less and less people die at a young age, many adult or elderly people suffer from diseases that heavily impact their lives. While innovative products are introduced everyday on the market, our planet shares precious feedback on how we are going beyond the boundaries of sustainable production[1]. The two challenges of producing goods in a sustainable way and of promoting the health of global population, belong to two seemingly unrelated fields. However, they share one key term (and solution): biopolymers.

Biopolymers are functional units in the broad, and still little-known, working principles of cells. A deeper understanding of their role in organisms can help not only gaining further insights on the beauty of life, but also finding better therapeutic protocols for pathological conditions. Moreover, biological tissues are a constant inspiration for the *in vitro* creation of innovative materials, with high functionality and low environmental impact.

Therefore, a deeper understanding of biopolymer properties, both at an intra- and inter-unit level, is worth pursuing for proactively facing the challenges stated above. Before delving more into the two classes of biopolymers that are particularly relevant for this thesis (amyloid fibrils and fibronectin), and before stating the open questions on their properties that our work tackled, we find beneficial sharing an overall picture of the role that some key biopolymers have in the life of cells and in the synthesis of advanced materials.

Some key biopolymers

Cells, when looked upon from a mechano-biology perspective, are extremely fascinating units; their ability in combining an impressive resistance to mechanical strain and stresses with being actively capable of re-configuring themselves, moving, and dividing, is astonishing. Much of such a beautifully-orchestrated ensemble of properties arise from entangled networks present within (cytoskeleton) and outside (extracellular matrix) cells, and from the interactions among them. Figure 1 shows the constituting units of the cytoskeleton and of the extracellular matrix, in panels a and b, respectively. It can be appreciated how monomers (G-actin, Tubulin, and other protein subunits) self-assemble into elongated colloids (actin, microtubules, and intermediate filaments, respectively), that entangle and give mechanical stability to cells from within. Adhesion complexes allow actin filaments to interact with integrins (Fig. 1c), transmembrane proteins that are also capable of interacting with collagen and other proteins in the extracellular matrix; in this way, a dynamic interplay of cells with their surroundings is promoted. Proteoglycans, fibronectin, and elastin also fill the extracellular space, creating a visco-elastic network where cells are embedded.

In the following sections, further details on some of the mentioned polymers are shared.

Actin

G-actin is a globular protein with a molecular mass of 42 kDa[3] that beautifully orchestrates many cell functions through interactions with other specific proteins (termed actin-binding proteins, ABPs). A first point to be highlighted is that, in specific physiological conditions, G-actin self-assembles
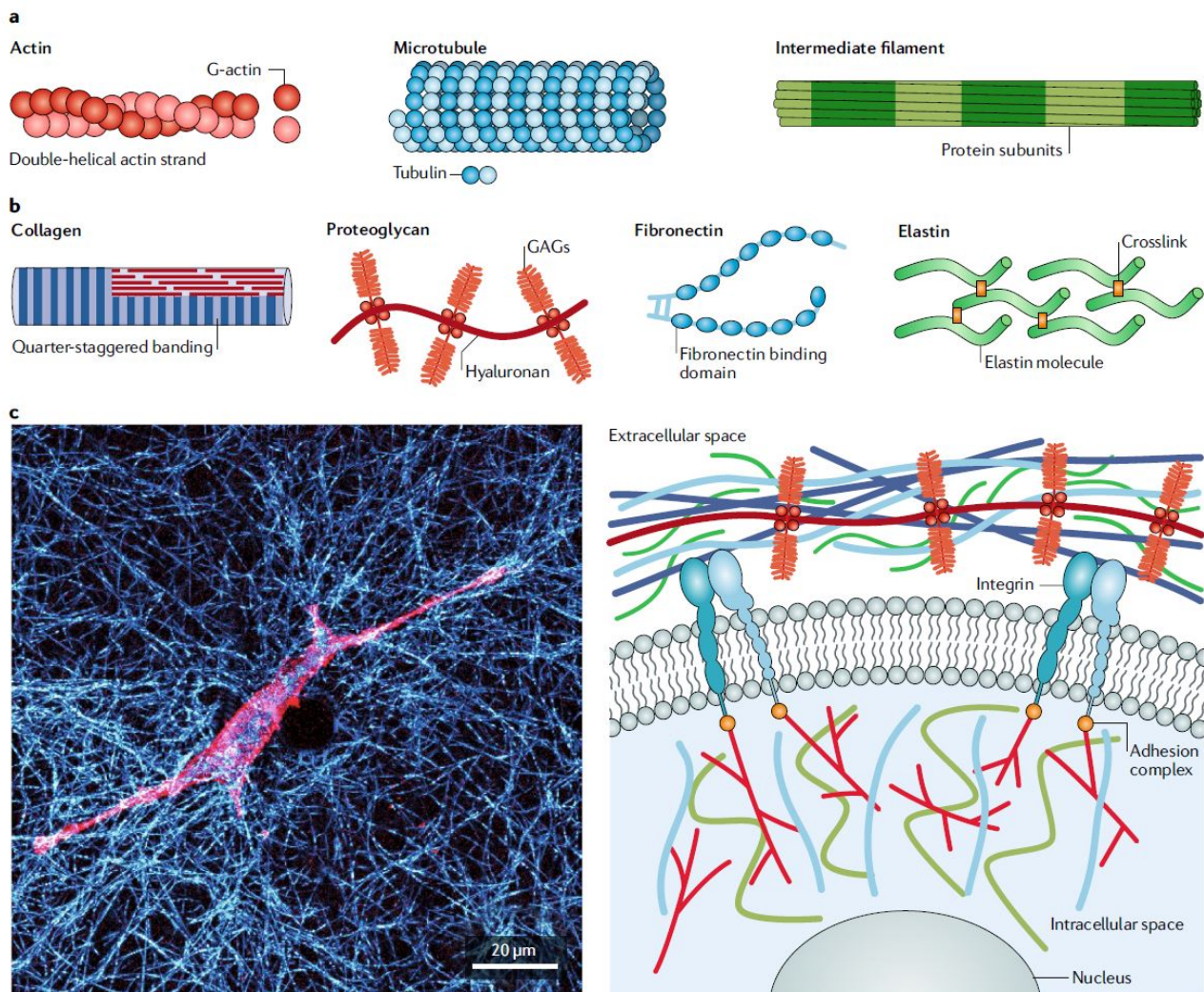
Figure 1. Representation of key biological units that, through entanglements and specific interactions, build the cytoskeleton and the extracellular matrix (panels a and b respectively) in cells and tissues. In panel c, a cell with its actin filaments visible in red is shown embedded in an extracellular collagen matrix (depicted in blue); the sub-panel on the right shows how integrins play a key role in adhering the cell to the extracellular matrix, by interacting with both actin and collagen. The figure is reprinted with permission from Nature Publishing Group.[2]

into semi-flexible fibrillar structures, comprising F-actin: the role of such elongated colloids in the cytoskeletal network is pivotal for determining the shape and the structural integrity of cells[4]. The above-mentioned ABPs have a key role in regulating the properties of F-actin networks; in fact, diverse proteins can act as network crosslinkers, as bundling-agents or can directly affect the properties of the formed filaments (by inhibiting their further elongation or by fragmenting them)[5]. Such fine tuning of the morphology and of the entanglement state of actin fibrils allow such elongated objects to take an important role in the wide-spanning functionality of cells, ranging from adsorption of nutrients in the epithelium to orienting the growth of nerves and capillaries; as an example, bristles, microvili, and stereocilia are all cell protrusions generated by bundled actin filaments.

Collagen

Collagen is a protein that, upon secretion in the extracellular space, allow cells to grow and move while reinforcing tissues[6]. More in detail, collagen is mainly responsible for the mechanism that allows tissues to be soft at small deformations, but stiff at large ones[7]: such a phenomenon is called strain-stiffening, and is pivotal for ensuring structural integrity[8]. It comes, therefore, with no surprise, that collagen is the most abundant protein in animals. The specific mechanical properties that stem from the presence of collagen strongly depend on how it spatially assembles: while in tendons it structures in bundles, other tissues (like skin) are characterised by a network with isotropic orientation. It was recently shown that, in isotropic networks, the fracture strain is a function of how the network junctions are coordinated, with benefits from plasticity at both the network and fibril levels[9]. It has also to be noted that, despite collagen being abundant in the extracellular matrix, its leading mechanical response is deeply affected by the presence of other components; as an example, the presence of hyaluronan determines synergistic effects that increase stiffness and delay strain stiffening[10].

Microtubules

α and β-tubulin are proteins often found in a heterodimeric form ($\alpha\beta$-tubulin), that associate in protofilaments whose lateral aggregation leads to hollow tubes: the microtubules[11]. The nucleation of these filaments preferentially happens in so-called 'microtubule organizing centers' (MTOC), and their elongation proceeds in the direction of the cell walls. Compared to other cytoskeletal filaments, microtubules are the most rigid: this property strongly influences their functionality. The rigidity of microtubules is, in fact, important for determining cell shape (especially for elongated conformations) and for enabling efficient and long-ranged intracellular transport[12].

While F-actin filaments work as large networks, microtubules mainly work individually or in small groups: for this reason, the mechanical properties of single tubules are very important and have been the subject of intensive research[13]. As an example, coherent microtubule vibrations *in vivo* are thought to enable cells to exhibit electromagnetic activity[14].

Intermediate filaments

Intermediate Filaments (IF) are elongated polymeric units that can be sub-divided in different classes, based on the monomeric units (termed IF proteins) that build them up[15]. As an example, while epithelial IF are composed of a large number of keratin units, the IF in muscles and in cells of mesenchymal origin are generated from desmin and vimentin, respectively[16]. The peculiar name of these pivotal cytoskeletal components arises from their diameter (~ 10 nm), which is intermediate between the one of actin filaments (~ 6 nm) and the one of microtubules (~ 23 nm)[17].

From a historical perspective, the composition and the huge variety of IF was discovered earlier than their wide functionality in cells[18]. A progressive understanding of the formation mechanisms of IF

paved the way for discovering that they do not only have a structural role, but can also sequester and position key signaling molecules[19], as the other cytoskeletal elements do: a broad range of diseases was discovered to be correlated with IF. Recent years witnessed further knowledge acquisition on how IF intervene in cell differentiation, lineage determination, and tissue homeostasis[20], confirming how our understanding of the many facets of this cytoskeletal component is limited and can be enriched with many further, fascinating discoveries.

In the following two sections, we will separately discuss two biopolymers that, in this thesis work, assume the role of main characters: amyloid fibrils and fibronectin.

Amyloids

Since the first X-ray diffraction studies on human-derived amyloids in 1968 more than 50 years have passed[21]. In these decades, our understanding of amyloid fibrils and plaques has dramatically increased: it went beyond the complex realm of amyloid diseases, towards the discovery of biologically functional amyloids and the *in vitro* synthesis of artificial amyloids, with wide-spanning applications in the materials science domain. Before focusing more in detail on these three classes of amyloids (pathological, functional, and artificial)[22], we would like to better define what they are.

Although scientist have been studying protein folding for decades, key features of this biological process are still elusive[23]. The functionality of a specific protein arises from how its amino-acid sequence (primary structure) drives intra-molecular interactions (secondary and tertiary structures), tuning in this way its overall spatial conformation (native state). Under several biological and environmental conditions (e.g. pH, ionic strength, and temperature), proteins can misfold and form a multitude of aggregates. One framework that offers an explanation for this behaviour is the folding funnel model, which sets an energy landscape where different protein aggregates can be located[22]. Amyloid fibrils were shown to represent the deepest valley of the protein energy landscape[24,25].

Micro- and mesoscopic properties

The fact that the formation of amyloid structures is energetically favoured points out their stability, which is directly connected to their structure. X-ray diffraction from amyloid fibrils generates a characteristic signal at 4.76-4.78 Å on the vertical axis (hydrogen bonds between β-strands), and another signal around the horizontal axis, which represents the distance between β-sheets (this is usually between 8 and 12 Å, but can vary as a function of the residues of the specific amyloidogenic proteins)[26,27]. The microscopic structure that drives the formation of the mentioned scattering pattern is termed cross-β, and is responsible for the high stability of amyloid aggregates. Other techniques that generated further insights on the structure of amyloid fibrils were AFM (Atomic Force Microscopy) and TEM/cryo-TEM (Transmission Electron Microscopy)[28–30]: each elongated object is composed of a varying number of protofilaments. These considerations drive our understanding of the mesoscopic properties of amyloids. The typical height of amyloid fibrils is in the nanometers scale, and their length can go up to several micrometers[31]. Moreover, the protofilaments that build the mature fibrils may twist, conferring them a specific handedness that usually (but not always) reflects the chirality of the constituting amino acids[32,33]. The internal contour length, needed for the protofilaments to perform a complete twist, defines the twist periodicity of amyloid fibrils. While such a property stems from microscopic features of the constituting units of the protofilaments, it can also be influenced by other factors, such as the linear charge density of the fibrils and the ionic strength of the surrounding medium[34,35].

The number of protofilaments and twist periodicity are not the only parameters that define the mesoscopic polymorphism of amyloids; individual fibrils were found to have different topologies, which could be described in terms of the mean (H) and Gaussian (K) curvatures of their surfaces. A broad

number of conformations was observed, ranging from twisted and helical ribbons to nanotubes and amyloid crystals, which occupy the absolute minimum of the amyloid energy landscape[36,37].

After having covered the aspects of single amyloid fibrils which are relevant for this thesis, we now focus on elucidating key aspects on the three different above mentioned classes of amyloids (pathological, functional and artificial), with the sharpest focus put on the last class.

Pathological amyloids

Amyloid fibrils and plaques have increasingly been brought under the spotlight of clinical research, due to their correlation with a large number of diseases.

Alzheimer's disease (AD) was found to be caused by the presence of aggregates that negatively affect synaptic function, consequently causing cognitive decline; such aggregates are built up by $A\beta$ fibrils[38,39] and hyperphosporylated tau tangles[40]. Type 2 diabetes was also found to be correlated with the presence of amyloid plaques in the pancreas, formed by a 37-residue peptide hormone. As a last example, Parkinson's disease is also associated to amyloids: α-synuclein was found to be the main component of intracellular protein aggregates, called Lewy bodies and neurites, which are the hallmarks of this impairing condition[41]. The briefness of our analysis should not make the reader think that amyloid fibrils and plaques are correlated only with the mentioned pathologies: there are several more diseases caused by these protein aggregates. We address the reader to recently published review articles[22,41] for a more complete analysis of this important topic, that goes beyond the scope of this thesis.

Functional amyloids

In the last sub-section, we pointed out the destructive role that amyloids can have in human physiology; we now briefly focus on the functional properties of these protein aggregates in living beings. Ranging from mammals to insects, amyloids can play a useful role[42,43], such as acting as cellular scaffolds or as inert storage of hormones. Another fascinating phenomenon lies in how bacteria strengthen the ExtraCellular Matrix (ECM) of the bio-films they form, through the incorporation of amyloids[44,45]. The study of how functional amyloids are synthesized not only unveils interesting biological routes, but can also serve as inspiration for designing therapeutic approaches for the amyloid diseases discussed above. In fact, nature shows us cleaver ways to control how these protein aggregates are formed both in time and space, and this can be a key direction that future research can follow.

Artificial amyloids

As stated at the beginning of this chapter, the impairing conditions generated by pathological amyloids are not the only challenge that global society faces. Another pressing issue is how to promote the well-being of human beings, while producing goods in a way that respects Earth and its climate[1]. This aim, the achievement of which was encouraged by the United Nations through the establishment of the 17 Sustainable Development Goals (SDGs)[47], can only be reached through drastic changes in many diverse fields, ranging from education to industrial production. A reshaping of industry does not only need a sustainable energy system, but also routes to produce materials that are environmentally-friendly[48]. Amyloid fibrils, in their artificial form, constitute a promising answer for the envisioned change of paradigm (Fig.2)[46,49].

With the term artificial, the scientific community refers to amyloid aggregates that are synthesised *in vitro* with the aim of creating functional materials. Due to the fact that amyloid fibrils constitute the absolute minimum of the protein energy landscape[37], they can be formed out of a large number of amino acid sequences present in many diverse proteins. A recent review article nicely showed that many food proteins, in appropriate conditions, can form amyloid fibrils[50]. In order to not threaten food
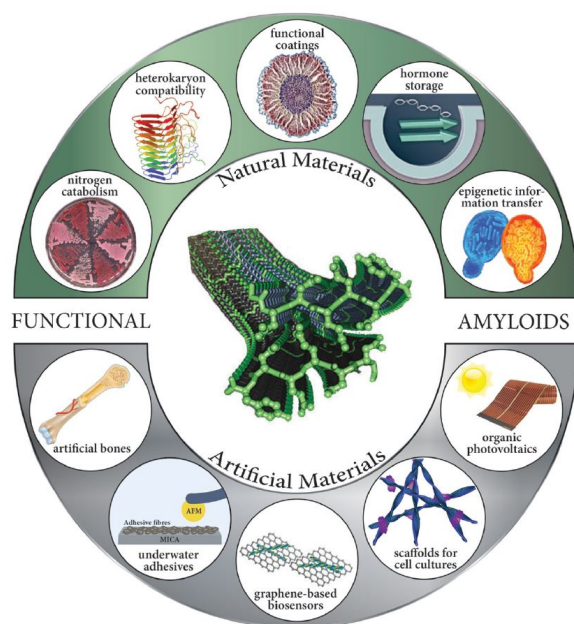
Figure 2. Amyloid fibrils, on the side of their pathological effects, also have key functional roles in biology: this is of inspiration for designing artificial amyloid aggregates with a broad functionality. The figure is reprinted with permission from Wiley-VCH publishing group.[46]

security, it is crucial to avoid the competition between using natural sources as nutrients suppliers and employing them as harbingers of innovative materials. In some contexts, such a conflict is potentially avoidable: this is the case for whey proteins, one of the major side-streams of cheese production.

The main protein fraction that constitutes whey proteins is β-lactoglobulin (βLG)[51], which can be obtained from Whey Protein Isolate (WPI) through denaturation, coagulation, and sedimentation of the other protein fractions, together with dialysis steps to remove further undesired salts and residues[52]. At acidic conditions (pH near 2) and high temperatures (90 °C), a water dispersion containing a modest quantity of β-Lactoglobulin monomers (approximately 2 wt%) can be transformed into an amyloid fibrils dispersion[53]. In fact, upon heating and stirring over the course of 5 hours, the β-Lactoglobulin monomers unfold and hydrolyze into shorter peptides that afterwards self-assemble and form the elongated colloidal structures of interest. βLG amyloid fibrils have been extensively characterised with many techniques[31,34,54]: they have a characteristic height of few nanometers and a contour length that can reach up to several micrometers. Another important mesoscopic parameter is the persistence length (l_p), related to the contour tangent deviations from a straight line, which is equal to the ratio between the bending rigidity of the filaments (κ) and the thermal energy (k_BT, with k_B being the Boltzmann constant and T being the absolute temperature). This quantity was found to be in the order of few micrometers[31]; its comparability with the contour length of βLG amyloid fibrils positions these colloidal objects in the realm of semi-flexible polymers.

The applications of βLG amyloid fibrils are wide-spanning. One of them, that convincingly emerged over the last five years, is water purification[55]. The extreme surface-to-volume ratio of amyloid fibrils, together with the broad variety of amino acids that constitute them, make these colloidal objects promising candidates for universal water purification from heavy metals[56,57], radioactive waste[58], organic contaminants[59], and bacteria[60].

Another field where βLG amyloid fibrils have successfully been employed is the creation of functional hydrogels and aerogels. Food gels are promising materials, the use of which can potentially become more widespread[61]. As examples, the βLG amyloid fibril-mediated reduction of gold salts towards the metallic state allowed to create 18-karat ultralight aerogels, with βLG fibrils only[62] or in combination with plastic beads[63] as a supporting structure. A similar approach was shown to be extendable to other metals[64].
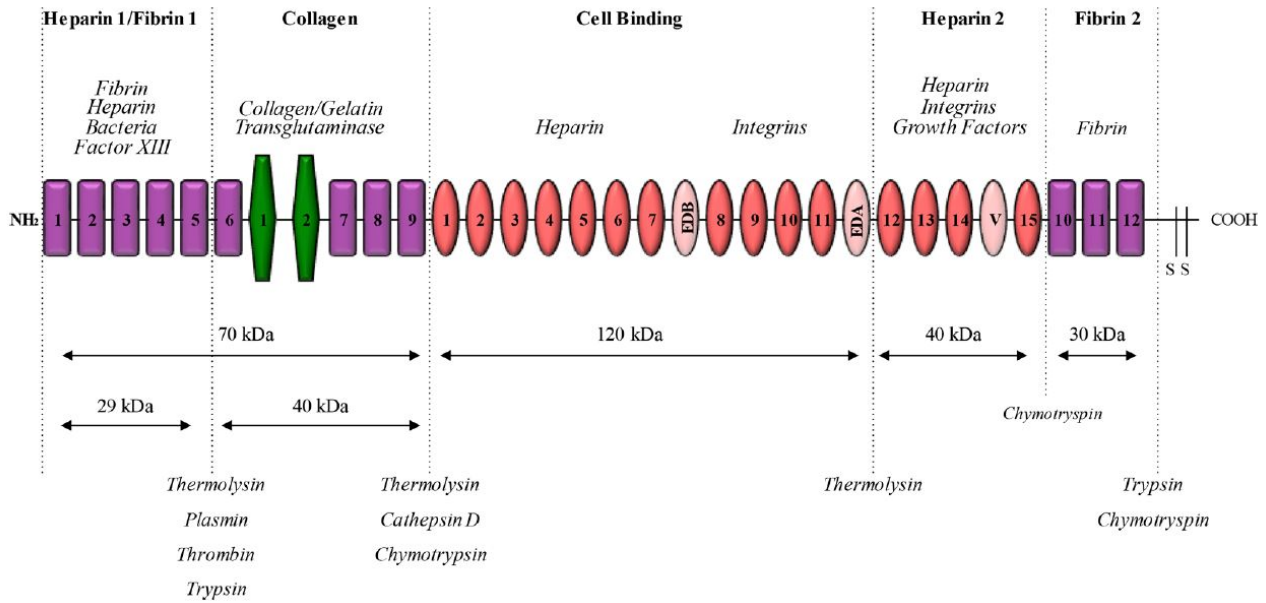
Figure 3. A single chain of dimeric fibronectin exhibits a complex architecture, structured into multiple modules of different types (I, II and III, in purple, green, and red colour, respectively). The structural sequence of different modules creates functional domains with binding affinities to other biomolecules; the domains can also act independently, after proteolytic action by the proteases mentioned in the bottom part of the graph. The figure is reprinted with permission from the American Chemical Society[76].

The pharmaceutical and medical worlds can also greatly benefit from the functionality of βLG amyloid fibrils. Shen and co-workers showed the possibility of growing iron nanoparticles on the surface of βLG amyloid filaments, with high bio-availability and a high potential for fighting the worldwide-spread human iron deficiency[65]. As a further example, amyloid aerogels (templated by the growth of ice crystals) could be used as a substrate for cell growth[66].

As a last, but not least, domain where βLG amyloid fibrils can play a pivotal role, we mention the creation of devices based on lyotropic liquid crystalline phases. Due to their extreme aspect ratio, amyloid fibrils above a certain concentration threshold self-orient along a common director and form a so-called nematic phase[67]. When the fibrils get shortened, their intra-fibrillar twist favours the generation of a new thermodynamic phase: the cholesteric one[68]. In this equilibrium state, the alignment direction of the fibrils rotates, making a complete twist over length-scales in the micrometer range[69]. The new periodicity that arises in the cholesteric phase (termed cholesteric pitch) beautifully interacts with light, causing the reflection of certain wavelengths: such a phenomenon is employed by nature to embellish animals[70] and fruits[71] with functional structural colours, and can also be used for designing devices[72]. Despite this being a relatively new field for amyloid fibrils, with fundamental and theoretical research being actively pursued to better elucidate the properties of the system of interest[73–75], it reveals a huge potential for the creation of innovative optical materials from renewable sources.

Fibronectin

Fibronectin is a glycoprotein that can be found in the extracellular matrix (in a fibrillar form) and in plasma (in a soluble form)[77]. The roles of this molecule are broad, as confirmed by its discovery journey: different research groups have come across unknown types of aggregates, until it was found out that they were generated by the same macromolecule, to which the name fibronectin was given[78]. The question marks on the mysterious role of fibronectin in human physiology were soon replaced by an awareness of the breadth of its activity: the macromolecule was "transformed from a protein

in search of a function to a protein with possibly too many functions"[79,80]. Fibronectin plays a role in opsonic activity[81], blood coagulation[82], morphogenetic movements while embryo develops[83], neovascularization[84], wound healing[85], and many more biological processes; further discoveries on the roles of fibronectin would come with no surprise, but as a confirmation of its multi-faced functionality. The question of where this broad functionality arises from finds an answer in the complex structure of fibronectin. It is a dimer composed of two polypeptide chains (encoded by one gene) linked by two disulfide bridges[86]. Studies performed with multiple techniques led to the discovery of how each polypeptide chain is built by modules[87–90], classified into three categories (I, II, and III, Fig.3). The modules, then, constitute different functional units with binding ability to several molecules. As examples, I_1-I_5 binds to fibrin and plays a key role for incorporating fibronectin in the extracellular matrix. I_6-I_9 binds with collagen and gelatin, and III_2-III_{11} are considered the cell-binding domains. The different modules not only drive the interactions of fibronectin with other macromolecules, but also tune the conformation of the polypeptide chains by interacting among themselves (inter-moduli interactions). Environmental conditions (pH, ionic strength), the presence of other molecules (e.g. glycerol and heparin), and biophysical processes (like adsorption and stretching) have a direct influence on the inter-moduli interactions, and affect therefore the conformation of fibronectin. Such an exquisite structural rearrangement possibility influences the functionality of fibronectin, by exposing or hiding its binding sites[76].

Heparin and heparan sulfate chains are molecules that, among the many others that interact with fibronectin, play a crucial role in determining its biological output in the extracellular microenvironment. They can bind on fibronectin in three different functional units, named Hep1, Hep2, and Hep3, which are located at the terminal parts of the macromolecule (I_1-I_5 and III_{12}-III_{14}) and in the central part (III_4-III_6), respectively. Hep2 is considered to be the main heparin-binding site, and the module that mainly contributes to the interactions is III_{13}[91] (although III_{14} was shown to also play a role[92]). One peculiarity of such an interaction is that it directly influences the conformation of fibronectin: upon association with heparin, fibronectin extends and consequently lowers its affinity for heparin itself. The result of this structure-driven thermodynamic change is the release of heparin, and the consequent possibility for it to repeat the cycle and extend other fibronectin molecules[76]. Heparin behaves, therefore, as a structural catalyst for the biomacromolecule of interest; this conformational change allows then fibronectin to expose cryptic binding sites on Hep2[93], which can interact with several growth factors (including Vascular Endothelial Growth Factor, VEGF)[94]. The fact that growth factors bind to fibronectin influences their signaling potential: the activity of VEGF, as an example, is regulated by binding to fibronectin through activation of diverse downstream signaling pathways[95–97]. In addition to exposing key binding sites, heparin also has a pivotal role in determining the fibrillogenic properties of fibronectin by also exposing self-association sites[98].

While there is much more that can be said about fibronectin, we prefer to focus on the aspects mentioned above, which have a key role for the research questions that inspired this thesis. We address the curious reader to a recently published review article[76], where it is possible to find more information on how the structural flexibility of fibronectin influences its biological output.

Research questions and structure of the thesis

After having shown that bio-fibrillar structures play a pivotal role both in living beings and in the synthesis of functional materials, we wish to elucidate the research questions that inspired the work presented in this doctoral thesis.

Ion-induced gelation dynamics of amyloid networks

The understanding of the entanglement and aggregation dynamics of amyloid fibrils is of extreme importance, both for unveiling the formation of amyloid plaques *in vivo*[22,41], and for optimising the

synthesis of materials *in vitro*[49]. The phase diagram of amyloid dispersion at different concentrations and ionic strengths was mapped out by Bolisetty and co-workers[99]; Cao and colleagues, then, refined the knowledge on amyloid gels by studying the scaling behaviour of their shear elastic modulus (G') as a function of the concentration of amyloid fibrils and of the ionic strength of the dispersion[100]. Key pieces of information, that are still missing in the broad puzzle that represents the knowledge on amyloid gels, are the dynamics that underlie their formation.

Salt-induced gels are often formed by directly mixing ion solutions with the initial colloidal dispersion. While this method is fast and robust, the way the salt spreads inside the material is a function of the mixing protocol; it has to be expected that the network-forming units, and the network morphology itself, might be affected by the specific used approach. To circumvent this obstacle, we formed gels of βLG amyloid fibrils by letting salt ions move into the initial colloidal dispersion through a semi-permeable membrane. We studied then the gelation dynamics of the samples through Photon Correlation Imaging, an optical techniques that blends the advantages of imaging and scattering, allowing to statistically analyse the motion of the network forming units (in the micro-scale) while detecting temporally and spatially heterogeneous rearrangement phenomena (in the macro-scale). The performed analysis detected a linear-in-time evolution of the gelation front, that was different from the expected diffusive behaviour, and showed how different ionic strengths tune both the frequency and the entity of rearrangement events. More details about this study are presented in chapter 2, «Unraveling amyloid fibril gelation by Photon Correlation Imaging: kinetics, microscopic dynamics, and temporal heterogeneity».

Characterization of the internal structure of amyloid networks

Amyloid fibrils, synthesized from food sources, were previously discussed to be promising building blocks for the synthesis of innovative materials[49]. For practical applications, it is often needed that the final materials, containing the amyloid fibrils, are in a solid state. This can be obtained by embedding the fibrils in already formed materials with the desired properties, or by creating arrested structures from the amyloids themselves.

At the synthesis conditions, a βLG amyloid fibril dispersion has extremely limited elastic properties. The viscous nature of the considered system stems from the fact that, although the fibrils are entangled and form a network, the entanglement points have a transient nature, as a consequence of the electrostatic repulsion between the positively-charged elongated colloids. To drive a sol-gel transition, it is necessary to lower the repulsive energy between the fibrils, driving in this way the transformation of entanglements into physical cross-links. This can be accomplished by either increasing the ionic strength of the solution, to promote screening of surface charges by counter-ions, or by shifting the pH of the solution towards the IsoElectric Point (IEP) of the amyloid fibrils, to decrease their linear charge density. Bolisetty and co-workers built a phase diagram of amyloid fibrils as a function of concentration and ionic strength of the solution[99]: the possibility of forming amyloid gels clearly emerged from this analysis. Cao and co-workers studied amyloid gels further, and established scaling relations between the shear elastic modulus of the gels (G', determined through oscillatory sweeps), concentration of the fibrils (c), and ionic strength of the dispersion (I)[100]. The results that emerged pointed out how the entanglements, upon addition of salt, transformed into long-lived physical cross-links, conferring an elastic nature to the samples.

Despite the described major steps in elucidating the properties of amyloid networks and gels, the picture is far from being complete. In gels composed of semi-flexible polymers, one important parameter that tunes the elastic properties is the average distance between the network-constituting units: namely, the mesh size (ξ_m)[101]. Despite the fact that the scaling law of this quantity as a function of the concentration of polymers is known since decades ($\xi_m \sim c^{-1/2}$), a quantitative estimation of the mesh size remains elusive. A promising technique that can fulfill this aim, in a non-invasive way, is Dynamic Light Scattering (DLS)[102]. Seminal theoretical studies on scattering functions from semi-flexible polymers showed the possibility of extracting, from experimental data, both single-filament

properties and the mesh size of the networks they form[103,104]. However, only the diameter and persistence length of individual filaments were extracted following this route[105–107], but not the mesh size.

The question that we addressed, therefore, was whether it is possible to measure the mesh size of amyloid fibril gels by combining the theory of semi-flexible polymer scattering with a proper framework for dealing with the nonergodicity of the examined materials[108]. We found a positive answer to this question, and compared the obtained results with theoretical estimations from a modified version of the cubic lattice model[100].

The results of this analysis are presented in chapter 3, «Probing the Structure of Filamentous Nonergodic Gels by Dynamic Light Scattering».

Enhancement of the mechanical properties of amyloid gels

The synthesis of amyloid gels, as explained in the sub-sections above, is typically performed by adding ions to amyloid solutions: the consequent screening of surface charges allows Brownian motion to overcame the repulsive energy barrier between the fibrils, until Van der Waals forces drive the formation of long-lived cross-links[100]. Despite this strategy being effective for creating solid structures (where G′, the elastic shear modulus, is one order of magnitude larger than G″, the viscous one), the strength of the formed gels often does not withstand the stresses and deformations encountered in many applications. Therefore, it is beneficial to find routes for strengthening the formed gels, while preserving the wide-spanning surface properties of the constituting amyloid fibrils[49].

A broadly-explored path for strengthening biological networks is through the incorporation of a second component. Up to recent times, βLG amyloid fibril gels have been strengthened through the inclusion of $CaCO_3$ nanoparticles[109], to create hybrid materials with self-healing properties, or through the growth of silicious shells around individual filaments[110], to structure organic-inorganic materials with enhanced mechanical properties that are transformable into aerogels with an extremely large specific surface area.

To comply with the sustainability requirements outlined by the SDGs[1], we searched for a method to strengthen amyloid fibril gels through the inclusion of widely-available polysaccharides. We found κ-carrageenan and low-acetylated Gellan Gum to be two promising candidates, and determined the structural and mechanical properties of hybrid amyloid-polysaccharide hydrogels and aerogels. We demonstrated that the polysaccharide component positively influences the strength of amyloid gels, while preserving their surface functionality.

The results of this analysis are presented in chapter 4, «Polysaccharide-reinforced amyloid fibril hydrogels and aerogels».

Fibronectin interactions with growth factors and their receptors

In the section dedicated to fibronectin, we highlighted that this biopolymer can interact with a multitude of macromolecules present in the extracellular microenvironemnt, including growth factors (GF). Many of these interactions are regulated by conformation: heparin was shown to act as a structural catalyst, which exposes or buries key binding sites on fibronectin and regulates therefore its binding activity[76].

An important GF is vascular endothelial growth factor (VEGF), which plays a pivotal role in regulating angiogenic activity[93]. The signaling of this molecule occurs upon binding to cell-surface cognate receptors, among which VEGFR2 is consider to play a particularly important role[111]. For this reason, the VEGF/VEGFR2 axis was considered as a key target for cancer therapeutic approaches[112], as solid tumor growth depends on angiogenesis. The results were unfortunately not aligned with the expectations, leading to ineffective therapies and considerable side effects[113]: this points out how important it is to gain further knowledge on how the VEGF/VEGFR2 signaling axis works. In this axis, fibronectin also plays a role: its ability to bind VEGF (upon conformational changes) influences the

biological output of this GF, by altering its bioavailability and inducing different downstream signaling pathways[96].

The questions that we addressed were whether fibronectin can also interact with VEGFR2 and, in case of a positive answer, to compare the binding kinetics and affinities of this macromolecule with both VEGF and VEGFR2. Our aim was to expand the knowledge on how the extracellular matrix, VEGF, and VEGFR2 interact, and add key pieces to the still mysterious puzzle of angiogenesis. We found a positive answer to the first question, and modelled Surface Plasmon Resonance (SPR) measurements to gain insights on the second query.

The results of our analysis are presented in chapter 5, «VEGF and VEGFR2 bind to similar pH-sensitive sites on fibronectin, exposed by heparin-mediated conformational changes».

Mechanism of crosslinked cyclodextrins in the treatment of Niemann-Pick disease Type C

In the appendix A («Investigating the Mechanism of Cyclodextrins in the Treatment of Niemann-Pick Disease Type C Using Crosslinked 2-Hydroxypropyl-β-cyclodextrin») we present a further-related manuscript, where the author of this thesis contributed to the characterization of cross-linked cyclodextrins through Static Light Scattering (SLS).

Bibliography

[1] J. D. Sachs, G. Schmidt-Traub, M. Mazzucato, D. Messner, N. Nakicenovic and J. Rockström, *Nature Sustainability*, 2019, **2**, 805–814.

[2] F. Burla, Y. Mulla, B. E. Vos, A. Aufderhorst-Roberts and G. H. Koenderink, *Nature Reviews Physics*, 2019, **1**, 249–263.

[3] R. Dominguez and K. C. Holmes, *Annual Review of Biophysics*, 2011, **40**, 169–186.

[4] H. Isambert and A. Maggs, *Macromolecules*, 1996, **29**, 1036–1040.

[5] C. Revenu, R. Athman, S. Robine and D. Louvard, *Nature Reviews Molecular Cell Biology*, 2004, **5**, 635–646.

[6] J. K. Mouw, G. Ou and V. M. Weaver, *Nature Reviews Molecular Cell Biology*, 2014, **15**, 771–785.

[7] Y. Lanir, *Journal of Elasticity*, 2017, **129**, 7–48.

[8] D. F. Holmes, Y. Lu, T. Starborg and K. E. Kadler, *Current Topics in Developmental Biology*, 2018, **130**, 107–142.

[9] F. Burla, S. Dussi, C. Martinez-Torres, J. Tauber, J. van der Gucht and G. H. Koenderink, *Proceedings of the National Academy of Sciences*, 2020, **117**, 8326–8334.

[10] F. Burla, J. Tauber, S. Dussi, J. van Der Gucht and G. H. Koenderink, *Nature Physics*, 2019, **15**, 549–553.

[11] J. B. Olmsted and G. G. Borisy, *Annual Review of Biochemistry*, 1973, **42**, 507–540.

[12] R. H. Wade, *Molecular Biotechnology*, 2009, **43**, 177–191.

[13] T. Hawkins, M. Mirigian, M. S. Yasar and J. L. Ross, *Journal of Biomechanics*, 2010, **43**, 23–30.

[14] O. Kučera, D. Havelka and M. Cifra, *Wave Motion*, 2017, **72**, 13–22.

[15] P. M. Steinert, A. C. Steven and D. R. Roop, *Cell*, 1985, **42**, 411–419.

[16] P. M. Steinert and D. R. Roop, *Annual Review of Biochemistry*, 1988, **57**, 593–625.

[17] E. Fuchs and K. Weber, *Annual Review of Biochemistry*, 1994, **63**, 345–382.

[18] H. Herrmann and U. Aebi, *Annual Review of Biochemistry*, 2004, **73**, 749–789.

[19] J. E. Eriksson, T. Dechat, B. Grin, B. Helfand, M. Mendez, H.-M. Pallari, R. D. Goldman *et al.*, *The Journal of Clinical Investigation*, 2009, **119**, 1763–1771.

[20] C. J. Redmond and P. A. Coulombe, *Current Opinion in Cell Biology*, 2021, **68**, 155–162.

[21] E. Eanes and G. Glenner, *Journal of Histochemistry & Cytochemistry*, 1968, **16**, 673–677.

[22] P. C. Ke, R. Zhou, L. C. Serpell, R. Riek, T. P. Knowles, H. A. Lashuel, E. Gazit, I. W. Hamley, T. P. Davis, M. Fändrich *et al.*, *Chemical Society Reviews*, 2020, **49**, 5473–5509.

[23] C. M. Dobson, *Nature Reviews Drug Discovery*, 2003, **2**, 154–160.

[24] D. Balchin, M. Hayer-Hartl and F. U. Hartl, *Science*, 2016, **353**, 6294.

[25] F. U. Hartl and M. Hayer-Hartl, *Nature Structural & Molecular Biology*, 2009, **16**, 574.

[26] O. S. Makin and L. C. Serpell, *The FEBS Journal*, 2005, **272**, 5950–5961.

[27] K. L. Morris and L. C. Serpell, *X-ray fibre diffraction studies of amyloid fibrils*, in Amyloid Proteins. Methods and Protocols, ed. E. Sigurdsson, M. Calero and M. Gasset, Humana Press, 2012, vol. 849, pp. 121–135.

[28] L. C. Serpell, M. Sunde, M. D. Benson, G. A. Tennent, M. B. Pepys and P. E. Fraser, *Journal of Molecular Biology*, 2000, **300**, 1033–1039.

[29] C. Goldsbury, K. Goldie, J. Pellaud, J. Seelig, P. Frey, S. Müller, J. Kistler, G. Cooper and U. Aebi, *Journal of Structural Biology*, 2000, **130**, 352–362.

[30] J. L. Jimenez, J. I. Guijarro, E. Orlova, J. Zurdo, C. M. Dobson, M. Sunde and H. R. Saibil, *The EMBO Journal*, 1999, **18**, 815–821.

[31] J. Adamcik, J.-M. Jung, J. Flakowski, P. De Los Rios, G. Dietler and R. Mezzenga, *Nature Nanotechnology*, 2010, **5**, 423–428.

[32] C. Lara, N. P. Reynolds, J. T. Berryman, A. Xu, A. Zhang and R. Mezzenga, *Journal of the American Chemical Society*, 2014, **136**, 4732–4739.

[33] I. Usov, J. Adamcik and R. Mezzenga, *ACS Nano*, 2013, **7**, 10465–10474.

[34] J. Adamcik and R. Mezzenga, *Soft Matter*, 2011, **7**, 5437–5443.

[35] S. Assenza, J. Adamcik, R. Mezzenga and P. De Los Rios, *Physical Review Letters*, 2014, **113**, 268103.

[36] N. P. Reynolds, J. Adamcik, J. T. Berryman, S. Handschin, A. A. H. Zanjani, W. Li, K. Liu, A. Zhang and R. Mezzenga, *Nature Communications*, 2017, **8**, 1–10.

[37] J. Adamcik and R. Mezzenga, *Angewandte Chemie International Edition*, 2018, **57**, 8370–8382.

[38] G. G. Glenner and C. W. Wong, *Biochemical and Biophysical Research Communications*, 1984, **120**, 885–890.

[39] G. Blessed, B. E. Tomlinson and M. Roth, *The British Journal of Psychiatry*, 1968, **114**, 797–811.

[40] I. Grundke-Iqbal, K. Iqbal, Y.-C. Tung, M. Quinlan, H. M. Wisniewski and L. I. Binder, *Proceedings of the National Academy of Sciences*, 1986, **83**, 4913–4917.

[41] P. C. Ke, M.-A. Sani, F. Ding, A. Kakinen, I. Javed, F. Separovic, T. P. Davis and R. Mezzenga, *Chemical Society Reviews*, 2017, **46**, 6492–6531.

[42] D. Otzen and R. Riek, *Cold Spring Harbor perspectives in biology*, 2019, **11**, a033860.

[43] R. Hervas, M. J. Rau, Y. Park, W. Zhang, A. G. Murzin, J. A. Fitzpatrick, S. H. Scheres and K. Si, *Science*, 2020, **367**, 1230–1234.

[44] F. Shewmaker, R. P. McGlinchey, K. R. Thurber, P. McPhie, F. Dyda, R. Tycko and R. B. Wickner, *Journal of Biological Chemistry*, 2009, **284**, 25065–25076.

[45] M. R. Chapman, L. S. Robinson, J. S. Pinkner, R. Roth, J. Heuser, M. Hammar, S. Normark and S. J. Hultgren, *Science*, 2002, **295**, 851–855.

[46] T. P. Knowles and R. Mezzenga, *Advanced Materials*, 2016, **28**, 6546–6561.

[47] D. Griggs, M. Stafford-Smith, O. Gaffney, J. Rockström, M. C. Öhman, P. Shyamsundar, W. Steffen, G. Glaser, N. Kanie and I. Noble, *Nature*, 2013, **495**, 305–307.

[48] M. F. Ashby, *Materials and sustainable development*, Butterworth-Heinemann, 2015.

[49] G. Wei, Z. Su, N. P. Reynolds, P. Arosio, I. W. Hamley, E. Gazit and R. Mezzenga, *Chemical Society Reviews*, 2017, **46**, 4661–4708.

[50] Y. Cao and R. Mezzenga, *Advances in Colloid and Interface Science*, 2019, **269**, 334–356.

[51] M. Boland, *Whey proteins*, in Handbook of food proteins, ed. G. O. Phillips and P. A. Williams, Woodhead Publishing, 2011, pp. 30–55.

[52] D. Vigolo, J. Zhao, S. Handschin, X. Cao, A. J. deMello and R. Mezzenga, *Scientific Reports*, 2017, **7**, 1–7.

[53] J.-M. Jung, G. Savin, M. Pouzot, C. Schmitt and R. Mezzenga, *Biomacromolecules*, 2008, **9**, 2477–2486.

[54] S. Bolisetty, J. Adamcik and R. Mezzenga, *Soft Matter*, 2011, **7**, 493–499.

[55] S. Bolisetty, M. Peydayesh and R. Mezzenga, *Chemical Society Reviews*, 2019, **48**, 463–487.

[56] S. Bolisetty and R. Mezzenga, *Nature Nanotechnology*, 2016, **11**, 365–371.

[57] M. Peydayesh, S. Bolisetty, T. Mohammadi and R. Mezzenga, *Langmuir*, 2019, **35**, 4161–4170.

[58] S. Bolisetty, N. M. Coray, A. Palika, G. A. Prenosil and R. Mezzenga, *Environmental Science: Water Research & Technology*, 2020, **6**, 3249–3254.

[59] M. Peydayesh, M. K. Suter, S. Bolisetty, S. Boulos, S. Handschin, L. Nyström and R. Mezzenga, *Advanced Materials*, 2020, **32**, 1907932.

[60] A. Palika, A. Rahimi, S. Bolisetty, S. Handschin, P. Fischer and R. Mezzenga, *Nanoscale Advances*, 2020, **2**, 4665–4670.

[61] Y. Cao and R. Mezzenga, *Nature Food*, 2020, **1**, 106–118.

[62] G. Nyström, M. P. Fernández-Ronco, S. Bolisetty, M. Mazzotti and R. Mezzenga, *Advanced Materials*, 2016, **28**, 472–478.

[63] L. van't Hag, S. Handschin, P. M. Gschwend and R. Mezzenga, *Advanced Functional Materials*, 2020, **30**, 1908458.

[64] G. Nyström, L. Roder, M. P. Fernández-Ronco and R. Mezzenga, *Advanced Functional Materials*, 2018, **28**, 1703609.

[65] Y. Shen, L. Posavec, S. Bolisetty, F. M. Hilty, G. Nyström, J. Kohlbrecher, M. Hilbe, A. Rossi, J. Baumgartner, M. B. Zimmermann *et al.*, *Nature Nanotechnology*, 2017, **12**, 642.

[66] G. Nyström, W.-K. Fong and R. Mezzenga, *Biomacromolecules*, 2017, **18**, 2858–2865.

[67] J. Zhao, S. Bolisetty, J. Adamcik, J. Han, M. P. Fernández-Ronco and R. Mezzenga, *Langmuir*, 2016, **32**, 2492–2499.

[68] G. Nyström, M. Arcari and R. Mezzenga, *Nature Nanotechnology*, 2018, **13**, 330–336.

[69] M. Bagnani, G. Nyström, C. De Michele and R. Mezzenga, *ACS Nano*, 2018, **13**, 591–600.

[70] M. Mitov, *Soft Matter*, 2017, **13**, 4176–4209.

[71] S. Vignolini, T. Gregory, M. Kolle, A. Lethbridge, E. Moyroud, U. Steiner, B. J. Glover, P. Vukusic and P. J. Rudall, *Journal of The Royal Society Interface*, 2016, **13**, 20160645.

[72] G. De Filpo, F. P. Nicoletta and G. Chidichimo, *Advanced Materials*, 2005, **17**, 1150–1152.

[73] M. Bagnani, P. Azzari, S. Assenza and R. Mezzenga, *Scientific Reports*, 2019, **9**, 1–9.

[74] M. Bagnani, P. Azzari, C. De Michele, M. Arcari and R. Mezzenga, *Soft Matter*, 2020.

[75] H. Almohammadi, M. Bagnani and R. Mezzenga, *Nature Communications*, 2020, **11**, 1–9.

[76] R. Mezzenga and M. Mitsi, *Biomacromolecules*, 2018, **20**, 55–72.

[77] A. J. Zollinger and M. L. Smith, *Matrix Biology*, 2017, **60**, 27–37.

[78] A. Vaheri and D. F. Mosher, *Biochimica et Biophysica Acta (BBA) - Reviews on Cancer*, 1978, **516**, 1–25.

[79] J. McDonagh, M. Hada and M. Kaminski, *Plasma fibronectin and fibrin formation*, in Plasma Fibronectin: Structure and Function, ed. J. McDonagh, CRC Press, 1985, pp. 121–148.

[80] D. F. Mosher, *Annual Review of Medicine*, 1984, **35**, 561–575.

[81] J. K. Czop, *Advances in Immunology*, 1986, **38**, 361–398.

[82] J. Cho and D. F. Mosher, *Journal of Thrombosis and Haemostasis*, 2006, **4**, 1461–1469.

[83] L. A. Davidson, B. D. Dzamba, R. Keller and D. W. Desimone, *Developmental Dynamics*, 2008, **237**, 2684–2692.

[84] S. Astrof and R. O. Hynes, *Angiogenesis*, 2009, **12**, 165–175.

[85] F. Grinnell, *Journal of Cellular Biochemistry*, 1984, **26**, 107–116.

[86] L. Kar, C. S. Lai, C. E. Wolff, D. Nettesheim, S. Sherman and M. E. Johnson, *Journal of Biological Chemistry*, 1993, **268**, 8580–8589.

[87] M. Y. Khan, M. Medow and S. A. Newman, *Biochemical Journal*, 1990, **270**, 33–38.

[88] P. F. de Carreira and F. J. Castellino, *Archives of Biochemistry and Biophysics*, 1985, **243**, 284–291.

[89] K. C. Ingham, S. A. Brew, T. Broekelmann and J. McDonald, *Journal of Biological Chemistry*, 1984, **259**, 11901–11907.

[90] L. Tatunashvili, V. Filimonov, P. Privalov, M. Metsis, V. Koteliansky, K. Ingham and L. Medved, *Journal of Molecular Biology*, 1990, **211**, 161–169.

[91] K. Ingham, S. Brew, M. Migliorini and T. Busby, *Biochemistry*, 1993, **32**, 12548–12553.

[92] F. Barkalow and J. E. Schwarzbauer, *Journal of Biological Chemistry*, 1991, **266**, 7812–7818.

[93] M. Mitsi, Z. Hong, C. E. Costello and M. A. Nugent, *Biochemistry*, 2006, **45**, 10319–10328.

[94] M. M. Martino and J. A. Hubbell, *The FASEB Journal*, 2010, **24**, 4711–4721.

[95] E. S. Wijelath, S. Rahman, M. Namekata, J. Murray, T. Nishimura, Z. Mostafavi-Pour, Y. Patel, Y. Suda, M. J. Humphries and M. Sobel, *Circulation Research*, 2006, **99**, 853–860.

[96] T. T. Chen, A. Luque, S. Lee, S. M. Anderson, T. Segura and M. L. Iruela-Arispe, *Journal of Cell Biology*, 2010, **188**, 595–609.

[97] S. M. Anderson, T. T. Chen, M. L. Iruela-Arispe and T. Segura, *Biomaterials*, 2009, **30**, 4618–4628.

[98] I. Raitman, M. L. Huang, S. A. Williams, B. Friedman, K. Godula and J. E. Schwarzbauer, *Matrix Biology*, 2018, **67**, 107–122.

[99] S. Bolisetty, L. Harnau, J.-m. Jung and R. Mezzenga, *Biomacromolecules*, 2012, **13**, 3241–3252.

[100] Y. Cao, S. Bolisetty, J. Adamcik and R. Mezzenga, *Physical Review Letters*, 2018, **120**, 158103.

[101] C. P. Broedersz and F. C. MacKintosh, *Reviews of Modern Physics*, 2014, **86**, 995.

[102] B. J. Berne and R. Pecora, *Dynamic light scattering: with applications to chemistry, biology, and physics*, Courier Corporation, 2000.

[103] E. Farge and A. C. Maggs, *Macromolecules*, 1993, **26**, 5041–5044.

[104] K. Kroy and E. Frey, *Physical Review E*, 1997, **55**, 3092.

[105] G. Arcovito, F. A. Bassi, M. De Spirito, E. Di Stasio and M. Sabetta, *Biophysical Chemistry*, 1997, **67**, 287–292.

[106] R. Götter, K. Kroy, E. Frey, M. Bärmann and E. Sackmann, *Macromolecules*, 1996, **29**, 30–36.

[107] M. Tassieri, R. Evans, L. Barbu-Tudoran, G. N. Khaname, J. Trinick and T. A. Waigh, *Physical Review Letters*, 2008, **101**, 198301.

[108] P. N. Pusey and W. Van Megen, *Physica A: Statistical Mechanics and its Applications*, 1989, **157**, 705–741.

[109] Y. Shen, G. Nyström and R. Mezzenga, *Advanced Functional Materials*, 2017, **27**, 1700897.

[110] Y. Cao, S. Bolisetty, G. Wolfisberg, J. Adamcik and R. Mezzenga, *Proceedings of the National Academy of Sciences*, 2019, **116**, 4012–4017.

[111] N. Ferrara, *European Cytokine Network*, 2009, **20**, 158–163.

[112] R. I. Teleanu, C. Chircov, A. M. Grumezescu and D. M. Teleanu, *Journal of Clinical Medicine*, 2020, **9**, 84.

[113] G. Lupo, N. Caporarello, M. Olivieri, M. Cristaldi, C. Motta, V. Bramanti, R. Avola, M. Salmeri, F. Nicoletti and C. D. Anfuso, *Frontiers in Pharmacology*, 2017, **7**, 519.

2. Unraveling amyloid fibril gelation by Photon Correlation Imaging: kinetics, microscopic dynamics, and temporal heterogeneity

Mattia Usuelli[‡], Vincenzo Ruzzi[‡], Stefano Buzzaccaro, Gustav Nyström, Roberto Piazza[*] and Raffaele Mezzenga[*]

The manuscript is in preparation for submission.

Summary

Despite the major recent advances in unveiling the phase diagram and the scaling behavior of βLG amyloid fibril gels, the dynamic processes behind their formation are still not clear. We studied, using Photon Correlation Imaging, the progressive dynamic arrest of βLG amyloid fibril solutions upon passage of ions through a semi-permeable membrane. We found a linear-in-time advance of the gelation front (in striking contrast with the expected diffusive behaviour), the physical origin of which we attribute being related to the Donnan effect and to electrostatic screening heterogeneity. On the side of influencing the speed of the evolution of the gelation front, the concentration of ions also tuned the entity and the spatial propagation of frozen-in stresses, that had formed over the structural arrest.

---

‡ These authors contributed equally to this work

Unraveling amyloid fibril gelation by Photon Correlation Imaging: kinetics, microscopic dynamics, and temporal heterogeneity

Mattia Usuelli,[a,‡] Vincenzo Ruzzi,[b,‡] Stefano Buzzaccaro,[b] Gustav Nyström,[a,c] Roberto Piazza[b,*] and Raffaele Mezzenga[a,d,*]

Abstract

Amyloid fibril gels, synthetised *in vitro*, are progressively emerging as appealing media for a broad reange of applications in material science; however, a fundamental understanding of how amyloid fibril gels form and evolve is still lacking. By means of Photon Correlation Imaging (PCI), we studied the gelation of β-Lactoglobulin amyloid fibril solutions upon passage of ions through a semi-permeable membrane. We observed a linear-in-time evolution of the gelation front and rich rearrangement dynamics of the gels, the entity of which depends on how effectively electrostatic interactions are screened by different ionic strengths. Our analysis confirms the pivotal role of salt concentration in tuning the properties of amyloid gels, and suggests potential routes for explaining the physical mechanisms behind the non-diffusive behaviour of the salt ions.

Introduction

Gels are, since decades, under the spotlight of both fundamental research and application advances[1–5]. Their widespread use is favoured by the possibility of gelating a wide range of colloidal systems through diverse mechanisms. At the same time, sustainability concerns encourage to narrow the virtually infinite range of synthesis routes, towards ecological sources and processes[6]. In this scenario, food sources can play a huge role, as they are both renewable and largely available[7]. Polysaccharides and proteins can, in fact, gel through modification of three main key parameters: temperature, pH or ionic strength of the initial dispersions. For instance, one can think about the percolation of TEMPO-oxidized CNFs (Cellulose Nanofibrils), upon decrease of pH towards the pKa of the carboxilic surface groups[8], the network formation of starch upon cooling[9] and the morphological transitions (both at the intra- and inter-chain levels) of κ-carrageenan and Gellan Gum upon addition of specific ions[10,11].

Among food gels, the ones made out of proteins are getting increasingly studied in many research fields. One class of proteinaceous aggregates of high relevance is amyloid fibrils[12]; synthesized *in vitro* from food sources, amyloid fibrils can form liquid-crystalline phases[13–15] and can build innovative materials with multiple functionalities (such as heavy metals removal from water[16], iron fortification[17] and sensing[18,19]). Amyloid fibrils can also originate *in vivo* from proteins or peptides that have a physiological role[20]; an enhanced understanding of this amyloidogenesis process would enable better treatment protocols of neuro-degenerative diseases correlated with the presence of amyloid-plaques (such as Alzheimer's and Parkinson's)[21]. In both the described scenarios, advances in understanding on how amyloid fibrils interact and entangle are pivotal for further steps in research and applications. An excellent model food protein for synthesising and studying amyloid fibrils is β-Lactoglobulin (βLG), which constitutes the main protein fraction of whey (a valuable side-stream of cheese production). High

---

‡ These authors contributed equally to this work.

[a] ETH Zürich, Department of Health Sciences and Technology, Schmelzbergstrasse 9, 8092 Zürich, Switzerland. E-mail: raffaele.mezzenga@hest.ethz.ch

[b] Department of Chemistry, Materials Science, and Chemical Engineering (CMIC), Politecnico di Milano, Edificio 6, Piazza Leonardo da Vinci 32, 20133 Milano, Italy. E-mail: roberto.piazza@polimi.it

[c] EMPA, Laboratory for Cellulose & Wood Materials, Überlandstrasse 129, 8600 Dübendorf, Switzerland

[d] ETH Zürich, Department of Materials, Wolfgang-Pauli-Strasse 10, 8093 Zürich, Switzerland

temperature and low pH conditions drive the unfolding and hydrolysis of βLG monomers; the formed shortened peptides, then, self-assemble into amyloid fibrils[22,23]. The resulting elongated colloidal objects (few nm in thickness and up to several μm in contour length) have a semi-flexible nature and an IsoElectric Point (IEP) close to 5[24]. At the synthesis pH (which usually ranges between 2 and 3) βLG amyloid fibrils are, therefore, positively charged and form a viscous suspension stabilized by electrostatic repulsion. Gelation is promoted by supplying ions, the role of which is to screen the surface charges and to consequently decrease the repulsive forces among the considered polyelectrolytes.

An analysis of the phase diagram of βLG amyloid fibrils suspensions, at different concentrations and ionic strengths, confirmed the potential of forming gels[25]. The scaling behaviours of the shear modulus (G) of amyloid fibril gels were found to be $G \sim c^{2.2}$ and $G \sim I^{4.4}$ (with c being the concentration of amyloids and I the ionic strength); the strong dependence of the shear modulus on I could be explained through the DLVO theory, confirming the pivotal role of salt in tuning the properties of amyloid entangled states[26]. Another recent study showed the possibility of correlating the plateau value of the intermediate scattering function of amyloid gels (extracted through a non-ergodic treatment of Dynamic Light Scattering data) to their mesh size (ξ_m)[27]. However, despite the mentioned major advances in the understanding of the static properties of already-formed amyloid gels, many unanswered questions on their dynamics still remain. How amyloid gels form, and how frozen-in stresses relax in time, are still open points in current literature.

By means of Photon Correlation Imaging (PCI), a light scattering technique able to follow dynamic phenomena with both spatial and temporal resolution, we followed the gelation of two amyloid fibril suspensions upon supply of monovalent ions (Na^+ and Cl^-) from salt reservoirs at different ionic strength. We found that the gelation front, in both cases, evolved linearly in time ($y \sim t$): such observation is in marked contrast with the expected diffusive behaviour ($y \sim \sqrt{t}$). This phenomenon was already observed in the case of a polysaccharide hydrogel[28]; its physical explanation is hypothesized to be related to a combination of Donnan effect and osmotic pressure unbalances. On the side of the interesting behaviour of the gelation front, we found out that the two gels formed at different ionic strength exhibited sudden rearrangement phenomena, the entity and the spatial extention of which was a function of the salt concentration.

The collected evidences and the performed analysis shed light onto the complex physical mechanisms that underlie amyloid gel formation, with precious benefits for enhancing the synthesis of functional materials *in vitro*.

Materials and Methods

βLG monomers purification

βLG monomers were purified from WPI (Whey Protein Isolate, Fonterra, New Zealand) according to an already published protocol[29]. To avoid the presence of residual salts during fibrillization, βLG monomers have been further purified through the following steps. 10 g of purified powder were dissolved in 90 g of Milli-Q water at neutral pH and, after complete dissolution, the pH of the solution was adjusted to 1.9 with a concentrated HCl solution (VWR Switzerland). Nylon syringe filters (FilterBio®, ⌀ 0.22 μm) were used to remove eventual aggregates and to pour the solution into dialysis membranes (Spectra/Por® Standard RC Tubing, MWCO 6-8 kDa, D = 32 mm, Spectrum Laboratories Inc.), which were afterwards closed with clips and put in 5 L of deionized water at pH 3. The equilibration bath was changed six further times with 5 L of Milli-Q water at neutral pH; the filled membranes were left in each bath for a minimum time of 6 hours. The used succession of the pH values of the equilibration baths (3 for the first, and neutral for six following ones) enabled keeping the pH of the βLG monomer solutions to values lower than the IEP of the protein, and allowed avoiding therefore undesired aggregation phenomena. At the end of the dialysis process, the pH of the βLG monomers solution was adjusted to 2 with a concentrated HCl solution. The mass fraction of monomers was determined through gravimetric analysis, by taking aliquotes of 400 μL and letting

them evaporate in a $60\,°C$ oven; as a consequence of dilution over the dialysis process, the weight fraction was determined to be 3.8 wt%. 120 mL of the solution were kept for preparing amyloid fibrils, while the rest was freeze-dried for further usage.

βLG amyloid fibrils synthesis and characterization

108 mL of Milli-Q at pH 2 were used to dilute the above-mentioned 120 mL of βLG monomers solution, to reach a final weight fraction of 2 wt%. The resulting solution was transferred in a Schott bottle and heated up at $90\,°C$ for 5 hours, while stirring with a $5 \times \varnothing\, 0.75$ cm Teflon-coated magnetic stirrer. The solution was stirred at 100 RPM for the first 1 h and 20 min of the process; successively, the Schott bottle was manually shaken to break the gel layer at the interface, and the stirring speed was increased to 120 RPM until the end of the process. After the 5 hours, the system was quenched with ice. The resulting solution of amyloid fibrils was centrifuged in 50 mL tubes to remove macroscopic aggregates, two times at 5000 g for 10 minutes, and one time at 20000 g for 15 minutes. The solution was stored in a 200 mL plastic beaker and, before further usage, was newly centrifuges in plastic vials at 10000 g for 10 minutes (to remove aggregates formed over the storing process).

The formed amyloid fibrils were characterized through AFM (Atomic Force Microscopy) imaging. For the preparation of the AFM sample, a 0.01 wt% solution of βLG amyloid fibrils was prepared through dilution with Milli-Q at pH 2. Afterwards, 20 μL of the mentioned dispersion was deposited on the surface of a freshly cleaved mica and subsequently rinsed with 1 mL of pH 2 Milli-Q, upon incubation for 2 minutes. Gentle drying with airflow completes the sample preparation, which was afterwards characterized in ambient conditions with a Dimension FastScan Bio scanning probe microscope (Bruker, USA), using a commercial cantilever (Bruker, USA) working in tapping mode.

The amyloid fibrils, together with a statistical analysis performed using the open-source software FiberApp[30], can be appreciated in Fig. S1.

βLG amyloid fibril gels preparation and rheological characterization

As stated in the introductory section, this work focuses on perfusion-induced amyloid fibril gels. The gels were prepared in PS cuvettes (with external dimensions of $12 \times 12 \times 45$ mm and optical path of 10 mm) with 4 optical windows (Kartell, Italy), by pouring 2 mL of 2 wt% amyloid fibril solutions. Successively, the piston of a 2.5 mL syringe (Terumo Europe) was removed and the remaining plastic part was transversely cut with a scissor, with the aim of creating a cylindrical reservoir for salt solution. One side of the cylindrical reservoir was sealed (using Parafilm®) with a dialysis membrane, obtained from one side of a dialysis tube (MWCO 12 kDa, D-9777, lot. 10B049777, Sigma-Aldrich Chemie GmbH) which had previously been washed with deionized water. 1.5 mL of pH 2 NaCl solutions (at either 150 or 300 mM, depending on the performed experiment) was poured into the sealed cylindrical reservoir, which had previously been put in contact with the βLG amyloid fibril dispersion in the plastic cuvette. In this way, the salt could pass through the dialysis membrane into the amyloid fibril dispersion. Before carrying out the experiments, the density of the used solutions (300 mM NaCl at pH 2, 150 mM NaCl at pH 2 and 2 wt% amyloid fibrils in pH 2 Milli-Q water) was determined by measuring the weight of volumetric aliquots. Such an analysis confirmed the higher density of the amyloid dispersion; considering that such a solution was placed in the bottom part of the cuvette, there were no inverse density gradients which could enhance the diffusion of salt through the creation of convective rolls[28]. The final system, before starting the measurement, was sealed with Parafilm® to avoid evaporation.

To show the gel nature of the prepared samples, three systems prepared with a 300 mM NaCl solution were characterized through oscillatory sweeps. An AR 2000 stress-controlled rheometer (TA Instruments) was used in a plate-plate (40 mm) geometry: after setting the temperature control to $20°C$, the upper reservoir containing the salt solution was removed from the cuvettes and ~ 500 μL of the formed gel was sampled with the use of a plastic spatula and deposited on the rheometer. After

reaching the geometry gap of 400 μm, a solvent trap was put on the rheometer and oscillator sweep measurements at 1% strain between 0.01 and 100 Hz were performed. The results of the statistical analysis of the three independent measurements are represented in Fig. S2.

Photon Correlation Imaging (PCI)

Before detailing the experimental setup and the image analysis approach used in our study, we find it beneficial to share key information on the used technique.

Photon Correlation Imaging measures the intensity time-correlation function of the light scattered by the studied sample, with both temporal and spatial resolution: this allows to probe the local dynamics within the scattering volume, with an eye open to temporally heterogeneous events.

In PCI experiments, a speckled image of the scattering volume at a given angle θ is formed on a multipixel detector. The imaging optics consist in a lens and a diaphragm placed at the focal distance, which select a precise scattering wave vector q, and cause in parallel the "speckled" appearance of the collected images. The intensity at each given point on the image plane originates from the interference of the light scattered by a finite-size region in the sample plane. Quantitatively, the detected speckle patterns, made by N pixels, are firstly divided into regions of interest (ROIs). Then, the *space-time degree of correlation* $c_I(\mathbf{r}, t, \tau)$ is computed as:

$$c_I(\mathbf{r}, t, \tau) = \frac{\langle I_p(t) I_p(t + \tau) \rangle_{\mathbf{r}}}{\langle I_p(t) \rangle_{\mathbf{r}} \langle I_p(t + \tau) \rangle_{\mathbf{r}}} - 1 \tag{1}$$

The notation $\langle ... \rangle_{\mathbf{r}}$ indicates the ensamble spatial average of a ROI centered in $\mathbf{r}$. To minimize the influence of imaging/analysis procedures[31], it is often useful to define a normalized version of the space-time degree of correlation $\hat{c}_I(\mathbf{r}, t, \tau)$ by introducing $c_I(\mathbf{r}, t, 0)$, the relative variance of the intensity measured in $\mathbf{r}$ at time t[28]:

$$\hat{c}_I(\mathbf{r}, t, \tau) = \frac{c_I(\mathbf{r}, t, \tau)}{c_I(\mathbf{r}, t, 0)} \tag{2}$$

The multi-speckle and the near-field scattering natures of the technique allow to keep a parametric dependence on the time from the beginning of the experiments (t) and on the position $\mathbf{r}$, respectively. One key consequence of this, is the possibility of catching both temporally and spatially heterogeneous phenomena. More in detail, decorrelation bursts can be highlighted by means of the so-called "Dynamic Activity Maps" (DAMs)[32], without loosing the possibility of averaging $\hat{c}_I(\mathbf{r}, t, \tau)$ over time to locally quantify the dynamics of the colloidal objects through the intensity correlation function $g^{(2)}(t, \mathbf{r}, \tau) - 1 = \langle \hat{c}_I(\mathbf{r}, t, \tau) \rangle_{\delta t}$. The time-span δt, over which the correlation index is averaged, has to be shorter than the characteristic timescale of the evolution of the system. This is favoured, in practice, by the multi-speckle nature of the technique, that allows a faster averaging compared to other correlation techniques that employ single-speckle detectors (like the majority of Dynamic Light Scattering setups).

For details about the PCI equipment used in this study, we refer to a recently published article where the same experimental configuration was used[33]. The cuvette containing the amyloid fibril solution was inserted in the thermostatic holder of the setup, which was connected to a recirculating bath. The temperature was kept constant over the course of the entire experiment, with oscillations that did not exceed ≈ 0.1 °C.

The sample was illuminated by a vertical laser sheet ($\lambda = 532$ nm, Ventus Diode-Pumped Solid State) and the scattering volume was imaged on a CMOS camera (Hamamatsu Orca Flash 4.0, 2048 × 2048 square pixels of size 6.5 µm, 16-bit depth), by an achromatic doublet set at $\theta = 90°$ with respect to the illumination plane. The mutual distances between the optical elements in the imaging segment set the magnification close to 1 (with a magnified pixel size having a size of 6.7 µm). The diaphragm placed in the focus of the imaging lens allowed to precisely select a specific scattering wave vector
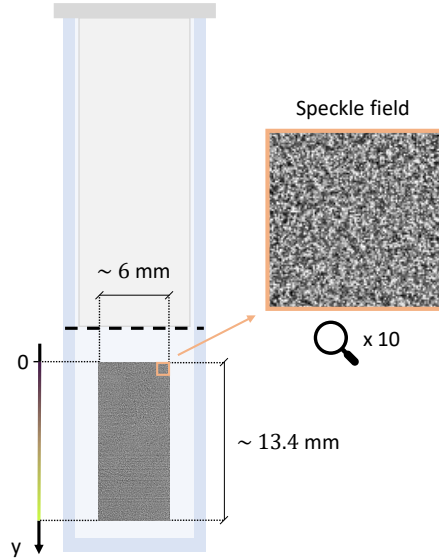
Figure 1. Schematic of the cuvette where the gelation is induced. The gelation front is considered to start from the dialysis membrane (dashed black line in the proximity of the syringe), and to evolve in the positive y direction. The 0 value of the y axis is taken in correspondence to the beginning of the imaged area: a progressive increment of the distance from the 0 value is color-coded with a shift from dark brown to bright yellow (as represented on the y axis itself). The probed area has a size around 13.4 × 6 mm and creates on the CMOS camera an image with a speckled appearance (as shown by magnification in the right-hand side of the figure).

$q = (4\pi/\lambda)n\sin(\theta/2) \approx 22$ µm^{-1}. In this configuration, the speckle size is $\sim 13 \times 13$ µm, which corresponds to 2×2 pixels.

Images of 2000 (V) × 900 (H) pixels were acquired with the above-mentioned CMOS camera, with an exposure time of 10 ms and a frame rate of 1/60 fps. The imaged area is shown in Fig.1, with a color-code that evolves from brown to yellow as the distance from the dialysis membrane increases; such a colour scheme will be thoroughly used in the upcoming sections. More precisely, the imaged area starts around 4 mm below the dialysis membrane, to let the gelation front properly adapt from the cylindrical reservoir to the squared cross-section of the cuvette. The speckled appearance of the images, once corrected for noise and not uniform illumination, can be appreciated in Fig. S3 and in the magnification on the right-hand side of Fig.1.

The correlation index $\hat{c}_I(\mathbf{r}, t, \tau)$ is then computed for each ROI using a custom-made code running on MATLAB®[34].

Results & Discussion

General considerations on sample gelation

The 2 wt % amyloid fibril suspensions were gelled with two NaCl salt solutions at pH 2, having a molarity of 300 mM and 150 mM, respectively. In the following, we will refer to the first mentioned sample as the one with higher salt molarity (HSM), and to the second as the one with lower salt molarity (LSM). Due to the finite size of the reservoir, for both samples, the concentration of the salt lowers as a consequence of diffusion. Considering the ratio between the volumes of the βLG and the salt solutions (respectively 2 mL and 1.5 mL), an homogeneous diffusion of the salt would lead to a final concentration of ~ 129 mM (for HSM) and of ~ 65 mM (for LSM). According to previous studies[25], the mentioned values of ionic strength allow to transform 2 wt% βLG amyloid fibril

solutions into gels. For the HSM sample (whose gel state was confirmed by rheology experiments, Fig.S2), there was actually the potential risk of the salt driving local agglomeration, and increasing therefore the turbidity of the sample; in the phase diagram shown by Bolisetty and co-workers, gels approach the state of translucent solutions, as the molarity increases. However, it has to be considered that the mentioned phase diagram refers to materials prepared by mixing[25]. In Fig.S4 it is possible to appreciate the transparency of the HSM gel prepared by perfusion: we attribute the difference to the lower quantity of agglomerates created with a gentle supply of salt, compared to the rapid local increase of salt molarity that accompanies the mixing method.

Another indication of the limited agglomeration of amyloid fibril, over the duration of the whole experiment, can be appreciated by analysing the temporal evolution of the scattered intensity of the HSM sample. Since during the gelation kinetics the scattered intensity and the correlation index are expected to depend only on the vertical position y, the speckle pattern images were each subdivided into 40 ROIs with a height of 50 pixels and laterally extending over the whole width of the investigated sample region (900 pixels). Each ROI contains therefore about 11250 speckles, a value which was found to yield a good vertical resolution with a limited statistical noise in the correlation function.

The time evolution of the normalized averaged scattered intensity ($\langle I_p(t)\rangle_{\mathbf{r}}/\langle I_p(0\ s)\rangle_{\mathbf{r}}$) for a ROI located at the bottom part of the cuvette is represented in Fig. S5. It can be appreciated how the scattered intensity increases of a factor slightly larger than 2: despite this being an indication of changes in the form factor of the scattering objects, the increase has a moderate entity if compared to the ones detected in other food gels. In fact, in alginate dispersions, it was possible to observe an increase of the scattered intensity of a factor 20, upon diffusion of divalent cations[28].

Besides, as we shall see, the final value of the ionic strength (~ 139 mM and ~ 65 mM, for HSM and LSM, respectively) notably affects the mechanical properties of the amyloid fibril networks. As mentioned in the introduction, Cao and co-workers showed that the shear elastic modulus (G) of amyloid gels scales with the ionic strength (I) with an exponent close to 4[26]; the result was explained with the DLVO theory, confirming that the ionic strength has a pivotal role in transforming entanglements into physical cross-links. In the two analysed samples, the factor 2 in the ratio between the final ionic strengths translated in a factor larger than 10 in the ratio between the probabilities of transforming entanglements into cross-links. As a consequence, we might expect the LSM sample to be weaker and more susceptible to stress relaxation events.

Evolution of the gelation front

Fig.2 shows the behaviour of the gelation front for both HSM and LSM. Accordingly with the schematic shown in Fig.1, it is possible to compute the values of the normalized correlation index for different ROIs, progressively distant from the dialysis membrane. If the values of the normalized correlation index (at $\tau = 1$ min) are plotted as a color map, as a function of the distance from the first ROI (y) and of the time from the beginning of the observation (t), it is possible to appreciate a progressive slowing down of the dynamics (Fig.2A and C). For HSM (panel A), after a time-scale of 600 minutes, the whole imaged area gets fully arrested. In the case of LSM (panel C), double the time is needed to gel the same area. As a consequence of the progressive evolution of the gelation front, the higher the distance of the ROIs from the membrane, the higher the characteristic time at which the dynamics shift from totally decorrelated (red colour) to arrested (dark blue color). If a characteristic value of $\hat{c}_I$ is considered as a benchmark for gelation, it is possible to compute the gelation time (t_g, calculated as the instant when $\hat{c}_I$ gets larger than 0.4) as a function of the distance from the first ROI. In Fig.2B and D, the position (y) of the different ROIs is plotted as a function of t_g for HSM and LSM, respectively. In both cases, the gelation front initially advances linearly with time with a speed of $v = 1.47 \cdot 10^{-2}$ mm/min and $v = 7.77 \cdot 10^{-3}$ mm/min for HSM and LSM, respectively. Approaching the bottom of the cell, the front velocity increases. Fig.2B and D show that this acceleration is more evident in LSM.

As already pointed out, βLG gelation is caused by the local increase of ionic strength, which lowers the electrostatic repulsion between fibrils and allows the formation of physical bonds. Assuming that
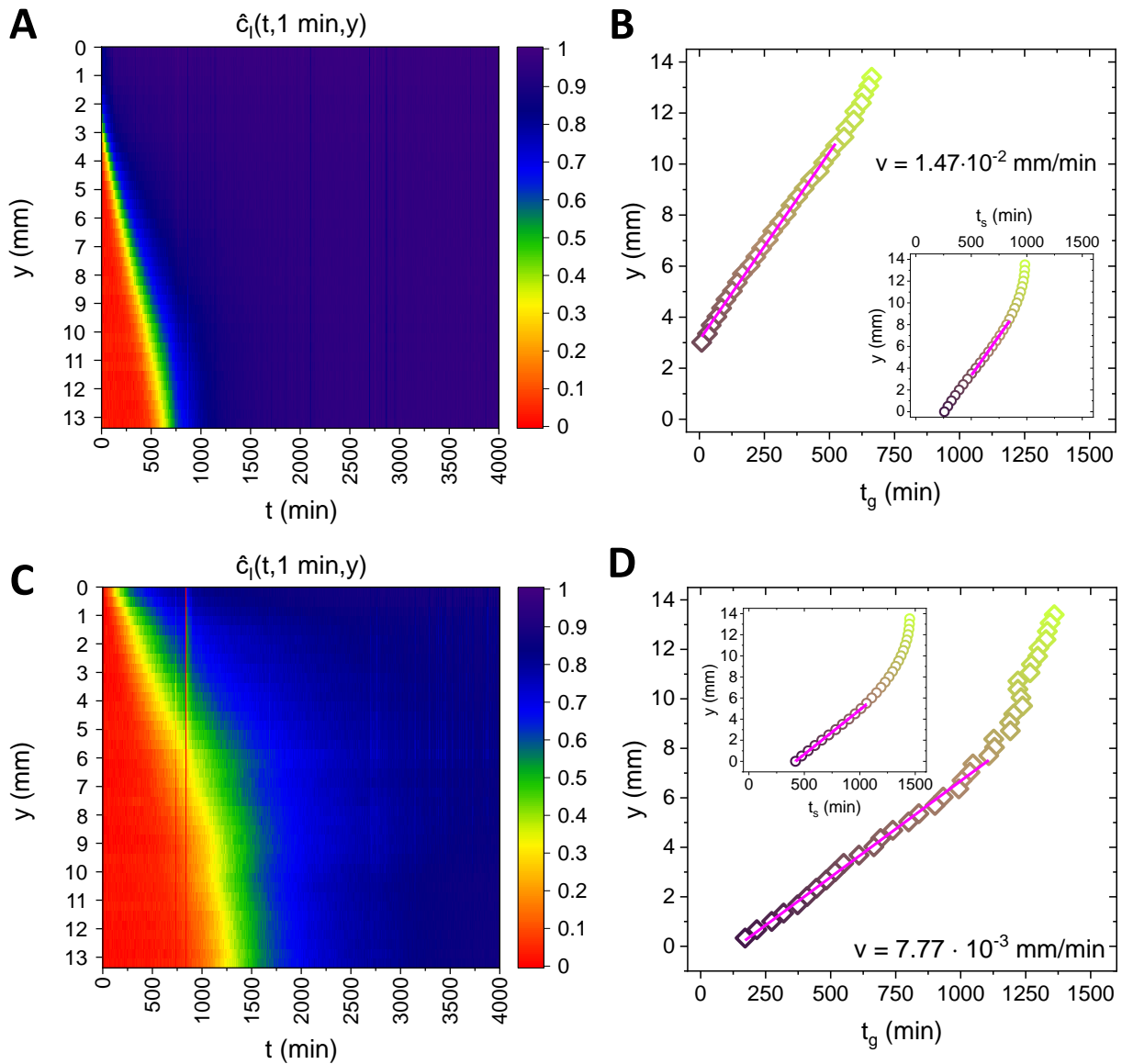
Figure 2. (**A**,**C**) Color map representing the behaviour of the correlation index calculated at a fixed $\tau = 1$ min, as a function of the distance from the first ROI (y axis) and of the time from the beginning of the observation (x axis), for HSM and LSM, respectively. (**B**,**D**) Distance from the first ROI (y axis) as a function of gelation time (t_g, x axis), for HSM and LSM, respectively. In the insets, the evolution of the gelation front computed from the performed simulations is shown.

gelation takes place instantaneously when the local ion concentration reaches a threshold value, we can suppose that the gel front kinetics resembles the one of the aforementioned threshold concentration. A simple diffusive behaviour of salt ions, which predicts an increase of the gel thickness as the square root of time ($y \sim \sqrt{D\,t}$), is clearly not able to account for the initial constant velocity. The observed linear evolution might indicate the existence of a net force that causes an advective behaviour.

To test this hypothesis, numerical simulations of the advection-diffusion of salt ions in aqueous solution were performed with the finite element software Flex PDE 7 Professional (Pde Solutions Inc., USA). We assume in our simulation that, in addition to diffusion, ions drift towards the cell bottom with a velocity v_d equal to the extracted experimental velocity of the gelation front.

The geometry of the problem allows us to consider a 1D coordinate system (y-axis positive direction towards the cell base) with a self-adaptive mesh of 10000 elements. The reservoir occupies the upper l=15 mm of the cell, while the whole simulated region has a vertical extension H=35 mm.

Denoting with $c(y,t)$ the salt concentration at time t and height y, v_d the drift velocity towards the positive y-direction and $D \simeq 1.5 \cdot 10^{-5}$ cm^2/s the Cl$^-$ ions diffusion coefficient, the generalized diffusion equation to be numerically solved is the following:

$$\frac{\partial c(y,t)}{\partial t} = -v_d \frac{\partial c(y,t)}{\partial y} + D \frac{\partial^2 c(y,t)}{\partial y^2} \tag{3}$$

with initial condition $c = c_0$ in the reservoir and $c = 0$ elsewhere and zero-flux boundary conditions in correspondence of the cell walls: $\partial c/\partial y|_0 = \partial c/\partial y|_H = 0$. Mass conservation is ensured by keeping constant the integral $\int_0^H c(y)dy = c_0 l$.

The two experimental conditions ($c_0 = 300$ mM, $v_d = 1.47 \cdot 10^{-2}$ mm/min and $c_0 = 150$ mM, $v_d = 7.77 \cdot 10^{-3}$ mm/min) were both simulated, and the results of the simulations are shown in Fig. S6. For both cases, it can be noted how the initial steep concentration gradient lowers with time, as a consequence of the concomitant advective and diffusive behaviours. It is important to outline that the simulated region includes the whole cell, while the region experimentally studied is 4 mm distant from the membrane and extends for 13.4 mm in the gelation direction. More considerations on the position of the membrane and on the physical phenomena that happen in its proximity are shared in Fig. S7 and in section 7 of the ESI. In the simulation counterpart, which assumes an ideal contact between the salt reservoir and the colloidal dispersion (without the need of the syringe being partially immersed in the dispersion itself), the distance of the beginning of the probed zone from the membrane is considered to be 6 mm and the analysed area extends, therefore, from such a starting point for 13 mm (as in the case of the performed experiments). As a consequence, in the following considerations only the simulated data-points with a distance between 6 and 19 mm from the membrane were considered. As shown in the inset of Fig.2B and D, by taking the temporal evolution of the relative concentration $c/c_{eq} \simeq 0.7$ along y, the measured advance of the gelation front is recovered for both samples: after the initial linear advance mainly ruled by the advective contribution, the ions concentration speeds up in proximity of the bottom part of the cuvette.

Further hints to clarify the time evolution of the gelation front can be taken from previous studies on food gels. Secchi and co-workers, while studying the evolution of the gelation front of alginate gels prepared by perfusion of Ca^{2+}, also noted a linear advance of the gelation front[28]. The reason was attributed to an alginate depletion layer in front of the gel, observed thanks to a minimum in scattered intensity; the existence of such layer was explained through a combination of the spatial advance of the gel with a concomitant shrinkage, the consequence of which was the creation of an alginate-free zone. The inverted density profile presumably caused natural micro-convective rolls, which are known to influence the diffusive behaviour by speeding up its dynamics. The mentioned mechanisms, in our case, may hardly account for the observed phenomenon: in fact, shrinkage phenomena in βLG amyloid fibril gels are very limited (as confirmed by Fig. S4). As an example of such statement, we observed that gels keep being transparent and without observable macroscopic shrinkage, even weeks after they have been prepared with the protocol mentioned in this manuscript (data not shown).

An hypothesis that better aligns with the observed gelation dynamics of amyloid gels relies on electrostatic effects. In a former study on the gelation of a pectin dispersion upon perfusion of divalent

cations[35], the front was observed to advance diffusively: it has to be noted that, in the mentioned experiment, the ionic strength of the medium was increased through dissolution of monovalent ions. The authors, comparing the different behaviours observed in the alginate (with no further salt added) and pectine (with further NaCl added) cases, hypothesized that the Donnan effect might be thought as responsible of what was observed[36]. More in detail, in systems where energetic contributions influence the entropy-driven spatial configuration of charged colloids, the electroneutrality of the whole system can be kept with a concomitant generation of an electrostatic potential. Such further energetic contributions have an additional influence on the spatial configuration of the charged species present in the system. This is the case, as an example, if two compartments containing ionic species are separated by a selectively permeable membrane[37,38]. Further evidences of the mentioned phenomenon can be observed in the barometric density profile of charged colloids, where an electrostatic potential difference has been both theoretically postulated and measured[39–41]. In our case, we may infer that the gelation front acts as a sort of moving membrane separating the salt-rich region from the one containing only βLG amyloid fibrils (that at pH 2 are polyelectrolytes)[38,42]. The electrostatic force that pushes the ions towards the bottom of the cell, and makes therefore the gelation front to advance linearly, is caused by the Donnan potential across this moving membrane. Moreover, on the side of the electric force that stems from the Donnan potential, changes in the elecrostatic screening length in the polyelectrolyte system as the salt advances might further encourage the described phenomenon[43].

Gel restructuring events

We focus now on analysing more in detail the behaviour of the normalized correlation index, for HSM and LSM.
In Fig.3A, the behaviour of $\hat{c}_I$ at $\tau = 1$ min for HSM, at different distances from the first ROI (same color-code as in Fig. 1), can be appreciated. Despite this being a different plot format than the one of Fig.2A, more information can actually be visualized, especially in terms of decorrelation events. The four arrows in panel A of Fig.3 refer to the other panels, with a color-scheme that relates the colours of the arrows to the ones of the frames of the panels. The mentioned panels consist of Dynamic Activity Maps, where the spatial distribution of the correlation index is represented by a false-color map. In order to better identify the temporal heterogeneities within the sample in both the horizontal and vertical directions, it is useful to redefine the ROIs as squares of 20×20 pixels.
After 50 minutes from the beginning of the observation (B), only the top part of the area is arrested (dark blue color), while the rest of the solution exhibits a totally decorrelated state (at the shortest computable delay $\tau = 1$ min). The explanation of the different dynamics of, respectively, solution and gelled states, requires to dig into the motion of semi-flexible polymers. Before doing so, it is useful to extract further static parameters of the network of interest. The cubic lattice (l_c) model allows to give an estimation of the mesh size (ξ_m) of the network at the studied concentration ($c_p \sim 2$ wt% ~ 20 mg/mL) of protein; assuming a conversion of monomers into amyloids (ϕ) of roughly 40%, a radius of the fibers (a) of 1.5 nm (Fig. S1) and a fibers density (ρ) of 1300 mg/mL we obtain[27]:

$$l_c = \sqrt{\frac{3a^2\pi\rho}{c_p\phi}} \sim 60\,nm. \tag{4}$$

It can be noted that the length-scale probed by the optical apparatus ($\delta = 2\pi/q \sim 300$ nm) is five times larger than the estimated mesh size, and is therefore sensitive to the characteristic dynamics of multiple filaments. Before the solution transforms into a gel, the single fibrils can bend, rotate or translate. All the mentioned typologies of motion are constrained by surrounding objects, due to the presence of entanglement points[44]; however, the non-fixed nature of such entanglements allows motions whose entity makes the correlation index fully decay. When the local concentration of salt gets higher, the probability of transforming entanglements into long-lived crosslinks increases, due to the
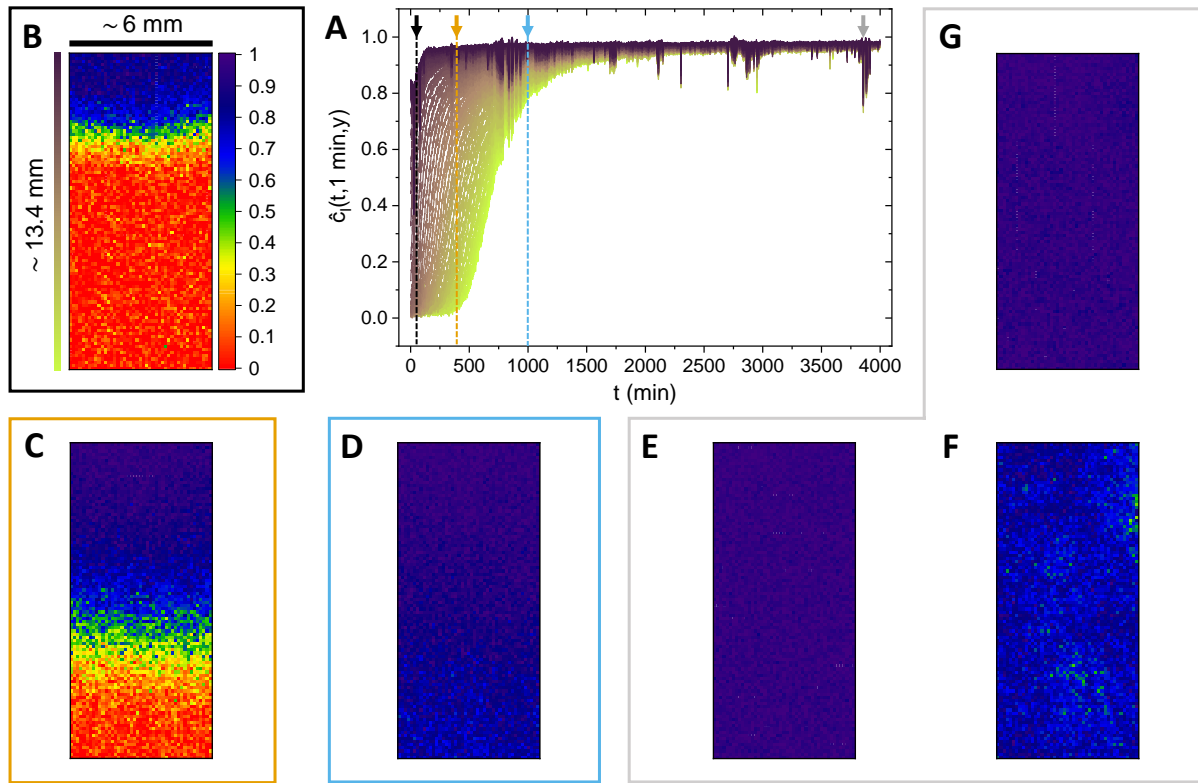
Figure 3. (**A**) Normalized correlation index ($\hat{c}_I$) of HSM, computed at a constant delay time $\tau = 1$ min, as a function of the time from the beginning of the observation (t). The different curves, accordingly with the color-scheme in Fig.1, represent ROIs at different distances from the membrane. The coloured arrows refer to the other panel that compose the figure, accordingly with the colour of the frames by which they are surrounded. (**B**) Dynamic Activity Map (DAM) at $t_B = 50$ min. (**C**) DAM at $t_C = 400$ min (**D**) Fully arrested state of the solution, which has transformed into a gel ($t_D = 1000$ min). (**E**-**F**-**G**) DAMs sequence that shows the occurrence of a rearrangement event of moderate entity. The three DAMs are at $t_{E,F,G} = 3856$, 3857 and 3858 min, respectively.

concomitant screening of electrostatic repulsive forces[26]. As a consequence, the rotational and translational degrees of freedom are further hindered and the fibrils only express bending fluctuations[45], whose entity is small compared to the probed length-scale. As a consequence, close-to-one values of $\hat{c}_I$ are observed.

As the gelation front proceeds, progressively more ROIs get arrested: panel C shows a situation where half of the area is arrested, and the other half still shows fully expressed decorrelation dynamics. After a time-scale of 1000 minutes (panel D), the entire examined area is arrested. However, biological and colloidal gels are often not truly fully arrested once formed. As a function of the underlying aggregation kinetics, stresses might freeze inside the structure, and subsequently release through time-intermittent rearrangement phenomena[28,34,46]. Intuitively, one may guess that a high salt concentration has two opposite effects on amyloid networks. On the one hand, it promotes the gelation faster than a lower concentration of ions would do: consequently, frozen in stresses are more likely present in the initial configuration. On the other hand, the higher probability of converting entanglements into cross-links determines a higher number of constraints for a single fibril; a more formal way to express such a concept, is by affirming that the cross-linking length approaches the entanglement one ($l_c \sim l_e$)[47]. In such a state, the relaxation of stresses is made more difficult by the high number of long-lived cross-links: heterogeneous phenomena are expected, as a consequence, to be not pronounced in entity. An evidence that supports the given picture is represented in panels E, F and G, where the evolution of the most pronounced rearrangement event over the entire measurement is represented. The occurrence of the mentioned event is indicated with the grey arrow in Fig.3A. At 3856 minutes the structure is fully arrested (E): then, a rearrangement event that spans the entire illuminated area happens, and causes the correlation index to drop to lower values (F). One minute later, the structure is again fully arrested in the new, less stressed configuration assumed after the rearrangement (G). The moderate entity of the re-configuration event is appreciable by the fact that $\hat{c}_I$ locally drops, at maximum, to values close to 0.7.

We now shift our focus on the sample gelled with a lower ionic strength (Fig.4). The arrows in Fig.4A refer to the other panels, accordingly with the used color code. As already pointed out for the HSM sample, reconfigurations events mostly occur after the full evolution of the gelation front. We may guess that the same applies, in an even more enhanced way, for the LSM sample. After the gelation front had encompassed the entire probed area, within the first 2500 min of observation (panels B, C and D), the behaviour of the correlation index from ~ 2500 min onward is characterized by a high number of sudden drops, of which the largest is displayed in the sequence (E-G). A fully arrested structure (E) suddenly exhibits hints of decorrelation that propagates over the entire upper part of the cuvette (F), with successive acquisition of a new arrested state over the timescale of few minutes (G). A first point of comparison between the mentioned event and the one of the HSM sample (discussed above), regards their entity and spatial propagation. While, in the case of HSM, $\hat{c}_I$ dropped to minimum values of ~ 0.7 in the whole imaged area, for LSM we appreciate hints of local full decorrelation in a relatively small portion of the illuminated region. The decorrelation entity can again be explained by a lower conversion of entanglements into crosslinks, which allow single fibrils to express more enhanced decorrelation dynamics. The spatial propagation of the relaxation events may instead be related to the different rigidity of the formed structures; indeed, as already observed, HSM is characterized by a higher elastic modulus G with respect to the LSM sample, because of its higher ionic strength[26]. It is interesting to notice that the region interested by the reconfigurations in the LSM gel is the most aged one, where the gel first forms, in contrast to what happens in alginate gels where the decorrelation always starts from the sol-gel interface[28].

A second point of comparison lies, instead, in the time needed for the system to reach again high correlation. While, in the case of the HSM sample, 1 minute was sufficient to bring $\hat{c}_I$ back to close-to-one values, the same statement does not hold true for the LSM sample. In the latter, more than 5 minutes are needed for $\hat{c}_I$ to raise to pre-rearrangements values, confirming that a lower salt concentration is less effective in driving the conversion of entanglements into cross-links.

In ESI, we present a similar analysis on the most drastic rearrangement events that happen during the
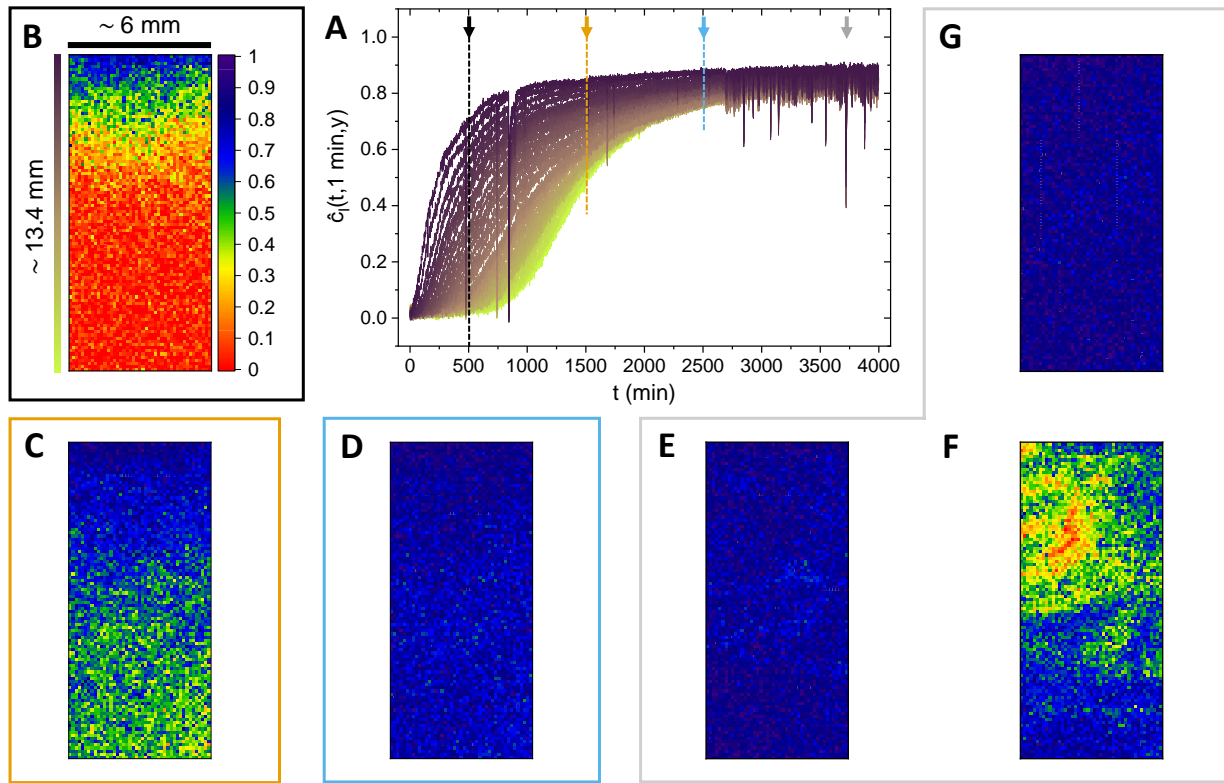
Figure 4. (**A**) Normalized correlation index ($\hat{c}_I$) of LSM, computed at a constant delay time $\tau = 1$ min, as a function of the time from the beginning of the observation (t). The different curves, accordingly with the color-scheme in Fig.1, represent ROIs at different distances from the membrane. (**B**) Dynamic Activity Map (DAM) at $t_B = 500$ min. (**C**) Further advance of the gelation front ($t_C = 1500$ min). (**D**) DAM at $t_D = 2500$ min. (**E-F-G**) DAMs sequence that shows the occurrence of a rearrangement event in the upper part of the cuvette ($t_E = 3720$ min, $t_F = 3721$ min and $t_G = 3730$ min min).

formation of the gels (Fig. S8 and section 8 therein). Despite it is not possible to reach clear conclusions on the spatial propagation of the stress-release events (due to the limited size of the region where the gel had already formed), the other considerations shared above hold true. More in detail, also for rearrangement events that happen during the gelation process, a higher ionic strength is correlated with less enhanced drops of the correlation index and to a faster regain of pre-reconfiguration values.

Conclusions

The performed analysis gives precious hints on the dynamic properties of amyloid fibril gels, prepared upon ion permeation into entangled networks. A first, pivotal point to be highlighted is the observed linearity of the advance of the gelation front; despite such phenomenon had already been observed in other systems, the discrepancy with an expected diffusive behaviour is, at first, confusing. We shared the hypothesis that the observed behaviour might be related to the Donnan effect and to electrostatic screening heterogeneity; we are currently working on developing a physical model to describe the mentioned observation. Another relevant point to be highlighted is the role of the salt concentration in tuning both the velocity of the gelation front and the entity of rearrangement events. A higher salt concentration not only allows the gelation front to proceed faster, but also has a role in converting many entanglement points into physical cross-links. As a consequence, the gel has a more fixed structure and is less sensitive to stress-releasing events spanning through the imaged area. On the other hand, a lower salt concentration makes the gelation front evolve slower; the parallel, lower conversion of entanglements into cross-links allows wide and drastic reconfigurations both during gelation and after an arrested structure is formed. In the case of lower salt molarity, more time is needed for the normalised correlation index to raise back to pre-stress release events values and the reconfigurations are mostly related to aged parts of the sample. The highlighted phenomena might be a common feature to all those systems that form arrested structures because of the screening of electrostatic repulsive forces, and have therefore an ionic strength-dependent crosslink length (l_c).

We believe that the shared observations and explanations widen the understanding of amyloid networks, and set a more solid background for future studies and analysis.

Author Contributions

The authors contributions are listed accordingly with the guidelines from CRediT, for standardised contribution descriptions. Mattia Usuelli: conceptualization, data curation, formal analysis, investigation, methodology, software, visualization, writing - original draft. Vincenzo Ruzzi: conceptualization, data curation, formal analysis, investigation, methodology, software, writing - review and editing. Stefano Buzzaccaro: resources (design and construction of the PCI setup), conceptualization, methodology, supervision, writing - review and editing. Gustav Nyström: conceptualization, methodology, supervision, writing - review and editing. Roberto Piazza: conceptualization, funding acquisition, methodology, project administration, resources, supervision, writing - review and editing. Raffaele Mezzenga: conceptualization, funding acquisition, methodology, project administration, resources, supervision, writing - review and editing.

Conflicts of interest

There are no conflicts to declare.

Acknowledgements

Bibliography

[1] E. Zaccarelli, *Journal of Physics: Condensed Matter*, 2007, **19**, 323101.

[2] D. Saha and S. Bhattacharya, *Journal of Food Science and Technology*, 2010, **47**, 587–597.

[3] G. Tiwari, R. Tiwari, B. Sriwastawa, L. Bhati, S. Pandey, P. Pandey and S. K. Bannerjee, *International Journal of Pharmaceutical Investigation*, 2012, **2**, 2.

[4] S. Zhao, W. J. Malfait, N. Guerrero-Alburquerque, M. M. Koebel and G. Nyström, *Angewandte Chemie International Edition*, 2018, **57**, 7580–7608.

[5] D. Arcos and M. Vallet-Regí, *Acta Biomaterialia*, 2010, **6**, 2874–2888.

[6] J. D. Sachs, G. Schmidt-Traub, M. Mazzucato, D. Messner, N. Nakicenovic and J. Rockström, *Nature Sustainability*, 2019, **2**, 805–814.

[7] Y. Cao and R. Mezzenga, *Nature Food*, 2020, **1**, 106–118.

[8] M. Arcari, R. Axelrod, J. Adamcik, S. Handschin, A. Sánchez-Ferrer, R. Mezzenga and G. Nyström, *Nanoscale*, 2020, **12**, 11638–11646.

[9] M. J. Miles, V. J. Morris, P. D. Orford and S. G. Ring, *Carbohydrate Research*, 1985, **135**, 271–281.

[10] M. Diener, J. Adamcik, A. Sánchez-Ferrer, F. Jaedig, L. Schefer and R. Mezzenga, *Biomacromolecules*, 2019, **20**, 1731–1739.

[11] M. Diener, J. Adamcik, J. Bergfreund, S. Catalini, P. Fischer and R. Mezzenga, *ACS Macro Letters*, 2020, **9**, 115–121.

[12] Y. Cao and R. Mezzenga, *Advances in Colloid and Interface Science*, 2019, **269**, 334–356.

[13] G. Nyström, M. Arcari and R. Mezzenga, *Nature Nanotechnology*, 2018, **13**, 330–336.

[14] M. Bagnani, G. Nyström, C. De Michele and R. Mezzenga, *ACS Nano*, 2018, **13**, 591–600.

[15] M. Bagnani, P. Azzari, S. Assenza and R. Mezzenga, *Scientific Reports*, 2019, **9**, 1–9.

[16] S. Bolisetty and R. Mezzenga, *Nature Nanotechnology*, 2016, **11**, 365–371.

[17] Y. Shen, L. Posavec, S. Bolisetty, F. M. Hilty, G. Nyström, J. Kohlbrecher, M. Hilbe, A. Rossi, J. Baumgartner, M. B. Zimmermann *et al.*, *Nature Nanotechnology*, 2017, **12**, 642.

[18] G. Nyström, M. P. Fernández-Ronco, S. Bolisetty, M. Mazzotti and R. Mezzenga, *Advanced Materials*, 2016, **28**, 472–478.

[19] Y. Han, Y. Cao, S. Bolisetty, T. Tian, S. Handschin, C. Lu and R. Mezzenga, *Small*, 2020, **16**, 2004932.

[20] M. G. Iadanza, M. P. Jackson, E. W. Hewitt, N. A. Ranson and S. E. Radford, *Nature Reviews Molecular Cell Biology*, 2018, **19**, 755–773.

[21] P. C. Ke, R. Zhou, L. C. Serpell, R. Riek, T. P. Knowles, H. A. Lashuel, E. Gazit, I. W. Hamley, T. P. Davis, M. Fändrich *et al.*, *Chemical Society Reviews*, 2020, **49**, 5473–5509.

[22] J.-M. Jung, G. Savin, M. Pouzot, C. Schmitt and R. Mezzenga, *Biomacromolecules*, 2008, **9**, 2477–2486.

[23] J. Adamcik, J.-M. Jung, J. Flakowski, P. De Los Rios, G. Dietler and R. Mezzenga, *Nature Nanotechnology*, 2010, **5**, 423–428.

[24] Y. Cao, S. Bolisetty, G. Wolfisberg, J. Adamcik and R. Mezzenga, *Proceedings of the National Academy of Sciences*, 2019, **116**, 4012–4017.

[25] S. Bolisetty, L. Harnau, J.-m. Jung and R. Mezzenga, *Biomacromolecules*, 2012, **13**, 3241–3252.

[26] Y. Cao, S. Bolisetty, J. Adamcik and R. Mezzenga, *Physical Review Letters*, 2018, **120**, 158103.

[27] M. Usuelli, Y. Cao, M. Bagnani, S. Handschin, G. Nyström and R. Mezzenga, *Macromolecules*, 2020, **53**, 5950–5956.

[28] E. Secchi, T. Roversi, S. Buzzaccaro, L. Piazza and R. Piazza, *Soft Matter*, 2013, **9**, 3931–3944.

[29] D. Vigolo, J. Zhao, S. Handschin, X. Cao, A. J. deMello and R. Mezzenga, *Scientific Reports*, 2017, **7**, 1–7.

[30] I. Usov and R. Mezzenga, *Macromolecules*, 2015, **48**, 1269–1280.

[31] A. Duri, H. Bissig, V. Trappe and L. Cipelletti, *Physical Review E*, 2005, **72**, 051401.

[32] A. Duri, D. A. Sessoms, V. Trappe and L. Cipelletti, *Physical Review Letters*, 2009, **102**, 085702.

[33] R. Piazza, M. Campello, S. Buzzaccaro and F. Sciortino, *Macromolecules*, 2021, **54**, 3897–3906.

[34] Z. Filiberti, R. Piazza and S. Buzzaccaro, *Physical Review E*, 2019, **100**, 042607.

[35] E. Secchi, F. Munarin, M. D. Alaimo, S. Bosisio, S. Buzzaccaro, G. Ciccarella, V. Vergaro, P. Petrini and R. Piazza, *Journal of Physics: Condensed Matter*, 2014, **26**, 464106.

[36] F. G. Donnan, *Chemical Reviews*, 1924, **1**, 73–90.

[37] A. Philipse and A. Vrij, *Journal of Physics: Condensed Matter*, 2011, **23**, 194106.

[38] T.-Y. Wang, Y.-J. Sheng and H.-K. Tsao, *Journal of Colloid and Interface Science*, 2009, **340**, 192–201.

[39] R. van Roij, *Journal of Physics: Condensed Matter*, 2003, **15**, S3569.

[40] A. P. Philipse, *Journal of Physics: Condensed Matter*, 2004, **16**, S4051.

[41] M. Raşa and A. P. Philipse, *Nature*, 2004, **429**, 857–860.

[42] M. Vis, V. F. Peters, R. H. Tromp and B. H. Erné, *Langmuir*, 2014, **30**, 5755–5762.

[43] A. V. Dobrynin and M. Rubinstein, *Progress in Polymer Science*, 2005, **30**, 1049–1118.

[44] D. C. Morse, *Physical Review E*, 2001, **63**, 031502.

[45] K. Kroy and E. Frey, *Physical Review E*, 1997, **55**, 3092.

[46] O. Lieleg, J. Kayser, G. Brambilla, L. Cipelletti and A. R. Bausch, *Nature Materials*, 2011, **10**, 236–242.

[47] C. P. Broedersz and F. C. MacKintosh, *Reviews of Modern Physics*, 2014, **86**, 995.

Unraveling amyloid fibril gelation by Photon Correlation Imaging: kinetics, microscopic dynamics, and temporal heterogeneity (Supporting Information)

Mattia Usuelli,[a,‡] Vincenzo Ruzzi,[b,‡] Stefano Buzzaccaro,[b] Gustav Nyström,[a,c] Roberto Piazza[b,*] and Raffaele Mezzenga[a,d,*]

AFM analysis of the formed amyloid fibrils
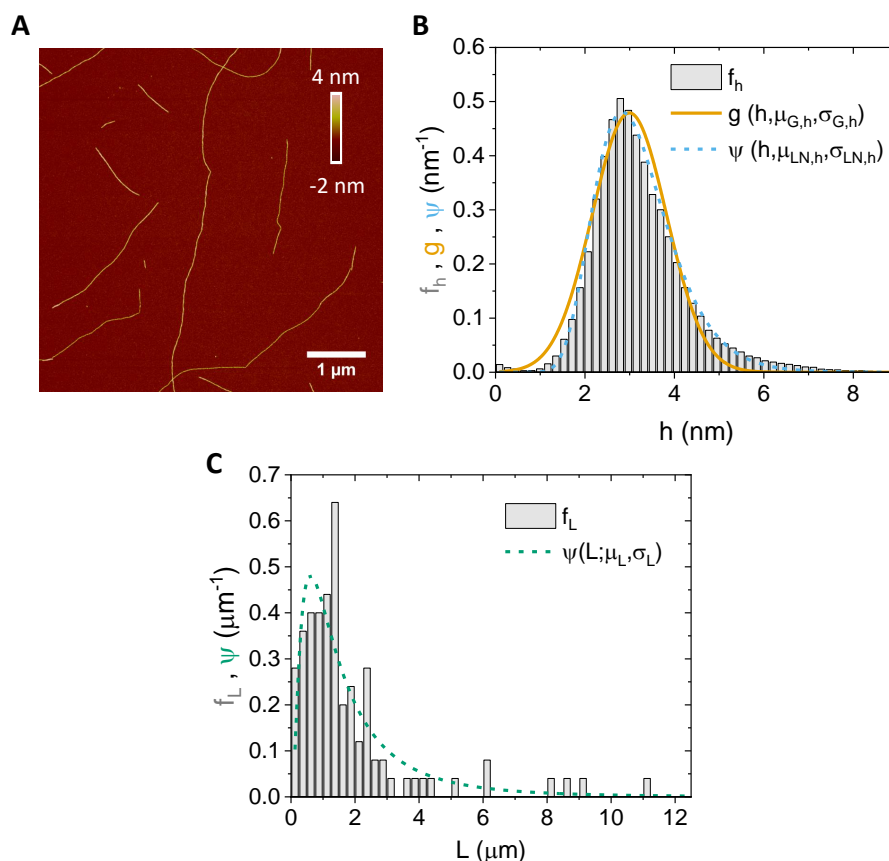
FigureS1. AFM (Atomic Force Microscopy) analysis of the formed amyloid fibrils, which were tracked using the open-source software FiberApp (ref. 30 of the main manuscript). (**A**) Cropped version of the original AFM image, where the semi-flexible fibrils are clearly visible. (**B**) Probability density function of the height of the fibrils, which can be approximated to their diameter. The two fittings are respectively Gaussian (g, ochre solid line) and log-normal (ψ, light blue dashed line): both of them have a most probable value around 3 nm. (**C**) Probability density function of the length of the fibrils. The log-normal fit (ψ, green dashed line), despite not being accurate due to the limited number of fibrils present in the examined AFM images, shows a significant fraction of the population having a length larger than 1 μm.

‡ These authors contributed equally to this work.
[a] ETH Zürich, Department of Health Sciences and Technology, Schmelzbergstrasse 9, 8092 Zürich, Switzerland. E-mail: raffaele.mezzenga@hest.ethz.ch
[b] Department of Chemistry, Materials Science, and Chemical Engineering (CMIC), Politecnico di Milano, Edificio 6, Piazza Leonardo da Vinci 32, 20133 Milano, Italy. E-mail: roberto.piazza@polimi.it
[c] EMPA, Laboratory for Cellulose & Wood Materials, Überlandstrasse 129, 8600 Dübendorf, Switzerland
[d] ETH Zürich, Department of Materials, Wolfgang-Pauli-Strasse 10, 8093 Zürich, Switzerland

Rheological characterisation of the gels
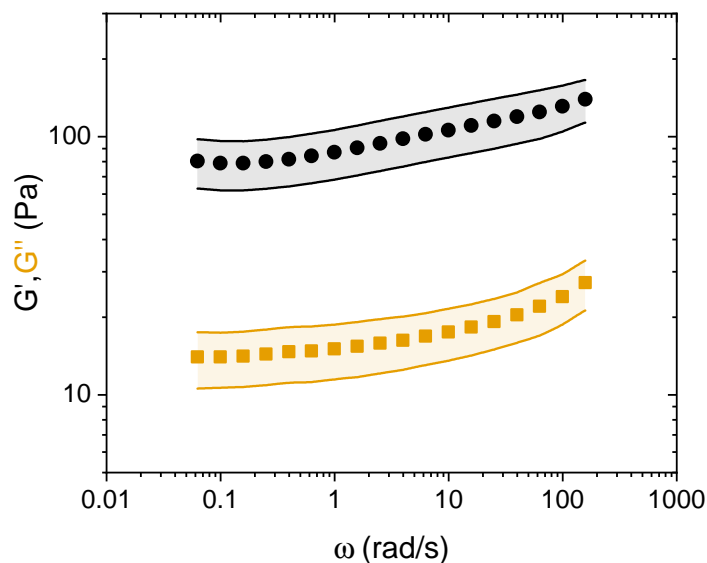
FigureS2. Rheological characterization of the βLG amyloid fibril gels, through oscillatory sweeps performed at 1% strain with a plate-plate geometry. The samples were prepared as stated in the Materials and Methods section of the main text: more in detail, the shown curves are relative to gels prepared with a 300 mM NaCl solution. It can be appreciated how G' is one order of magnitude larger than G'', confirming the elastic properties of the sample.

# Appearance of collected images before and after correction
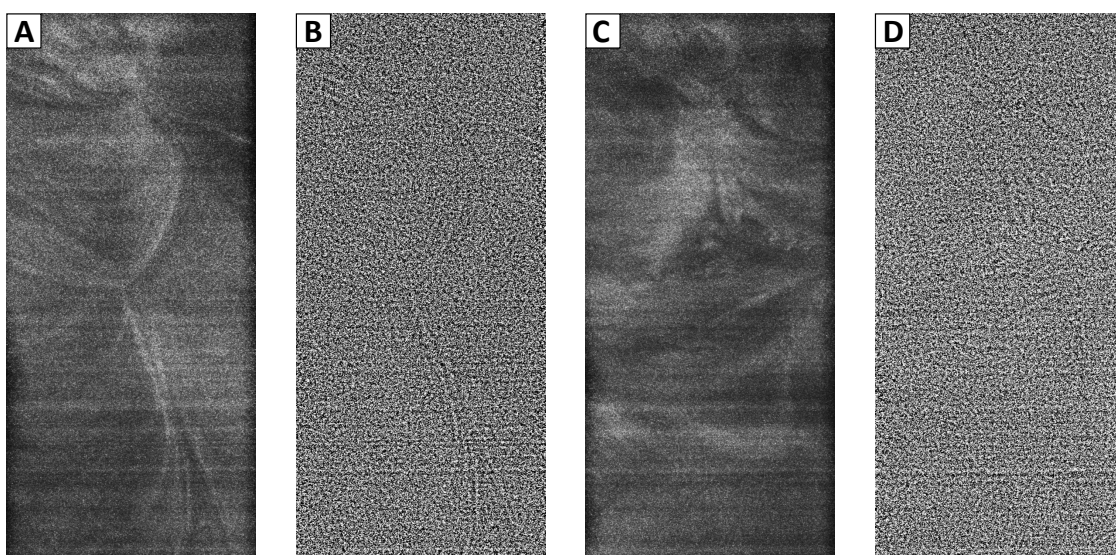
FigureS2. Images acquired with the PCI (Photon Correlation Imaging) setup. (**A**) Image acquired 500 min after the beginning of the 300 mM NaCl experiment. The background noise has been previously subtracted. (**B**) Same image as in panel A, after correction for the uneven background. (**C**) Image acquired 500 min after the beginning of the 150 mM NaCl experiment. The background noise has been previously subtracted. (**D**) Same image as in panel C, after correction for the uneven background.

Appearance of a formed amyloid fibril gel

FigureS2. Picture of the transparency of a βLG amyloid fibril gel prepared through perfusion of ions from a 300 mM NaCl solution at pH 2. The well-known mathematical equation, behind the cuvette, can be clearly seen and read. The picture was taken eight days after the preparation of the system, to show the negligible role of shrinkage in βLG amyloid fibril gels.

Temporal evolution of the scattered intensity
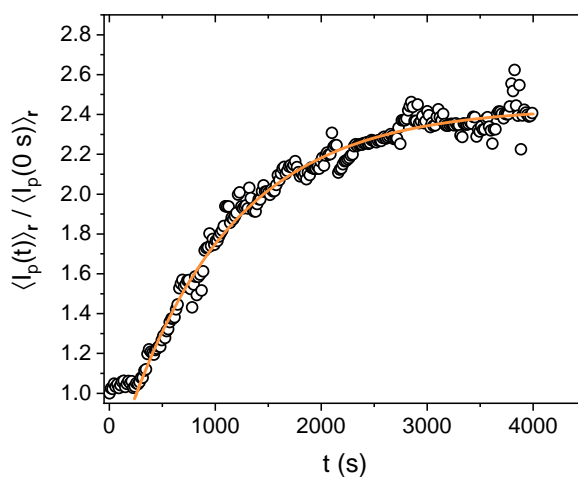
FigureS2. Evolution of the average intensity in a ROI (50 V x 900 H) located at the bottom part of the cuvette, normalized to the average intensity at the beginning of the experiment. The presented data have been obtained from the 300 mM NaCl experiment, analysing the images to which the background had been previously subracted. In fact, a similar analysis on the images after correction for uneven illumination would have lead to a constant value of 1 over the whole experiment.

It can be appreciated how the intensity more than doubled, indicating a change in the form factor of the scattering objects; the observation is confirmed by the exponential fit $(\langle I_p(t)\rangle_{\mathbf{r}}/\langle I_p(0\ s)\rangle_{\mathbf{r}} = I_0 + A(1 - e^{(t-t_0)/\tau}))$.

Evolution of salt concentration - simulations
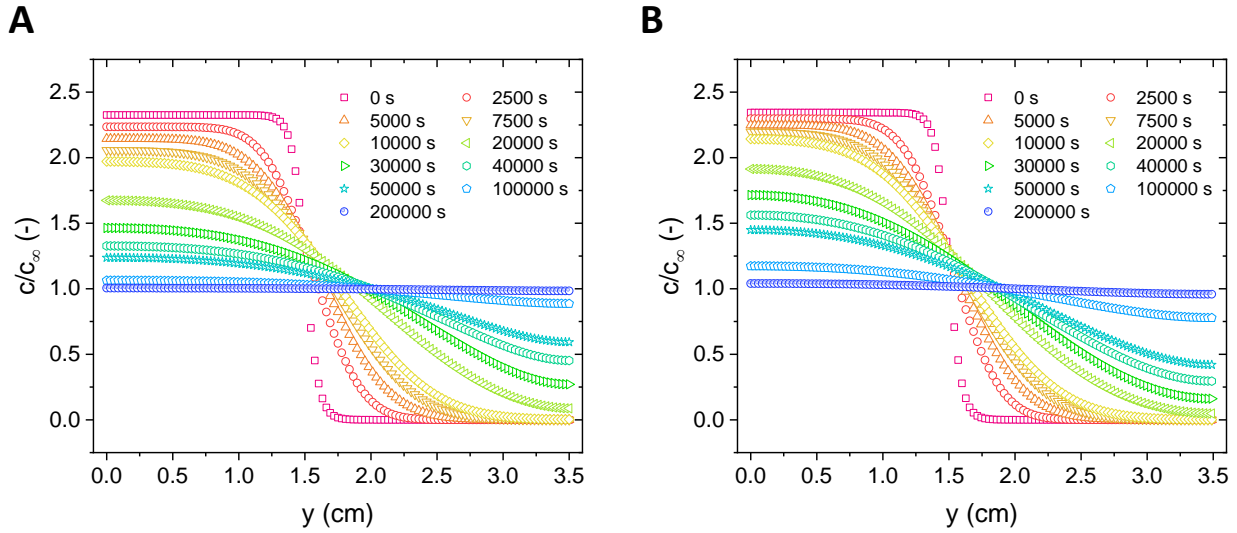
FigureS2. Simulated normalized concentration profiles of NaCl over the cell length, with a parametric dependence from the time from the beginning of the experiment. The profiles were obtained as detailed in the main text, through a numerical resolution of a generalized diffusion equation that comprehends both diffusive and advective terms. The simulations were performed for both the 300 mM NaCl sample (**A**) and the 150 mM NaCl one (**B**).

Beginning of the observations and physical phenomena in the proximity of the membrane
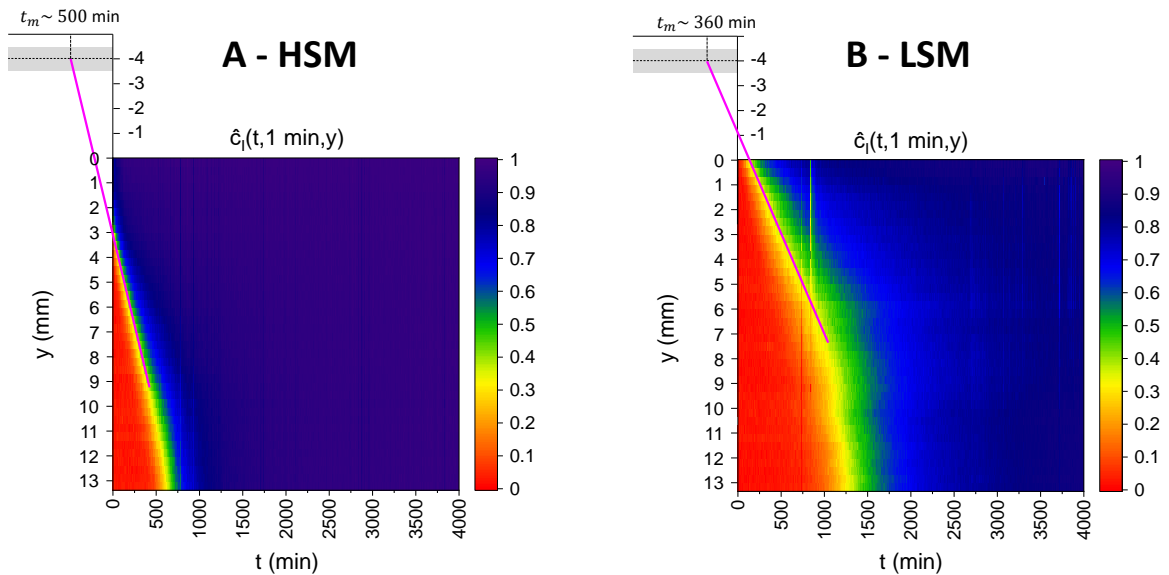
FigureS2. Extrapolation of the observed linear behavior of the gelation front towards negative time values (in panels A and B for HSM and LSM, respectively), to shed light onto the physical phenomena that occur in the proximity of the membrane. The membrane is assumed to be at $y = -4$ mm, with an error bar (grey area) of 0.5 mm.

Preparation of the samples and beginning of the observation

As mentioned in the main manuscript, the time 0 for both measurements corresponds to the beginning of the observations. When looking at panels A and C of Fig.2 in the main manuscript, some differences emerge. While for HSM, at t = 0 min, the upper 3 cm of the imaged area are already in a gel state (dark blue colour), for LSM it takes around 200 min for the first ROI to show hints of gelation. This difference can be explained considering that, for the two cases, the delays between the preparation of the sample and the beginning of the observation differ. In the case of HSM, the observation started more than 90 minutes after the preparation of the sample, as over the mentioned time span a further characterization was carried out (data not shown). In the case of LSM, the measurement started instead within 20 min from the preparation of the sample.
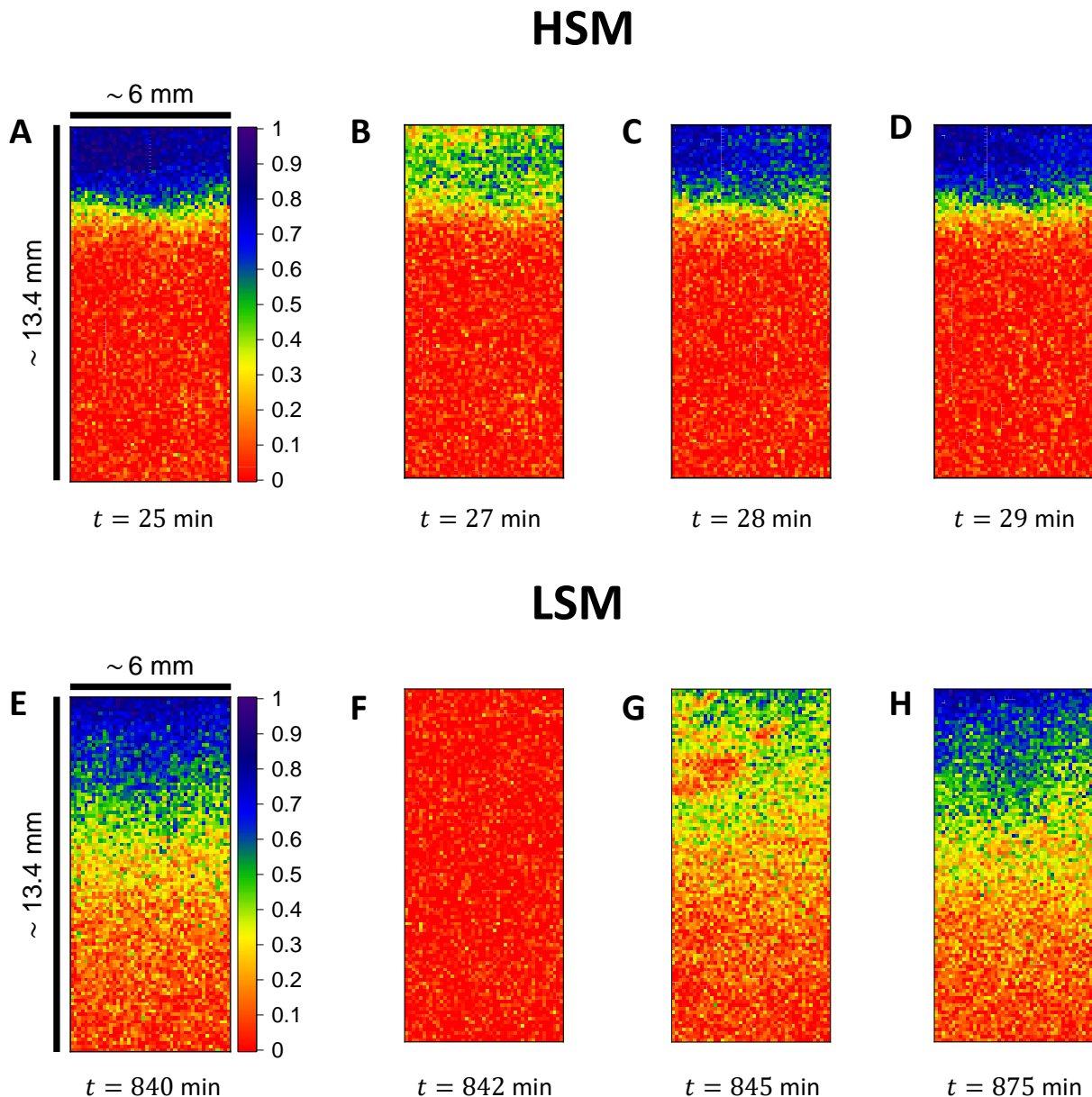
Physical phenomena in the proximity of the membrane

The different delays from the preparation of the samples to the beginning of the observations are, however, not sufficient to fully describe the physical phenomena that happen in the proximity of the membranes. On the basis of the observed linear advance of the gelation front, it is possible extrapolate the behaviour of the probed systems at times that lie outside the observation window. For both HSM and LSM, we used the extracted velocities of the evolving front (1.47×10^{-2} mm/min and 7.77×10^{-3} mm/min, respectively), together with the assumed position of the dialysis membrane ($\sim$ - 4 mm for both cases), to check whether an extrapolation towards negative time values allows to obtain delay times, that are compatible with the ones reported above (90 and 20 min for HSM and LSM, respectively). The obtained results are reported in Fig.S7 ($\sim$ 500 min and $\sim$ 360 min for HSM and LSM, respectively) and hardly agree with the reported delays: in the following, we share hypotheses that might explain this mismatch.

Firsly, we hypothesize that the reported value of the position of the membrane is inaccurate. It might be that inaccuracies, in cutting and in positioning the syringe inside the cuvette, introduce complications in determining the exact position of the dialysis membrane. If the membrane was nearer to the observation area than the reported value (- 4 mm), the results of the extrapolation would get closer to the reported delay times. However, this first hypothesis is not sufficient to fully explain the observed difference.

As second hypothesis, we assume that the linear behaviour observed in the probed area is not valid in the proximity of the membrane. A first fact that supports this hypothesis is that, after adding salt to the syringes, the studied systems were sealed with parafilm. It might be that this manual operation induced a shaking that speed-ed up the salt perfusion at an initial stage. A second point that aligns with this hypotheses is the difference between the liquid height within and outside from the syringe. Despite the syringe was partially immersed in the amyloid fibrils solution, to ensure contact between the colloidal dispersion and the dialysis membrane, the level of the liquid inside the syringe was higher than the the one of the liquid between the syringe and the cuvette (despite a modest increase related to the mentioned immersion). As a consequence, the arising hydrodynamic unbalance could favour the passage of a modest quantity of salt solution, that further speeded up the gelation phenomena in the proximity of the membrane. A more detailed analysis of this hypothesis is inhibited from the fact that the system, being sealed with parafilm, is not in contact with atmospheric pressure; therefore, a passage of liquid from the syringe to the cuvette would decrease the pressure inside the syringe while increasing the one in the cuvette.

The combination of the shared hypotheses allows to qualitatively describe the mismatch between the reported delay times and the computed extrapolation. A deeper analysis of this point goes beyond the scope of this work: in fact, the decision of sampling an area with a few mm distance from the membrane was done appositely to avoid dealing with hard-to-describe physical phenomena in its proximity, among which we also account the change in cross-section (from circular to quadratic) between the syringe and the cuvette.

Stress releasing events during the advance of the gelation front

HSM

~6 mm

~13.4 mm

A $t = 25$ min

B $t = 27$ min

C $t = 28$ min

D $t = 29$ min

LSM

~6 mm

~13.4 mm

E $t = 840$ min

F $t = 842$ min

G $t = 845$ min

H $t = 875$ min

FigureS2. Stress-releasing events that happened while the gel was forming in the probed area, shown through DAMs computed at a constant delay time (τ) of 1 min. (A-D) Modest and fast-recovering decorrelation burst in HSM. (E-H) Significative and slow-recovering decorrelation burst in LSM.

In the main text, we discussed stress-releasing events that happened after the gel had formed in the entire probed area, for both HSM and LSM. Here we show (Fig.S8) that stress-releasing events also accompanied the creation of an arrested phase. In panels A-D, a decorrelation burst that characterizes HSM gelation is reported. At 25 minutes (A), a gel layer is formed in the upper part of the cuvette, while the middle and bottom parts shows a fully decorrelated state. Two minutes later (B) the correlation index drops where the gel had already formed: despite very limited hints of total correlation, the area shows a green-like colour that is associated to $\hat{c}_I$ values close to 0.5. One and two minutes later (C and D, respectively), the upper part of the cuvette shows again high correlation values.

A similar (but more drastic) phenomenon happened in LSM (E-H). At 840 minutes from the beginning

of the observation, the upper part of the cuvette showed the formation of a gel layer (E). Two minutes later (F) all the ROIs in the DAM gets fully uncorrelated (F): this is related to a major stress-release event that allows the network to reconfigure itself, in a configuration which is energetically more stable. Later on, the system slowly re-gains higher correlation values in the zone where the gel already formed (G-H).

When comparing the entity of the two decorrelation burst and the recovery time after them, key differences emerge between HSM and LSM. While in LSM the correlation index drops everywhere to close-to-0 values, in HSM hints of local correlation remain. Even more remarkably, while in HSM close-to-1 values of the correlation index are regained within 1 minutes, LSM needs many more minutes to find and fix a new configuration. In fact, as mentioned above, the lower concentration of salt reduces the probability of transforming entanglements into physical cross-links, with consequent larger susceptibility of the network to further motion of the forming units.

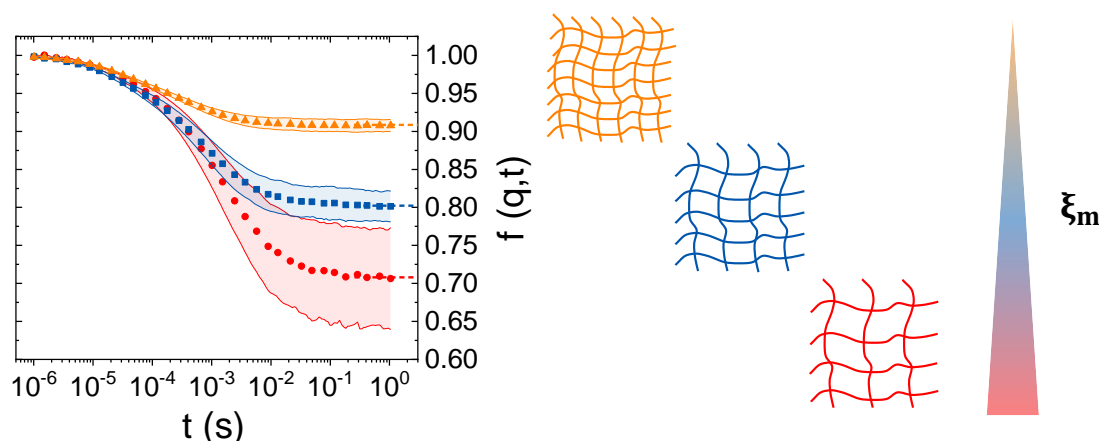# 3. Probing the Structure of Filamentous Nonergodic Gels by Dynamic Light Scattering

Mattia Usuelli, Yiping Cao, Massimo Bagnani, Stephan Handschin, Gustav Nyström and and Raffaele Mezzenga*

Summary

More than two decades ago, a theoretical analysis of light scattering from semi-flexible polymers showed the possibility of extracting quantitative information about single filaments (their diameter and their persistence length) and about the mesh size of the networks they form. While diameter and persistence length were extracted following this approach, a DLS-based extraction of the mesh size remained up to now elusive. In this work, we show that the theory of dynamic scattering from semi-flexible polymers can be combined with a rigorous treatment of nonergodicity, to quantitatively extract the mesh size of amyloid fibril gels from the plateau value of their intermediate scattering function. The obtained values are in quantitative agreement with a theoretical estimate, made with a modified version of the cubic lattice model.

Reproduced with permission from authors and publisher
© 2020 American Chemical Society

Probing the Structure of Filamentous Nonergodic Gels by Dynamic Light Scattering

Mattia Usuelli, Yiping Cao, Massimo Bagnani, Stephan Handschin, Gustav Nyström, and Raffaele Mezzenga*

Cite This: *Macromolecules* 2020, 53, 5950−5956

Read Online

ACCESS | Metrics & More | Article Recommendations | Supporting Information

ABSTRACT: Mesh size is a crucial parameter that governs the behavior of gels made of semiflexible polymers. We show that the average mesh size of amyloid fibril gels can be extracted from simple dynamic light scattering experiments. The data analysis is performed combining theoretical descriptions of nonergodicity and semiflexible polymer dynamics. The described method works in a range of concentrations where the mesh size is comparable with the characteristic length scale associated with the probed wave-vector.
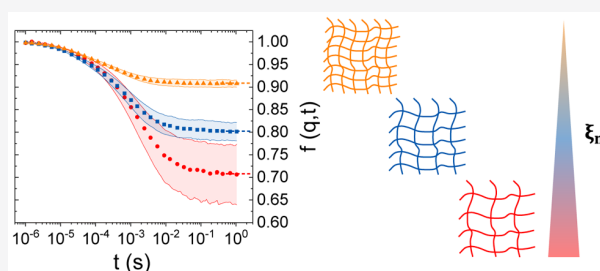
INTRODUCTION

Semiflexible polymers are ubiquitous in nature and have a pivotal role in biology and colloidal science.[1] A classical example is actin filaments, whose presence in the cytoskeleton enhances cells mechanical stability.[2] Amyloid fibrils are another important class of semiflexible colloidal objects.[3] Their synthesis in vitro from various proteins leads to functional applications,[4] ranging from ultralight aerogels loaded with inorganic particles[5] to iron fortification[6] and water purification.[7] In many biological contexts or engineered products, semiflexible polymers form a network. A relevant parameter in the description of such entangled states is the typical spacing among chains,[1] namely, the mesh size (ξ_m). A precise experimental determination of this quantity would allow a better bottom-up characterization and optimization of fibrillar gels for specific applications.

The power law behavior of the mesh size as a function of concentration is well captured by polymer physics through scaling arguments.[8] In more detail, in semidilute solutions of semiflexible polymers, $\xi_m \sim c^{-1/2}$. Schmidt and co-workers determined the mesh size of polymerized actin networks through the hindered diffusion of latex beads in the medium, showing that $\xi_m \approx 0.3\ c_a^{-1/2}$ (with c_a expressed in mg/mL and ξ_m expressed in μm).[9] However, further studies on actin solutions, exploiting multiple particle tracking techniques, showed heterogeneities in the formed network and consequent inhomogeneous behavior of embedded beads.[10] Size and surface chemistry of added tracers were also shown to play a significant role in the extracted properties.[11,12] Therefore, a non-invasive characterization method, which avoids addition of colloids, would reduce ambiguities in the analysis and interpretation of the data.

Dynamic light scattering (DLS) is a technique that can fulfill this aim. Theoretical studies on the motion of semiflexible polymers in solution showed the possibility of extracting key parameters from DLS analysis; the obtainable quantities are the diameter and persistence length of the fibrils (d and l_p, respectively) and the mesh size of the networks they form (ξ_m).[13,14] While single actin filament properties (d, l_p) have been experimentally characterized following this route,[15−18] ξ_m has remained until now elusive. We combine the mentioned theoretical works on semiflexible polymers dynamics[14] with a rigorous treatment of nonergodicity,[19] to link the mesh size of fibrillar gels to the plateau value of the intermediate scattering function ($f(q, t)$, ISF) obtained through scattering experiments. We show, to our knowledge, for the first time, that ξ_m of semiflexible polymer gels can be experimentally determined through DLS measurements.

MATERIALS AND METHODS

βLG Amyloid Fibril Preparation. β-lactoglobulin (βLG)-freeze-dried powder was dissolved in MQ water to a concentration equal to 2 wt %. The pH was adjusted to 1.8 using concentrated HCl solution. To induce the formation of amyloid fibrils, 75 mL of solution was taken and heated up at 90 °C for 5 h in a 100 mL Schott bottle. While heating up, the solution was stirred at 300 rpm with a 3 × ⌀0.5 cm magnetic stirrer. After the reaction, the system was quenched with ice
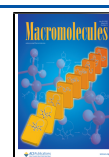
and centrifuged at 12 074g for 10 min to remove macroscopic aggregates. The fibril solution was kept at 4 °C before further usage.

Conversion of Monomers into Amyloid Fibrils. The conversion of monomers of βLG into amyloid fibrils was measured through a centrifugation method. An aliquot of the initial stock solution of amyloid fibrils was diluted at a factor 2 with pH 2 MQ water, to a final concentration of ~1 wt %. The diluted solution (3 mL) was added to a centrifugal filter unit (Amicon Ultra, 100 kDa, Merck Millipore Ltd.) and afterward centrifuged for 25 min at 3824g. The weight fractions of both the initial diluted solution and of the filtrate were measured through gravimetrical analysis (upon drying at 60 °C overnight). The conversion was calculated as

$$\chi = 1 - \frac{\text{wt\%}_{\text{filtrate}}}{\text{wt\%}_{\text{initial solution}}} = 0.38$$

The concentration of amyloid fibrils (c) can be computed as the product between the measured conversion (χ) and the total concentration of proteins (c_p): $c = c_p \chi$.

AFM Sample Preparation and Imaging Conditions. An aliquot of βLG amyloid fibrils was diluted to a final total protein concentration of 0.01 wt % using pH 2 MQ water. After fresh cleaving of a mica substrate, 20 μL of solution was deposited on the surface and incubated for 2 min. The surface of the mica has been successively rinsed with 1 mL of pH 2 MQ water and dried with compressed air flow. AFM measurements have been performed with a Dimension FastScan Bio scanning probe microscope (Bruker, USA) in tapping mode using a commercial cantilever (Bruker, USA). Images were acquired under ambient conditions, and the AFM was covered with an acoustic hood to minimize noise.

DLS Samples Preparation. βLG fibril suspensions at different concentrations were prepared diluting an initial stock solution with pH 2 MQ water. Fibril suspensions (2 mL) were transferred in a Soda glass cuvette (D_{ext} = 10 mm, D_{int} = 8 mm, VWR, Switzerland). The piston of a 1 mL syringe (Norm-Ject, Henke Sass Wolf, Germany) was removed, and the outlet part of the syringe was cut. The syringe was covered with a dialysis membrane (Spectra/Por, MWCO 6−8 kDa, Spectrum Laboratories Inc.), previously washed with MQ water and dried over tissue paper (KimTech, Kimberly-Clark Professional). The membrane was afterward tightened to the walls of the syringe using parafilm (PM-996, Parafilm, USA). The syringe was put inside the cuvette, so that the membrane was in contact with the amyloid fibrils solution. A 900 mM NaCl pH 2 solution (1 mL) was put inside the syringe, and the system was sealed with parafilm (PM-996, Parafilm, USA), to avoid evaporation; see Figure S4 for a schematic representation of this process. Before measurement, the system has been let equilibrating for 2 days. A homogeneous diffusion of the salt in the final available volume would lead to a NaCl concentration of 300 mM. To check if this hypothesis is verified, we measured the total concentration of two 0.38 mg/mL fibril gels made accordingly with this protocol, using the gravimetric method. Subtracting the total protein concentration (1 mg/mL) to the obtained result, we obtained an average value of 15.76 mg/mL. This is related to a salt concentration of $I = \frac{c_{\text{NaCl}}}{\text{MW}_{\text{NaCl}}} = \frac{15.76\,\text{g / L}}{58.44\,\text{g / mol}} = 0.27\,\text{M} = 270\,\text{mM}$, which closely agrees with the theoretical estimation made above.

DLS Sample Measurement and Data Treatment. A cuvette containing the gel was placed in static and dynamic light scattering equipment (3D-LS Spectrometer, LS Instruments, Switzerland). For each sample, at a specific goniometer angle, the ensemble-averaged scattered intensity ($\langle I(q) \rangle_E$, kHz) was measured running 100 s measurements where the sample was continuously rotated, making sure that it could perform at least one entire revolution. $\langle I(q) \rangle_E$ is the resulting time-averaged count rate measured in this process. At the same goniometer angle, several other measurements spanning from 5 to 20 s were made (at least 5 and up to 7 measurements). In this case, for each measurement the sample was kept fixed and the time-averaged scattered intensity ($\langle I(q) \rangle_T$) and the intensity correlation function ($g^{(2)}(q, t) - 1$) were collected. From $g^{(2)}(q, t) - 1$, it is possible to extract the mean-squared intensity fluctuations $\sigma_T^2 = g^{(2)}(q, t \to 0) - 1$ (the value is automatically given by the software of the

equipment). Between different measurements, the sample was rotated to probe different subensembles. Single data sets from measurements at a fixed position were corrected and then statistically analyzed as represented in the schematic in Figure S5a. For the 0.19 and 0.76 mg/mL samples, measurements at 110 and 135° were performed. For the 0.38 mg/mL sample, measurements at 60, 90, 110, and 135° were performed. The relationship between angles, q values, and characteristic length scales is shown in the Supplemental Information (Table S1).

■ RESULTS AND DISCUSSION

Intuitive Excursus of DLS on Fibrillar Gels. Dynamic light scattering probes the dynamics of colloidal samples at length scales determined by the q vector:[20]

$$q = \frac{4\pi n}{\lambda}\sin\left(\frac{\theta}{2}\right) \tag{1}$$

Here, n is the refractive index of the solvent, λ is the wavelength of the laser (nm), and θ is the angle at which the measurement is performed. An increase in θ determines an increase in q, which in turn reflects smaller probed length scales $\delta = \frac{2\pi}{q}$.[21] Semiflexible fibrils translate, rotate, and vibrate when they are in dilute conditions. In the semidilute regime, entanglement points among fibrils limit the degrees of freedom of single objects. Moreover, when the colloids are charged, changes in pH or ionic strength can transform such entanglements in cross-links and promote gelation.[22] Translational and rotational motions are mainly suppressed in gels, and the transversal vibrations of the fibrils are also influenced; the smaller the spacing among polymers, the shorter the fractions of the contour that can fluctuate. Such a hindered motion is reflected in a correspondent nonzero plateau value of the $f(q, t)$ of the system.[14] To be able to catch such a behavior with DLS, it is important to isolate the contribution of single fibril vibrations. This can be done through the following length-scale separation requirement, where d and l_p have been defined above and L is the contour length of the fibrils:[14]

$$d \ll \delta \ll l_p,\ L \text{ and } \delta < \xi_m \tag{2}$$

βLG: From Monomers to Transparent Fibrillar Gels. As a model system to prove this concept, we consider β-lactoglobulin (βLG) amyloid fibril gels. βLG monomers were purified from whey proteins (Fonterra, New Zealand) with a protocol already reported in the literature.[23] βLG-freeze-dried powder was dissolved in MQ water to a concentration equal to 2 wt % and converted into amyloid fibrils through heating up at 90 °C in acidic conditions for 5 h.[24] In Figure 1a, we show an atomic force microscopy (AFM) image of the prepared amyloid fibrils, which was analyzed using FiberApp.[25] In Figure 1b, the height relative frequency (f_h) is reported. The fitting was performed with a Gaussian distribution: the extracted expected height of the fibrils is $\langle h \rangle$ = 2.82 nm, and the standard deviation is σ_h = 0.85 nm. The characteristic radius of the fibrils, approximated as cylindrical objects, is $a = \frac{\langle h \rangle}{2} = 1.41$ nm. Figure 1c shows the contour length relative frequency, which is well described by a log-normal distribution; the fitting gives an expectation value of $\langle L \rangle = e^{\mu_L + \sigma_L^2/2} \approx 1420$ nm. The persistence length is $l_p \approx 2155$ nm (Figure S1).

As previously outlined, gelation of amyloid fibril suspensions requires entanglement points to be transformed into rigid connections. An increase in ionic strength has a dramatic effect
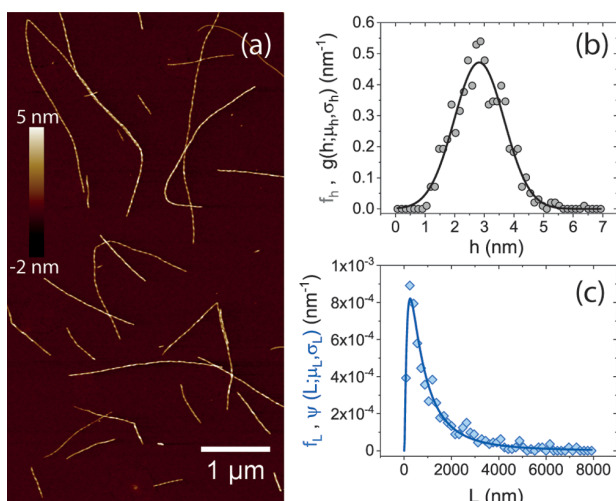
Figure 1. (a) AFM height image of βLG amyloid fibrils. (b) Height relative frequency (f_h, gray dots) fitted with a Gaussian distribution ($g(h; \mu_h, \sigma_h)$: continuous black line). (c) Contour length relative frequency (f_L, blue diamonds) fitted with a log-normal distribution ($\psi(L; \mu_L, \sigma_L)$: continuous blue line).

in enhancing the elastic properties of amyloid gels, suggesting the formation of long-lived cross-links.[26] We prepared amyloid fibril gels by making Na^+ and Cl^- ions diffuse into semidilute suspensions through a semipermeable membrane (Figures S2 and S4): in this way, we avoided possible heterogeneities related to mixing processes. Moreover, thanks to the diffusion method, the gels are fully transparent.[26,27] To visualize the cross-linked structure of a fibril gel, we report a scanning electron microscopy (SEM) image of a βLG aerogel (Figure S3), which was obtained through supercritical CO_2 drying of a gel with 5 mg/mL total protein content.

Nonergodicity and Data Correction Schemes. The formed gels are nonergodic; therefore, particular care has to be used in performing and analyzing DLS measurements. In arrested systems, there are physical constraints that inhibit colloidal objects to decorrelate from their initial position. In this case, nonergodicity arises and time-averaged quantities do not reflect properties of the whole Hamiltonian phase space (ensemble-averaged quantities).[28] In light scattering, the total field $E(q, t)$ scattered by an illuminated subensemble of a nonergodic sample is the sum of a constant component ($E_C(q, t)$) and a fluctuating one ($E_F(q, t)$).[19] $E_C(q, t)$ is related to the specific configuration of objects in the scattering volume and changes as different subensembles are considered. $E_F(q, t)$, in a homogeneous material, is common for all subensembles and is a zero-mean complex Gaussian variable. Pusey and co-workers derived a method to determine the intermediate scattering function $f(q, t)$ (an ensemble-averaged quantity) from a time-averaged measurement of a specific subensemble.[19] The key quantities that play a role in the correction scheme are the following: $\langle I(q)\rangle_E$, $\langle I(q)\rangle_T$, σ_T^2, and $g^{(2)}(q, t) - 1$.

$\langle I(q)\rangle_E$ is the ensemble-averaged scattered light, determined from the time-averaged detected count rate (kHz) while displacing/rotating the sample. This experimental procedure forces the analysis of different subensembles. $\langle I(q)\rangle_T$ is the time-averaged scattered light, determined as in the case of $\langle I(q)\rangle_E$ but keeping the sample at a fixed position (single subensemble). The ratio between the above-defined quantities is called $Y = \langle I(q)\rangle_E/\langle I(q)\rangle_T$; different subensembles are

characterized by different values of Y. σ_T^2 is the mean-square intensity fluctuation ($\sigma_T^2 = \langle I^2(q)\rangle_T/\langle I(q)\rangle_T^2 - 1$), which coincides with the reduced intercept of $g^{(2)}(q, t) - 1 = \langle I(q, t) I(q,0)\rangle_T/\langle I(q)\rangle_T^2 - 1$ (the intensity correlation function). An independent determination of $\langle I(q)\rangle_E$ allows afterward correction of single DLS measurements, every one of which is characterized by the quantities $\langle I(q)\rangle_T$ (and therefore Y), σ_T^2, and $g^{(2)}(q, t) - 1$. The correction can be applied through the following formula, which directly gives the intermediate scattering function $f(q, t)$:[29]

$$f(q, t) = 1 + \frac{1}{Y}\left[\sqrt{g^{(2)}(q, t) - \sigma_T^2} - 1\right]$$

$$\overset{t\to\infty}{=} 1 + \frac{1}{Y}\left[\sqrt{1 - \sigma_T^2} - 1\right] \tag{3}$$

It is important to note that, for $t \to \infty$, $g^{(2)}(q, t) \to 1$.[19] Despite the intermediate scattering function being obtained through a dynamic technique (DLS), its plateau value is actually independent from the characteristic dynamics of the system; it expresses the totality of configurations that can be explored by its forming units. For our system of interest (amyloid fibril gels), such configurations are the sum of the bending fluctuations explorable by single and multiple filaments. When the conditions expressed by eq 2 are met (both $d \ll \delta \ll l_p$, L and $\delta < \xi_m$), single-filament undulations mainly build up the sum of possible configurations; however, when the probed length scale is considerably larger than the mesh size ($\delta > \xi_m$), multifilament relaxation modes add to the mentioned contribution. Furthermore, the gels might also be subject to intermittent restructuring events, which mainly consist of relaxation of frozen-in stresses and rupture/formation of long-lived cross-links. The nature of such events is both temporally and spatially heterogeneous[30−33] and gives rise to sudden correlation drops.[34] In the following, we neglect such rearrangement events and consider only single/multifilament vibrations as characteristic decorrelation phenomena.

DLS measurements (3D-LS Spectrometer, LS Instruments, Switzerland) allowed probing $\delta = \frac{2\pi}{q}$ spanning from ∼250 nm (135°) to ∼500 nm (60°). The potential range that is coverable by the equipment is actually larger. However, we decided to limit the lower measurement angle to 60°, to avoid spurious effect from micrometer-sized heterogeneities potentially present in the gels. In the mentioned measurement range, the first of the two conditions of eq 2 ($d \ll \delta \ll l_p$, L) is easily met; the second one ($\delta < \xi_m$) is respected or not depending on how concentrated the system is. A simple hint on the concentration of fibrils to be used can be gained by modeling the polymer network as a cubic lattice made of infinitely long rods. The lattice constant (l_c) can be defined as[9]

$$l_c = \sqrt{\frac{3a^2\pi\rho}{c\phi_{L_m}}} \tag{4}$$

Here, $a = 1.41$ nm is the radius of the rods, $\rho \approx 1300$ mg/mL is the density of fibrils,[26] and c is their concentration (mg/mL), equal to the product between the concentration of proteins and the conversion of monomers to fibrils ($c = c_p\chi$). We introduce in the equation the quantity ϕ_{L_m}, which is the mass fraction of rods that are long enough to form the network. In the classical approach, this quantity is equal to 1, in the assumption of an infinite contour length. In the present

modified approach, ϕ_{L_m} is allowed to be less than one, to reflect a finite length, and can be computed from the contour length distribution (see later below). For a quick check, by imposing $\phi_{L_m} = 1$ and $l_c > 250$ nm, we obtained that c has to be in the order of 0.5 mg/mL to be probed by our DLS setup. We decided therefore to study gels formed at 0.19, 0.38, and 0.76 mg/mL fibrils (0.5, 1, and 2 mg/mL total protein concentration, respectively). Gels for DLS analysis were directly formed inside cylindrical glass cuvettes through the above-mentioned diffusion method (Figure S4). The final ionic strength in the gels was measured to be ~300 mM; such a high value favors a close-to-unity conversion of entanglements into cross-links.[26] Measurement protocols and data treatment are further detailed in the Supplemental Information (Table S1 and Figure S5a). Figure 2a shows the intensity correlation
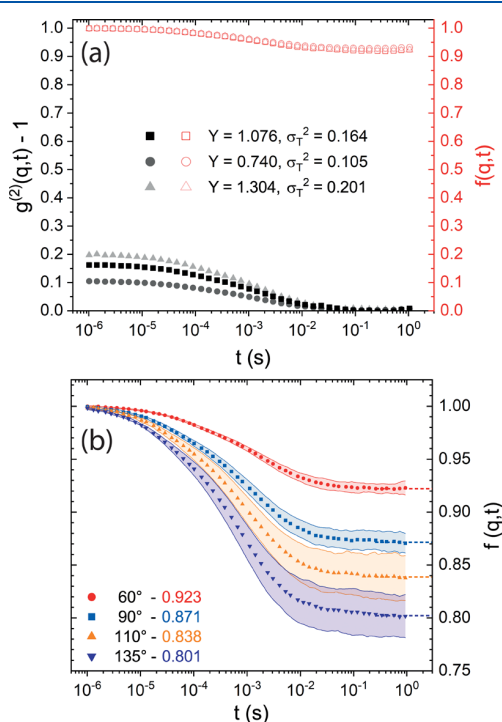
Figure 2. (a) Filled gray symbols: intensity correlation functions determined measuring three different subensembles of a 0.38 mg/mL βLG amyloid fibril gel at 60°. Empty red symbols: overlapping intermediate scattering functions, obtained applying the nonergodicity correction. (b) Intermediate scattering functions $(\overline{f}(q, t) \pm \sigma_f)$ of the same sample, measured at different angles. The numbers reported in the caption are the plateau values of the curves.

functions $(g^{(2)}(q, t) - 1$, in gray/black symbols) of three different subensembles of the 0.38 mg/mL sample, measured at 60°. The corrected intermediate scattering functions $(f(q, t))$ are reported in the same panel in red empty symbols. The benchmark of nonergodicity clearly appears in the reduced intercept of the ICFs: a common normalization of the data, as usually performed in DLS experiments, would lead to unreliable results.[19] It can be noted how, after correction (through eq 3), the $f(q, t)$ curves almost perfectly overlap. This shows that different subensembles have similar dynamics. In Figure S6, the same correction is applied to measurements performed at 90, 110, and 135°. After statistical analysis, we plotted in Figure 2b the average value of $f(q, t)$ (with the

associated standard deviation) from measurements at different angles. It can be noted how, with increasing q vector, the plateau value of $f(q, t)$ decreases and the standard deviation increases. Both observations can be explained by the fact that higher q vectors are associated with smaller probed length scales δ. On the one hand, decreasing values of δ are increasingly sensitive to the same absolute displacement, showing higher decorrelation. On the other hand, reduced probed length scales are also more sensitive to local heterogeneities of the network, with a consequent increase in standard deviation of local dynamics.

$f(q, t)$ Plateau Is Related to the Mesh Size. To extract quantitative information from the intermediate scattering function, it is necessary to use a model that describes the dynamics of semiflexible polymers. Kroy and Frey,[14] starting from a Rouse-like linear equation, unveiled the behavior of $f(q, t)$ at different time scales for the system of interest. As explained before, when a gel is formed, single-filament vibrations and multifilament relaxation modes are the main contributions that rule the decay of $f(q, t)$. When the requirements of eq 2 are met, single-fibril vibrations dominate; however, the filaments cannot fluctuate freely. In fact, only contour fractions between successive clamped points can properly express bending dynamics. The characteristic size of such contour segments is $L_m = (3/2\xi_m^2 l_p)^{1/3}$, the entanglement length.[14] The mentioned steric hindrance makes $f(q, t)$ decay to a nonzero plateau value, which is directly related to the mesh size and to the probed length scale (demonstration in the Supplemental Information):

$$\frac{f(q, t \gg \tau_{L_m})}{f(q, 0)} = e^{-q^2 \xi_m^2 / 2\pi^4} \quad (5)$$

Combining eq 5 with eq 3, we derive eq 6, which is the key equation of this work:

$$\xi_m = \sqrt{-\frac{2\pi^4}{q^2} \ln \frac{f(q, \infty)}{f(q, 0)}}$$
$$= \sqrt{-\frac{2\pi^4}{q^2} \ln\left[1 + \frac{1}{Y}\left(\sqrt{1 - \sigma_T^2} - 1\right)\right]} \quad (6)$$

The obtained equation is amazingly simple: the only input parameters, which are needed for the calculation of the mesh size, are the probed wave vector (q) and the plateau value of the intermediate scattering function ($f(q, \infty)$). Surprisingly, the persistence length (l_p) of the semiflexible objects does not appear. This is due to a subtle cancellation effect: a larger stiffness of the polymer backbone decreases the thermal undulations of segments between entanglement points ($\langle u^2 \rangle \sim L_m^3/l_p$)[1] but increases at the same time the characteristic length of such segments ($L_m = (3/2\xi_m^2 l_p)^{1/3}$). The two discussed competing effects perfectly balance each other.

An alternative scaling of the entanglement length, as a function of ξ_m and l_p, can be found in the literature ($L_m \sim (\xi_m^4 l_p)^{1/5}$). Such an expression was first derived by Semenov through geometrical considerations[35] and successively broadly used by many other authors.[1,36−38] The existence of two different expressions for L_m is puzzling.[39] However, Morse showed that both the mentioned scaling dependencies can be obtained, upon different assumptions on the nature of the forces that confine single chains.[40] When a hypothetical test chain is considered to interact with nearby medium chains and

elastic relaxation modes from the whole network are neglected (binary collision approximation, BCA), L_m follows the same scaling outlined by Semenov ($L_m \sim (\xi_m^4 l_p)^{1/5}$). On the other hand, when the surrounding network is treated as an elastic continuum in which a hypothetical test chain is embedded (effective medium approximation, EMA), $L_m \sim (\xi_m^2 l_p)^{1/3}$. As EMA describes more accurately the confinement forces acting on an amyloid fibril in a cross-linked network, we focus on the results derived above through the scaling law suggested by Kroy and Frey[14] ($L_m = (3/2\xi_m^2 l_p)^{1/3}$). In the Supplemental Information, we discuss the results that would be obtained using, instead, the scaling law derived through the BCA model ($L_m \sim (\xi_m^4 l_p)^{1/5}$).

Figure 3a shows the ISFs extracted from measurements performed at 135° for gels formed at different concentrations
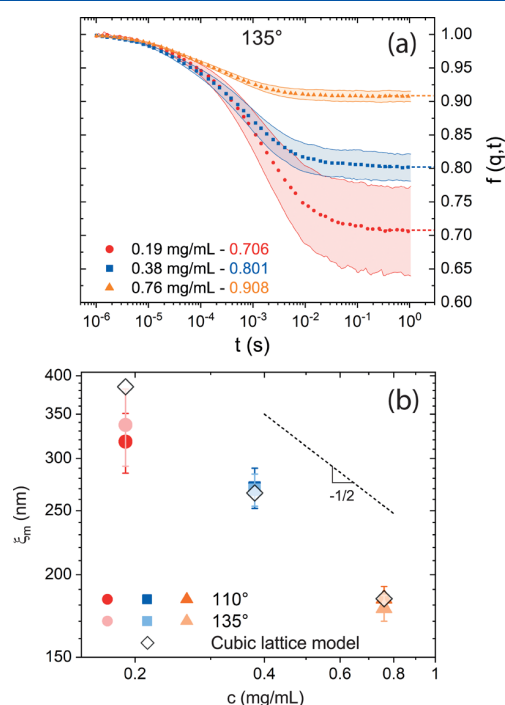

Figure 3. (a) Intermediate scattering function determined measuring βLG amyloid fibril gels formed in three different concentrations, at an angle of 135°. The numbers reported in the caption are the plateau values of the curves. (b) Calculated mesh size, compared with an estimation from the modified cubic lattice model. The dashed line ($\xi_m \sim c^{-1/2}$) is a guide to the eye.

of fibrils (0.19, 0.38, and 0.76 mg/mL). The lower the concentration, the larger the characteristic spacing among polymers: the consequent higher possibility of motion is reflected in lower plateau values. At the same time, lower concentrations also show higher standard deviations. We attribute this behavior to the higher heterogeneity of the network at more diluted conditions due to increased difficulty in creating entanglement points. Similar trends were obtained at a measurement angle of 110° (Figure S7). Through eq 6 and following the statistical analysis outlined in Figure S5b, we extracted the mesh size from the plateau values of the curves and plotted it as a function of concentration (Figure 3b). Measurements performed at 110 and 135° show nearly identical values of the mesh size. It can be noted how the

points follow closely the characteristic slope estimated through scaling arguments ($\xi_m \sim c^{-1/2}$).

To check if the determined values could match the theoretical description, we compare them with the output of the modified cubic lattice model (eq 4). As described earlier, classically $\phi_{L_m} = 1$ assuming infinitely long rods. However, with finite-sized objects, only the fibrils longer than L_m take part in the formation of the network. Therefore, we computed ϕ_{L_m} from the contour length distribution of the prepared amyloid fibrils. As such calculation depends on the mesh-size value (through the entanglement length $L_m = (3/2\xi_m^2 l_p)^{1/3}$), the experimentally determined ξ_m were used as inputs in a recursive algorithm, which allows the extraction of self-consistent values of l_c (Figure S8).

The output of the cubic lattice analysis is plotted in Figure 3b (white diamonds): the agreement with experimental results is remarkable. We would like to discuss further the data collected with the 0.19 and 0.76 mg/mL fibril gels. Considering the first of the two mentioned concentrations, experimental results are lower than the theoretical prediction. At first sight, this may sound unexpected: in fact, both measurement angles ensure full agreement with the conditions expressed by eq 2. We explain such observation by the finite contour length of the network-forming objects. At such low concentration, the number fraction of fibrils that are shorter than the entanglement length is significant. The modified cubic lattice model neglects the contribution of such fibrils in forming the network; however, they probably have a concrete role in making the gel less homogeneous and in further inhibiting the motion of the gel-forming units. As a result, the mesh size is underestimated. The 0.76 mg/mL fibril gel shows instead excellent agreement between the estimated mesh size and the calculated cubic lattice (ξ_m, $l_c \approx 180$ nm), despite the length-scales probed at 135 and 110° ($\delta \approx 250$ and 290 nm, respectively) being slightly larger than the mentioned values. We speculate that, despite the second condition of eq 2 ($\delta < \xi_m$) not being strictly fulfilled, multifilament relaxation modes play a marginal role in the mentioned q vectors. To further test our hypothesis, we plot in Figure 4 the values of the mesh size of the 0.38 mg/mL sample, extracted at measuring angles ranging from 135° ($\delta \approx 250$ nm) to 60° ($\delta \approx 480$ nm). With
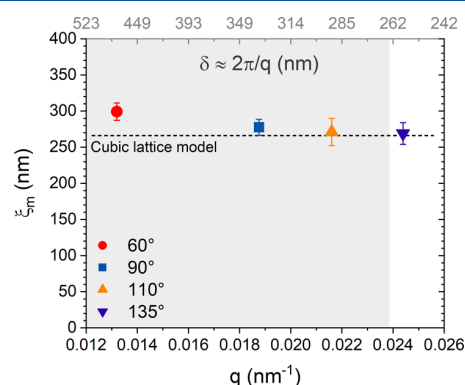
Figure 4. Extraction of the mesh size of the network for the 0.38 mg/mL sample at different angles. The horizontal dotted black line represents the estimation of ξ_m with the modified cubic lattice model. The gray zone represents the range where the characteristic probed length scale δ is larger than the output of the modified cubic lattice model.

46

decreasing measurement angles, ξ_m is progressively over-estimated. Data points at 90 and 110° ($\delta \approx 340$ and 290 nm, respectively) show a good agreement between experimental and theoretical estimations. In fact, the probed length scales are still reasonably close to the mesh size; moreover, multifilament dynamics do not play a significant role in these measurement conditions. On the other hand, at 60°, the mesh size is overestimated. We infer that this is due to the increased significance of gel relaxation modes at the characteristic probed length scale ($\delta \approx 480$ nm). Collective degrees of freedom sum up to the conformations available to single fibrils; the resulting higher decorrelation results in a lower plateau value, which in turn leads to an overestimation of ξ_m.

CONCLUSIONS

In the literature, DLS has already been used to study the morphology of polymer and colloidal hydrogels,[41,42] whose fractal structure gives rise to elastic modes spanning over a wide range of length scales.[43] In this work, we show that this technique can also be used to extract structural information (ξ_m, the mesh size) of semidiluted fibrillar gels. Despite the complex nature of amyloid fibril gels (polydisperse height of fibrils, potentially inhomogeneous network, wide distribution of contour lengths), the results follow the theoretical scaling law of mesh size as a function of concentration and are quantitatively in agreement with the modified cubic lattice model. One limit of the outlined technique is the length scale requirements ($d \ll \delta \ll l_p, L$ and $\delta < \xi_m$). In the discussion above, we saw that accurate values of ξ_m can be extracted even when δ is not strictly lower than the mesh size but still comparable to it. Such a statement holds true for those q vectors where multifilament dynamics play a marginal role.

With traditional light scattering equipment, ~200 nm is the minimum mesh size that can be detected with reasonable accuracy. More concentrated systems would fall out the suggested range and require characterization with other techniques recommended in the literature.[44−47] However, as many biological and colloidal samples build significantly strong gels at moderate concentrations, we foresee a potential application of this technique to characterize the microstructure of innovative and promising materials.

ASSOCIATED CONTENT

Ⓢ Supporting Information

The Supporting Information is available free of charge at https://pubs.acs.org/doi/10.1021/acs.macromol.0c00610.

> Statistical analysis of amyloid fibrils, amyloid aerogel preparation through CO_2 drying, SEM imaging of the aerogel, gel preparation for DLS measurements, DLS measurements protocol, ϕ_m computation, discussion on the alternative scaling law for the entanglement length ($L_m \sim (\xi_m^4 l_p)^{1/5}$), and derivation of equations in the article (PDF)

AUTHOR INFORMATION

Corresponding Author

Raffaele Mezzenga − *Department of Health Sciences and Technology and Department of Materials, ETH Zürich, 8092 Zürich, Switzerland;* ⓞ orcid.org/0000-0002-5739-2610; Email: raffaele.mezzenga@hest.ethz.ch

Authors

Mattia Usuelli − *Department of Health Sciences and Technology, ETH Zürich, 8092 Zürich, Switzerland;* ⓞ orcid.org/0000-0003-1459-7250

Yiping Cao − *Department of Health Sciences and Technology, ETH Zürich, 8092 Zürich, Switzerland*

Massimo Bagnani − *Department of Health Sciences and Technology, ETH Zürich, 8092 Zürich, Switzerland;* ⓞ orcid.org/0000-0002-1326-1600

Stephan Handschin − *Department of Health Sciences and Technology, ETH Zürich, 8092 Zürich, Switzerland*

Gustav Nyström − *Department of Health Sciences and Technology, ETH Zürich, 8092 Zürich, Switzerland; Laboratory for Cellulose & Wood Materials, EMPA, 8600 Dübendorf, Switzerland;* ⓞ orcid.org/0000-0003-2739-3222

Complete contact information is available at:
https://pubs.acs.org/10.1021/acs.macromol.0c00610

Notes

The authors declare no competing financial interest.

REFERENCES

(1) Broedersz, C. P.; MacKintosh, F. C. Modeling semiflexible polymer networks. *Rev. Mod. Phys.* **2014**, *86*, 995.

(2) Bausch, A. R.; Kroy, K. A bottom-up approach to cell mechanics. *Nat. Phys.* **2006**, *2*, 231.

(3) Knowles, T. P. J.; Mezzenga, R. Amyloid fibrils as building blocks for natural and artificial functional materials. *Adv. Mater.* **2016**, *28*, 6546−6561.

(4) Cao, Y.; Mezzenga, R. Food protein amyloid fibrils: origin, structure, formation, characterization, applications and health implications. *Adv. Colloid Interface Sci.* **2019**, *269*, 334−356.

(5) Nyström, G.; Fernández-Ronco, M. P.; Bolisetty, S.; Mazzotti, M.; Mezzenga, R. Amyloid templated gold aerogels. *Adv. Mater.* **2016**, *28*, 472−478.

(6) Shen, Y.; et al. Amyloid fibril systems reduce, stabilize and deliver bioavailable nanosized iron. *Nat. Nanotechnol.* **2017**, *12*, 642.

(7) Bolisetty, S.; Mezzenga, R. Amyloid−carbon hybrid membranes for universal water purification. *Nat. Nanotechnol.* **2016**, *11*, 365.

(8) De Gennes, P.-G.; Pincus, P.; Velasco, R. M.; Brochard, F. Remarks on polyelectrolyte conformation. *J. phys.* **1976**, *37*, 1461−1473.

(9) Schmidt, C. F.; Baermann, M.; Isenberg, G.; Sackmann, E. Chain dynamics, mesh size, and diffusive transport in networks of polymerized actin: a quasielastic light scattering and microfluorescence study. *Macromolecules* **1989**, *22*, 3638−3649.

(10) Valentine, M. T.; Kaplan, P. D.; Thota, D.; Crocker, J. C.; Gisler, T.; Prud'homme, R. K.; Beck, M.; Weitz, D. A. Investigating the microenvironments of inhomogeneous soft materials with multiple particle tracking. *Phys. Rev. E* **2001**, *64*, No. 061506.

(11) Wong, I. Y.; Gardel, M. L.; Reichman, D. R.; Weeks, E. R.; Valentine, M. T.; Bausch, A. R.; Weitz, D. A. Anomalous diffusion probes microstructure dynamics of entangled F-actin networks. *Phys. Rev. Lett.* **2004**, *92*, 178101.

(12) Valentine, M. T.; Perlman, Z. E.; Gardel, M. L.; Shin, J. H.; Matsudaira, P.; Mitchison, T. J.; Weitz, D. A. Colloid surface chemistry critically affects multiple particle tracking measurements of biomaterials. *Biophys. J.* **2004**, *86*, 4004−4014.

(13) Farge, E.; Maggs, A. C. Dynamic scattering from semiflexible polymers. *Macromolecules* **1993**, *26*, 5041−5044.

(14) Kroy, K.; Frey, E. Dynamic scattering from solutions of semiflexible polymers. *Physical Review E* **1997**, *55*, 3092.

(15) Arcovito, G.; Bassi, F. A.; De Spirito, M.; Di Stasio, E.; Sabetta, M. Dynamic light scattering study of fine semiflexible fibrin networks. *Biophys. Chem.* **1997**, *67*, 287−292.

(16) Götter, R.; Kroy, K.; Frey, E.; Bärmann, M.; Sackmann, E. Dynamic light scattering from semidilute actin solutions: a study of hydrodynamic screening, filament bending stiffness, and the effect of tropomyosin/troponin-binding. *Macromolecules* **1996**, *29*, 30−36.

(17) Janmey, P. A.; Hvidt, S.; Käs, J.; Lerche, D.; Maggs, A.; Sackmann, E.; Schliwa, M.; Stossel, T. P. The mechanical properties of actin gels. Elastic modulus and filament motions. *J. Biol. Chem.* **1994**, *269*, 32503−32513.

(18) Tassieri, M.; Evans, R. M. L.; Barbu-Tudoran, L.; Nasir Khaname, G.; Trinick, J.; Waigh, T. A. Dynamics of semiflexible polymer solutions in the highly entangled regime. *Phys. Rev. Lett.* **2008**, *101*, 198301.

(19) Pusey, P. N.; Van Megen, W. Dynamic light scattering by non-ergodic media. *Physica A: Statistical Mechanics and its Applications* **1989**, *157*, 705−741.

(20) Berne, B. J.; Pecora, R. *Dynamic light scattering: with applications to chemistry, biology, and physics*; Courier Corporation, 2000.

(21) Zemb, T.; Lindner, P. *Neutrons, X-rays and light: scattering methods applied to soft condensed matter*; North-Holland, 2002.

(22) Loveday, S. M.; Anema, S. G.; Singh, H. β-Lactoglobulin nanofibrils: The long and the short of it. *Int. Dairy J.* **2017**, *67*, 35−45.

(23) Vigolo, D.; Zhao, J.; Handschin, S.; Cao, X.; deMello, A. J.; Mezzenga, R. Continuous Isotropic-Nematic Transition in Amyloid Fibril Suspensions Driven by Thermophoresis. *Sci. Rep.* **2017**, *7*, 1211.

(24) Jung, J.-M.; Savin, G.; Pouzot, M.; Schmitt, C.; Mezzenga, R. Structure of heat-induced β-lactoglobulin aggregates and their complexes with sodium-dodecyl sulfate. *Biomacromolecules* **2008**, *9*, 2477−2486.

(25) Usov, I.; Mezzenga, R. FiberApp: an open-source software for tracking and analyzing polymers, filaments, biomacromolecules, and fibrous objects. *Macromolecules* **2015**, *48*, 1269−1280.

(26) Cao, Y.; Bolisetty, S.; Adamcik, J.; Mezzenga, R. Elasticity in physically cross-linked amyloid fibril networks. *Phys. Rev. Lett.* **2018**, *120*, 158103.

(27) Bolisetty, S.; Harnau, L.; Jung, J.-M.; Mezzenga, R. Gelation, phase behavior, and dynamics of β lactoglobulin amyloid fibrils at varying concentrations and ionic strengths. *Biomacromolecules* **2012**, *13*, 3241−3252.

(28) Bergenholtz, J.; Fuchs, M.; Voigtmann, T. Colloidal gelation and non-ergodicity transitions. *J. Phys.: Condens. Matter* **2000**, *12*, 6575.

(29) Joosten, J. G. H.; McCarthy, J. L.; Pusey, P. N. Dynamic and static light scattering by aqueous polyacrylamide gels. *Macromolecules* **1991**, *24*, 6690−6699.

(30) Cipelletti, L.; Bissig, H.; Trappe, V.; Ballesta, P.; Mazoyer, S. Time-resolved correlation: a new tool for studying temporally heterogeneous dynamics. *J. Phys.: Condens. Matter* **2003**, *15*, S257.

(31) Duri, A.; Sessoms, D. A.; Trappe, V.; Cipelletti, L. Resolving long-range spatial correlations in jammed colloidal systems using photon correlation imaging. *Phys. Rev. Lett.* **2009**, *102*, No. 085702.

(32) Secchi, E.; Munarin, F.; Alaimo, M. D.; Bosisio, S.; Buzzaccaro, S.; Ciccarella, G.; Vergaro, V.; Petrini, P.; Piazza, R. External and internal gelation of pectin solutions: microscopic dynamics versus macroscopic rheology. *J. Phys.: Condens. Matter* **2014**, *26*, 464106.

(33) Buzzaccaro, S.; Alaimo, M. D.; Secchi, E.; Piazza, R. Spatially: resolved heterogeneous dynamics in a strong colloidal gel. *J. Phys.: Condens. Matter* **2015**, *27*, 194120.

(34) Filiberti, Z.; Piazza, R.; Buzzaccaro, S. Multiscale relaxation in aging colloidal gels: From localized plastic events to system-spanning quakes. *Phys. Rev. E* **2019**, *100*, No. 042607.

(35) Semenov, A. N. Dynamics of concentrated solutions of rigid-chain polymers. Part 1.Brownian motion of persistent macromolecules in isotropic solution. *J. Chem. Soc., Faraday Trans. 2* **1986**, *82*, 317−329.

(36) Isambert, H.; Maggs, A. C. Dynamics and rheology of actin solutions. *Macromolecules* **1996**, *29*, 1036−1040.

(37) MacKintosh, F. C.; Käs, J.; Janmey, P. A. Elasticity of semiflexible biopolymer networks. *Phys. Rev. Lett.* **1995**, *75*, 4425.

(38) Käs, J.; Strey, H.; Sackmann, E. Direct imaging of reptation for semiflexible actin filaments. *Nature* **1994**, *368*, 226−229.

(39) Tassieri, M. Dynamics of semiflexible polymer solutions in the tightly entangled concentration regime. *Macromolecules* **2017**, *50*, 5611−5618.

(40) Morse, D. C. Tube diameter in tightly entangled solutions of semiflexible polymers. *Phys. Rev. E* **2001**, *63*, No. 031502.

(41) Barretta, P.; Bordi, F.; Rinaldi, C.; Paradossi, G. A dynamic light scattering study of hydrogels based on telechelic poly (vinyl alcohol). *J. Phys. Chem. B* **2000**, *104*, 11019−11026.

(42) Krall, A. H.; Weitz, D. A. Internal dynamics and elasticity of fractal colloidal gels. *Phys. Rev. Lett.* **1998**, *80*, 778.

(43) Krall, A. H.; Huang, Z.; Weitz, D. A. Dynamics of density fluctuations in colloidal gels. *Phys. A* **1997**, *235*, 19−33.

(44) Pescosolido, L.; Feruglio, L.; Farra, R.; Fiorentino, S.; Colombo, I.; Coviello, T.; Matricardi, P.; Hennink, W. E.; Vermonden, T.; Grassi, M. Mesh size distribution determination of interpenetrating polymer network hydrogels. *Soft Matter* **2012**, *8*, 7708−7715.

(45) Canal, T.; Peppas, N. A. Correlation between mesh size and equilibrium degree of swelling of polymeric networks. *J. Biomed. Mater. Res.* **1989**, *23*, 1183−1193.

(46) Hule, R. A.; Nagarkar, R. P.; Altunbas, A.; Ramay, H. R.; Branco, M. C.; Schneider, J. P.; Pochan, D. J. Correlations between structure, material properties and bioproperties in self-assembled β-hairpin peptide hydrogels. *Faraday Discuss.* **2008**, *139*, 251−264.

(47) Horkay, F.; Basser, P. J.; Hecht, A.-M.; Geissler, E. Structural investigations of a neutralized polyelectrolyte gel and an associating neutral hydrogel. *Polymer* **2005**, *46*, 4242−4247.

Supplemental Information

Probing the Structure of Filamentous Nonergodic Gels by Dynamic Light Scattering

Mattia Usuelli[†], Yiping Cao[†], Massimo Bagnani[†], Stephan Handschin[†], Gustav Nyström[†,‡], and Raffaele Mezzenga[*,†,¶]

[†] ETH Zürich, Department of Health Sciences and Technology, Schmelzbergstrasse 9, 8092 Zürich, Switzerland

[‡] EMPA, Laboratory for Cellulose & Wood Materials, Überlandstrasse 129, 8600 Dübendorf, Switzerland

[¶]ETH Zürich, Department of Materials, Wolfgang-Pauli-Strasse 10, 8093 Zürich, Switzerland

E-Mail: raffaele.mezzenga@hest.ethz.ch

Statistical Analysis of the prepared amyloid fibrils
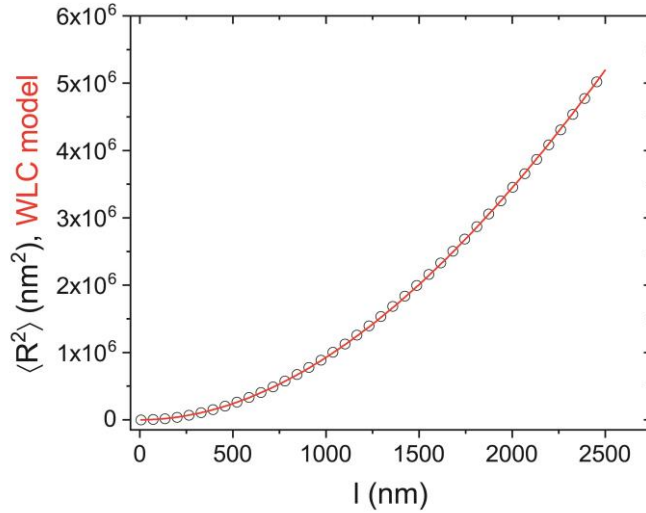
Figure S1: AFM characterization of βLG amyloid fibrils: Mean end-to-end distance ($\langle R \rangle^2$, empty circles) as a function of the internal contour length (l).The fit in red is based on the worm-like chain model: $\langle R \rangle^2 = 4l_p \left[l - 2l_p \left(1 - e^{-l/l_p} \right) \right]$. The value of the extracted persistence length of amyloid fibrils is $l_p = 2155$ nm.

In the main text the height relative frequency (f_h) and the internal contour length relative frequency (f_L) are reported. In the first case, the fitting is performed with a gaussian distribution $g(h; \mu_h, \sigma_h) = \frac{1}{\sigma\sqrt{2\pi}} e^{-\frac{(h-\mu_h)^2}{2\sigma_h^2}}$: the fitting parameters are reported in the main text. In the second case the fitting is performed with a log-normal distribution $\psi(L; \mu_L, \sigma_L) = \frac{1}{L\sigma_L\sqrt{2\pi}} e^{-\frac{(ln(L)-\mu_L)^2}{2\sigma_L^2}}$. The values of the extracted parameters are μ_L=6.69 and σ_L=1.07 (with L given in nm).

βLG amyloid fibril aerogel preparation and SEM Imaging

βLG amyloid fibril aerogel preparation

The outlet part of a 10 mL syringe (InkJet, B.Braun) was cut and, after having pulled the piston partially down, 1 mL of a 5 mg/mL total proteins solution was transferred inside the syringe. The syringe was covered with a dialysis membrane (Spectra/Por®, MWCO 6-8 kDa, Spectrum Laboratories Inc.), previously washed with MQ water and dried over a paper tissue (KimTech, Kimberly-Clark Professional). The membrane was afterwards tightened to the walls of the syringe using parafilm (PM-996, Parafilm, USA). After being turned upside-down (to put the amyloid fibrils solution in contact with the membrane), the syringe was partially immersed in a pH 2, 300 mM NaCl solution bath. In this way, the ions could diffuse inside the colloidal dispersion through the membrane and promote gelation. This process is illustrated in figure S2.

S2

The syringe was afterwards removed from the salt bath and the gel was transferred inside a home-made aluminium cage with small holes, which was then put in a ∼ 50% EtOH solution to promote solvent exchange for at least 24 hours. The ∼ 50% EtOH solution was prepared adding MQ at pH 2 to a 99.8% EtOH solution. Two further successive bath exchanges against 99.8% EtOH solution, with similar time-scale as the first one, were made to promote total solvent exchange inside the gel. An alcohol-gel was formed as a consequence of this process.

The alcohol-gel was then CO_2 dried through an automatic process inclusive of stasis cycles (to enhance the diffusion of CO_2 inside the sample), using a commercially available equipment (Autosamdri®-931, Tousimis, USA). The obtained aerogel was removed from the cage and put in a petri-dish. The petri-dish was afterwards sealed with parafilm (PM-996, Parafilm, USA).
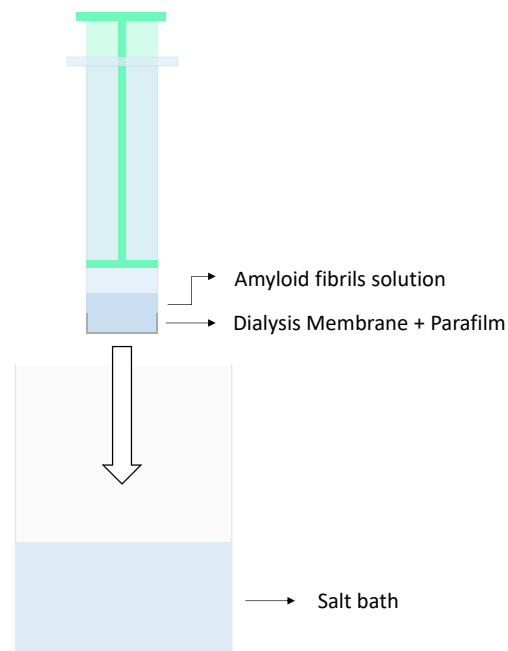
Figure S2: Schematic of the process for preparing a βLG gel with ions diffusion through a dialysis membrane.

SEM Imaging

Small pieces of the aerogels were mounted on SEM aluminium pin stubs with double adhesive carbon tape. The samples were additionally fixed with conductive silver paint (Plano, DE) all around it. After drying, the samples were carefully cut with a razor blade and sputter-coated with 4 nm of platinum/palladium (CCU-10, Safematic, CH). SE-inlens images were recorded at a working distance of 4-5 mm with a scanning electron microscope (Merlin FE-SEM, Zeiss, DE), operated at an accelerating voltage of 1.5 kV.
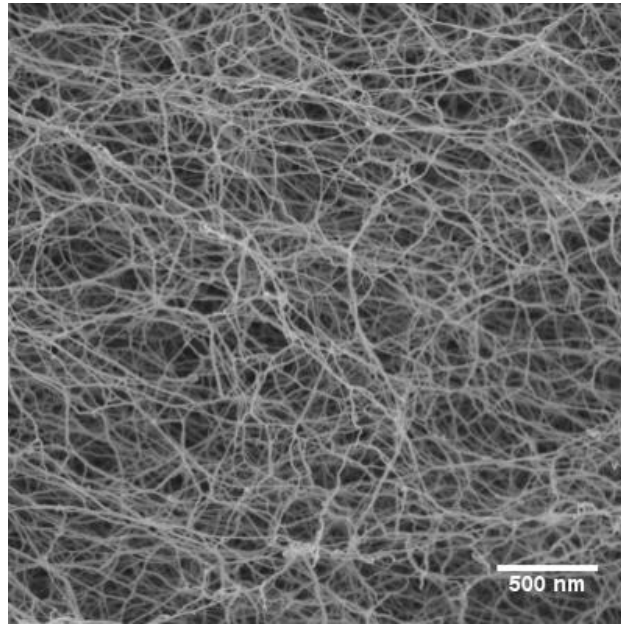
S3

Figure S3: SEM Image of a CO_2 dried 5 mg/mL ßLG gel where the cross-linked structure of the amyloid fibrils network is evident.

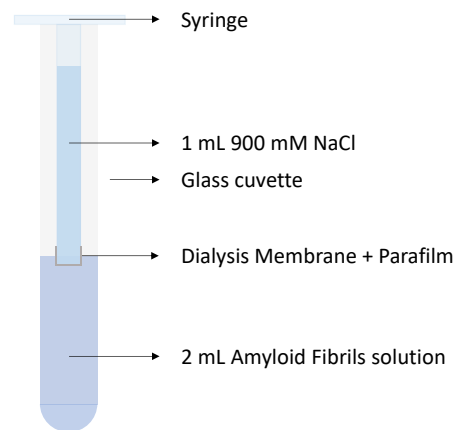# DLS samples preparation and measurement

DLS samples preparation

Syringe

1 mL 900 mM NaCl

Glass cuvette

Dialysis Membrane + Parafilm

2 mL Amyloid Fibrils solution

Figure S4: Schematic of the preparation of ßLG gels for Dynamic Light Scattering (DLS) measurements.
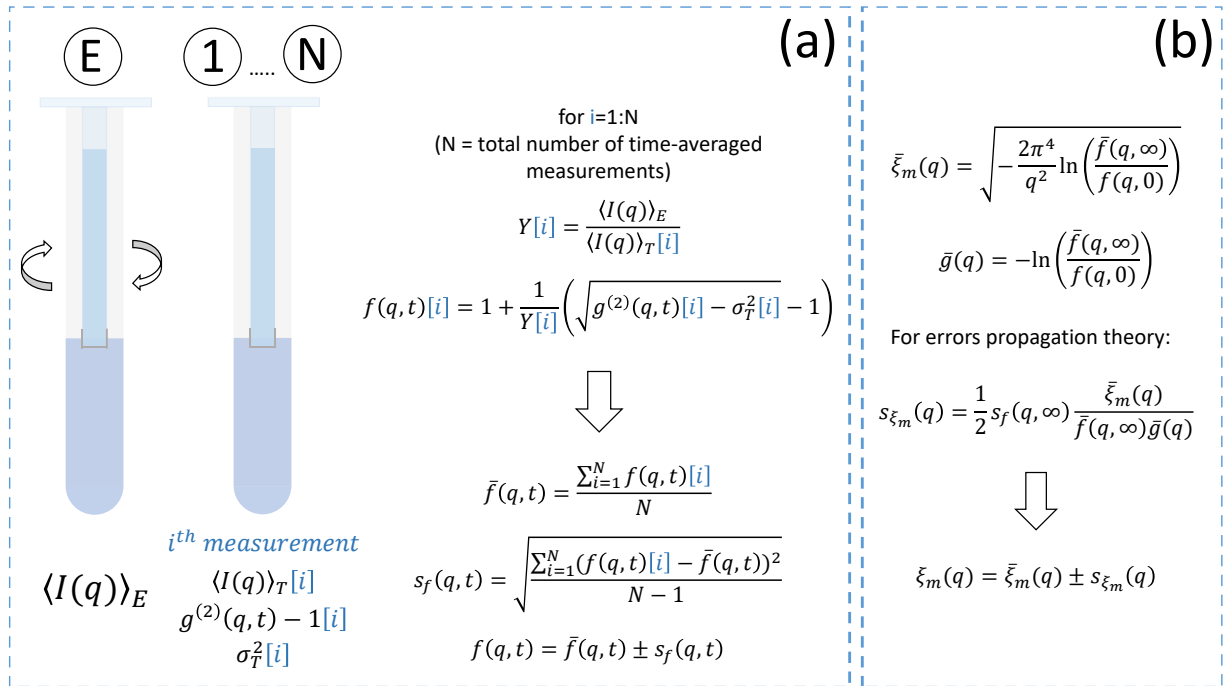
S4

DLS samples measurements and data treatment

Figure S5: Panel a): Schematic of DLS measurements and data correction. Panel b): Extraction of the mesh size from the f(q,t).

Table S1: Relationship between measurement angle (°), probed q-vector (nm⁻¹) and characteristic length-scale (nm). The calculations have been performed considering the refractive index of water (n = 1.33) and the wavelength of the laser source (633 nm, He-Ne Laser).

Measurement angle (°)	q (nm⁻¹)	$\delta = \frac{2\pi}{q}$ (nm)
60	$1.32 \cdot 10^{-2}$	476
90	$1.87 \cdot 10^{-2}$	337
110	$2.16 \cdot 10^{-2}$	291
135	$2.44 \cdot 10^{-2}$	258

Derivation of equation (5) – Plateau value of $f(q,t)$

According to Kroy and Frey[1], for $t \gg \tau_{L_m}$, the Intermediate Scattering Function is decaying to a plateau value equal to:

$$\frac{f\left(q, t \gg \tau_{L_m}\right)}{f(q,0)} = e^{-\frac{\left(\gamma_q \tau_{L_m}\right)^{3/4}}{3\pi}} \qquad (S1)$$

To derive the final formula for the determination of the mesh size, we consider the definition of the following quantities:

S5

$$\tau_L = \frac{\tilde{\zeta}_\perp}{\kappa}\left(\frac{L}{\pi}\right)^4 \tag{S2}$$

$$\tilde{\zeta}_\perp = \frac{4\pi\eta}{\ln\left(\frac{\xi_h}{a}\right)} \tag{S3}$$

$$L_m = \left(\frac{3}{2}\xi_m^2 l_p\right)^{1/3} \tag{S4}$$

$$\gamma_q = \frac{k_B T}{\tilde{\zeta}_\perp} q^{8/3} l_p^{-1/3} \tag{S5}$$

In the previous equations, $\tilde{\zeta}_\perp$ represents the effective transverse friction coefficient, with ξ_h being the hydrodynamic screening length, η the viscosity of the solvent and a the characteristic radius of the semi-flexible rods. τ_L is the Rouse-like decay time of a vibrational mode with length $2L$ and $\kappa = l_p k_B T$ is the bending rigidity of the rods. γ_q is the characteristic decay factor that governs the evolution of $f(q,t)$.

Substituting equation (S3) and (S4) into equation (S2) and equation (S3) into equation (S5), it is possible to define the following quantity:

$$\gamma_q \tau_{L_m} = \frac{k_B T \ln\left(\frac{\xi_h}{a}\right)}{4\pi\eta} q^{8/3} l_p^{-1/3} \frac{4\pi\eta}{\ln\left(\frac{\xi_h}{a}\right) k_B T l_p}\left(\frac{3\xi_m^2 l_p}{2\pi^3}\right)^{4/3} = q^{8/3}\left(\frac{3\xi_m^2}{2\pi^3}\right)^{4/3} \tag{S6}$$

Therefore, substituting in equation (S1):

$$\frac{f(q,t \gg \tau_{L_m})}{f(q,0)} = e^{-\frac{(\gamma_q \tau_{L_m})^{3/4}}{3\pi}} = e^{-\frac{\left(q^{8/3}\left(\frac{3\xi_m^2}{2\pi^3}\right)^{4/3}\right)^{3/4}}{3\pi}} = e^{-\frac{q^2 \xi_m^2}{2\pi^4}} \tag{S7}$$

As written in the main manuscript, the plateau value of the intermediate scattering function is actually a quantity that does not depend on the characteristic dynamics of the system. In fact, it is related to the sum of the possible configurations assumable by the network-forming units. Therefore, it should be possible to derive equation (S7) in a way that does not involve dynamic quantities: this is evident by the fact that $\tilde{\zeta}_\perp$ cancels out in equation (S6).

As a possible route, we express the plateau value of $f(q,\infty)$ as function of the probed q-vector (q) and of the characteristic mean-squared transverse displacement of the filaments ($\langle u^2\rangle$):

$$f(q,\infty) = e^{-Cq^2\langle u^2\rangle}$$

S6

54

The quantity C is a yet undetermined constant. The transverse undulations of a filament with contour L can be expressed as[2] $\langle u^2 \rangle \sim L^3/l_p$. Considering that the characteristic length-scale which undergoes fluctuations is L_m, and using the scaling derived through the EMA model $\left(L_m \sim l_p^{1/3} \xi_m^{2/3} \right)$:

$$\langle u^2 \rangle \sim \frac{L_m^3}{l_p} \sim \frac{\left(l_p^{1/3} \xi_m^{2/3} \right)^3}{l_p} \sim \xi_m^2$$

Consequently:

$$f(q, \infty) = e^{-C' q^2 \xi_m^2}$$

This equation is equivalent to Eq. (S7): the only difference is in the presence of an undetermined numerical pre-factor, that in the derivation of Kroy and Frey assumes a specific value ($C' = (2\pi^4)^{-1}$).

Dependance of L_m on ξ_m and l_p

In the main text, we show that two different scaling laws for the entanglement length could be found in the literature: $L_m \sim \left(\xi_m^4 l_p \right)^{1/5}$ and $L_m \sim \left(\xi_m^2 l_p \right)^{1/3}$. In this section, our aim is to discuss in a more detailed way the derivation of such expressions and to compare them with already published experimental data.

For the fore-coming considerations, we will use the following notation.

l_p : Persistence length of the polymer. In the case of the worm-like chain model (WLC), such quantity is half of the Kuhn length; we will use l_p for describing the bending rigidity of considered objects.

L_m : Entanglement length, which can be regarded as the mean distance between neighbouring contacts of a chain with the surrounding network.

ξ_m : Mesh size of the network, defined as the typical spacing between polymers in solution.

L : Contour length of the semi-flexible rods.

R_e : Characteristic radius of the tube where, in an entangled state, a single chains is confined for times shorter than the reptation one.

Further quantities will be introduced directly in the discussion.

The dependence $L_m \sim \left(\xi_m^4 l_p \right)^{1/5}$ has been pointed out by many authors, and is based on scaling considerations. A first derivation was made by Semenov[3], who used the slip-link model (previously introduced by Doi and Edwards) to study the behaviour of rigid-chain polymers in concentrated solutions. According to the author[3], segments confined between successive clamped points can bend within angles $\Delta\theta \sim \left(L_m/l_p \right)^{1/2}$, with consequent transverse fluctuations $\sqrt{\langle u^2 \rangle} \sim L_m \Delta\theta \sim \left(L_m^3/l_p \right)^{1/2}$. The tube in which, as a consequence of entanglements, a polymer is confined, can be

S7

regarded as a cylinder having a characteristic radius $\sqrt{\langle u^2 \rangle}$; the number of times such tube is intersected by surrounding chains is $N \sim cLL_m\sqrt{\langle u^2 \rangle}$, where c is the number concentration of chains per volume. Imposing $N \sim 1$:

$$1 \sim cLL_m\sqrt{\langle u^2 \rangle} \, ; \, 1 \sim cLL_m^{5/2}l_p^{-1/2} \, ; \, L_m \sim L^{-2/5}l_p^{1/5}c^{-2/5}$$

Considering that $\xi_m \sim c^{-1/2}$ in a semi-diluted solution of semi-flexible polymers, then[2]:

$$L_m \sim l_p^{1/5}\xi_m^{4/5}$$

Other authors arrived at the same result following similar considerations[2,4–6]. The expression used in our work $\left(L_m = \left(3/2 \, l_p\xi_m^2 \right)^{1/3} \right)$ differs for two main aspect from the expression derived by Semenov. Firstly, the scaling exponents are different. Secondly, it has a specific pre-factor $\left(\left(3/2 \right)^{1/3} \right)$ that makes it an equality and not a scaling. Such expression is used by Kroy and Frey in their work on dynamic scattering from solutions of semi-flexible polymers[1], without any reference to previously published articles. The existence of two different scaling laws for describing the same quantity is puzzling: we searched further in the literature for solving this dilemma.

A theoretical work from Morse can shed light on such controversy[7]. The aim of the author is to "*give a quantitative theoretical treatment of the forces confining each polymer to a tube in tightly entangled solutions, and thereby predict values for the tube diameter and plateau modulus in such solutions*" [7]. The term "tightly entangled" refers to solutions where semi-flexible polymers are confined in tubes, where the tube diameter and entanglement length (respectively $2R_e$ and L_m) are considerably shorter than L and l_p. To pursue such aim, the author performs a statistical mechanics description of the transverse fluctuations of a test chain, embedded in a network made of uncrossable medium chains. The two-dimensional transverse displacement vector $\boldsymbol{h}(s) = (h_1(s), h_2(s))$ of the test chain can be decomposed in two Cartesian components, locally perpendicular to the tube tangent, which can be Fourier transformed ($\boldsymbol{h}(q) = (h_1(q), h_2(q))$). The characteristic radius of the tubes, in which single chains are confined, is directly related to the variance of each transverse displacement component; this quantity can be expressed either in the direct or in the Fourier Space.

$$R_e^2 \equiv \overline{\langle h_\alpha^2(s) \rangle_0} = \int \frac{dq}{2\pi} \frac{T}{Tl_pq^4 + \gamma(q)}$$

In the equation, $\overline{\dots}$ denotes an average over all possible network topologies, $\langle \dots \rangle$ denotes a thermal average and T is the temperature expressed in energy units (so that $k_B \equiv 1$). From the equation above, it is possible to see that transverse fluctuations in the Fourier space are ruled by two different terms. Tl_pq^4 is related to the bending energy of the test chain, while $\gamma(q)$ is a spring constant which takes into account confinement forces by the surrounding network. Intuitively, L_m is the characteristic length-scale that rules which of the two terms dominates. When $qL_m \gg 1$, the focus is on chain

S8

sections that are shorter than entanglements, where bending energetics dominate ($Tl_pq^4 \gg \gamma(q)$). On the other hand, when $qL_m \ll 1$, confinement forces win the game and damp fluctuations down ($Tl_pq^4 \ll \gamma(q)$).

To analytically derive R_e^2, the author had to find possible self-consistent models for $\gamma(q)$, from different assumptions on confinement potentials. Once the analytical expression of $\gamma(q)$ is derived, it can be used for estimating quantitatively the entanglement length as well, which the author defined as:

$$\frac{1}{L_m} \equiv \int \frac{dq}{2\pi} \frac{\gamma(q)}{Tl_pq^4 + \gamma(q)}$$

Therefore, the defined models not only provide scaling exponents for the quantities of interest, but are also able to determine numerical pre-factors.

Morse describes three models: namely, Binary Collision Approximation (BCA), Effective Medium Approximation (EMA) and Elastic Network Approximation (ENA). We will focus on the first two models, as the third one is a combination of the two and does not allow expressing the relationship among L_m, ξ_m and l_p through simple scaling laws.

The first model, BCA, considers interactions of the test chains with nearby medium chains, neglecting however elastic relaxation modes that arise from the whole network. Detailed calculations show that[7], in such assumptions, the following scaling for the tube diameter can be extracted: $R_e \sim l_p^{-1/5}\rho^{-3/5}$ (where ρ is the total contour length per unit volume, and is directly related to the concentration of polymer chains). Considering that $L_m \sim l_p^{1/3}R_e^{2/3}$ (accordingly with the derivation of Odijk[8]), the author derived $L_m \sim l_p^{1/5}\rho^{-2/5} \sim l_p^{1/5}\xi_m^{4/5}$. Such expression is consistent with the scaling arguments outlined before by simple geometrical analysis [2–6].

In the second model, EMA, the network that surrounds the test chain is treated as an elastic continuum with a shear modulus G determined in a self-consistent way. The quantity $\gamma(q)$, in such hypothesis, represents an effective spring constant with L_m as a short wave-length cut off. Such theoretical analysis allowed the author to obtain the following scaling laws[7]:

$$R_e \sim \rho^{-1/2} \sim \xi_m$$
$$L_m \sim l_p^{1/3}R_e^{2/3} \sim l_p^{1/3}\xi_m^{2/3}$$

We can note that the scaling behaviour obtained through EMA is the same as the one used by Kroy and Frey[1].

As the derivation of Kroy and Frey[1], which is used to build up our model, considers an infrared-cut off to the oscillation, it seems to us that the underlying assumptions are more similar to the ones of the EMA model than to the ones of BCA. Such similarity can be appreciated from the following statements of the authors in the two articles. In the case of Kroy and Frey: «*The lower limit of the integral serves*

S9

to exclude modes of wavelength longer than $2L_m$. By L_m we denote the contour length between adjacent clamped points along the contour. This infrared cutoff is a heuristic way to take into account the effects of steric constraints, so-called entanglements»[1] (pag. 3095). In the case of Morse: «*The length L_m appears within the logarithm in Eq. (20) because it has been introduced into the continuum mechanical calculation as a short-wavelength cutoff length, thus effectively smearing the forces applied to the chain over a region with a radius of order L_m around the test chain*»[7] (pag.5, where L_m has been substituted to the notation L_e used by the author). Morse also adds that «*The effective medium approximation allows the environment of a test chain to deform like an elastic continuum, but then unrealistically forces the test chain to rigidly follow the surrounding continuum*»[7]. In the case of our amyloid fibril gels, such approximation is not unrealistic due to the long-lived cross-links between amyloid fibrils in the network upon addition of salt[9].

It seems, therefore, that Kroy and Frey obtained the expression $L_m = \left(3/2\, l_p \xi_m^2\right)^{1/3}$ with assumptions similar to the EMA model. In the case of EMA, the author could calculate numerical pre-factors assuming a specific functional form for the function $H(q)$[7]; it appears probable to us that Kroy and Frey calculated the prefactor $\left(3/2\right)^{1/3}$ with a similar approach.

Analysing the two models (BCA and EMA) developed by Morse[7], we saw that both scaling laws $\left(L_m \sim l_p^{1/5} \xi_m^{4/5}\right.$ and $\left.L_m \sim l_p^{1/3} \xi_m^{2/3}\right)$ found in literature are possible, depending on the assumption of the nature of acting confinement forces. The question, which still needs to be answered, is whether BCA or EMA describes more accurately the behaviour of tightly entangled solutions of semi-flexible polymers.

To answer this question, it is profitable to extend the analysis to the field where L_m is used most: rheology. In the following, we will focus both on tightly entangled solutions (with no cross-links) and on tightly entangled cross-linked solutions (more compatible to our case). To fully understand the influence of the presence of cross-links, it is worth discussing the different contributes which build up the viscoelastic response of semi-flexible polymer networks. At a single chain level, intramolecular stress is built up by curvature, orientation and tension contributes (plus an osmotic pressure contribute that will be here neglected)[10,11]. Morse performed a detailed analysis on the quantities that play a leading role in the viscoelastic response, and found curvature and tension being the dominating terms[11]. Which of the two terms dominates, actually depends on the time-scales at which the system is probed. Considering the two characteristic timescales $\tau_{rep} \sim L^3$ (reptation) and $\tau_e \sim \frac{L_m^4}{L}$ (oscillatory mode with length L_m), an oscillatory sweep with characteristic frequency $f \gtrsim \tau_{rep}^{-1}$ allows single chains to relax oscillatory modes, but does not allow reptation to fully express itself. As a consequence,

S10

curvature stress contributes are the dominating ones, leading to a modulus which can be expressed as:

$$G \sim \frac{T\rho}{L_m}$$

On the other hand, when the probed frequency fulfils the condition $\tau_{rep}^{-1} \ll f \lesssim \tau_e^{-1}$, the internal tension can not fully relax. Such condition made Morse[11] retrieving a scaling law equivalent to the one previously found by MacKintosh[5] and co-workers, which is based on the assumptions of the tension contribute being the dominating one and of the inability of the system to relax such tension. As expressed before, such hypothesis is valid for high probing frequencies; however, there is another condition where such assumptions are met: in the case of the presence of physical/chemical long-lived cross-links. These considerations allowed the development of the affine thermal model, where the shear modulus can be expressed as[5]:

$$G \sim T l_p^2 \xi_m^{-2} L_m^{-3}$$

In the following table, we combine the discussed expressions describing the shear modulus with the scaling obtained in BCA and EMA models. For the calculations, the scaling $\xi_m \sim \rho^{-1/2}$ has also been used[2]:

Table S2: Scaling laws of G on ρ and l_p, as a function of the probed frequency, of the presence/absence of cross-links and of the model (BCA/EMA) for describing the behaviour of a test chain in the entangled network.

	BCA $\left(L_m \sim l_p^{1/5} \rho^{-2/5} \right)$	EMA $\left(L_m \sim l_p^{1/3} \rho^{-1/3} \right)$
Tightly entangled solutions (no-crosslinks, low frequency) $G \sim \dfrac{T\rho}{L_m}$	$G \sim T\rho^{7/5} l_p^{-1/5}$	$G \sim T\rho^{4/3} l_p^{-1/3}$
Tightly entangled solutions (crosslinks) or (no-crosslinks, high frequency) $G \sim \dfrac{T l_p^2}{\xi_m^2 L_m^3}$	$G \sim T\rho^{11/5} l_p^{7/5}$	$G \sim T\rho^2 l_p$

As outlined in the table, Morse obtained $G \sim T\rho^{7/5} l_p^{-1/5}$ in the Binary Collision Approximation and $G \sim T\rho^{4/3} l_p^{-1/3}$ in the Effective Medium Approximation (for tightly entangled solutions with no-crosslinks, probed at low frequency). When commenting on which model describes the system at best for $\rho l_p^2 \gg 1$, the author says: «*Because these two approaches describe two essentially independent mechanisms for displacement of the test chain (i.e., displacement of the test chain relative to the*

average displacement of a partially frozen environment in the BCA and collective elastic displacement of that environment in the EMA), the tube diameter is presumably controlled by whichever mechanism predicts a larger tube diameter. In the limit ρl_p^2 of interest, the EMA prediction for the tube radius is larger than the BCA prediction by a factor proportional to $\left(\rho l_p^2\right)^{1/10}$, suggesting that it is actually the EMA that yields the correct asymptotic scaling in the limit of extremely tightly entangled chains. It is important to note, however, that the values of the exponents obtained in these two approaches are numerically quite close (e.g., $G \propto \rho^{1.33}$ vs $G \propto \rho^{1.4}$), so that the competing physical mechanisms assumed in these two approaches could remain comparable in importance at all but truly enormous values of ρl_p^2» [7].

We believe, therefore, that both models can profitably describe the dependence of G on ρ at intermediate values of ρl_p^2. A clearer answer on the accuracy of the models can come, instead, from an analysis of the dependence of G on l_p. First of all, we want to emphasize that such dependence is a scaling law with a negative exponent. In fact, according to the described models, the larger the persistence length, the larger the entanglement length: the fewer resulting contacts among chains result in a drop of the value of $G \sim \frac{T\rho}{L_m}$. However, the characteristic scaling exponents of the persistence length in the two described models are significantly different (G $\propto l_p^{-0.2}$ vs G $\propto l_p^{-0.33}$, respectively for BCA and EMA): precise experiments should allow to discriminate which model describes better the rheology of tightly entangled solutions.

Tassieri and co-workers studied F-actin networks in solution, where different buffers allowed to tune the persistence length of the biopolymers[12]. Combining PVPTM (passive video particle tracking microrheology) with DLS (dynamic light scattering), the authors determined independently the plateau elastic modulus G of the dispersions and the persistence length l_p of the network-forming units. By taking the ratio of values measured for two suspensions at different conditions, the authors showed that EMA described better the experimental data they collected.

However, in a recently published work[13], Schuldt and co-workers used DNA n-helix tubes (whose persistence length can be finely tuned) to characterize the scaling of G as a function of l_p in tightly entangled states, without cross-links: instead of finding a negative exponent, as predicted by both BCA ($G \sim T\rho^{7/5}l_p^{-1/5}$) and EMA ($G \sim T\rho^{4/3}l_p^{-1/3}$), the authors surprisingly found that $G \sim \rho^{7/5}l_p$.

Combining existing evidence in literature, Tassieri pointed out that it is not clear weather BCA or EMA describes better the behaviour of semiflexible polymers in the tightly entangled state[14]. In fact, while both models adequately capture the scaling of G as a function of ρ, both fail in explaining experimental data on the dependence of G on l_p; according to the author, G should follow scaling on ρ and l_p with both positive exponents.

S12

The only theoretical expression which respects such evidence is the above described one derived by MacKintosh and colleagues[5] ($G \sim T l_p^2 \xi_m^{-2} L_m^{-3}$). In their analysis the authors, using the scaling law of Semenov[3] $\left(L_m \sim l_p^{1/5} \rho^{-2/5} \right)$ and, considering that $\xi_m \sim \rho^{-1/2}$, derived:

$$G \sim T l_p^2 \xi_m^{-2} L_m^{-3} \sim T l_p^2 \rho l_p^{-3/5} \rho^{6/5} \sim T \rho^{11/5} l_p^{7/5}$$

Here, the positive exponent of l_p arises from the intra-filament tension experienced by the semi-flexible polymers[5], which scales quadratically with the bending modulus $\kappa = k_B T l_p$. Tassieri points out that[14], if the EMA scaling had instead been used by MacKintosh and co-workers[5], the final result would have been $G \sim \rho^2 l_p$ (bottom-right equation in the table S2). Such result would explain the experimental data of Schuldt et al. [13] in terms of the dependence of G on l_p, but not the one of G on ρ.

To address such discrepancy between theoretical models and available experimental data from different systems, Tassieri affirms that R_e and L_m might be quantities with a concentration-dependent distributions $P(R_e)$ and $P(L_m)$, which might be non-symmetric Gaussian functions; he encourages therefore the development of new models that take into account such important aspect[14].

To resume and extend the above-made analysis to our system, we point out that there is no broad agreement in literature on the correct scaling laws $\left(L_m \sim l_p^{1/3} \xi_m^{2/3} \text{ or } L_m \sim l_p^{1/5} \xi_m^{4/5} \right)$. The hypotheses on which EMA is based are similar to the ones that Kroy and Frey used for describing dynamic scattering from semiflexible polymers solutions. Moreover, the gel state of our system further corroborates the EMA assumption of the test chain rigidly following the surrounding medium, as explained above. It seems to us that these considerations justify the use of the equation $L_m = \left(\frac{3}{2} \xi_m^2 l_p \right)^{1/3}$ in the main text.

At the same time, we recognize that the equation from MacKintosh and co-workers[5] $\left(G \sim \rho^{11/5} l_p^{7/5} \right)$ has already been used to profitably describe the behaviour of the shear modulus G of amyloid fibril gels as a function of concentration (c) and ionic strength (I)[9], and that such scaling is based on the work of Semenov[3] $\left(L_m \sim l_p^{1/5} \xi_m^{4/5} \right)$. Therefore, we derive here alternative equations based on the BCA scaling laws and use them to describe the experimental data.

S13

Derivation of alternative equation for correlating the plateau value of $f(q,t)$ to ξ_m, based on BCA model

The starting point for the derivation are equations (S1), (S2), (S3) and (S4). Equation (S4), $L_m = \left(\frac{3}{2}\xi_m^2 l_p\right)^{1/3}$, is replaced by the characteristic scaling of the BCA model, $L_m \sim \left(\xi_m^4 l_p\right)^{1/5}$. To make such scaling quantitative, we introduce an adimensional pre-factor A, which is not yet determined:

$$L_m = A\left(\xi_m^4 l_p\right)^{1/5} \tag{S8}$$

Using this expression in the product $\gamma_q \tau_{L_m}$, it is possible to obtain:

$$\gamma_q \tau_{L_m} = \frac{k_B T \ln\left(\frac{\xi_h}{a}\right)}{4\pi\eta} q^{8/3} l_p^{-1/3} \frac{4\pi\eta}{\ln\left(\frac{\xi_h}{a}\right) k_B T l_p} \left(\frac{A^5 \xi_m^4 l_p}{\pi^5}\right)^{4/5} = \frac{A^4}{\pi^4} q^{8/3} \xi_m^{16/5} l_p^{-8/15}$$

Substituting in equation (S1):

$$\frac{f(q, t \gg \tau_{L_m})}{f(q,0)} = e^{-\frac{(\gamma_q \tau_{L_m})^{3/4}}{3\pi}} = e^{-\frac{\left(\frac{A^4}{\pi^4} q^{8/3} \xi_m^{16/5} l_p^{-8/15}\right)^{3/4}}{3\pi}} = e^{-\frac{A^3}{3\pi^4} q^2 \xi_m^{12/5} l_p^{-2/5}}$$

The equation can be inverted to determine the mesh size:

$$\xi_m = \left(-\frac{3\pi^4}{A^3 q^2 l_p^{-2/5}} \ln\left(\frac{f(q,\infty)}{f(q,0)}\right)\right)^{5/12} \tag{S9}$$

S14

ICFs and ISFs measured at different angles
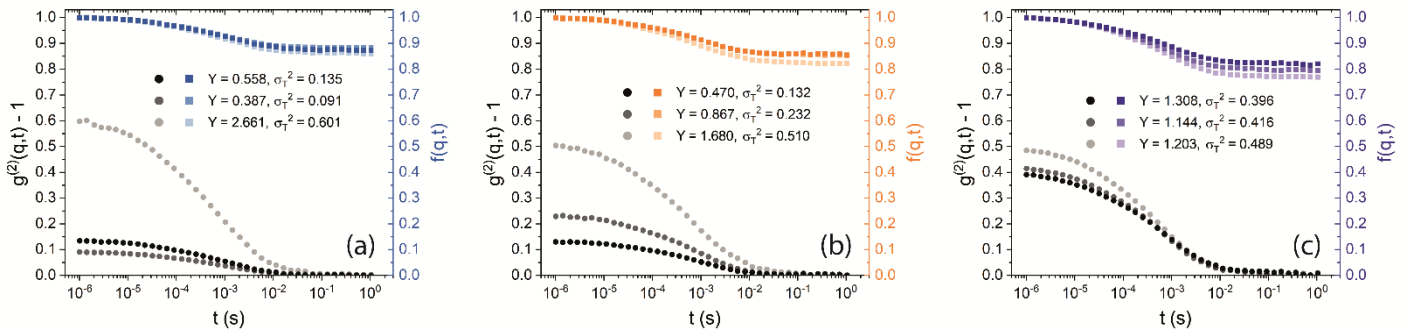
Figure S6: Examples of intensity correlation functions $(g^{(2)}(q,t) - 1)$ and corrected intermediate scattering functions $(f(q,t))$ for a 0.38 mg/mL βLG amyloid fibril gel. The measurements were performed at 90° (panel a), 110° (panel b) and 135° (panel c).
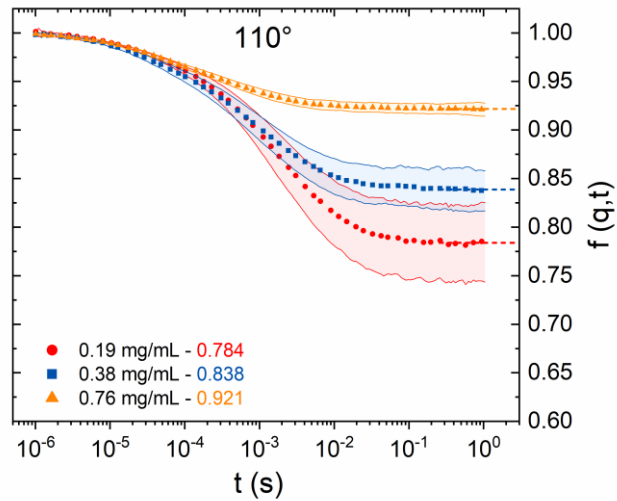
Figure S7: Corrected intermediate scattering functions $(f(q,t))$ of βLG amyloid fibril gels at three different concentrations (0.19 mg/mL, 0.38 mg/mL, 0.76 mg/mL), measured at an angle of 110°.

Derivation of $\boldsymbol{\phi_{L_m}}$

$$\phi_{L_m} = 1 - \frac{\int_0^{L_m} \psi(L; \mu, \sigma_L) \pi a^2 \rho L dL}{\int_0^\infty \psi(L; \mu, \sigma_L) \pi a^2 \rho L dL} = 1 - \frac{\int_0^{L_m} \psi(L; \mu, \sigma_L) L dL}{\int_0^\infty \psi(L; \mu, \sigma_L) L dL}$$

S15

Here $\psi(L; \mu_L, \sigma_L)$ represents the log-normal distribution used to describe the contour length relative frequency, with $\mu_L = 6.69$ and $\sigma_L = 1.07$. Further calculation show that the desired quantity can be directly estimated from the standard normal cumulative distribution function:

$$\int_0^{L_m} \psi(L; \mu, \sigma) L dL = \int_0^{L_m} \frac{1}{L\sigma\sqrt{2\pi}} e^{-\frac{(ln(L)-\mu)^2}{2\sigma^2}} L dL = \int_0^{L_m} \frac{1}{\sigma\sqrt{2\pi}} e^{-\frac{(ln(L)-\mu)^2}{2\sigma^2}} dL$$

It is possible to introduce the following auxiliary variables:

$$z = \frac{ln(L) - (\mu + \sigma^2)}{\sigma} \ ; \ L = e^{\mu+\sigma^2} e^{\sigma z} \ ; \ dL = e^{\mu+\sigma^2} e^{\sigma z} \sigma \ ; \ \lambda_m = \frac{ln(L_m) - (\mu + \sigma^2)}{\sigma}$$

Then:

$$\int_0^{L_m} \frac{1}{\sigma\sqrt{2\pi}} e^{-\frac{(ln(L)-\mu)^2}{2\sigma^2}} dL = e^{\mu+\sigma^2} \int_{-\infty}^{\lambda_m} \frac{1}{\sqrt{2\pi}} e^{-\frac{z^2}{2}} dz = e^{\mu+\sigma^2} \Phi(\lambda_m)$$

From this equation it is possible to show that:

$$\phi_{L_m} = 1 - \frac{\int_0^{L_m} \frac{1}{L\sigma\sqrt{2\pi}} e^{-\frac{(ln(L)-\mu)^2}{2\sigma^2}} L dL}{\int_0^{\infty} \frac{1}{L\sigma\sqrt{2\pi}} e^{-\frac{(ln(L)-\mu)^2}{2\sigma^2}} L dL} = 1 - \frac{e^{\mu+\sigma^2}\Phi(\lambda_m)}{e^{\mu+\sigma^2}\Phi(\infty)} = 1 - \Phi(\lambda_m)$$

Recursive algorithm for the determination of ξ_m with the cubic lattice model and equation (S4)
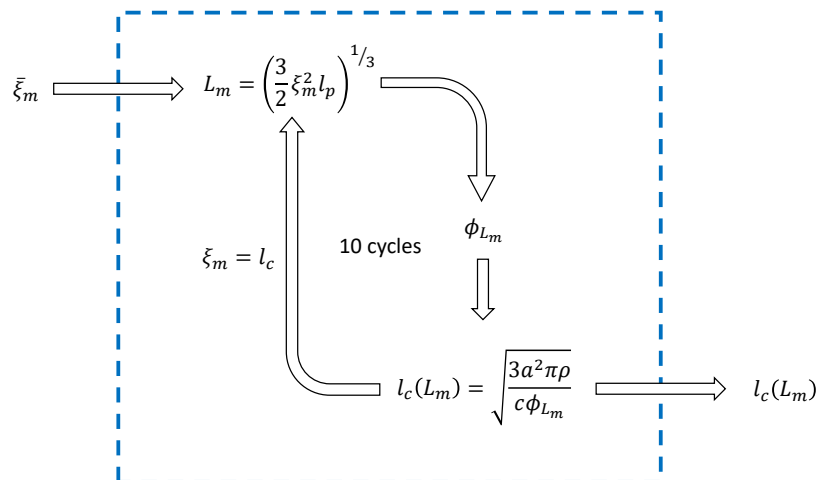
Recursive algorithm for the determination of ξ_m with the cubic lattice model and equations (S 8-9)

All the considerations written in the main text on Figures 3 and 4 are done using equation (6), which is obtained from Kroy and Frey's estimation of the entanglement length[1] $\left(L_m = \left(\frac{3}{2} \xi_m^2 l_p \right)^{1/3} \right)$. Here we extract the mesh size of the networks using instead equation (S9), and compare the obtained values with predictions from the modified cubic lattice model.

Compared to the analysis in the main text, the following calculations are made more complex by presence of the prefactor A, in the definition of the entanglement length $\left(L_m = A \left(\xi_m^4 l_p \right)^{1/5} \right)$. In fact, the value of A influences both the experimental determination and the theoretical calculation: we therefore estimate the value of this quantity through a function minimum research, as outlined in Figure S9.
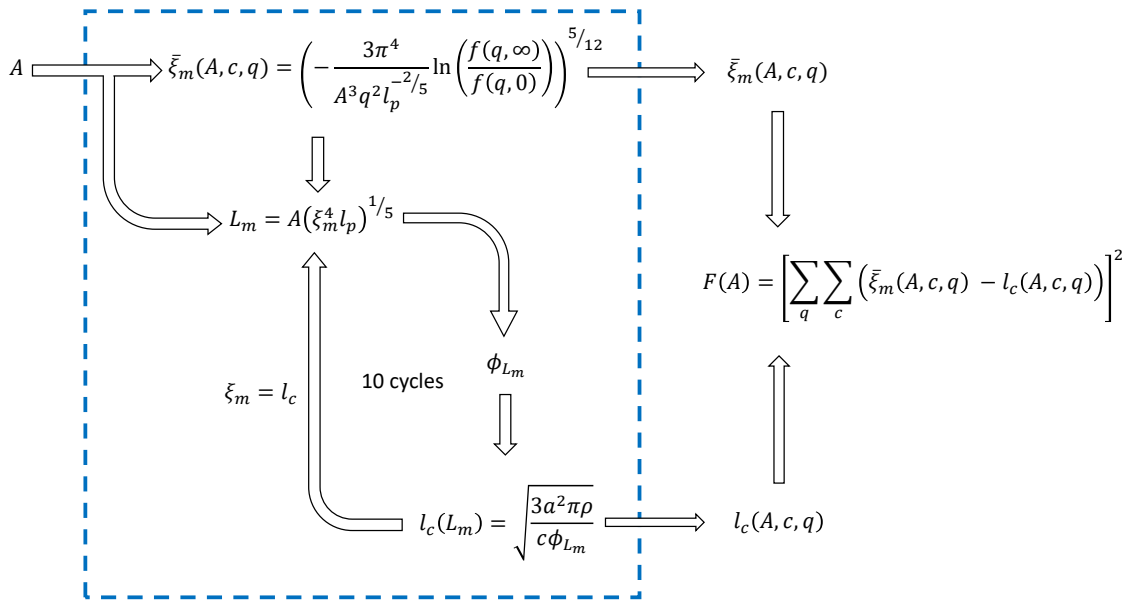
Figure S9: Structure of the algorithm that minimize the value of the function F(A). Starting from an initial value of the parameter A ($A_0 = 1$), the algorithm determines both the experimental value of the mesh size and the theoretical estimation of the cubic lattice, through minimization of the function F(A).

S17

The minimization of the function $F(A)$, when applied to the measurements at 110° and 135° for $c = 0.19, 0.38, 0.76$ mg/mL, gives a value $A = 1.4347$. Fig. (S10) shows the experimentally determined mesh sizes and the theoretically estimated cubic lattices.
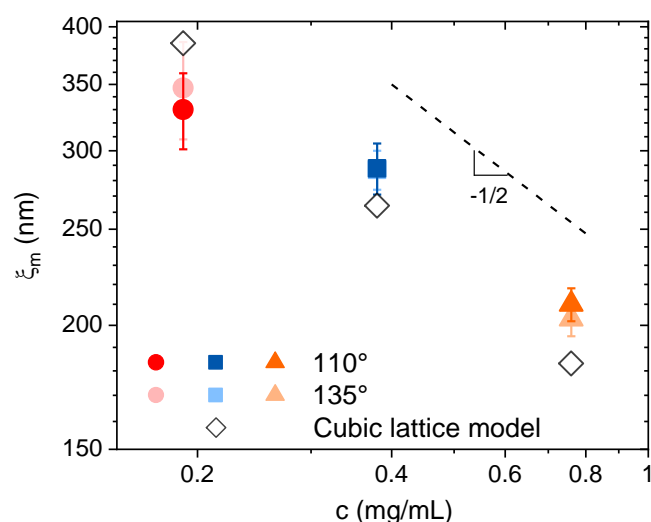
Figure S10: Determination of the mesh size of the networks through equation (S9). The calculations are performed accordingly with the algorithm outlined in Fig. S9.

Comparing Fig. (S10) with Fig. 3(b), we can speculate that the two models perform quantitatively similar estimations of the mesh size. However, the derivation based on the EMA model $\left(L_m = \left(\frac{3}{2}\xi_m^2 l_p\right)^{1/3}, \text{Fig. 3(b)}\right)$ shows a closer agreement between experimental data and theoretical calculations.

Bibliography (Supplemental Information)

(1)   Kroy, K.; Frey, E. Dynamic Scattering from Solutions of Semiflexible Polymers. *Phys. Rev. E* **1997**, *55* (3), 3092–3101.

(2)   Broedersz, C. P.; Mackintosh, F. C. Modeling Semiflexible Polymer Networks. *Rev. Mod. Phys.* **2014**, *86* (3), 995–1036. https://doi.org/10.1103/RevModPhys.86.995.

(3)   Semenov, A. N. Dynamics of Concentrated Solutions of Rigid-Chain Polymers. Part 1. - Brownian Motion of Persistent Macromolecules in Isotropic Solution. *J. Chem. Soc. Faraday Trans. 2 Mol. Chem. Phys.* **1986**, *82* (3), 317–329. https://doi.org/10.1039/F29868200317.

(4)   Isambert, H.; Maggs, A. C. Dynamics and Rheology of Actin Solutions. *Macromolecules* **1996**, *29* (3), 1036–1040. https://doi.org/10.1021/ma946418x.

(5)   Mackintosh, F. C.; Kas, J.; Janmey, P. A. Elasticity of Semi-Flexible Polymer Networks. *Phys. Rev. Lett.* **1995**, *75* (24), 4425.

(6)   Käs, J.; Strey, H.; Sackmann, E. Direct Imaging of Reptation for Semiflexible Actin Filaments. *Nature* **1994**, *368* (6468), 226–229. https://doi.org/10.1038/368226a0.

(7)   Morse, D. C. Tube Diameter in Tightly Entangled Solutions of Semiflexible Polymers. *Phys. Rev. E* **2001**, *63* (3), 1–22. https://doi.org/10.1103/PhysRevE.63.031502.

(8)   Odijk, T. On the Statistics and Dynamics of Confined or Entangled Stiff Polymers. *Macromolecules* **1983**, *16* (8), 1340–1344. https://doi.org/10.1021/ma00242a015.

(9)   Cao, Y.; Bolisetty, S.; Adamcik, J.; Mezzenga, R. Elasticity in Physically Cross-Linked Amyloid Fibril Networks. *Phys. Rev. Lett.* **2018**, *120* (15), 158103. https://doi.org/10.1103/PhysRevLett.120.158103.

(10)   Morse, D. C. Viscoelasticity of Concentrated Isotropic Solutions of Semiflexible Polymers. 1. Model and Stress Tensor. *Macromolecules* **1998**, *31* (20), 7030–7043. https://doi.org/10.1021/ma9803032.

(11)   Morse, D. C. Viscoelasticity of Concentrated Isotropic Solutions of Semiflexible Polymers. 2. Linear Response. *Macromolecules* **1998**, *31* (20), 7044–7067. https://doi.org/10.1021/ma980304u.

(12)   Tassieri, M.; Evans, R. M. L.; Barbu-Tudoran, L.; Khaname, G. N.; Trinick, J.; Waigh, T. A. Dynamics of Semiflexible Polymer Solutions in the Highly Entangled Regime. *Phys. Rev. Lett.* **2008**, *101* (19), 7–10. https://doi.org/10.1103/PhysRevLett.101.198301.

(13)   Schuldt, C.; Schnauß, J.; Händler, T.; Glaser, M.; Lorenz, J.; Golde, T.; Käs, J. A.; Smith, D. M. Tuning Synthetic Semiflexible Networks by Bending Stiffness. *Phys. Rev. Lett.* **2016**, *117* (19), 1–6. https://doi.org/10.1103/PhysRevLett.117.197801.

(14)   Tassieri, M. Dynamics of Semiflexible Polymer Solutions in the Tightly Entangled Concentration Regime. *Macromolecules* **2017**, *50* (14), 5611–5618. https://doi.org/10.1021/acs.macromol.7b01024.

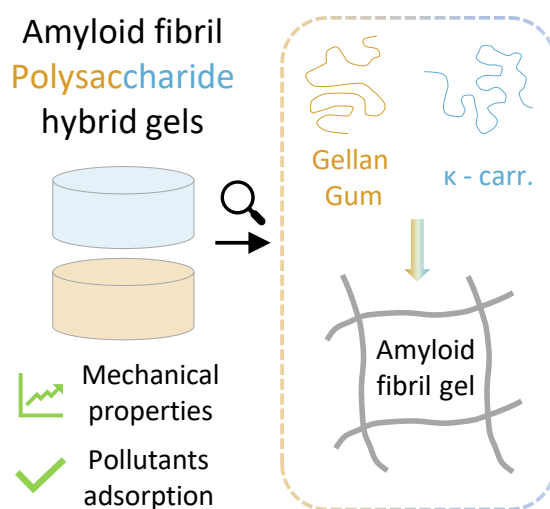# 4. Polysaccharide-reinforced amyloid fibril hydrogels and aerogels

Mattia Usuelli, Till Germerdonk, Yiping Cao, Mohammad Peydayesh, Massimo Bagnani, Stephan Handschin, Gustav Nyström and and Raffaele Mezzenga*

Summary

Amyloid βLG fibril gels blend the exquisite surface reactivity of the elongated proteinaceous colloids, together with the facilitated processing that comes from their solid nature. However, pure amyloid fibril gels hardly resist high deformations; such a sensitivity to large strains hinder their use in an application basin that is broader than the actual one. We show that amyloid fibril gels can be sustainably reinforced through inclusion of polysaccharides, namely low-acetylated Gellan Gum and κ-carrageenan; our protocol relies on a diffusion-based inclusion, accompanied by a further strengthening upon immersion in a secondary gelation bath. The established reinforcement route effectively improves the large-strain resistance of amyloid gels, without affecting the surface functionality of the single fibrils.

PAPER

View Article Online
View Journal | View Issue

Polysaccharide-reinforced amyloid fibril hydrogels and aerogels†

Mattia Usuelli, [ID] [a] Till Germerdonk,[a] Yiping Cao,‡[a] Mohammad Peydayesh, [ID] [a] Massimo Bagnani, [ID] [a] Stephan Handschin,[b] Gustav Nyström [ID] [a,c] and Raffaele Mezzenga [ID] *[a,d]

β-Lactoglobulin amyloid fibrils are bio-colloids of high interest in many fields (*e.g.* water purification, cell growth, drug delivery and sensing). While the mechanical properties of pure amyloid fibril gels meet the needs of some applications, mechanical fragility often hinders a wider usage basin. In this work, we present a simple and sustainable approach for reinforcing amyloid fibril hydrogels and aerogels, upon the diffusion of polysaccharides (low-acetylated Gellan Gum and κ-carrageenan) inside their mesh. The formed hybrid materials show enhanced resistance upon compression, without any loss of the exquisite surface reactivity of the amyloid fibrils. The proposed approach can pave the way for designing composite materials that are both highly functional and environmentally friendly.

Hydrogels are versatile materials, comprising a solid skeleton interpenetrated by water. When the liquid phase is replaced by air, while minimizing structural damage, hydrogels transform into aerogels.[1,2] The resulting arrested structures exhibit a large variety of functionalities and can be used for a wide range of applications that encompass drug delivery,[3] bone regeneration,[4] dehumidification[5] and electrochemistry.[6] Among the many potential building blocks of hydrogels and aerogels, the ones that respect sustainability criteria are more often being brought under the spotlight.[7,8] In fact, increasing effort is put in pursuing a more equitable global society while operating within Planetary Boundaries (PB), which define a safe space for using the resources of Earth without affecting its resilience.[9,10] Thus, functional properties and sustainable design should be increasingly blended, aiming at materials that positively impact human activities while safeguarding our planet.[11]

One promising answer to promote both requirements lies in synthesising hydrogels and aerogels out of under-exploited food sources;[12,13] changes in temperature, pH or ionic strength allow to generate networks of proteins and polysaccharides with a broad range of functionalities. As a remarkable example, amyloid fibrillar structures (formed upon the self-assembly of hydrolyzed peptides) are used in a wide spectrum of applications, including water purification,[14–16] iron fortification,[17] regulation of gut microbial dysbiosis[18] and creation of conductive materials.[19,20] Thus, *in vitro* prepared amyloid fibrils are a promising candidate for designing eco-friendly, functional materials. However, the poor mechanical properties of pure amyloid gels are an often-encountered limitation. While this is not a drawback for some specific applications, where the mechanical strength is of secondary importance (*e.g.* drug delivery), enhancement of mechanical properties is desired for those contexts where gels are subjected to significant strains and stresses. Therefore, the functional amyloid fibril community is highly interested in ways to strengthen the fibrillar networks while preserving their surface functionality.[21]

From a historical perspective, biological networks have been combined with inorganic components (*e.g.* silica) to create synergistic effects. For example, there are reports of silica gels strengthened through the incorporation of a cellulose scaffold,[22] pectin–silica hybrid materials[23] and fibrillar networks with an amyloid core and a silicious shell.[24] Although these strategies were proven to be effective in enhancing the properties of the materials, they might reduce their

[a]*ETH Zürich, Department of Health Sciences and Technology, Schmelzbergstrasse 9, 8092 Zürich, Switzerland. E-mail: raffaele.mezzenga@hest.ethz.ch*
[b]*ETH Zürich, Scientific Center for Optical and Electron Microscopy (ScopeM), 8093 Zürich, Switzerland*
[c]*EMPA, Laboratory for Cellulose & Wood Materials, Überlandstrasse 129, 8600 Dübendorf, Switzerland*
[d]*ETH Zürich, Department of Materials, Wolfgang-Pauli-Strasse 10, 8093 Zürich, Switzerland*

†Electronic supplementary information (ESI) available: pH equilibration of the amyloid fibril hydrogels, computation of the persistence length of the polymeric units, dissolution of κ-carrageenan and low-acetylated Gellan Gum at pH 2, loss tangent (rheological data), alternative normalization of the compression experiments on the hydrogels, AuCl₄⁻ and methylene blue adsorption, hypotheses on the network structure. See DOI: 10.1039/D1NR03133C

‡Present address: Department of Chemical Engineering, Massachusetts Institute of Technology, Cambridge, MA 02139, USA.

surface activity; moreover, the abovementioned sustainability concerns encourage the exploration of alternative routes based on renewable secondary components. Such exploration has been attempted with some classes of biopolymer gels (like those based on alginate,[25] lentil protein[26] and myofibrillar protein[27]) but not with gels containing amyloid fibrils as the main, functional component.

In this work, we present a simple approach for reinforcing β-lactoglobulin (βLG) amyloid fibril gels through the inclusion of polysaccharides (namely, low-acetylated Gellan Gum and κ-carrageenan). The protocol we follow nicely complies with the sustainability criteria, by being entirely based on largely available sources and salt solutions. In fact, βLG, Gellan Gum (GG) and κ-carrageenan (κ-carr) are obtained from whey proteins[28] (a side stream of cheese production), bacterial fermentation[29] and marine algae,[30] respectively. All of them have, in the current global food scenario, a marginal role in nutrient and calorie intake. The risk of competition between their usage as food and their usage as harbingers of functional materials is therefore minimized.

We report a comprehensive analysis of the morphology of the network-forming units through a statistical evaluation of Atomic Force Microscopy (AFM) images, showing the potential of the polysaccharide chains to diffuse inside a mesh of amyloid fibrils. The macroscopic appearance (hydrogels and aerogels) and the microscopic structure (aerogels) of the synthesised materials are then analysed, and the mechanical properties of the hydrogels and aerogels are presented; such analyses confirm the diffusion of the polysaccharide units and show their ability to mechanically reinforce the materials. Finally, through adsorption experiments, we show that the mechanical enhancement does not come at the expense of the surface functionality of the amyloid component. The performed analyses corroborate the knowledge on synthesising materials that are both functional and renewable.

1. Materials and methods

1.1. βLG monomer purification

The purification of βLG monomers was carried out using Whey Protein Isolate (WPI; Fonterra, New Zealand) based on a simplified version of the protocol reported by Vigolo and co-workers.[31] 10 g of WPI was dissolved in 90 g of Milli-Q water, and the pH of the solution was adjusted to 4.2 with a concentrated HCl solution. A Schott bottle containing the solution was incubated in a shaking water bath (VWR, Switzerland) for more than 2 hours at 60 °C, until the solution became turbid suggesting the agglomeration of α-lactalbumin due to the proximity to its isoelectric point. The turbid solution was then transferred into plastic Falcon tubes and centrifuged at 12 074g for 20 minutes to precipitate the separated α-lactalbumin fraction. The obtained transparent solution, containing mainly βLG monomers and residual salts and sugars, was transferred into a Schott bottle and its weight fraction was determined through gravimetric analysis.

1.2. βLG amyloid fibril synthesis

The pH of the βLG monomer solution generated as described above was adjusted to 2 using a concentrated HCl solution, and the solution was further diluted to 2 wt% using Milli-Q water at pH 2. The formation of amyloid fibrils was driven by heating at 90 °C for 5 hours, while stirring (at 120 rpm for the first 3 hours and at 170 rpm for the last 2 hours) with a 3 cm long Teflon magnetic stirrer. Afterwards, the Schott bottle containing the solution was cooled on ice and stored at 4 °C.

1.3. Preparation of polysaccharides and salt solutions

κ-Carrageenan (Sigma Life Science, lot. 1432063) and low-acetylated Gellan Gum (Opal Biotech, lot. 18100601) solutions were prepared following the same protocol. Briefly, 1 g of polysaccharide was dissolved in 199 g of Milli-Q water by stirring for 1 hour at 90 °C. The resulting solutions were then cooled and stored at 4 °C. We decided to form 0.5 wt% solutions of both polysaccharides as this concentration corresponds to their reported maximum solubility in hot water (at the mentioned temperature).

Salt (KCl, NaCl and CaCl$_2$) solutions of different molarities were prepared using the following reagents: calcium chloride dihydrate for analysis (Merck kGaA, lot. A0263182 203), sodium chloride for analysis (Merck kGaA, lot. K43132604 207) and potassium chloride BioXtra ≥ 99.0% (Sigma, lot. BCBP9964 V). In the case of NaCl, the final solutions were prepared with Milli-Q water, the pH of which had been previously adjusted to 2 with a concentrated HCl solution. In the case of the other two salts, Milli-Q water at neutral pH was used.

1.4. AFM characterisation

The samples for AFM characterization were prepared following the protocols described below.

For βLG amyloid fibrils, an aliquot of the 2 wt% dispersion was diluted to a final concentration of 0.01 wt%, using Milli-Q water at pH 2. Twenty μL of the abovementioned solution was then deposited on freshly cleaved mica and, after incubating for 2 minutes, the mica surface was rinsed with 1 mL of Milli-Q water at pH 2. Finally, the surface of the mica substrate was gently dried under a compressed air flow.

For κ-carrageenan and Gellan Gum, the initial 0.5 wt% dispersions were diluted with neutral Milli-Q water to a final concentration of 1 μg mL^{-1}. (3-Aminopropyl)triethoxysilane (APTES, CAS 919-30-2, 99.9%, Sigma-Aldrich) was used to modify the surface charge of the mica substrate. After dilution with Milli-Q water, 20 μL of a 0.05 v/v % APTES solution was deposited on freshly cleaved mica and incubated for 1 minute. The surface was then rinsed with 3 mL of Milli-Q water and dried under compressed air flow. Subsequently, 20 μL of each of the diluted polysaccharide solutions was deposited on the surface-modified mica and incubated for 30 seconds. Finally, the deposited solutions were rinsed with 1 mL of Milli-Q water and dried under compressed air flow. AFM characterization was performed with a commercial cantilever (Bruker, USA) installed onto a Dimension FastScan Bio probe microscope
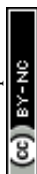
(Bruker, USA), run in the tapping mode. The analysis of the colloidal units was performed using the open-source software FiberApp.[32]

1.5. Amyloid fibril hydrogel preparation

For the gelation of the amyloid fibril dispersion, 1 mL of the 2 wt% solution was transferred into a plastic syringe, the top part of which had been previously cut. In order to allow ions to diffuse in, but fibrils not to diffuse out, the plastic syringe was covered with a cut section of a dialysis tube (Spectra/Por®, MWCO 6–8 kDa, Spectrum Laboratories Inc.) and sealed with parafilm. Before usage, the dialysis tube was rinsed with de-ionized water. The tip of the syringe was then placed in contact with an excess of a 300 mM NaCl solution at pH 2 for at least 48 h to allow for the gelation of the entire sample. For a schematic representation of the process, we refer to the upper-left corner of Fig. 1.

1.6. Amyloid–polysaccharide hybrid hydrogel preparation

To allow for the diffusion of polysaccharides into the pre-formed βLG amyloid fibril hydrogels, it was necessary to first adjust their pH. As a calibration experiment, the preformed gels were placed into different 100 mL Milli-Q water solutions, the pH of which had been adjusted to a value ranging from 7 to 11 using a concentrated NaOH solution. After an equilibration time of at least 48 h, the final pH was measured again with a commercial pH meter (pHenomenal®, VWR, 1000 L or 1100 L). In this way, it was possible to construct an equilibration curve that allowed the determination of the final pH as a function of the initial one: the data points and the used fitting function are reported in Fig. S1.† Accordingly, the gels used for preparing pure βLG hydrogels/aerogels or the βLG/Gellan Gum hybrid ones were put in contact with a bath at pH 10.42 to reach a final pH value of ~ 6.5, whereas the pH of the equilibration bath used for the preparation of βLG/κ-carrageenan hybrid hydrogels/aerogels was adjusted to 10.54 to reach a final pH of approximately 8.3.

To mechanically reinforce the pure amyloid fibril gels, polysaccharides were allowed to diffuse inside their mesh for six days, according to the following protocol. The βLG hydrogels were transferred into plastic Petri dishes and were completely submerged in 5 mL of the polysaccharide solutions (either κ-carrageenan or low-acetylated Gellan Gum at a concentration of 0.5 wt%). Pure amyloid networks used as control were instead immersed in 5 mL of Milli-Q water for the same period of time.

Following the incubation in the polysaccharide solution, the hydrogels were removed from the Petri dishes using a metal spatula and were immersed in different salt solutions in new Petri dishes. In the case of the pure amyloid networks and the βLG/κ-carrageenan hybrid hydrogels, the salt bath consisted of 5 mL of a 100 mM KCl solution. In the case of the βLG/GG hybrid hydrogels, a 10 mM CaCl$_2$ solution was used instead. To facilitate the formation of salt-induced intra- and inter-chain modifications of the polysaccharide units, the hydrogels remained immersed in the corresponding salt solutions for two days. All the mentioned steps are illustrated in Fig. 1.
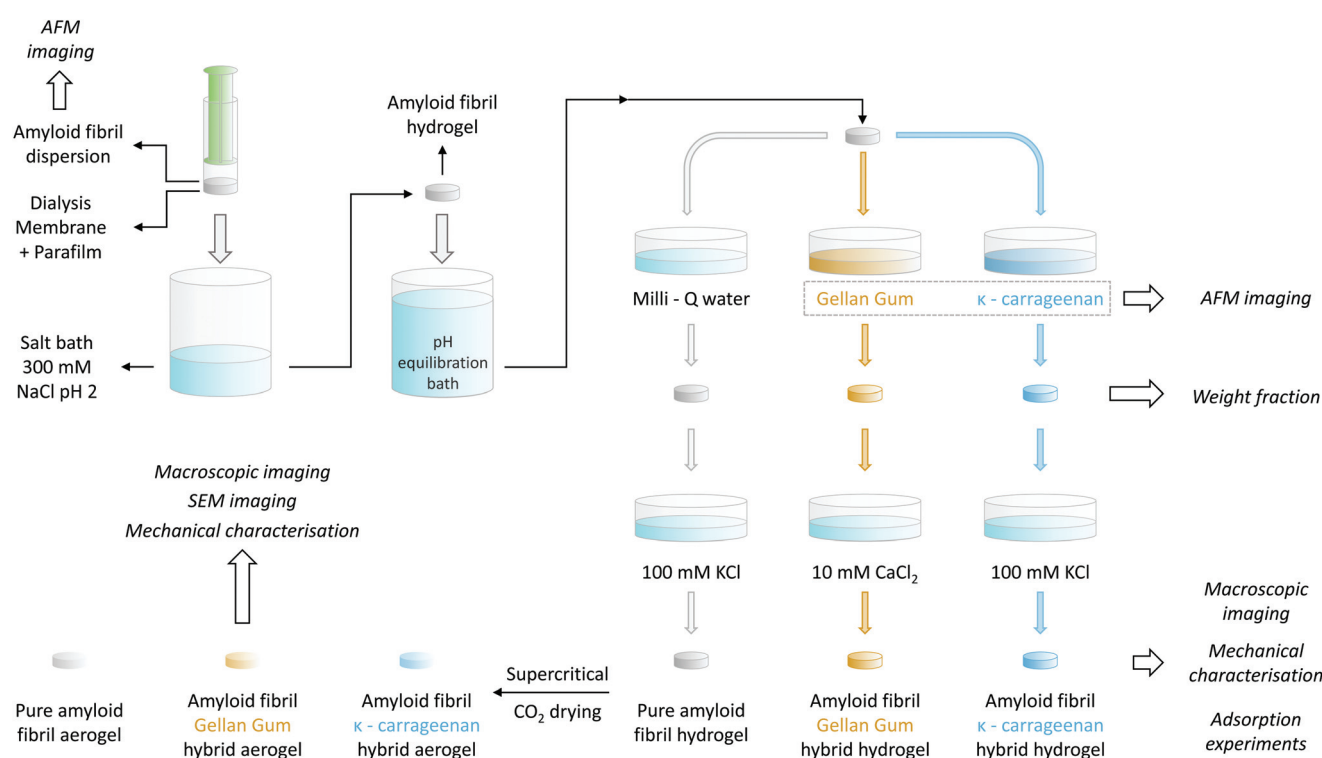
Fig. 1 Schematic representing the different steps for the preparation of the amyloid fibril/polysaccharide hybrid hydrogels and aerogels. The details of the used protocol are explained in the Materials and methods section.

71
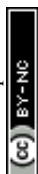
1.7. Weight fraction determination

For weight fraction determination, the hydrogels were placed in aluminum disks and dried at 60 °C in an oven until the weight became stable. Their weight fraction was calculated by measuring the initial weight of the hydrogels and that of their dry mass, after evaporation, using a precision balance with an accuracy of 2 µg (Mettler AT20, Mettler Toledo). To avoid the influence of the presence of salt on weight fraction characterisation, the measurements were performed directly after the diffusion of the polysaccharides (without the gels being immersed in the salt baths mentioned above).

1.8. Aerogel preparation

Pure amyloid hydrogels and polysaccharide-reinforced amyloid hydrogels, prepared as described above, were transformed into aerogels using the following protocol. The hydrogels were transformed into alcogels by solvent exchange through immersion in ethanol baths with increasing volume fractions of the alcoholic component (20%, 50%, 94% and 99.8% v/v ethanol). The alcogels were then transferred into home-made aluminum cages and the alcoholic medium was replaced with a gaseous environment through CO_2 supercritical drying (Autosamdri®-931, Tousimis, USA).

1.9. Mechanical characterisation

A stress-controlled rheometer (AR2000, TA Instruments) was used to characterize the hydrogels through oscillatory strain and frequency sweeps. The used geometry consisted of a plate–plate arrangement with a diameter of 40 mm, which was covered with a solvent trap during the measurements to prevent solvent loss, and was maintained at a constant temperature of 25 °C. To perform the measurements, the hydrogels were carefully transferred and centered in the above-mentioned geometry with a spatula and the upper plate was lowered to a gap value of 300 µm (with a concomitant gentle rotation in one direction to promote a nice spread of the gel under the plate). For the frequency sweeps (between the values of 0.01 Hz and 100 Hz), the elastic (G') and the viscous (G'') moduli were determined by oscillations at a strain equal to 0.1%; the strain sweeps (between 0.01% and 1000%) were instead performed at the constant frequency of 1 Hz.

Compression tests on hydrogels and aerogels were conducted with a Zwick Z010 (ZwickRoell GmbH & Co. KG, Germany) with a 100 N cell and a 75 mm diameter plate. Measurements were set to start (0% strain) when a force value of 0.05 N was reached: the applied force was then measured every 0.01 mm while the plate was descending at a constant speed of 0.5 mm min^{-1}, until a distance equal to 90% of the geometry gap at the beginning of the measurement was reached. For determining the intrinsic properties of the probed materials, the data needed to be normalized. The compressive strain was computed as:

$$\varepsilon(t) = \frac{(H_0 - H(t)) \cdot 100}{H_0} \tag{1}$$

In the reported formula, H_0 is the height of the geometry at the beginning of the measurement and $H(t)$ is the height at a

specific instant t. The pressure applied by the plate was determined instead by dividing the instantaneous force measured by the equipment by the initial cross-section of the probed hydrogel or aerogel:

$$P(t) = \frac{F(t)}{A_0} \tag{2}$$

We are aware that, due to the incompressibility of water in the experimental pressure range, the assumption of the constant cross-section of hydrogels over the course of the experiment might be inaccurate. Nonetheless, we followed this procedure in order to better compare experiments between hydrogels and aerogels, and we present an alternative normalisation in the ESI, which takes into account the constancy of the water volume (Fig. S5†).

Before performing any statistical analysis (experiments for each type of hydrogel/aerogel were performed at least in triplicate), the curves were further re-normalized to take into account the potential imprecisions of the starting point of the measurements.

1.10. Pictures of hydrogels/aerogels and SEM imaging

Pictures of the hydrogels and of the aerogels were acquired with a Canon EOS 550D camera. For SEM-imaging, small pieces of the aerogels were mounted on SEM aluminium pin stubs with double adhesive carbon tape. The samples were additionally fixed with conductive silver paint (Plano, DE) by coating all around them. After drying, the samples were carefully cut with a razor blade and sputter-coated with 4 nm of platinum/palladium (CCU-10, Safematic, CH). SE in-lens images were obtained at a working distance of 4–5 mm using a scanning electron microscope (Merlin FE-SEM, Zeiss, DE), operated at an accelerating voltage of 1.5 kV.

2. Results & discussion

2.1. Characterisation and analysis of the gel building blocks

Since the diffusion of the polysaccharides in the network depends on the geometry of the polymers, we first performed an AFM characterisation and analysis at the individual molecule/fibril level. In Fig. 2, the morphological properties of β-lactoglobulin amyloid fibrils (panel A), low-acetylated Gellan Gum (panel B) and κ-carrageenan (panel C) are presented.

Visual inspection of the AFM images reveals profound differences, in morphology and shape, between the βLG amyloid fibrils and the polysaccharide units. A quantitative analysis (performed using the open-source software FiberApp[32]), together with further calculations, confirmed the visual impression (Table 1).

In panels D, E and F of Fig. 2, the height (h) distributions of the tracked points are reported, along with the performed Gaussian fits. In panels G, H and I, the length distributions of the tracked objects, along with log–normal fits, are shown. The average length of the semi-flexible polymers was computed from the extracted parameters (μ and σ) through the formula

72
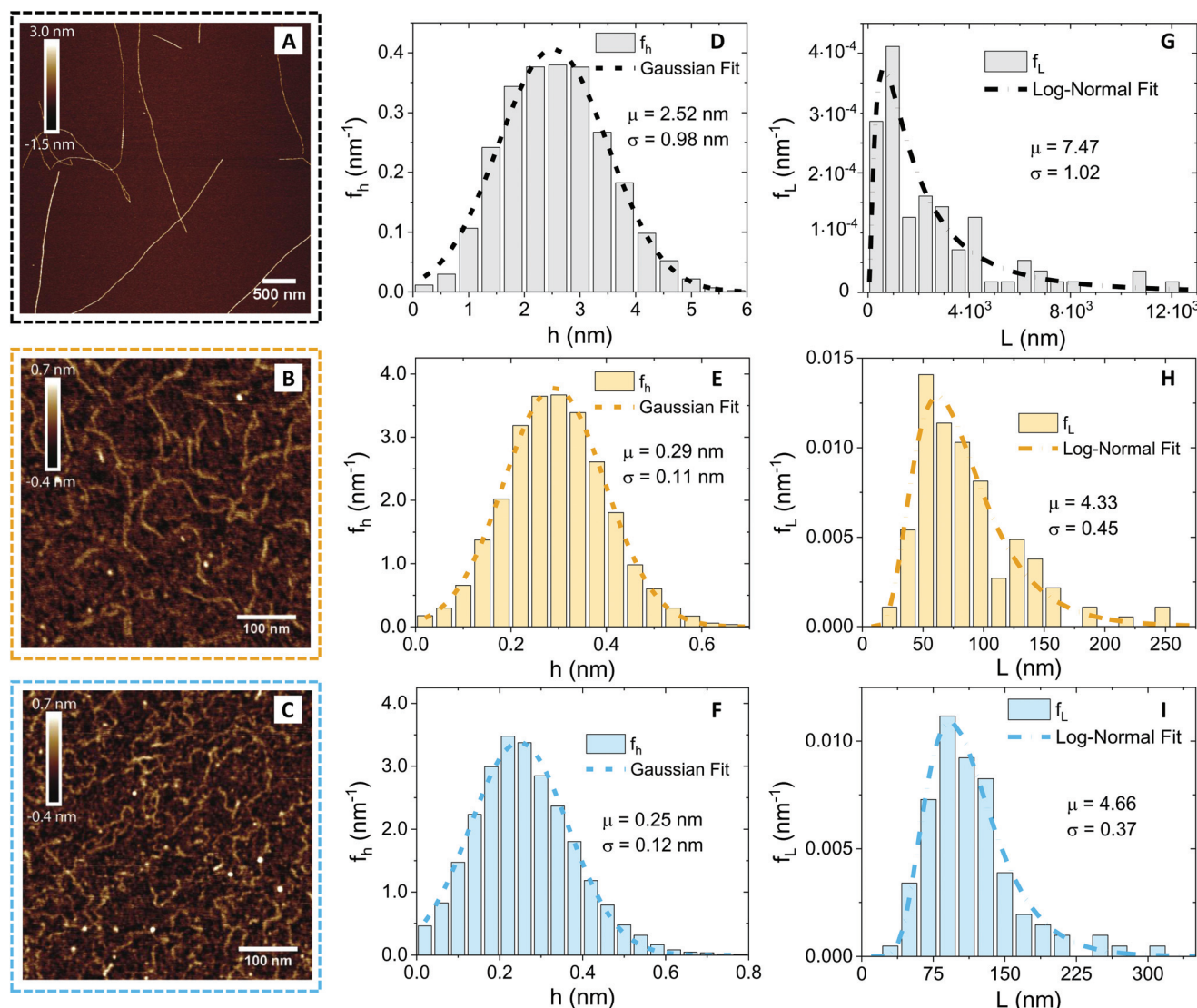
Fig. 2 Atomic force microscopy characterisation of the prepared amyloid fibrils and of the used polysaccharide units (κ-carrageenan and low-acetylated Gellan Gum). (A−C) Cropped section of AFM images obtained for β-lactoglobulin amyloid fibrils, low-acetylated Gellan Gum and κ-carrageenan, respectively. The color code associated with the three food units (gray/black for βLG, ochre for Gellan Gum and light blue for κ-carrageenan) is kept coherent in the other panels as well. (D−F) Height distributions, computed from the software FiberApp using the tracked points as raw data, together with a Gaussian fit $g(h; \mu, \sigma) = (1/\sigma\sqrt{2\pi}) \cdot \exp(-(h - \mu)^2/(2\sigma^2))$. The parameters extracted from the fitting (μ and σ) are reported in the panels, with the units of nm. (G−I) Contour length distributions, computed from the software FiberApp using the tracked objects as raw data, together with a log−normal fit $\psi(L; \mu, \sigma) = (1/\sigma L\sqrt{2\pi}) \cdot \exp(-(\ln(L) - \mu)^2/(2\sigma^2))$. The parameters extracted from the fitting (μ and σ) are reported in the panels, with a dimensional units (due to the fact that the natural logarithm is applied to the contour length). The contour length data and the probability densities were fed in the fitting algorithm with the units of nm and nm^{-1}, respectively, for all the three considered polymers.

Table 1 Properties of the single colloidal units. The parameters $\langle h \rangle$, $\langle L \rangle$ and l_p were extracted through statistical analysis of the acquired Atomic Force Microscopy images (using the software FiberApp[32]). The R_g values were calculated through eqn (3) and the mesh size of the amyloid fibrillar networks was computed through the cubic lattice model, using eqn (4)

Food unit	$\langle h \rangle$ (nm)	$\langle L \rangle$ (nm)	l_p (nm)	R_g (nm)	ξ_m (nm)
βLG	2.52	2950	5150	806	**50**
Gellan Gum	0.29	84	33	**20**	—
κ-Carrageenan	0.25	115	25	**23**	—

$\langle L \rangle = e^{(\mu + \sigma^2/2)}$. Despite the possible inaccuracies in tracking (due to difficulties in properly following the contour of not-well-resolvable objects), the performed analysis shows how both the characteristic length and height of the polysaccharide units are one order of magnitude smaller than those of the amyloid fibrils. It is important to consider that not only the contour length L but also the persistence length (l_p) defines the size of the semi-flexible polymers. For this reason, we report in the ESI (Fig. S2†) the computation of l_p for the three filamentous colloids, extracted through fitting the mean-squared end-to-end distance of the polymers as a function of

73
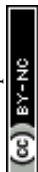
their internal contour length (l). Knowing both the contour and the persistence lengths, the three-dimensional radius of gyration (R_g) of the semi-flexible polymers can be computed as:[33,34]

$$R_g = \sqrt{l_p^2 \left(2 \frac{e^{-L/l_p} - 1 + L/l_p}{(L/l_p)^2} - 1 + \frac{L}{3l_p} \right)} \qquad (3)$$

The characteristic dimensions of the polysaccharide units should not be compared with the single-filament properties of the amyloid fibrils but with the mesh size (ξ_m) of the network they form. Through the cubic lattice (l_c) model, it is possible to estimate ξ_m at the studied protein concentration ($c \sim 2$ wt%– 20 mg mL^{-1}). Assuming a 40% conversion (ϕ) of monomers into amyloids and a fibril radius (a) of 1.26 nm (Fig. 2D), and considering the density of the fibrils (ρ) equal to 1300 mg mL^{-1}, we obtain:[35]

$$l_c = \sqrt{\frac{3a^2\pi\rho}{\phi c}} \sim 50 \text{ nm} \qquad (4)$$

The radius of gyration of the polysaccharide units and the estimated mesh size of the amyloid network are similar, which makes the diffusion of the small chains inside the protein gels possible. This concept is schematically represented in Fig. 3A.

2.2. Considerations of polysaccharide diffusion in amyloid hydrogels

Our βLG amyloid fibril hydrogels were prepared by the diffusion of ionic species (Na$^+$ and Cl$^-$) into amyloid fibril semi-diluted solutions with the aim of transforming entanglements into long-living physical crosslinks.[36] The inclusion of the polysaccharides inside the mesh occurs then in a separate step, which allows for the diffusion of the chains into the formed hydrogels. Two conditions need to be fulfilled for this phenomenon to occur.

The first condition, discussed above, is related to the relative size of the polysaccharide chains, compared to the average mesh size of the network; the AFM analysis shows that the κ-carrageenan and the Gellan Gum chains are small enough to be able to diffuse into the mesh. The second condition consists of the bio-colloids bearing surface charges of the same sign and is achieved by bringing the pH of the βLG hydrogels towards neutral values (upon immersion in alkaline baths). In fact, at the synthesis conditions (pH = 2), the amyloid fibrils are positively charged; if the used polysaccharides were brought directly in contact with the formed hydrogels at the mentioned pH conditions, we would have observed different phenomena as a function of the used polysaccharide (Fig. S3†). κ-Carrageenan is a linear sulphated galactan, the
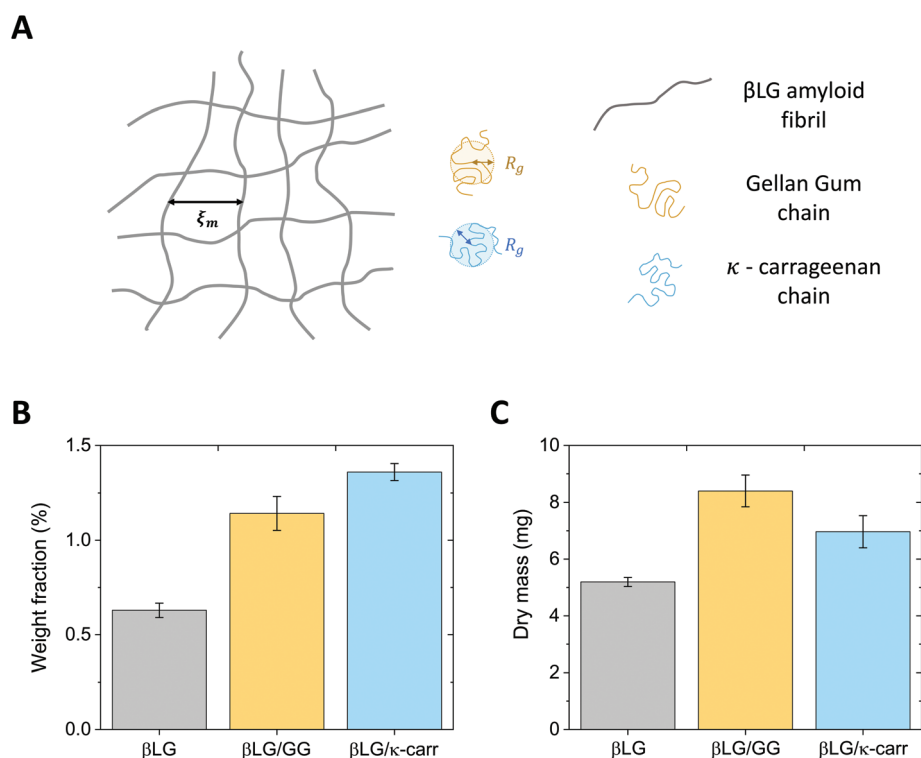
Fig. 3 (A) Schematic representing the amyloid network together with the polysaccharide units. The characteristic dimensions that tune the possibility for the sugar chains, to diffuse inside the gel, are the mesh size of the amyloid network (ξ_m) and the radius of gyration (R_g) of low-acetylated Gellan Gum and κ-carrageenan. (B) Weight fraction characterisation of the pure βLG hydrogels and of the hybrid ones that clearly shows higher values for the protein–polysaccharide hybrid materials, confirming the diffusion of the chains inside the amyloid network. (C) Dry mass analysis of the pure βLG hydrogels and of the hybrid ones, which is aligned with the content of panel B when taking into account the shrinkage observed for the βLG/κ-carrageenan hybrid systems.

74

Paper

repeating disaccharide of which contains one sulfate group;[30] the low pK_a of this unit makes κ-carrageenan negatively charged at both neutral and acidic (pH ∼ 2) conditions, and consequently promotes its dissolution in both scenarios (Fig. S3A†). However, despite the fact that κ-carrageenan dissolves at both conditions, at acidic conditions it was shown to interact with βLG amyloid fibrils by decorating their surface through the formation of globular aggregates.[37] This phenomenon is undesired as it would inhibit the efficient strengthening of the network. Gellan Gum is composed of a linear tetrasaccharide repeating unit that contains one carboxylic group.[29] The pK_a of this group is larger than the pH at which the βLG amyloid fibrils are usually synthesized; as a consequence, GG is expected to have a close-to-neutral surface charge at pH ∼ 2. The low surface charge drives, at such pH conditions, the flocculation and sedimentation of the carboxylated polysaccharide, inhibiting its solubility (Fig. S3B†). The reported analysis suggests the importance, for an effective diffusion of the polysaccharides, to shift the pH of the amyloid fibril hydrogels to values that are larger than the isoelectric point of βLG (IEP ∼ 5) to avoid both electrostatic complexation and limited solubility of the sugar chains.

Although the analysis described above supports the possibility that the polysaccharide units can diffuse inside the protein network, additional factors may have a negative effect. In particular, if the food units bear the same surface charge, electrostatic repulsion might hinder the diffusive phenomena. Furthermore, it has to be considered that the measured radius of gyration (R_g) does not reflect the real hydrodynamic dimensions of the units, which can actually be larger than the reported values. These concerns prompted the design of an experimental protocol whereby the amyloid hydrogels remained immersed in polysaccharide solutions for six days, to allow the dynamic phenomena to reach completion. The experimental confirmation of chain diffusion in the mesh is presented in Fig. 3B, which reports the weight fraction of the dry component of the gels, upon evaporation of the wet component in an oven at 60 °C. Although the initial βLG amyloid gels were synthesised from a 2 wt% protein solution, their effective solid content after pH equilibration was much lower (smaller than 0.75 wt%). This may appear surprising, but it is important to consider that the percentage of single protein molecules converted into amyloid fibrils depends on the used protocol and is still an open point in the current literature.[38] As reported above, in the case of βLG, a recently published study reported a conversion of around 40% in weight,[35] which is compatible with our observed reduction in weight fraction. In fact, during the pH equilibration towards close-to-neutral values, the isoelectric point of βLG is crossed, which may lead to the coagulation and sedimentation of unreacted peptide and protein units. Indeed, such a phenomenon was visually observed as white sedimented aggregates in the proximity of the gels (data not shown).

After the gels remained for six days in 0.5 wt% polysaccharide solutions, the weight fraction of the dry component increased to values larger than 1 wt%. While the average value

of the weight fraction of βLG/GG hybrid hydrogels strongly reflects diffusive dynamics (due to limited shrinkage), we believe that the value reported for the βLG/κ-carrageenan hybrid hydrogels overestimates the truly diffused polysaccharide component (as a consequence of visible shrinkage that lowered the initial wet weight of the material). Such a phenomenon can give a misleading interpretation of the dry content of the hydrogels (due to different water content in the wet state). Fig. 3C shows the plot of the measured dry mass of the pure βLG and hybrid gels. It is evident that, while the βLG/GG system shows an appreciable degree of diffused polysaccharides (compatible with the weight fraction analysis shown in panel B), the βLG/κ-carrageenan one shows hints of less-effective diffusion (if one considers the shrinkage-induced water loss, the apparent contradiction of this observation with the weight fraction analysis disappears).

The different behaviours observed for the two polysaccharides, considering the morphological similarities of the single chains, probably stem from their different chemical compositions. The different pK_a values of the charged groups of Gellan Gum and κ-carrageenan (carboxylic and sulfate, respectively), together with their diverse recurrency (one group per tetra-saccharide and one group per di-saccharide, respectively), make κ-carrageenan more charged than Gellan Gum, with two consequences that we experimentally observed. Firstly, κ-carrageenan diffused less effectively in the βLG amyloid fibril gels due to enhanced electrostatic repulsion. Secondly, protein gels immersed in κ-carrageenan exhibited a more pronounced shrinkage due to osmotic pressure imbalance between the arrested structure and the surrounding solution: the water phase was driven by thermodynamics to dilute the highly charged polysaccharide dispersion.

2.3. Macro- and microscopic appearances of the pure amyloid and hybrid hydrogels and aerogels

After having embedded the polysaccharides inside the proteinaceous matrix, we further promoted their network strengthening role by leaving the gels immersed in salt solutions (10 mM $CaCl_2$ and 100 mM KCl, respectively for the βLG/GG and βLG/κ-carrageenan hybrid systems). In fact, Diener and co-workers recently showed how the cations of the used salts trigger drastic intra- and inter-chain modifications in both polysaccharides[39,40] by driving a coil-to-helix morphological change and further bundling of the resulting structures. To investigate how far such morphological rearrangements are possible within already formed arrested structures, we analysed the macro-, meso- and microstructural properties of the synthesized hydrogels and aerogels (Fig. 4).

Fig. 4A shows the macroscopic appearance of a pure βLG hydrogel: its transparency can be immediately appreciated, together with its self-standing properties. Upon diffusion and reconfiguration of the Gellan Gum units (Fig. 4B) the hydrogel still shows remarkable transparency and has a size that is comparable to the initial size. In the case of κ-carrageenan (Fig. 4C), instead, we can observe a certain degree of hydrogel shrinkage, both at global (overall size) and local (morphology)
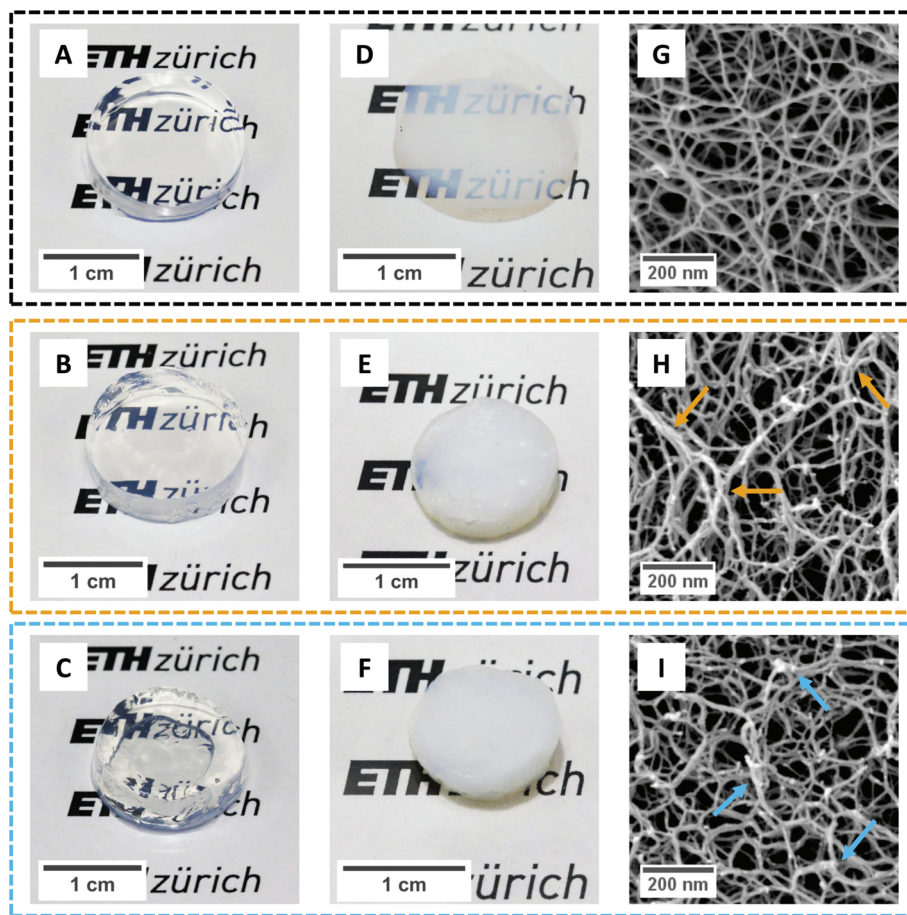
Fig. 4 Macro- and microscopic appearances of the synthesised hydrogels and aerogels. The images surrounded by black, ochre and light blue dashed frames are representative of hydrogels and aerogels made out of pure βLG amyloid fibrils, of βLG/Gellan Gum hybrid networks and of βLG/κ-carrageenan hybrid materials, respectively. (A–C) Pictures of the pure/hybrid hydrogels. (D–F) Pictures of the pure/hybrid aerogels. (G–I) Microscopic characterization of the formed aerogels through Scanning Electron Microscopy (SEM) imaging. In panels H and I, the coloured arrows highlight local bundles.

scales. We also noticed that the degree of shrinkage depended on the pH of the system (data not shown). However, due to complexities in fine tuning the final pH without a buffer system (the reader is addressed to the caption of Fig. S1†), we decided not to pursue such an analysis further but to leave it open for future studies. As mentioned above, the observed shrinkage can be attributed to the osmotic pressure imbalance between the amyloid fibril gel and the surrounding κ-carrageenan dispersion.

Gentle removal of the liquid component allowed the transformation of the synthesized hydrogels into aerogels. In order to preserve the state of the network as close as possible to its initial wet state, we used supercritical CO_2 drying, employing ethanol as an intermediate solvent.[7] Despite the lack of capillary forces that could drastically destroy the structure, the solvent exchange steps can have a large influence on the gels. In fact, a recent perspective article showed how a change in the dielectric properties of the continuous phase (together with changes in its ability to provide hydrogen bonding) can drive the shrinkage phenomena in biopolymer gels, especially

relevant at small mass fractions of the solid component.[41] In our case, although we used a protocol with a step-wise solvent exchange, we observed marked shrinkage effects on the materials containing polysaccharides (and limited ones in pure amyloid networks).

Fig. 4D shows the appearance of a pure βLG amyloid fibril aerogel. Only a slight shrinkage was observed and the material showed high transparency (the ETH Zürich logo behind it can still be easily read). We hypothesize that enhanced turbidity compared to the liquid state is not caused by a change in the morphology of the network-forming units but instead by a higher refractive index difference between the amyloid fibrils and air (compared to the one between the bio-fibrillar colloids and water). This result is compatible with the considerations discussed above, because βLG amyloid fibrils have both hydrophilic and hydrophobic properties;[15] as a consequence, solvent exchange steps are not drastically modifying the aggregation state of the formed network, as will be confirmed later on in the analysis of the acquired SEM images. However, in the case of hybrid aerogels containing Gellan Gum and κ-carrageenan

(Fig. 4E and F, respectively), a certain degree of shrinkage (more accentuated for the κ-carrageenan case) and much higher turbidity (the ETH Zürich logo cannot be read anymore through the aerogels) were observed. This significant change in optical properties, different from what was observed with the pure βLG case, can be attributed to an aggregation-driven morphological change of the network forming units. In fact, shrinkage-induced bundling of the bio-polymeric components can lead to the formation of aggregates, the size of which becomes comparable with the wavelength of light in the visible range (in the order of hundreds of nm), leading to enhanced scattering phenomena and a more turbid appearance of the final materials.[42] In this case, we hypothesize that the presence of the polysaccharides (for whom ethanol is a bad/non-solvent) makes the material more sensitive to the solvent exchange procedure, influencing the properties of the network. This is evidenced by the fact that pure polysaccharide hydrogels usually showed a large shrinkage when transformed into aerogels (at mass fractions compatible with the ones used in our study).[41]

To test the expected correlation between the diverse macroscopic appearances of the synthesised materials with the underlying microscopic structures, we performed Scanning Electron Microscopy imaging of the aerogels (Fig. 4G–I). Although the overall appearance looks similar for all the three materials, a higher degree of local aggregation is observed in the case of the protein–polysaccharide hybrid aerogels: brighter spots in the images (highlighted by means of coloured arrows) can be interpreted as fractures of local bundles and strands during crossfracturing of the aerogels. It is not clear whether such bundles stem from the protein–polysaccharide interactions, from a secondary polysaccharide network or from the aggregation phenomena during the shrinkage process. In addition, it is not possible to clearly identify, from these images, the location of the polysaccharide units upon being embedded in the network. To gain further insights indirectly, we analysed the effect of the diffused polysaccharides on the mechanical properties of the materials.

### 2.4. Network-strengthening role of the polysaccharide component

The question that we would now like to address is whether the diffused polysaccharide units can efficiently strengthen the mechanical properties of the final material. To gain experimental evidence on this point, we performed oscillatory sweeps (both frequency and amplitude ones, only for hydrogels) and mechanical compression tests (for both hydrogels and aerogels). The results of the oscillatory rheology characterization are shown in Fig. 5A. The first point that clearly emerges is the solid-like nature of the materials: for all the three types of networks, the elastic modulus (G') dominates over the viscous one (G''). At the same time, it can be observed that the loss tangent (tan δ, defined as the ratio between G'' and G'), for the βLG/GG case, shifts towards higher values as the oscillatory frequency decreases (Fig. S4†). This can be attributed to Gellan Gum chains being not fully embedded in

the network structure. We hypothesized that such units contribute to storing mechanical energy at fast deformation rates but increasingly relax and contribute to viscous dissipation as the probation frequency decreases.

A second point, that is more surprising, is how the absolute values of the elastic moduli are close to each other. In the case of the hybrid hydrogels, the networks are both denser (exhibiting an almost double weight fraction) and are supposedly further strengthened by the interactions between the protein and the polysaccharide fractions, leading to an expected enhanced elastic component.[24] We believe that this point can be explained by considering the compression properties of the materials that are presented in Fig. 5B. In fact, while the shear elastic moduli of the materials look similar, the compression of the materials shows astonishingly different features. A clear difference can be seen among the three curves, both in absolute values and in overall behaviour. Regarding the values, the three materials need three different orders of magnitude of pressures to be compressed down to more than 80% of their initial height. In particular, the βLG/GG hydrogels require pressures two orders of magnitude larger than those needed for the pure βLG hydogels, while the βLG/κ-carrageenan ones need pressure one order of magnitude larger than those of the pure amyloid fibril networks. This comparison can be better appreciated in Fig. 5C, where the same information as in panel B is shown in a semi-logarithmic plot. It can be seen that the pure amyloid fibril network starts showing fluctuations in the measured pressure after a deformation rate of a few percentage points (less than 10%). For both hybrid gels, this behavior is observed instead much later (approximately 40% for the κ-carrageenan case and more than 60% for the Gellan Gum one). These observations suggest that the polysaccharide component has two drastic effects: it reinforces the materials and makes them withstand more severe deformations before being structurally affected. As reported in the Materials and methods section, the presented analysis is performed by normalizing the compressing force ($F(t)$) by the initial cross-section of the samples (A_0). Although this approximation is not fully met in reality, it allows comparing the extracted values with the ones of the aerogels discussed below and for which the constant cross-section approximation is more valid. For completeness, in the ESI (Fig. S5†) we report an analysis based on the assumption of the conservation of the total volume of the gels being compressed, due to the incompressibility of the water phase. Despite the fact that the absolute values are inevitably different, the relative differences are very similar to the ones reported in Fig. 5B and C, thereby confirming the different mechanical responses of the three materials.

The observations on the compression behaviour of the pure amyloid and hybrid hydrogels can help better understand the oscillatory rheology properties shown in Fig. 5A. The plate–plate geometry setup used for the oscillatory tests had a diameter of 4 cm and a gap of 300 μm; therefore, the initial materials were subjected to considerable compression to fill the probation volume. It is probable that the composite networks did not spread under the plate as homogeneously as the
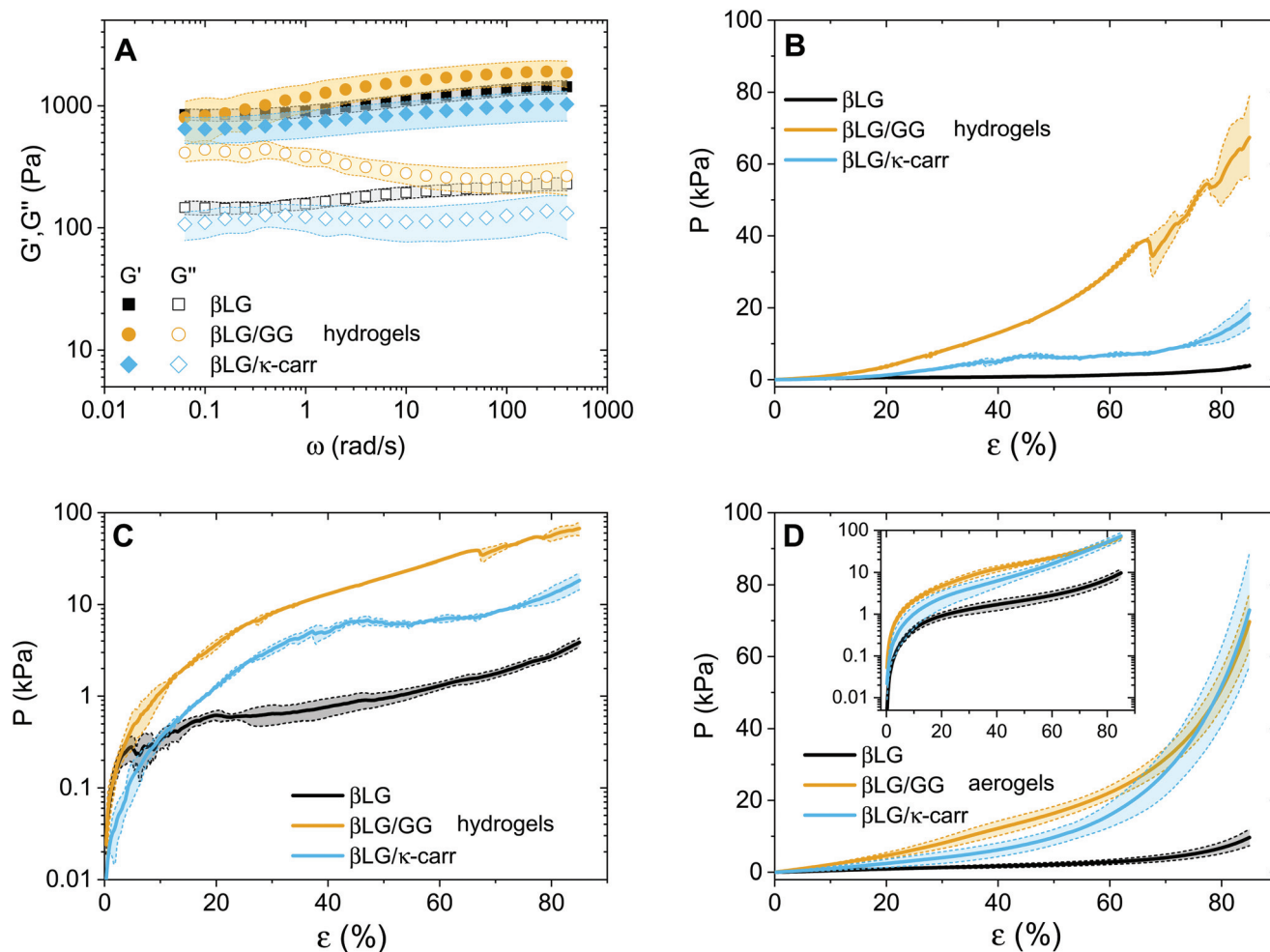
Fig. 5 Mechanical characterisation of hydrogels and aerogels. In all the panels, light colors indicate error bars over multiple individual measurements. (A) Oscillatory frequency sweeps applied to the three typologies of hydrogels. (B and C) Mechanical compression experiments on pure and hybrid hydrogels. The same information is respectively plotted in a linear plot (B) and in a semi-logarithmic plot (C). (D) Mechanical compression experiments on pure and hybrid aerogels. Inset: The same information is plotted in a semi-logarithmic plot.

pure βLG ones due to the highlighted difference in their compression properties. The consequent presence of potential inhomogeneous zones could influence the absolute values of the measured elastic and viscous moduli, making the comparison between the different materials less straightforward.

After having discussed the properties of the hydrogels, we can now focus on the mechanical properties of the aerogels (Fig. 5D). A similar trend as in panels B and C can be observed with two main differences. The first is the smoother behaviour of the curves, which can be attributed to the absence of the water phase. Water, in fact, tends to escape from the hydrogels while the compression measurements are performed, due to its incompressibility in the pressure range of interest. This further affects the networks and introduces fluctuations in the reported pressure values. The second difference is that the hybrid material curves are closer to each other due to the enhancement of the mechanical properties of the βLG/κ-carrageenan aerogels. A direct explanation of this experimental observation lies in the more pronounced shrinkage of

these samples compared to that of the βLG/Gellan Gum ones; their denser networks can be assumed to be responsible for the observed phenomenon.

The experimental evidences presented so far show clearly the reinforcing role of the included polysaccharides. Moreover, in the ESI (section 6 and Fig. S6†), we share experimental evidence (through adsorption of water pollutants) that the strengthening of the materials does not negatively influence the surface reactivity of the amyloid fibrils. This observation, together with the other ones discussed in this work, makes us formulate the hypothesis that the polysaccharide component forms either local bundles or an independent network within the already-formed amyloid gels (section 7 in the ESI and Fig. S7†).

3. Conclusions

In this study we presented a sustainable pathway for reinforcing βLG amyloid fibril gels with polysaccharide chains

(namely low-acetylated Gellan Gum and κ-carrageenan). The sugar chains were shown to effectively diffuse inside the initial networks and to reinforce their mechanical properties, while still allowing amyloid fibrils to express their surface functionality. The combination of the performed experiments allowed us to draw preliminary conclusions on how the polysaccharide component is embedded inside the network: the creation of local, thicker bundles with high bending rigidity or the creation of an independent network is the hypothesis that mostly aligns with the collected evidence.

The developed approach shows a simple and bioresource-based route for synthesizing functional, innovative hydrogels and aerogels with a broad range of potential applications and paves the way for further studies aimed at up-scaling the production protocol (through direct mixing of the protein and polysaccharide components) and at better elucidating the role of the synthesis and final pH in the properties of the prepared materials.

Conflicts of interest

There are no conflicts to declare.

Acknowledgements

References

1 S. S. Kistler, *Nature*, 1931, **127**, 741–741.
2 S. S. Kistler, *J. Phys. Chem.*, 1932, **36**, 52–64.
3 T. Coviello, P. Matricardi and F. Alhaique, *Expert Opin. Drug Delivery*, 2006, **3**, 395–404.
4 J. J. Chung, S. Li, M. M. Stevens, T. K. Georgiou and J. R. Jones, *Chem. Mater.*, 2016, **28**, 6127–6135.
5 X. Zheng, K. Chen and Z. Lin, *Ind. Eng. Chem. Res.*, 2020, **59**, 5760–5767.
6 O. Lev, Z. Wu, S. Bharathi, V. Glezer, A. Modestov, J. Gun, L. Rabinovich and S. Sampath, *Chem. Mater.*, 1997, **9**, 2354–2375.
7 S. Zhao, W. J. Malfait, N. Guerrero-Alburquerque, M. M. Koebel and G. Nyström, *Angew. Chem., Int. Ed.*, 2018, **57**, 7580–7608.
8 I. Smirnova and P. Gurikov, *J. Supercrit. Fluids*, 2018, **134**, 228–233.
9 W. Steffen, K. Richardson, J. Rockström, S. E. Cornell, I. Fetzer, E. M. Bennett, R. Biggs, S. R. Carpenter, W. de Vries, C. A. de Wit, C. Folke, D. Gerten, J. Heinke, G. M. Mace, L. M. Persson, V. Ramanathan, B. Reyers and S. Sörlin, *Science*, 2015, **347**, 1259855.
10 J. D. Sachs, G. Schmidt-Traub, M. Mazzucato, D. Messner, N. Nakicenovic and J. Rockström, *Nat. Sustain.*, 2019, **2**, 805–814.
11 E. A. Olivetti and J. M. Cullen, *Science*, 2018, **360**, 1396–1398.
12 Y. Cao and R. Mezzenga, *Nat. Food*, 2020, **1**, 106–118.
13 S. Assenza and R. Mezzenga, *Nat. Rev. Phys.*, 2019, **1**, 551–566.
14 S. Bolisetty and R. Mezzenga, *Nat. Nanotechnol.*, 2016, **11**, 365–371.
15 M. Peydayesh, M. K. Suter, S. Bolisetty, S. Boulos, S. Handschin, L. Nyström and R. Mezzenga, *Adv. Mater.*, 2020, **32**, 1907932.
16 M. Peydayesh and R. Mezzenga, *Nat. Commun.*, 2021, **12**, 1–17.
17 Y. Shen, L. Posavec, S. Bolisetty, F. M. Hilty, G. Nyström, J. Kohlbrecher, M. Hilbe, A. Rossi, J. Baumgartner, M. B. Zimmermann, *et al.*, *Nat. Nanotechnol.*, 2017, **12**, 642.
18 B. Hu, S. Yu, C. Shi, J. Gu, Y. Shao, Q. Chen, Y. Li and R. Mezzenga, *ACS Nano*, 2020, **14**, 2760–2776.
19 Y. Han, Y. Cao, S. Bolisetty, T. Tian, S. Handschin, C. Lu and R. Mezzenga, *Small*, 2020, **16**, 2004932.
20 G. Nyström, M. P. Fernández-Ronco, S. Bolisetty, M. Mazzotti and R. Mezzenga, *Adv. Mater.*, 2016, **28**, 472–478.
21 G. Wei, Z. Su, N. P. Reynolds, P. Arosio, I. W. Hamley, E. Gazit and R. Mezzenga, *Chem. Soc. Rev.*, 2017, **46**, 4661–4708.
22 J. Fu, S. Wang, C. He, Z. Lu, J. Huang and Z. Chen, *Carbohydr. Polym.*, 2016, **147**, 89–96.
23 W. G. Willats, J. P. Knox and J. D. Mikkelsen, *Trends Food Sci. Technol.*, 2006, **17**, 97–104.
24 Y. Cao, S. Bolisetty, G. Wolfisberg, J. Adamcik and R. Mezzenga, *Proc. Natl. Acad. Sci. U. S. A.*, 2019, **116**, 4012–4017.
25 T. Ramdhan, S. H. Ching, S. Prakash and B. Bhandari, *Trends Food Sci. Technol.*, 2020, **106**, 150–159.
26 M. Joshi, P. Aldred, J. Panozzo, S. Kasapis and B. Adhikari, *Food Hydrocolloids*, 2014, **35**, 226–237.
27 Y. L. Xiong and S. P. Blanchard, *J. Food Sci.*, 1993, **58**, 164–167.
28 A. Kilara and M. N. Vaghela, in *Proteins in food processing*, ed. R. Y. Yada, Elsevier, 2nd edn, 2018, ch. 4, pp. 93–126.
29 G. Sworn and L. Stouby, in *Handbook of hydrocolloids*, ed. G. O. Phillips and P. A. Williams, Elsevier, 3rd edn, 2021, ch. 28, pp. 855–885.
30 V. L. Campo, D. F. Kawano, D. B. da Silva Jr. and I. Carvalho, *Carbohydr. Polym.*, 2009, **77**, 167–180.
31 D. Vigolo, J. Zhao, S. Handschin, X. Cao, A. J. deMello and R. Mezzenga, *Sci. Rep.*, 2017, **7**, 1211.
32 I. Usov and R. Mezzenga, *Macromolecules*, 2015, **48**, 1269–1280.
33 K. Kroy and E. Frey, in *Scattering in polymeric and colloidal systems*, ed. W. Brown and K. Mortensen, Taylor & Francis Group, London, 1st edn, 2000, ch. 5, pp. 197–248.
34 H. Benoit and P. Doty, *J. Phys. Chem.*, 1953, **57**, 958–963.

35 M. Usuelli, Y. Cao, M. Bagnani, S. Handschin, G. Nyström and R. Mezzenga, *Macromolecules*, 2020, **53**, 5950–5956.

36 Y. Cao, S. Bolisetty, J. Adamcik and R. Mezzenga, *Phys. Rev. Lett.*, 2018, **120**, 158103.

37 O. G. Jones, S. Handschin, J. Adamcik, L. Harnau, S. Bolisetty and R. Mezzenga, *Biomacromolecules*, 2011, **12**, 3056–3065.

38 Y. Cao and R. Mezzenga, *Adv. Colloid Interface Sci.*, 2019, **269**, 334–356.

39 M. Diener, J. Adamcik, A. Sánchez-Ferrer, F. Jaedig, L. Schefer and R. Mezzenga, *Biomacromolecules*, 2019, **20**, 1731–1739.

40 M. Diener, J. Adamcik, J. Bergfreund, S. Catalini, P. Fischer and R. Mezzenga, *ACS Macro Lett.*, 2020, **9**, 115–121.

41 P. Gurikov, R. SP, J. S. Griffin, S. A. Steiner III and I. Smirnova, *Ind. Eng. Chem. Res.*, 2019, **58**, 18590–18600.

42 H. C. van de Hulst, *Light scattering by small particles*, Dover Publications, 1981.

80

Polysaccharide-reinforced amyloid fibril hydrogels and aerogels (Supporting Information)

Mattia Usuelli,[a] Till Germerdonk,[a] Yiping Cao,[a,‡] Mohammad Peydayesh,[a] Massimo Bagnani,[a] Stephan Handschin,[b] Gustav Nyström,[a,c] and Raffaele Mezzenga[a,d,*]

1 pH equilibration of the amyloid fibril hydrogels
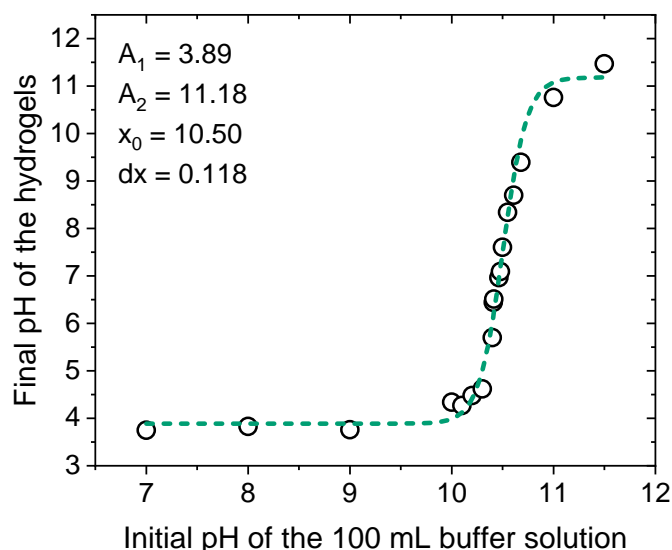
Fig. S1 Equilibration of the pH of the initial βLG hydrogels towards neutral values, by putting 1 mL gels at pH 2 in contact with 100 mL of basic solutions. The decision of using Milli-Q water (adjusted with a concentrated NaOH solution), instead of a more stable buffer system, was made to avoid the presence of salts inside the gel, which could then influence the behaviour of the polysaccharide diffusing units. Before any attempt in fitting the experimental data (black empty circles), it can be appreciated how the pH of the system stays around 4 until the pH of the basic solutions is brought to values larger than 10. The final pH evolves then very steeply as a function of the initial one, encompassing values between 5 and 10 for starting solutions with a pH between 10 and 11; this (expected) behaviour makes a fine adjustment of the final pH delicate, as it is very sensitive to small fluctuations of the initial one. Such sensitiveness was experimentally detected, as we found the final pH of the systems to have a significant standard deviation (up to 2 pH points) from the desired values. The fit of the experimental data is performed with a Boltzmann function ($y = A_2 + (A_1 - A_2)/\exp((x - x_0)/dx)$, green dashed line), that nicely captures the evolution of the data-points (but it would fail at higher pH, as it would saturate instead of following the expected increase of the values).

[a]ETH Zürich, Department of Health Sciences and Technology, Schmelzbergstrasse 9, 8092 Zürich, Switzerland. E-mail: raffaele.mezzenga@hest.ethz.ch

[b]ETH Zürich, Scientific Center for Optical and Electron Microscopy (ScopeM), 8093 Zürich

[c]EMPA, Laboratory for Cellulose & Wood Materials, Überlandstrasse 129, 8600 Dübendorf, Switzerland

[d]ETH Zürich, Department of Materials, Wolfgang-Pauli-Strasse 10, 8093 Zürich, Switzerland

‡ Present address: Department of Chemical Engineering, Massachusetts Institute of Technology, Cambridge, MA 02139, USA

1

# 2 Computation of the persistence length
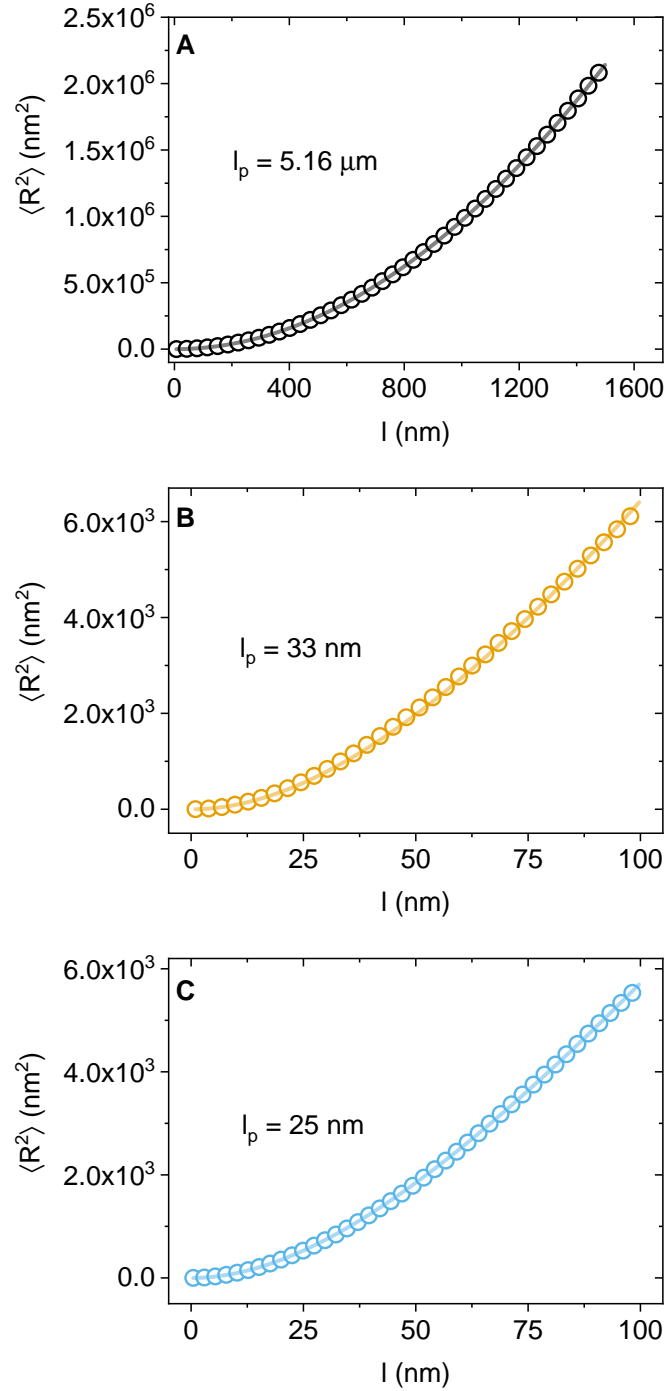
Fig. S2 Determination of the persistence length (l_p) of the analysed polymers (βLG amyloid fibrils, low-acetylated Gellan Gum and κ-carrageenan, in panels A, B and C, respectively), by fitting the mean-squared end-to-end distance ($\langle R^2 \rangle$) as a function of the internal contour length (l)[1]: $\langle R^2 \rangle = 4 l_p [l - 2 l_p (1 - \exp(-l/2l_p))]$. The obtained values are reported in Table 1 of the main manuscript.

2

3 Dissolution of κ-carrageenan and low-acetylated Gellan Gum at pH 2
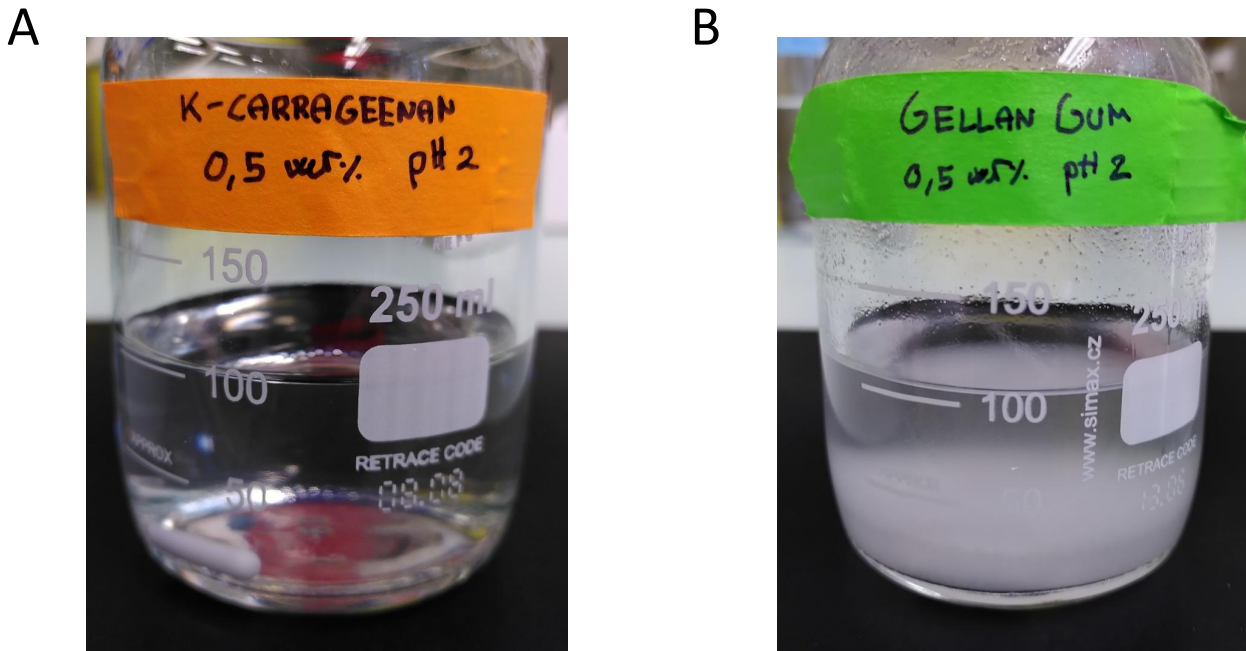
Fig. S3 Dissolution of κ-carrageenan (A) and low-acetylated Gellan Gum (B) at pH 2. The solutions were prepared by adding 0.5 g of the polysaccharides to 99.5 g of Milli-Q water at pH 2, followed by stirring for 1 h while heating at 90°C.

4 Rheological data - Loss tangent
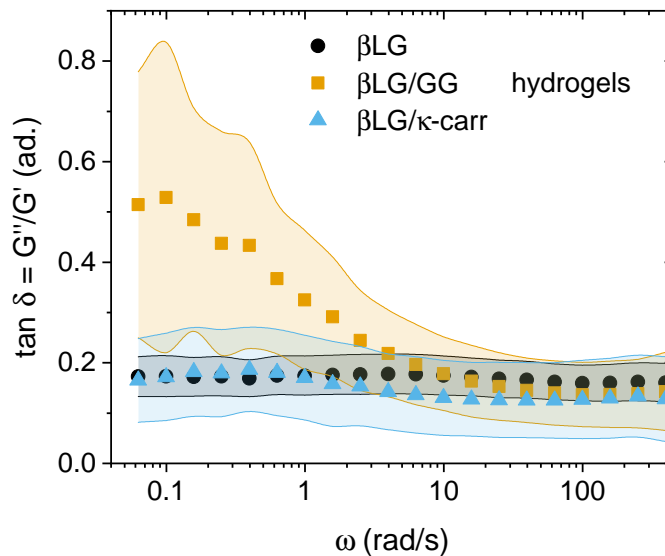
Fig. S4 Loss tangent ($\tan \delta = G''/G'$) calculated from the data reported in Fig.5A in the main manuscript. It can be appreciated how, while both βLG and βLG/κ-carrageenan networks exhibit average values smaller than 0.2, the values for the βLG/GG case raise to 0.5 (and are affected by larger error) as the probation frequency decreases. The error bars were computed using the formula $\sigma_\delta = (\sigma_{G'}/\langle G' \rangle + \sigma_{G''}/\langle G'' \rangle) \cdot \langle \delta \rangle$

3

5 Compression experiments on hydrogels - Alternative normalization
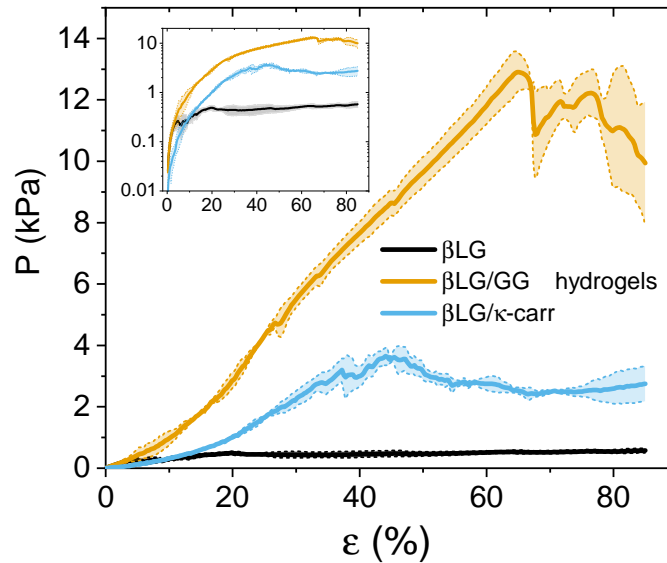
Fig. S5 Compression experiments on βLG amyloid fibril pure and hybrid hydrogels (in linear and semi-logharitmic scale, respectively in the main panel and in the inset). This figure was obtained similarly as Fig.5B and 5C of the main manuscript, but applying a different normalization that takes into account the incompressibility of water. In other words, as the upper plate of the geometry lowers and compresses the material, the effective cross-section of the sample is considered to increase to keep the total volume constant. If $V_0 = A_0 \cdot H_0$ is the initial volume of the gel, the assumption of the conservation of the entire volume leads to $A(t) = A_0 \cdot H_0/H(t)$, and the consequent real compression pressure is $P(t) = F(t)/A(t)$. Despite the reported pressure values are lower than the ones of the main manuscript (as a consequence of increasing compression area), the behaviour of the curves is similar and allows to draw the same conclusions on the relative compression properties of the examined materials.

6 Gold and methylene blue adsorption

6.1 Materials and methods

In order to characterize the ability of the synthesized gels for removing inorganic and organic pollutants from water, we decided to adsorb gold (in the form of HAuCl$_4$) and methylene blue as representative chemicals. For determining the adsorption capacity of the synthesized pure βLG and hybrid hydrogels, each of them was placed in contact with 4 mL of either a 2.5 mM solution of HAuCl$_4$ or a 2.5 ppm solution of methylene blue; the experiments were run over the course of 4 days, to allow the completion of the adsorption kinetics. Afterwards, the supernatants of the HAuCl$_4$ and the methylene blue solutions were sampled (1.5 mL and 2 mL, respectively) and analysed by AAS (Atomic Adsorption Spectroscopy) and UV-Vis Spectroscopy. The experiments were performed in triplicates, for each gel type, and the results were compared with those obtained from solutions where no gels were immersed. In the case of pure Gellan Gum gels (used as a control for determining the adsorption capacity of the polysaccharide unit), the gel was left immersed in a $\sim$ 70 ppm HAuCl$_4$ solutions (in duplicate, 4 mL each), and the experiment was then conducted as described above (after the system reached saturation). The pure Gellan Gum gels were prepared following the same protocol as the pure βLG amyloid fibril gels, with the difference that their formation was driven by immersing the cut syringe in a 100 mM KCl solution at pH 7, without further pH adjustment steps.

6.2 βLG amyloid fibrils preserve their surface functionality

In previous studies, it was shown that amyloids have a high binding capacity for heavy metal ions and organic pollutants[2–4], and therefore, show a significant potential for universal water purification. The way the polysaccharide fraction is embedded in the final hybrid materials can be deduced from the adsorption efficiency of the composite materials: if the protein-polysaccharide hydrogels show similar adsorption performances as the pure βLG networks, and if the polysaccharides do not play an active role in adsorbing the pollutants, then it is likely that the carbohydrate fraction forms an independent network (or local bundles). On the other hand, if the adsorption performance of the βLG component is

4
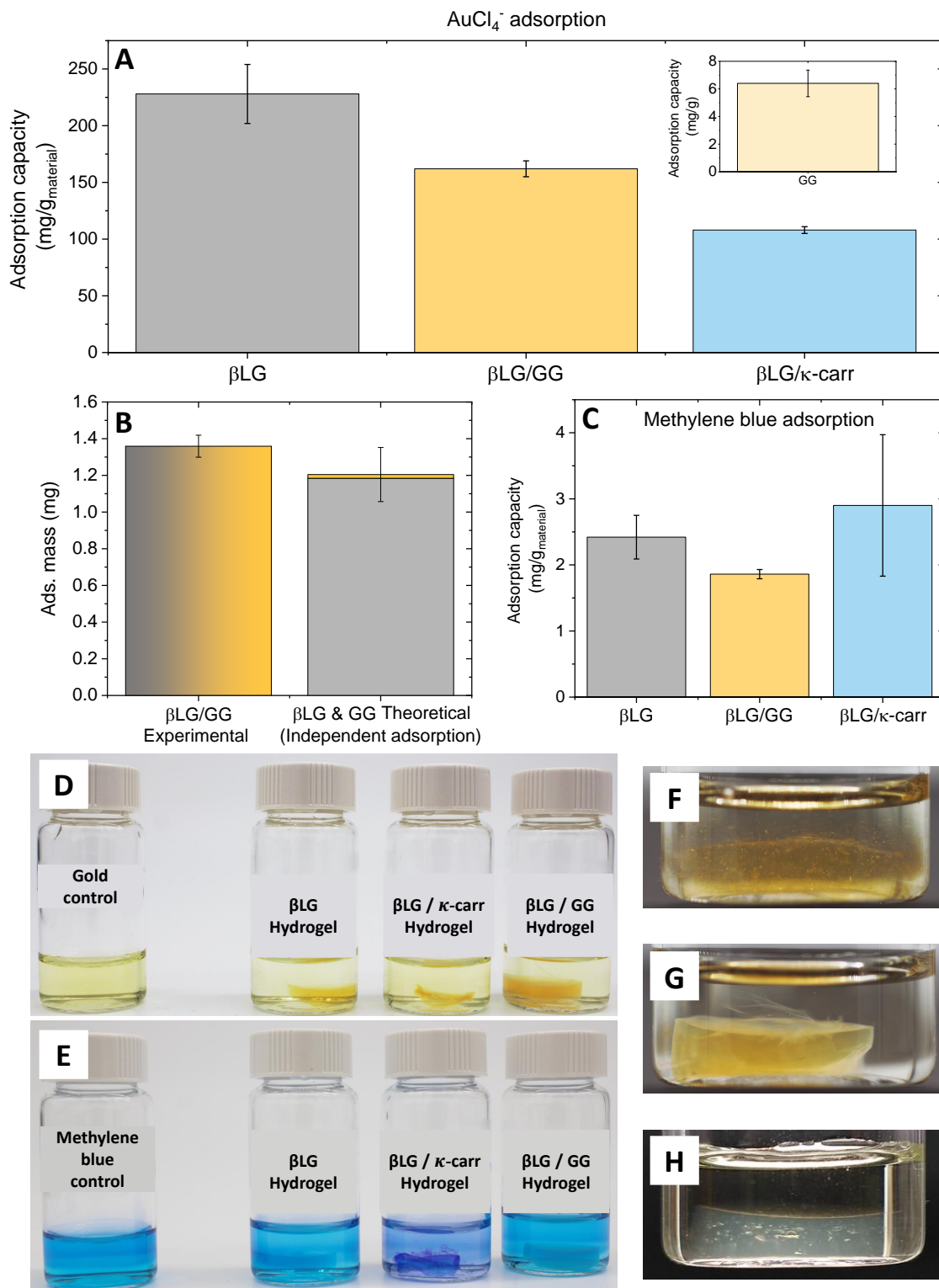
Fig. S6 Adsorption of the synthesised pure βLG amyloid fibril hydrogels and hybrid ones towards a gold salt (HAuCl$_4$) or of an organic pollutant (methylene blue). (A) Adsorption capacity of the three systems towards the gold salt. Inset: Adsorption capacity of a pure Gellan Gum gel towards the same chemical specie. (B) Comparison between the experimentally measured adsorbed mass (of the gold salt) by the hybrid βLG/GG gels, and the theoretical adsorbed mass of a fictitious material (built up by the identical masses of the protein and polysaccharide), where an independent action of the two components is assumed. (C) Adsorption capacity of the three systems towards methylene blue. The results for the βLG/κ-carrageenan case are affected by specific interactions that modify the visible light absorption spectrum of the considered dye. (D) Visual inspection on the ability of the gels to adsorb HAuCl$_4$. (E) Visual inspection on the ability of the gels to adsorb an organic dye (methylene blue). (F-G) Closer look on a pure βLG amyloid fibril gel (F) and a βLG/GG hybrid gel (G) immersed in a HAuCl$_4$ solution. (E) Picture of a pure Gellan Gum gel immersed in a HAuCl$_4$ solution.
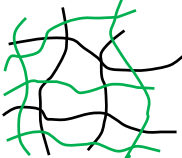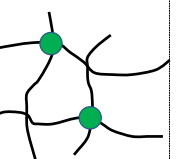
5
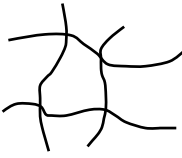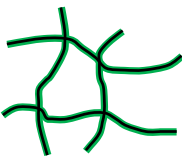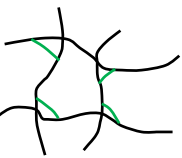
severely hindered, and the sugar units show limited binding capacities, it is instead likely that the polysaccharide units cover the fibrils and prevent them from interacting with the pollutants.

Fig.S6A shows the adsorption capacities of the pure amyloid fibril and hybrid gels towards gold (in an anionic form, $AuCl_4^-$). While the pure βLG samples show an average value higher than 225 mg/g, the hybrid materials show lower performances (approximately 160 and 120 mg/g for the βLG/GG and the βLG/κ-carrageenan gels, respectively). Although this may be interpreted as a hint that the polysaccharide fraction inhibits the adsorption of the pollutant, we need to consider that the adsorption capacity is calculated by dividing the adsorbed quantities by the masses of the adsorbing materials (that we considered equivalent to the average dry masses reported in Fig.3C of the main manuscript). Therefore, as the normalization is performed by also considering the masses of the polysaccharide fractions (that we hypothesize to play a small role in the adsorption), the data do not reflect the real adsorption capacity of the protein. Before proceeding with the analysis, we verified the accuracy of this hypothesis, by determining the adsorption capacity of Gellan Gum (inset of Fig.S6A). While all the gels containing the protein fraction are characterised by values higher than 100 mg/g, the pure polysaccharide system shows much poorer performances (close to 6 mg/g). Thus, our hypothesis that Gellan Gum plays a marginal role in the examined adsorption phenomena is verified.

This analysis leads to Fig.S6B, where the experimentally measured performance of the βLG/GG hydrogels (in terms of adsorbed mass) is compared to the theoretically-determined performance of a system where the same average quantities of βLG amyloid fibrils and Gellan Gum act independently. To do so, we considered that the hybrid materials have an average dry mass of 8.4 mg, 5.2 mg of which can be assumed to be the βLG amyloid fibrils and the difference (3.2 mg) to be the polysaccharide fraction (Fig.3C in the main manuscript). An ideal hybrid material, constituted by protein and polysaccharide components that act independently, would adsorb the same quantity of pollutants as the pure βLG amyloid fibril gels (gray bar), plus the quantity that can be ascribed to the polysaccharide fraction (ochre bar), determined by multiplying the measured adsorption capacity of Gellan Gum (inset of Fig.S6A) by the mass of the just-mentioned polysaccharide component. The result is very interesting: the average experimental adsorbed quantity from the hybrid system (bar with gray/ochre gradient) is in close agreement with the theoretically determined one. Therefore, it can be stated that the presence of Gellan Gum does not alter the adsorption capacity of the amyloid fibril fraction. However, the same scenario might not be true for the κ-carrageenan case: in fact, both the total dry mass (Fig.3C in the main manuscript) and the adsorption capacity are lower when compared to the other hybrid network. The reduced adsorption capacity might be ascribed to the shrinkage observed in this system (which reduces the specific surface area), and not resulting instead from specific interactions between the proteins and the considered sulfated polysaccharide fraction.

A visual inspection of the adsorption performances of the analyzed materials towards the used gold salt is shown in Fig.S6D, F, G and H, that report preliminary experiments with gold solution whose concentration was higher than the adsorption capacity of the materials. In panel D, it is possible to clearly appreciate how the color of the gels is darker than the one of the surrounding solution, clearly stating the ability of the considered materials to adsorb gold. Panels F and G show a closer look to pure βLG and βLG/GG hybrid gels, respectively, after they were left immersed in a gold solution for many days. In the case of the pure protein sample, the gold is transformed from its ionic form to its metallic counterpart, with creation of gold crystals[5] (visible as golden fragments that get released). Such release phenomenon is not visible in the hybrid gel case, potentially as a consequence of the stronger nature of the network: we believe this being an advantage of the mentioned hybrid material over the pure protein one, as it would less likely re-pollute the treated water in real-life applications. Panel H shows, instead, a pure Gellan Gum gel immerse in a gold solution. The image was acquired with a dark background to show the extremely limited adsorption capacity of the mentioned polysaccharide towards the considered ionic species. In fact, there is not hint of gold-like colour inside the gel mesh.

We extended the adsorption analysis further, including a dye (methylene blue) as a representative of organic pollutants. From Fig.S6B, it can be seen again how the hybrid systems show a performance similar to the pure βLG amyloid fibril networks. However, the performance of the βLG/κ-carrageenan hybrid system appears to be superior (despite the significant experimental error), in contrast to what was observed for gold adsorption. Considering the appearance of the gels after adsorption in preliminary trial experiments (Fig.S6E), where the used methylene blue concentration was much higher than the adsorption capacity of the material, we can clearly state that this result is caused by modifications in the optical absorption properties of the dye. In fact, the different color of the final system from that of the control solution (purple instead of blue) is a benchmark of specific interactions between the gel and the dye[6], or of pH induced structural changes of methylene blue[7] (in fact, βLG/κ-carrageenan hybrid gels were formed at a slightly higher pH than the others, to lower shrinkage effects). Therefore, we believe that the higher adsorption capacity observed in this case is an artifact

6

Hypotheses on network structure vs. Experimental evidences	A	B	C	D	E
Dry fraction	✗	✓	✓	✓	✓
Imaging (macro- and microstructure)	✗	✗	✓	?	✓
Mechanical response	✗	✓	?	✓	✓
Adsorption experiments	✓	✗	✓	✓	✓

Fig. S7 Analysis on how different embedding models of the polysaccharides inside the βLG amyloid fibril network align with the results of the performed experiments. (A) Pure amyloid network, where no polysaccharides could diffuse in. (B) Core-shell structure, with the protein fraction surrounded by the diffused polysaccharides. (C) Cross-linked network, where the polysaccharides interact with the amyloid fibrils and, without coating behaviour, strengthen the interactions among them. (D) Interpenetrating network, where the polysaccharide fraction builds up a secondary network that exists in parallel to the amyloid one. (E) Local bundling, where the polysaccharides concentrate in specific parts of the network and strengthen it with the formation of local thicker strands. In the discussion, the different hypothesis are compared with the results of the performed experiments.

induced by such phenomena. For methylene blue, we did not attempt to evaluate the adsorption performance of the pure polysaccharide fraction separately, as the adsorption performance of amyloid fibrils towards this dye is lower compared to gold. As a consequence, it would have been more complex to clearly identify the contributes of the protein and of the polysaccharide fractions.

To conclude, the experimental evidence presented here suggests that, apart from shrinkage-induced surface area reduction, the presence of the polysaccharide (especially in the Gellan Gum case) does not alter the adsorption performances of the amyloid fibrils. This is a key piece of information that suggests a good degree of preservation of the surface reactivity of amyloid fibrils.

7 Hypotheses on network structure

In our analysis on the synthesised pure protein and hybrid hydrogels and aerogels, carried our in the main manuscript and enriched by further insights presented here, we showed an effective diffusion of the sugar chains inside the networks (confirmed by the increase in the dry fraction of the final materials). Then, by analysing the macro- and microscopic appearance of the materials, by probing their mechanical properties through oscillatory sweeps and compression experiments, and by studying their performances in adsorbing water pollutants, we gained further insights on their structure and performances. While the higher compressibility and the remarkable adsorption capacity of the hybrid materials were confirmed by the performed experiments, the individual characterizations did not allow to draw conclusions on the microstructure of the arrested fibrillar networks. In fact, in the SEM images (Fig.4G, H and I in the main manuscript) the polysaccharide component could not be identified in a straightforward way: the presence of bundles in the aerogels could be interpreted both as characteristic interactions between the two components, or as shrinkage-induced lateral aggregation of filaments. Therefore, to draw stronger conclusions on how the polysaccharides are present in the final hybrid gels and aerogels, we compare all the collected evidence against different hypotheses (Fig.S7). A first hypothesis (A) consists in assuming that, due to repulsive charges and steric hindrance, the polysaccharide do not effectively diffuse inside the amy-

loid mesh. As such hypothesis is contradicted by the dry fraction analysis, by the performed imaging and by the measured mechanical reinforcement, it can be rejected. A second hypothesis (B) assumes that the polysaccharides, upon diffusion inside the amyloid fibril mesh and after getting in touch with the gelling salt solution, cover the amyloid fibrils and create a core-shell network. While this hypothesis is potentially aligned with the dry fraction measurements and the mechanical characterization (where the increased resistance to compression could be interpreted as an increase in bending stiffness of single filaments), the results from the imaging characterisation and from the adsorption measurements contradict such scenario. In fact, in the SEM images it is possible to appreciate only local hints of aggregation, and in the adsorption of the gold salt and of methylene blue the amyloid network almost fully express its surface reactivity. We believe therefore that it is safe to reject this second hypothesis.

A third scenario (C) consists in assuming that the diffused polysaccharide units interact with the fibril network by the creation of local cross-links. While such structure could be aligned with almost all the described evidences, we are skeptical of it being able to explain the observed mechanical response. In fact, upon diffusion of ions, amyloid fibrils create long-lived physical crosslinks that strongly tune their rheological response[8]: while it is possible that crosslinking with the polysaccharide units further reinforces the networks, it is doubtful that the mentioned process could strengthen the materials to the observed extent. The forth hypothesis (D) we consider consists in the polysaccharide chains being morphologically affected by the added specific ions, and creating therefore a secondary network that interpenetrates the amyloid fibrils one. This hypothesis is aligned with the dry fraction analysis, with the observed increase in mechanical properties and with the adsorption characterization; at the same time, the SEM images presented in the main manuscript do not show a network which is appreciably denser for the hybrid aerogel cases. In fact, the presence of a secondary network is not the most straightforward interpretation of the mentioned pictures; however, it could also be assumed that a secondary network was present before the CO_2 drying process, and then collapsed and reinforced the primary network over the solvent exchange (this phenomenon is confirmed by the fact that polysaccharide aerogels, at the mass fraction values compatible to the ones of our work, usually shrink a lot). The last hypothesis that we share (E) is that the polysaccharide component, upon diffusion and ion-induced morphological modifications, forms local bundles that strengthen the βLG network by locally increasing the bending stiffness. This hypothesis is not contradicted by the collected experimental evidence and, together with the hypotheses (C) and (D), builds different pathways that could explain the properties of the observed networks. The hypothesis that the hybrid materials consist in double network gels (DN) is not considered, as such materials are usually built by combining a rigid and brittle cross-linked polyelectrolite network, together with a neutral, soft and ductile polymer present at much higher molarity[9,10].

References

1 I. Usov and R. Mezzenga, *Macromolecules*, 2015, **48**, 1269–1280.

2 S. Bolisetty and R. Mezzenga, *Nature Nanotechnol.*, 2016, **11**, 365–371.

3 M. Peydayesh, S. Bolisetty, T. Mohammadi and R. Mezzenga, *Langmuir*, 2019, **35**, 4161–4170.

4 M. Peydayesh, M. K. Suter, S. Bolisetty, S. Boulos, S. Handschin, L. Nyström and R. Mezzenga, *Adv. Mater.*, 2020, **32**, 1907932.

5 G. Nyström, M. P. Fernández-Ronco, S. Bolisetty, M. Mazzotti and R. Mezzenga, *Adv. Mater.*, 2016, **28**, 472–478.

6 M. Diener, J. Adamcik and R. Mezzenga, *ACS Macro Lett.*, 2020, **9**, 1310–1317.

7 G. Singhal and E. Rabinowitch, *J. Phys. Chem.*, 1967, **71**, 3347–3349.

8 Y. Cao, S. Bolisetty, J. Adamcik and R. Mezzenga, *Phys. Rev. Lett.*, 2018, **120**, 158103.

9 J. P. Gong, *Soft Matter*, 2010, **6**, 2583–2590.

10 Q. Chen, H. Chen, L. Zhu and J. Zheng, *J. Mater. Chem. B*, 2015, **3**, 3654–3676.

8

5. VEGF and VEGFR2 bind to similar pH-sensitive sites on fibronectin, exposed by heparin-mediated conformational changes
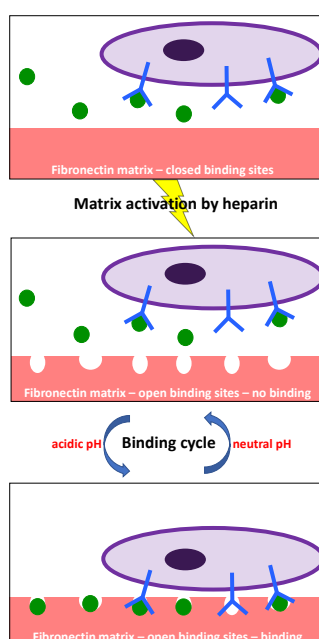
Mattia Usuelli, Timmy Meyer, Raffaele Mezzenga* and Maria Mitsi*

Summary

The intra- and inter-molecular reactivity of fibronectin is ruled by its conformation, which is tuned by the catalytic binding of heparin; the heparin-driven exposure of interaction sites allows the formation of complexes between fibronectin and other key biomacromolecules. VEGF (Vascular Endothelial Growth Factor), which has a key role in blood endothelial cell biology, is one of such macromolecules: the interplay between fibronectin and this growth factor regulates its activity and signaling, and tunes therefore the creation of new blood vessels. In this work we show, with both kinetic and static studies, that fibronectin can also interact with extracellular domain of VEGFR2, the main receptor of VEGF. The interactions of both VEGF and VEGFR2 with fibronectin were shown to happen thanks to two different classes of sites, having different kinetics and affinities, that were exposed upon heparin-induced conformational changes and that showed enhanced binding at acidic pH. Moreover, this study also highlights the possibility of forming triple complexes among these key biological units, unveiling key pieces of information to deepen the understanding on how angiogenesis works.

VEGF and VEGFR2 bind to similar pH-sensitive sites on fibronectin, exposed by heparin-mediated conformational changes

Mattia Usuelli, Timmy Meyer, Raffaele Mezzenga*, and Maria Mitsi*
From the Laboratory of Food and Soft Materials, Department of Health Sciences and Technology, ETH Zurich, Zurich, Switzerland

Edited by Enrique De La Cruz

Physical interactions between vascular endothelial growth factor (VEGF), a central player in blood endothelial cell biology, and fibronectin, a major fibrillar protein of the extracellular matrix, are important determinants of angiogenic activity in health and disease. Conditions signaling the need for new blood vessel growth, such as hypoxia and low extracellular pH, increase VEGF–fibronectin interactions. These interactions can be further fine-tuned through changes in the availability of the VEGF-binding sites on fibronectin, regulated by conformational changes induced by heparin and heparan sulfate chains within the extracellular matrix. These interactions may alter VEGF bioavailability, generate gradients, or alter the way VEGF is recognized by and activates its cell-surface receptors. Here, using equilibrium and kinetic studies, we discovered that fibronectin can also interact with the extracellular domain of the VEGF receptor 2 (VEGFR2). The VEGFR2-binding sites on fibronectin show great similarity to the VEGF-binding sites, as they were also exposed upon heparin-induced conformational changes in fibronectin, and the interaction was enhanced at acidic pH. Kinetic parameters and affinities for VEGF and VEGFR2 binding to fibronectin were determined by surface plasmon resonance measurements, revealing two populations of fibronectin-binding sites for each molecule. Our data also suggest that a VEGF/VEGFR2/fibronectin triple complex may be formed by VEGF or VEGFR2 first binding to fibronectin and subsequently recruiting the third binding partner. The formation of such a complex may lead to the activation of distinct angiogenic signaling pathways, offering new possibilities for clinical applications that target angiogenesis.

Fibronectin is a major protein of the extracellular matrix, with the ability to interact with a multitude of cell surface and matrix components such as integrins, collagen, and heparan sulfate proteoglycans, as well as many growth factors (1, 2). It plays a crucial role in angiogenesis, the formation of new blood vessels from the preexisting vasculature. Fibronectin null mice die early during embryonic development because of severe vascular defects (3). Furthermore, in many *in vivo* and *in vitro* systems of sprouting angiogenesis, fibronectin is essential for tip cell migration (4–6), suggesting that it acts as substrate for the growth of the newly formed vessels. Additionally, fibronectin can bind vascular endothelial growth factor (VEGF), a major regulator of angiogenesis, and directly influence its signaling output (7–9).

Alternative splicing generates several VEGF isoforms, containing a basic domain of increasing length, which interacts with heparan sulfate proteoglycans (10). Traditionally, long VEGF isoforms (*e.g.*, $VEGF_{206}$) with high heparin affinity have been considered matrix-bound, whereas the shorter isoforms (*e.g.*, $VEGF_{121}$), lacking the heparin-binding domain, have been considered completely soluble. Early studies showed that each VEGF isoform has the ability to stimulate angiogenesis *in vivo*, but the morphology and density of the resulting vascular network were aberrant unless the correct balance between all isoforms was maintained (11). However, heparan sulfate proteoglycans are not the only extracellular matrix components interacting with VEGF. Fibronectin is a major binding partner for VEGF isoforms that are considered soluble ($VEGF_{121}$) or exhibiting medium affinity for heparan sulfate proteoglycans ($VEGF_{165}$) (7, 12, 13). Thus, when considering VEGF function, our definition of matrix-bound VEGF should be expanded to include interactions with fibronectin as well as heparan sulfate proteoglycans.

Earlier studies showed that the VEGF-binding sites on fibronectin are cryptic and become exposed upon conformational changes induced by heparin (7). The mechanism of heparin action in this case is fundamentally different from the known allosteric effects of heparin on other proteins, such as antithrombin and FGF, as it does not involve the formation of a ternary complex between VEGF, fibronectin, and heparin (14). Instead, the fast kinetics of the heparin–fibronectin interaction allow for a structural catalysis to take place, whereby substoichiometric amounts of heparin, given enough time, can change the conformation of fibronectin within the entire matrix, by sequential binding to and releasing from neighboring fibronectin molecules. In a physiologic setting, this could be observed locally in the extracellular matrix through the action of heparan sulfate proteoglycans or alternatively, through heparin secreted by mast cells upon

* For correspondence: Maria Mitsi, maria.mitsi@alumni.ethz.ch; Raffaele Mezzenga, raffaele.mezzenga@hest.ethz.ch.

inflammation or any other appropriate stimulus. Consequently, such heparin/heparan sulfate–mediated changes in fibronectin conformation within the extracellular matrix will increase VEGF binding and alter its angiogenic potential.

The fact that VEGF binding to the extracellular matrix is an important determinant of its biological output (15–17) can be partly explained by indirect effects, such as VEGF sequestration in the matrix that alters its bioavailability and generates gradients that influence cellular response (18, 19). However, it has been shown that matrix-bound VEGF, at the same effective amounts as soluble VEGF, in the absence of gradients activates distinct downstream signaling pathways (20, 21). VEGF signals upon binding to cell-surface cognate receptors (VEGFRs), which belong to the family of Receptor Tyrosine Kinases (RTKs) and they regulate a large number of physiological processes in vascular biology (22). There are three known isoforms of VEGFR encoded by different genes: VEGFR1, VEGFR2, and VEGFR3. They are mainly expressed in endothelial cells and, although they share a similar overall architecture, they have significant differences in cellular localization, ligand specificity, structure, and function. VEGFR1 seems to act mostly as a decoy receptor, regulating ligand availability and the signaling strength of VEGFR2, while VEGFR3 functions are limited almost exclusively to the lymphatic system (23). VEGFR2, on the other hand, is the major player in blood endothelial cell biology; it is considered one of the central players in regulating angiogenesis in a number of physiological and pathological conditions, such as embryonic development, wound healing, and cancer growth and metastasis (24).

Canonical VEGF signal transduction proceeds *via* dimerization of VEGFR2 and propagation of conformational changes, which are not yet fully understood, but eventually lead to a precise juxtaposition and activation of the intracellular kinase domain of the receptors (22). Subsequently, a series of tyrosine residues in the intracellular part of VEGFR2 become phosphorylated, initiating various signaling cascades. There is evidence that VEGFR2 signaling is modulated by various coreceptors, including integrins that interact with extracellular matrix components. Thus, matrix-bound VEGF could recruit different coreceptors to the VEGF/VEGFR2 complex, leading to distinct VEGFR2 activation patterns (25–28). Indeed, the distinct phosphorylation profile of VEGFR2 activated by immobilized VEGF involves β_1 integrin-induced VEGFR2 clustering (20) and numerous studies suggest extensive cross talk between $\alpha_v\beta_3$ and $\alpha_5\beta_1$ integrins—the major fibronectin receptors—and VEGFR2 (29). Thus, complex formation between VEGF and fibronectin could bring together VEGFR and integrins into a large signaling complex leading to distinct pathway activation.

The early recognition of the importance of angiogenesis for cancer growth and metastasis (30), led to the development of several cancer therapeutic approaches that target the VEGF/VEGFR2 signaling axis (31). However, despite great promise from initial studies, their clinical outcome has been at best meagre, accompanied by severe side effects (32). Although the ineffectiveness of antiangiogenic therapies cannot be ascribed to a single factor, considering the complexity of the biology and clinical manifestation of cancer, it certainly highlights the need to draw a more complete picture of the mechanisms underlying VEGFR2 activation and signaling. In particular, targeting specifically matrix-bound VEGF and the interactions that hold the VEGF/VEGFR2 complex together may offer exciting new opportunities for the design of more specific and effective drugs (33). Therefore, it is important for both basic research and clinical applications to understand the dynamic interactions between VEGF, VEGFR2, and fibronectin.

In this study, we discovered that the catalytic effect of heparin on fibronectin structure exposes also binding sites for the extracellular domain (ECD) of VEGFR2. Equilibrium and kinetic studies revealed that ECD binding and VEGF binding to fibronectin followed a very similar pattern and were enhanced at acidic pH. We found that the affinity of ECD for fibronectin was higher than that of VEGF. Furthermore, VEGF and ECD could bind simultaneously to fibronectin. Such binding events could influence the activation of VEGF/VEGFR2 complexes, as well as the formation of higher-order complexes with other cell-surface receptors and extracellular matrix proteins, regulating angiogenesis in health and disease.

Results

Equilibrium binding by enzyme-linked immunoassay (ELISA)-based experiments

To study the interactions between fibronectin and the angiogenic factors $VEGF_{165}$ (termed VEGF for simplicity) and ECD in a simple and fast way that would not require protein labeling, we developed an ELISA-based solid-phase binding assay. Fibronectin was adsorbed on 96-well plates and allowed to interact with the ligand (VEGF or ECD) until equilibrium was reached. The fraction of the ligand that was specifically bound to fibronectin was then extracted with a solution of high ionic strength (5 M NaCl), adsorbed onto a second 96-well plate, and detected using a primary antibody against the ligand and a corresponding HRP-labeled secondary antibody. The signal was detected by luminescence. The ligand extraction step was necessary because of the high levels of VEGF nonspecific binding, which could not be reduced by blocking agents either added in the binding buffer or adsorbed on the plate. The steps for the assay optimization are described in Figs. S1–S6.

Using this assay, we evaluated the binding of VEGF and ECD to surface-immobilized fibronectin. VEGF binding followed the same pattern as previously reported, with higher binding occurring at acidic pH only after fibronectin was treated with heparin (Fig. 1A). The measured values reflect the VEGF fraction specifically bound to fibronectin, since no VEGF was extracted from the naked substrate or from adsorbed bovine serum albumin (BSA). Interestingly, a very similar binding pattern was observed with ECD (Fig. 1*B*). For both ligands, significant binding was observed at pH 5.5 after incubating the surface-immobilized fibronectin with heparin. Thus, we chose this condition to further analyze the protein interactions.
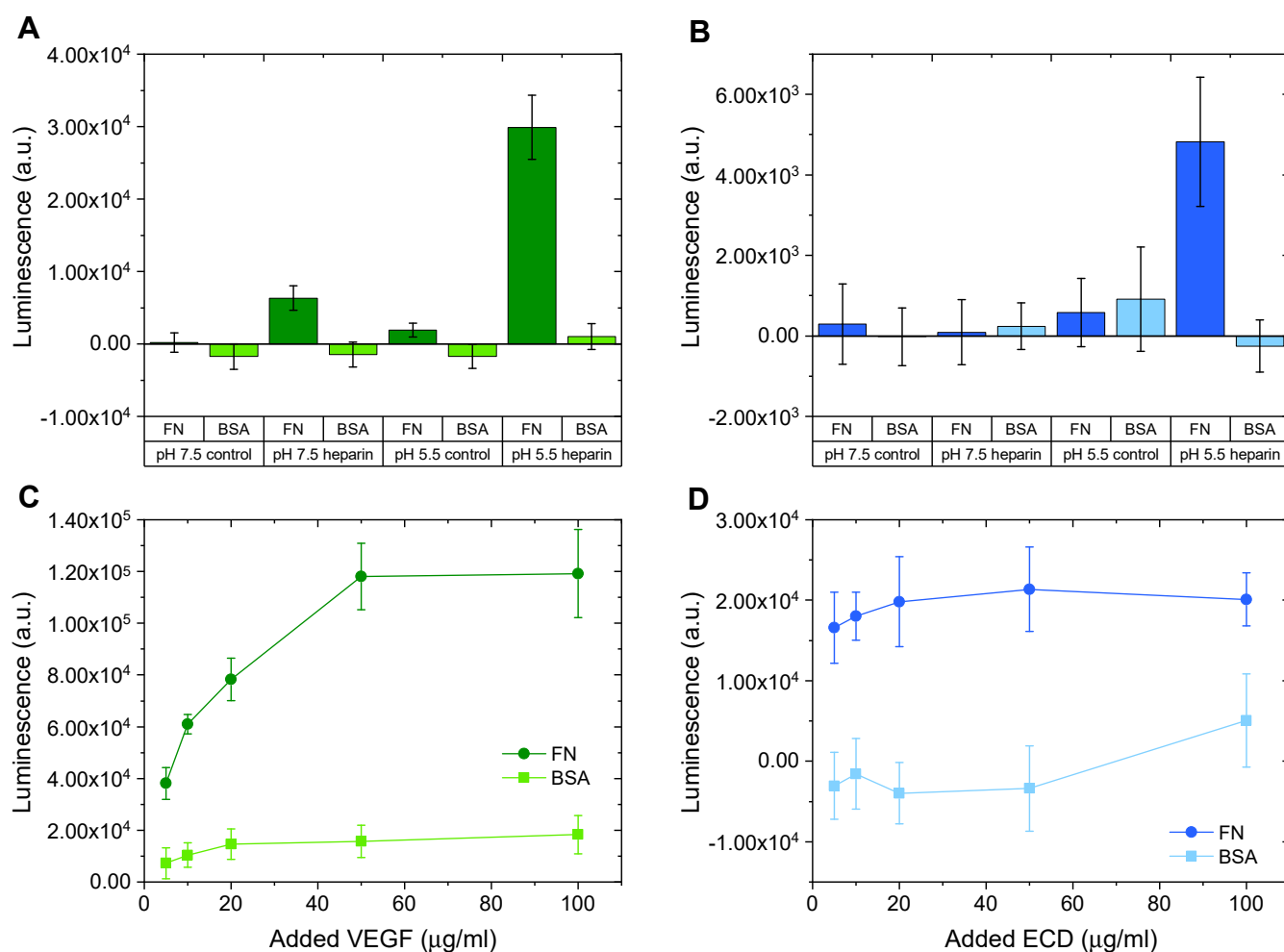
Figure 1. Acidic pH and pretreatment of fibronectin with heparin increase VEGF and ECD binding. *A* and *B*, Fibronectin (*dark green/blue bars*) or bovine serum albumin (BSA) (*light green/blue bars*) was adsorbed on 96-well polystyrene plates (20 μg/ml; 50 μl/well) overnight at 4 °C. The plate was incubated for 1 h on ice with 5 μg/ml VEGF (*A*) or ECD (*B*) in binding buffer (150 mM NaCl, 25 mM Hepes) at pH 7.5 or 5.5, in the absence (control) or presence (heparin) of pretreatment of the adsorbed proteins with 100 μg/ml heparin in PBS (1 h on ice). Bound VEGF or ECD was extracted with 5 M NaCl, 25 mM Hepes, pH 7.5 for 1 h on ice, readsorbed on a second plate, and detected by ELISA with an anti-His primary antibody (1:1000) and an HRP-labeled secondary antibody (1:2000). Both antibody incubations were performed in ELISA blocking buffer (1 mg/ml BSA + 0.05% Tween20 in PBS). Samples were measured in quadruplicate, and the data are presented as mean values ± standard deviation. *C* and *D*, Fibronectin (*dark green/blue lines*) or BSA (*light green/blue lines*) was adsorbed on 96-well polystyrene plates (20 μg/ml; 50 μl/well) overnight at 4 °C. The plate was incubated for 1 h on ice with increasing concentrations of VEGF (*C*) or ECD (*D*) in binding buffer (150 mM NaCl, 25 mM Hepes) at pH 5.5 in the presence of pretreatment of the adsorbed proteins with 100 μg/ml heparin in PBS (1 h on ice). VEGF and ECD extraction and detection were performed as in (*A*) and (*B*). Samples were measured in quadruplicate, and the data are presented as mean values ± standard deviation.

Dose–response experiments showed that ECD binding to surface-immobilized fibronectin reached saturation at significantly lower concentrations than those for VEGF, suggesting that ECD binds to fibronectin with higher affinity than VEGF (Fig. 1, *C* and *D*). This conclusion is further reinforced if we consider that the binding was performed with equal masses for the two ligands, which, given the difference in molecular weight between VEGF (45 kDa) and ECD (83 kDa), means lower molarity for ECD. We did not attempt to calculate affinities at this stage, because of the many intermediate assay steps between the binding event and the final measurement. However, we observed significantly lower luminescence values for ECD than for VEGF (Fig. 2). These differences could originate from different recognition of VEGF and ECD by the primary antibody and/or different degrees of adsorption of the two proteins. Indeed, calibration curves revealed different signals for the same amount of VEGF and ECD, which

depended on both the ionic strength of the buffer and the protein concentration (Fig. S6). Taken all this into account, it appears that ECD possesses higher affinity for fibronectin than VEGF, but the absolute amount of VEGF and ECD bound to fibronectin cannot be determined by this experimental setup.

Since VEGF and ECD bind to fibronectin following a very similar pattern, we wanted to elucidate whether they share the same binding sites and if their binding is mutually exclusive. To do so, we compared the combined binding of VEGF and ECD to fibronectin when they were added simultaneously or sequentially, using an anti-His antibody that can recognize both ligands (as they both contain a His-tag; see Experimental Procedures) or an anti-VEGFR2 antibody that recognizes specifically ECD (Fig. 2). We confirmed that both the anti-His and anti-VEGFR2 antibodies could detect their respective ligands when bound individually to fibronectin. When both VEGF and ECD were added to fibronectin, the signal detected
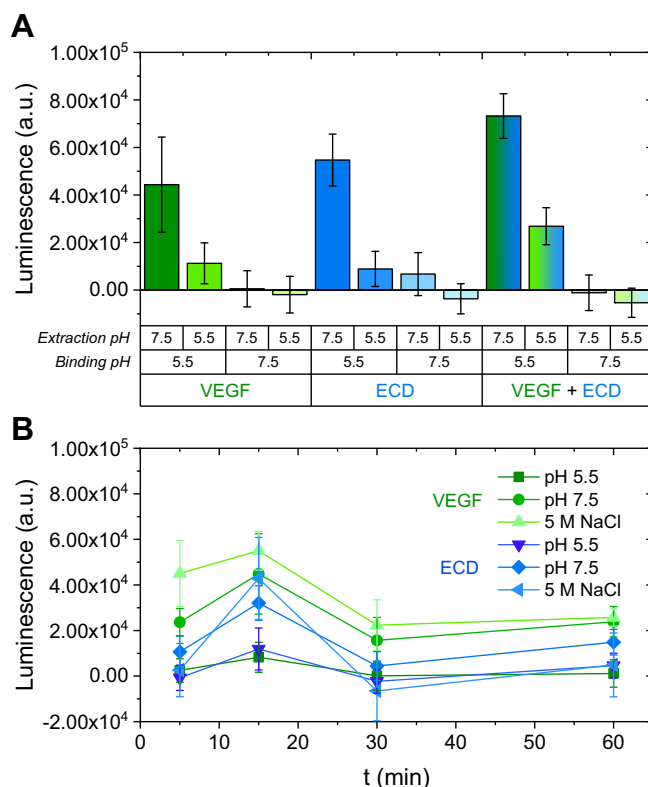
VEGFR2 binding to fibronectin
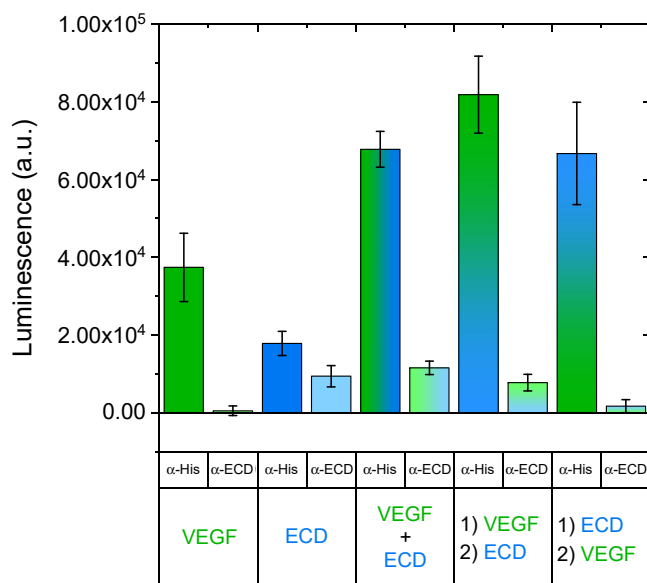
Figure 2. VEGF and ECD can bind simultaneously to fibronectin. Fibronectin was adsorbed on 96-well polystyrene plates (20 μg/ml; 50 μl/well) overnight at 4 °C. The plate was incubated for 1 h on ice with 50 μg/ml of VEGF or ECD alone or in combination (VEGF + ECD). Additionally, some wells were treated first with 50 μg/ml of VEGF or ECD for 1 h, followed by a second 1 h incubation with 50 μg/ml ECD or VEGF, respectively (conditions labeled as '1) VEGF 2) ECD' and '1) ECD 2) VEGF', respectively). Ligand binding was studied in binding buffer (150 mM NaCl, 25 mM Hepes) at pH 5.5 after pretreatment of the adsorbed fibronectin with 100 μg/ml heparin in PBS (1 h on ice). Bound VEGF and/or ECD were extracted with 5 M NaCl, 25 mM Hepes, pH 7.5 for 1 h on ice, readsorbed on a second plate, and detected by ELISA with an anti-His or an anti-VEGFR2 primary antibody (1:1000) and an HRP-labeled secondary antibody (1:2000). Both antibody incubations were performed in ELISA blocking buffer (1 mg/ml bovine serum albumin + 0.05% Tween20 in PBS). Samples were measured in quadruplicate, and the data are presented as mean values ± standard deviation.

by the anti-His antibody was always higher than if VEGF or ECD was added alone, irrespectively of the order of ligand addition, suggesting that their binding to fibronectin is not mutually exclusive. The anti-VEGFR2 antibody detected the presence of ECD under all conditions, except when ECD was added before VEGF. Since no binding scenario predicts the complete absence of ECD under this condition (Fig. S7), this result suggests that when fibronectin-bound ECD is allowed to interact with VEGF as well, the epitope for this particular antibody is masked. The only possibility consistent with all these observations is that VEGF and ECD are likely to share binding sites on fibronectin, and when bound to fibronectin, they retain their ability to recognize each other and lead to the formation of a VEGF/ECD/fibronectin triple complex (Fig. S7).

Both VEGF and ECD could be released from fibronectin by changing the pH from 5.5 to 7.5, even if the ionic strength of the extraction solution was not increased (Fig. 3A). Indeed, gradually increasing the ionic strength of the extraction buffer did not result in higher release (Fig. S8). This suggests that the interaction depends on pH-sensitive amino acids. The release was very fast, occurring within a few minutes after buffer change. Interestingly, longer extraction times led to a decrease in the amount of released VEGF or ECD (Fig. 3B), which may be the result of ligand readsorption (Fig. S8).

Figure 3. Switching the pH from acidic (5.5) to neutral (7.5) is sufficient to release fibronectin bound VEGF and ECD. *A*, Fibronectin was adsorbed on 96-well polystyrene plates (10 μg/ml; 50 μl/well) overnight at 4 °C. The plate was incubated for 1 h on ice with 50 μg/ml of VEGF (*green*) or ECD (*blue*) alone or in combination (VEGF + ECD) in binding buffer (150 mM NaCl, 25 mM Hepes) at pH 7.5 or 5.5 after pretreatment of the adsorbed fibronectin with 100 μg/ml heparin in PBS (1 h on ice). Bound VEGF and ECD were extracted with binding buffer (150 mM NaCl, 25 mM Hepes) at pH 7.5 or 5.5, for 1 h on ice, readsorbed on a second plate, and detected by ELISA with an anti-His primary antibody (1:1000) and an HRP-labeled secondary antibody (1:2000). Both antibody incubations were performed in ELISA blocking buffer (1 mg/ml bovine serum albumin + 0.05% Tween20 in PBS). Samples were measured in quadruplicate, and the data are presented as mean values ± standard deviation. *B*, Fibronectin was adsorbed on 96-well polystyrene plates (10 μg/ml; 50 μl/well) overnight at 4 °C. The plate was incubated for 1 h on ice with 50 μg/ml of VEGF (*green*) or ECD (*blue*) in binding buffer (150 mM NaCl, 25 mM Hepes) at pH 5.5 after pretreatment of the adsorbed fibronectin with 100 μg/ml heparin in PBS (1 h on ice). Bound VEGF and ECD were extracted with binding buffer (150 mM NaCl, 25 mM Hepes) at pH 7.5 or 5.5, or with 5 M NaCl, 25 mM Hepes, pH 7.5 for 5, 15, 30 or 60 min (each time interval in a different set of wells) on ice, readsorbed on a second plate, and detected by ELISA with an anti-His primary antibody (1:1000) and an HRP-labeled secondary antibody (1:2000). Both antibody incubations were performed in ELISA blocking buffer (1 mg/ml bovine serum albumin + 0.05% Tween20 in PBS). Samples were measured in quadruplicate, and the data are presented as mean values ± standard deviation.

Structural determinants of the interactions

Circular dichroism (CD) spectra of VEGF and ECD were acquired at pH 7.5 and pH 5.5 (Fig. 4). The ionic strength of the buffer prevented data collection below 205 nm, and at low ionic strength buffers, the structure of VEGF was altered, suggesting significant unfolding (Fig. S9). Therefore, the spectra could not be subjected to structure deconvolution with certainty, especially, since both VEGF and ECD are beta-sheet dominated and the CD spectra of beta-sheet proteins show significant variability, rendering their deconvolution
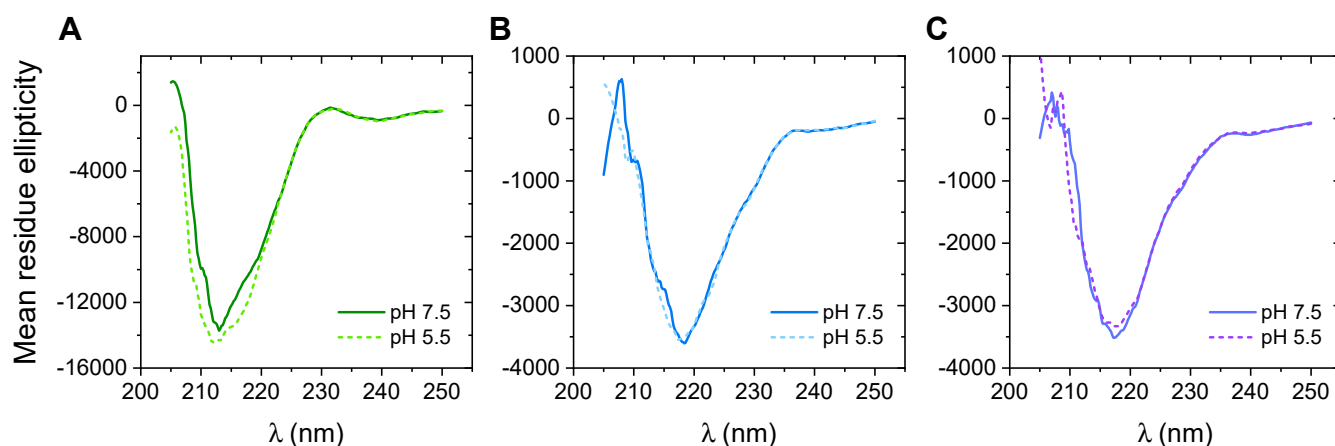
Figure 4. The secondary structure of VEGF and ECD does not undergo significant changes between neutral and acidic pH. Circular dichroism spectra were acquired for VEGF (*A*; 0.3 mg/ml), ECD (*B*; 0.3 mg/ml), and VEGF/ECD complex (*C*; 0.5 mg/ml) in binding buffer (150 mM NaCl, 25 mM Hepes) at pH 7.5 (*solid lines*) and pH 5.5 (*dashed lines*) at 4 °C. The data are presented in mean residue ellipticity units (deg*cm²/dmol).

problematic (34). However, the spectra at pH 7.5 and 5.5 were very similar, suggesting that the pH does not cause a major change in the protein secondary structure. If there is a pH-sensitive conformational change of VEGF and ECD, it should be slight or local. Therefore, it is more likely that the increased binding observed at pH 5.5 would depend on the protonation state of critical amino acids in the binding site rather than large conformational changes. We decided to further study this point, by computing the pH dependance of the protonation state of surface amino acids for both the ligands (VEGF and ECD) and the domain of fibronectin where the binding is likely to happen (FNIII 12–14) (7).

Based on the known structures of VEGF and ECD, we calculated the pKa values of surface-exposed amino acids (35), and we identified several residues with a pKa value between 5.5 and 7.5, whose protonation state would change between these two pH values (Table 1) and thus, could belong to the fibronectin-binding sites on each molecule. In the case of ECD, most of the candidate residues were His residues, which often function as pH sensors (36–38). Whereas for ECD almost all candidate residues seem to be free of interactions with the ligand, the majority of the pH-sensitive residues on VEGF were on the receptor-binding domain and were involved in interactions in the VEGF dimer or between VEGF and the

Table 1

Surface-exposed amino acid residues on VEGF and ECD predicted to change protonation state between pH 7.5 and 5.5

	Protein domain	Residue	pKa	Protonation probability		Free of interactions
				pH 5.5	pH 7.5	
VEGF	Receptor-binding domain	Arg23	6.82	0.994	0.074	No
		Lys84	6.46	0.973	0.017	No
		His86	6.33	0.963	0.012	No
		Glu93	6.37	0.967	0.015	No
	Heparin-binding domain	His125	5.96	0.847	0.002	Yes
ECD	Domain1–domain2 linker	Arg122	6.46	0.980	0.020	Yes
		His133	6.52	0.980	0.020	Yes
	Domain2	Arg176	6.35	0.970	0.010	Yes
		Glu201	6.37	0.970	0.010	Yes
	Domain3	His232	6.33	0.960	0.010	Yes
		Glu235	6.89	1.000	0.100	Yes
		Arg249	6.20	0.930	0.010	Yes
		His267	6.21	0.930	0.010	Yes
		His269	6.44	0.970	0.020	Yes
		Asp295	6.80	0.990	0.070	Yes
	Domain3–domain4 linker	Arg323	6.31	0.960	0.010	No
		His325	6.69	0.990	0.040	Yes
	Domain4	His375	6.25	0.950	0.010	Yes
		His381	6.25	0.950	0.010	Yes
		His411	6.72	0.990	0.040	Yes
	Domain5	His454	6.13	0.870	0.010	Yes
		His455	6.00	0.770	0.010	Yes
		His457	6.46	0.940	0.030	Yes
		His546	7.02	1.000	0.140	Yes

Structure-based predictions of pKa values of individual amino acid residues at the surface of VEGF and ECD were performed with the DelPhiPKa web server, using the known high-resolution structures of VEGF and ECD fragments (pdb files used: 2VPF and 2VGH for VEGF and 3V2A, 2X1W, 2X1X, 3S35, 3S36, 3S37, 5OYJ, and 3KVQ for ECD). It is also indicated whether the side chains of the candidate amino acids are free from known interactions (hydrogen bonds and salt bridges) with other parts of the protein or holding together the VEGF/ECD complex.

receptor, leaving free of interactions only a His residue at the C-terminal domain of VEGF. However, since full-length structures are lacking for both VEGF and ECD, these results should be interpreted with caution since prediction of pKa values is very sensitive to the local environment of the amino acid (39, 40). Because of the pH sensitivity of His residues, we would like to mention that experiments with nontagged VEGF conducted in an earlier study showed the same binding profile (7). Moreover, His-tagged VEGF-E showed no binding to heparin-treated fibronectin at acidic pH (data not shown). These observations support the conclusion that the His tag in the recombinant proteins used in this study is unlikely to affect the enhanced binding observed at acidic pH.

As mentioned above, we performed a similar analysis on the C-terminal 40 kDa fragment of fibronectin encompassing domains FNIII 12–14, which was identified earlier as the VEGF-binding site on fibronectin (7, 8). Interestingly, no pH-sensitive residues with a pKa value between 5.5 and 7.5 were identified in this region. We run the analysis using two different conformations reported for this fibronectin domain (pdb codes: 1FNH and 3R8Q), obtaining almost identical results: 22 acidic residues (pKa < 4), 32 basic residues (pKa > 10), and no exposed pH-sensitive residues. This suggests that, after being exposed by the heparin action, this binding site on fibronectin is not regulated further by changing the local pH. Instead, it remains always available for binding, which occurs only when key amino acids in the ligand become protonated at acidic pH.

Mechanistic insights on the interactions by SPR kinetic experiments

To further understand mechanistically the interactions between fibronectin and VEGF/ECD, we followed the kinetics of the interactions by surface plasmon resonance (SPR). Fibronectin was immobilized *via* N-hydroxysuccinimide (NHS) chemistry on the surface of the carboxymethyldextran hydrogel of the biosensor chip (Fig. S10). VEGF or ECD was added in the mobile phase under flow. Based on the results of the equilibrium studies, all experiments were performed at pH 5.5. Binding in the absence of any heparin treatment of the surface-immobilized fibronectin was minimal, even at a high fibronectin density (Fig. S11). We tested the effect of injecting 1 mg/ml BSA into both flow cells, which could act as a blocking protein, reduce nonspecific binding of VEGF to both flow cells, and unmask specific associations between VEGF and the immobilized fibronectin. However, the low levels of VEGF binding persisted. Interestingly, BSA injection stabilized the sensogram values for background VEGF binding after repeated injection and regeneration cycles (Fig. S12) and was, therefore, employed in all subsequent experiments. Heparin treatment of the immobilized fibronectin was thus necessary in order to observe any appreciable binding. Based on the resulting resonance units (RU) values following heparin treatment, we chose an intermediate fibronectin density (2 µg/ml) to get values within the recommended range for SPR experiments (Fig. S11).

To test the action of heparin in the SPR setup, ∼10x molar excess of heparin was injected prior to the binding assay, was allowed to associate with the surface-immobilized fibronectin for 1 min and then dissociate for increasing periods of time (0, 10, or 30 min) by changing accordingly the flow rate (Fig. 5, *A* and *B*). This experimental design was based on a previous study, describing the catalytic mechanism by which heparin mediates the conformational change on fibronectin that exposes the VEGF-binding sites (14). According to this model, fibronectin–heparin interactions are transient and characterized by multiple rebinding and release events, resulting in a low amount of bound heparin at equilibrium. In the SPR setup, heparin rebinding could occur during the long dissociation phase, increasing the contact time between heparin and fibronectin and resulting in maximal conversion of fibronectin to the open form, exposing the binding sites. At the same time, the longer dissociation times would allow for a more complete heparin release, thus, minimizing the amount of heparin present on the surface-immobilized fibronectin during the binding assay with VEGF/ECD. Unfortunately, an estimation of the amount of heparin bound to fibronectin directly from the SPR sensograms was not possible, because of the low signal generated by this amount of heparin (Figs. S13 and S14), further demonstrating the low levels of heparin binding to fibronectin. However, the VEGF sensograms show that the duration of the dissociation step following heparin treatment did not affect VEGF binding (Fig. 5A). This supports the idea that a 1-min association time was sufficient for this amount of heparin (1 µg/ml) to convert the immobilized fibronectin to the open conformation (this structural rearrangement has been reported earlier to be fast (14)) and that the subsequent VEGF binding occurs on fibronectin and not on any residual heparin remaining bound to fibronectin. Interestingly, ECD binding stabilized only after at least 10 min of heparin dissociation (Fig. 5B). If no dissociation was performed following heparin treatment, there was no ECD binding. This would be explained if ECD shared binding sites with heparin, and in order to observe appreciable binding, heparin must be completely released. Based on these results, we performed all further experiments after heparin treatment of the surface-immobilized fibronectin by 1 min association, followed by 10 min dissociation.

To extract kinetic rates, we collected association and dissociation data with a concentration series of VEGF or ECD (Fig. 5, *C* and *D*). Already a visual inspection of the binding curves, prior to any attempt to fit a model for the macromolecular interaction, reveals certain characteristics. First, there was a very fast initial burst during the association phase, especially evident at higher VEGF/ECD concentrations, followed by a slower increase. Second, dissociation was slow, resulting in a significant amount of ligand remaining bound at the end of the experiment, which was increased with VEGF/ECD concentration.

A conventional one-site model (Fig. 6) failed to fit the data (section 6 in Experimental Procedures; Figs. S15 and S16), even when considering mass transfer effects. Given the
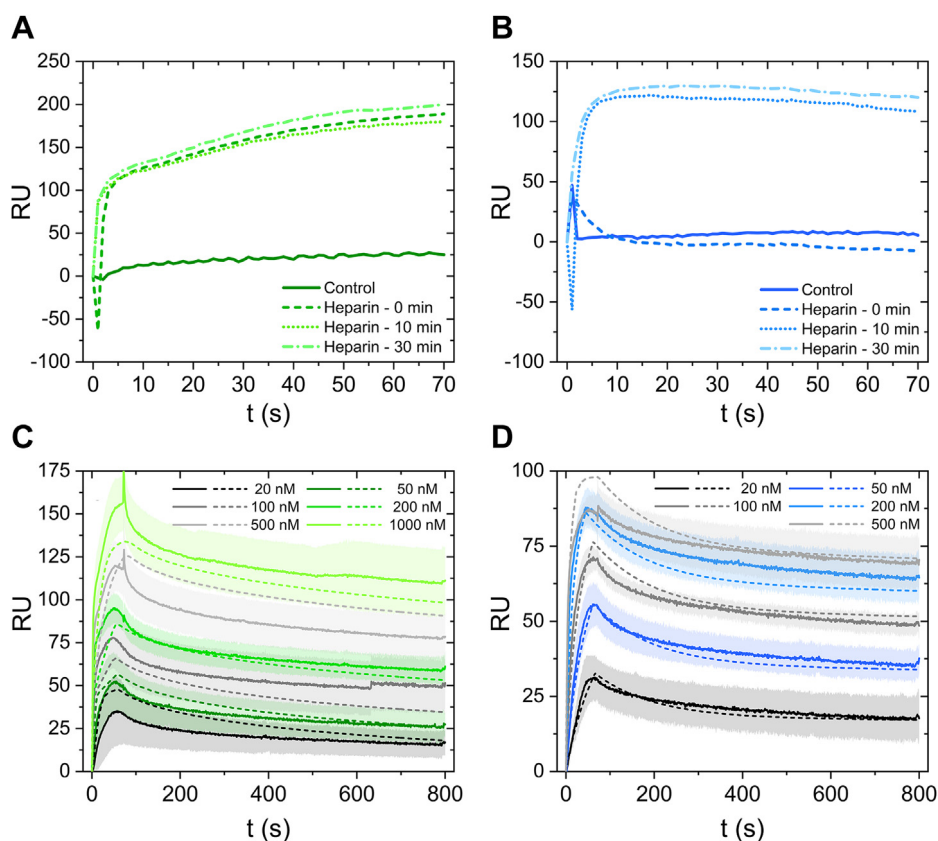
**Figure 5. Direct monitoring of interactions between fibronectin and VEGF or ECD by SPR.** *A* and *B*, VEGF (*A*) or ECD (*B*) (60 μl of 1000 nM) was injected at a flow rate of 50 μl/min on a chip with 2 μg/ml immobilized fibronectin (140 ng) in the absence (control) or presence of a heparin pretreatment of the immobilized fibronectin, followed by heparin dissociation for 0 min, 10 min, or 30 min. *C* and *D*, Heparin (50 μl of 1 μg/ml) was injected at a flow rate of 50 μl/min on a chip with 2 μg/ml immobilized fibronectin (140 ng). Following association, heparin was allowed to dissociate for 10 min, and immediately afterward, VEGF (*C*) or ECD (*D*) was injected (60 μl at 50 μl/min) at different concentrations: 20 nM, 50 nM, 100 nM, 200 nM, 500 nM, and 1000 nM for VEGF and 20 nM, 50 nM, 100 nM, 200 nM, and 500 nM for ECD (the color code is explained in the figure). Mean values from triplicate measurements are shown, with the shaded area representing the standard deviation. Following association, VEGF and ECD were allowed to dissociate for 720 s. The different VEGF/ECD concentrations were injected following a random order in order to ensure that the measurements were free of systematic errors, and the progressive increase in VEGF/ECD binding with increasing concentration reflected the true binding. The surface was regenerated with 2 M NaCl and 0.05 N NaOH after every VEGF/ECD binding cycle. The experimental data (*solid lines*) were fitted to a two-sites model (*dashed lines*) considering mass transfer for VEGF (*C*) and rapid mixing for ECD (*D*).

observed slow dissociation, we considered a model whereby the ligand upon dissociation from one receptor molecule performs a random walk across the surface and rebinds to neighboring receptor molecules multiple times before diffusing back to the bulk phase (41). However, this model also failed to capture the binding behavior, as it could not account for the fact that the dissociation rate depended on the VEGF/ECD concentration (Fig. S17). We considered also models whereby each monomeric chain of fibronectin possesses two binding sites for VEGF or ECD, which could act independently (parallel reactions model) or affect each other (consecutive reactions model) (Fig. 6). Although the consideration of two binding sites improved somewhat the fitting, there were still significant deviations from the experimental data (Figs. S15 and S16). The model that generated the best fit was the two-sites model, assuming two populations of fibronectin molecules, each possessing a single binding site per monomeric chain that interacts with the ligand (VEGF or ECD) with distinct association/dissociation rate constants (Fig. 5, *C* and *D*; Table 2). Interestingly, only VEGF binding required

consideration of mass transfer phenomena for better fitting, which may be related to the faster association rates for VEGF than ECD, rendering the process diffusion limiting. The kinetic parameters governing fibronectin-VEGF/ECD interactions extracted from the two-sites model are summarized in Table 3. Instead of single values, we report intervals, which were either calculated during fitting for the parameters extracted directly from the model or derived from these values for the K_d estimates.

Statistical analysis indicates that the discrepancies observed between experimental and fitted data can be ascribed to experimental error (section Statistical analysis of curve fitting in Experimental Procedures; Figs. S18 and S19; Table S2). Additional uncertainties in parameter estimation could originate from the limited number of experimental points during the initial association burst. However, it is possible that a simple two-sites model fails to describe certain aspects of the macromolecular interactions, such as rebinding events, and it should be considered only as an approximation of the experimental observations.
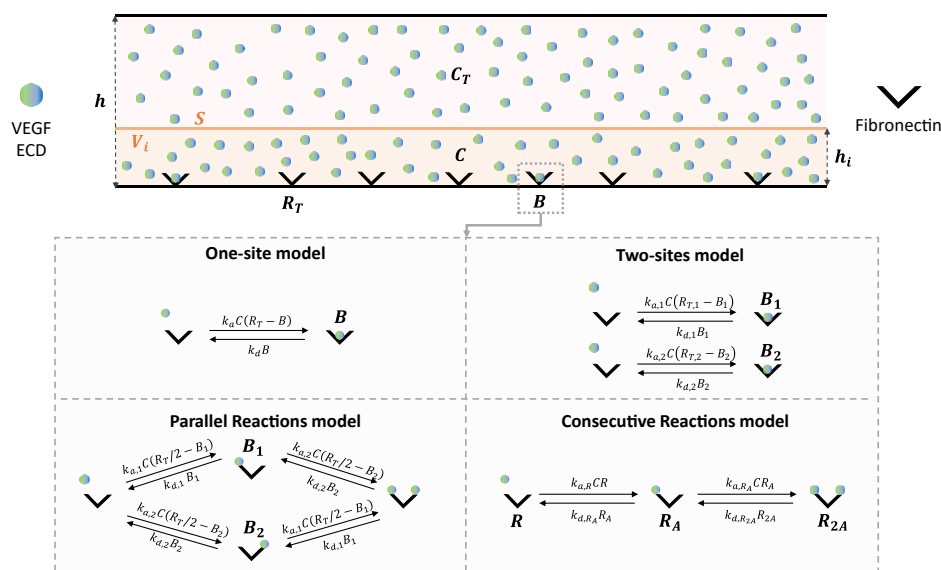
Figure 6. Modeling of interactions between fibronectin and VEGF or ECD during an SPR experiment. The SPR experimental setup was modeled using the two-compartment model considering (1) a flowing bulk phase with a time-invariant concentration (C_T) of ligands (VEGF or ECD) and (2) a narrow volume slit (V_i) in the proximity of the surface (S) where receptors (fibronectin) have been immobilized at an initial concentration R_T. Ligand molecule exchange occurs between the flowing bulk phase and V_i (mass transfer), as well as between V_i and S (binding/unbinding events). For simplicity, the two monomeric chains of a fibronectin molecule are considered to act independently, and the surface-immobilized receptors depicted correspond to each monomeric chain and not to the complete fibronectin dimer. Four different models were used to describe ligand–receptor interactions, generating ligand-bound (B) receptor molecules: the one-site model, assuming one ligand binding site per receptor; the two-sites model, assuming a heterogeneous receptor population composed of two types of molecules, each with a single binding site with distinct association/dissociation kinetics; the parallel reactions model, assuming that each receptor contains two ligand-binding sites that act independently; and the consecutive reactions model, assuming that each receptor contains two allosterically linked ligand binding sites, where a second ligand can bind only after the first site has already been engaged. From a modeling perspective, we consider the concentration of binding sites for the one-site (B), two-sites (B_1 and B_2), and parallel reactions (B_1 and B_2) models, and the concentration of the various receptor molecular species (R, R_A, and R_{2A}) for the consecutive reactions model.

Discussion

VEGF binding to the extracellular matrix has been recognized as an important event regulating angiogenesis (2). Previous studies have shown that fibronectin, a major component of the extracellular matrix, possesses cryptic binding sites for VEGF, which become available when fibronectin undergoes a conformational change, catalyzed by heparin and heparan sulfate chains within the extracellular matrix (7, 8, 13). VEGF binding to these sites is enhanced at acidic pH (7, 12). Here, we report for the first time a similar class of heparin-sensitive binding sites on fibronectin that interact with the ECD of VEGFR2, also at acidic pH. VEGFR2 is a major cell-surface receptor for VEGF, and it is possible that interactions between VEGF, VEGFR2, and fibronectin are important for the regulation of VEGF/VEGFR2 signaling, which is critical for angiogenesis (42). In this study, we developed assays in order to characterize these protein–protein interactions by equilibrium and kinetic studies *in vitro*.

Table 2
Statistical evaluation of different models describing the interaction between fibronectin and VEGF or ECD

		One-site model		Two-sites model		Parallel reactions model		Consecutive reactions model	
		Rapid mixing	Mass transfer	Rapid mixing	Mass transfer	Rapid mixing	Mass transfer	Rapid mixing	Mass transfer
VEGF	Data points	4800	4800	4800	4800	4800	4800	4800	4800
	Parameters	3	4	6	7	5	6	5	6
	RMS	7.34E+05	8.89E+05	5.17E+05	4.93E+05	7.02E+05	7.71E+05	3.98E+05	3.27E+05
	σ^2	153	185	108	103	146	161	83	68
	σ	12	14	10	10	12	13	9	8
	AIC	10,493	10,895	9769	9670	10,404	10,602	9221	8814
	Ranking	6	8	4	3	5	7	2	1
ECD	Data points	4000	4000	4000	4000	4000	4000	4000	4000
	Parameters	3	4	6	7	5	6	5	6
	RMS	9.09E+04	4.78E+05	5.02E+04	5.48E+04	7.26E+04	1.27E+05	6.84E+04	5.79E+04
	σ^2	23	120	13	14	18	32	17	14
	σ	5	11	4	4	4	6	4	4
	AIC	5432	8318	4407	4563	5047	6014	4943	4655
	Ranking	6	8	1	2	5	7	4	3

The experimental data presented on Fig. 5, *C* and *D* for the interaction between fibronectin and VEGF or ECD were fitted with the models shown on Fig. 6, and the fits that generated well-defined solutions (Figs. S15 and S16 and Table S2) were evaluated with measures for absolute fit (RMS and σ^2) and model parsimony (AIC), as described in the section. Statistical analysis of curve fitting' under Experimental Procedures. The number of data points is lower for ECD than for VEGF, since the curve corresponding to 1000 nM ligand was not considered for the fitting in the case of ECD because the interaction reached saturation already at 500 nM ligand and additionally, the data associated with 1000 nM ECD displayed a large experimental error. The number of parameters for each model is derived from Fig. 6, and the corresponding parameter estimates are shown in Table S2.

Table 3
Kinetic parameters describing the interactions between fibronectin and VEGF or ECD

| | Site A | | | Site B | | | | | |
	k_a ($M^{-1}s^{-1}$)	k_d (s^{-1})	K_d (nM)	k_a ($M^{-1}s^{-1}$)	k_d (s^{-1})	K_d (nM)	α	R_T (mol^1m^{-2})	k_m (m^1s^{-1})
VEGF	$9.0*10^6$	$2.9*10^{-3}$	0.07	$6.3*10^4$	$5.3*10^{-5}$	6.5	0.32	$3.0*10^{-9}$	$2.2*10^{-6}$
	$3.1*10^7$	$1.0*10^{-4}$	0.6	$6.7*10^4$	$1.9*10^{-4}$	8.7	0.34	$3.0*10^{-9}$	$3.7*10^{-6}$
ECD	$8.8*10^5$	$7.0*10^{-3}$	0.8	$2.1*10^5$	$2.8*10^{-5}$	0.1	0.23	$1.2*10^{-9}$	
	$1.1*10^6$	$8.2*10^7$	2.9	$2.1*10^5$	$9.2*10^{-5}$	0.4	0.26	$1.2*10^{-9}$	

The experimental data presented on Fig. 5, *C* and *D* were fitted with the two-sites model (considering mass transfer for VEGF and rapid mixing for ECD). Association and dissociation rates (k_a and k_d) for each site, the site occupancy α (Site A/Site B), the density of total binding sites (R_T), and the mass transfer rate (k_m), when applicable, were extracted from the model. Instead of single values, the lower and upper boundaries of the confidence intervals for each parameter, calculated during fitting, are given. Dissociation affinity constants for each site were calculated by dividing k_d by k_a. The intervals for the K_d values were derived from those associated with the k_d by k_a values according to the formula: for Z = A/B, $(\Delta Z/Z)^2 = (\Delta A/A)^2 + (\Delta B/B)^2$, where ΔA, ΔB, and ΔZ are the errors associated with quantities A, B, and Z, respectively.

For equilibrium studies, we followed an ELISA-based approach, which does not require ligand labeling. This not only increases the versatility and simplicity of the assay, but also circumvents the need for testing the potential effects of labeling on the structure, activity, and stability of the ligand. However, we noticed high levels of nonspecific VEGF binding to the plate surface, which masked the specifically bound VEGF to fibronectin and prevented its direct detection. Several blocking protein-based agents (BSA, egg white albumin, beta-lactoglobulin, gelatin, hemoglobin, and milk) were tested, either by coadsorption on the substrate or by inclusion in the binding buffer, but none could suppress VEGF nonspecific binding consistently. Therefore, we used an indirect approach, whereby we extracted the bound ligand by either increasing the ionic strength of the buffer or changing the pH back to neutral, readsorbed it on another assay plate, and detected it with a typical ELISA. Negative controls with the uncoated substrate or with adsorbed BSA instead of fibronectin confirmed that the extraction step released only the fraction of the ligand that interacted specifically with fibronectin (Fig. 1). In our experiments, we used recombinant VEGF and ECD proteins carrying a His-tag, which allowed the detection of both proteins by the same anti-His primary antibody, rendering the assay uniform. However, the assay worked well also with ligand-specific antibodies (Fig. 2). A drawback of this assay design is the number of intermediate steps before ligand detection (ligand binding, extraction, readsorption, and ELISA), which makes it difficult to extract equilibrium constants for the interactions. Nonetheless, our ELISA-based binding assay can be readily applied to compare the specific binding of different VEGF/VEGFR isoforms, fragments, and mutants, and potentially additional growth factors and cytokines, to fibronectin.

The results of our ELISA-based binding assay show that binding of both VEGF and ECD to surface-adsorbed fibronectin requires opening up of cryptic binding sites on the fibronectin molecules through the catalytic action of heparin and is enhanced at acidic pH. The heparin-exposed VEGF-binding sites have been localized on the 40 kDa C-terminal domain of fibronectin, comprising domains FNIII 12–14 (7, 8, 13). Although it is possible that the heparin-catalyzed structural changes may affect more than one region of fibronectin, our binding experiments with sequential ligand addition suggest that VEGF and ECD may share binding sites on

fibronectin, and binding of either one can bring the entire VEGF/VEGFR2 complex in contact with fibronectin (Fig. 2). This is consistent with previous studies showing the ability of fibronectin-bound VEGF to interact with VEGFR2 (21).

Mechanistic insights on the interactions between fibronectin and VEGF/VEGFR2 were gained by SPR kinetic experiments. Similar to the results of the equilibrium studies, binding of either VEGF or ECD to fibronectin at acidic pH was minimal in the absence of any heparin treatment. To achieve the maximum effect of heparin on the conformation of the immobilized fibronectin, while minimizing VEGF or ECD binding to any residual heparin remaining bound to fibronectin, we allowed fibronectin to interact with ~10x molar excess heparin during a 1-min association phase, followed by a 10-min dissociation phase (Fig. 5). Previous research has shown that heparin–fibronectin interactions are transient and governed by repeated rebinding and release events whereby a heparin molecule dissociating from a fibronectin molecule will rebind to neighboring fibronectin molecules multiple times before diffusing into the bulk (14). Accordingly, the combined heparin association and dissociation phases should offer sufficient time for heparin to interact with the majority of the immobilized fibronectin layer and be almost completely released prior to VEGF or ECD binding. Interestingly, the presence of the dissociation phase during heparin pretreatment had no effect on VEGF binding. This suggests that the 1-min association phase at that heparin concentration was sufficient to expose all available VEGF-binding sites on the immobilized fibronectin layer. Indeed, the heparin-catalyzed structural rearrangement of fibronectin is very fast and able to reach completion within 1 min (14). At the same time, the fact that VEGF binding remained the same, even in the absence of heparin dissociation, confirms that, in this experimental setup, VEGF interactions with fibronectin-bound heparin were negligible. For ECD, however, heparin dissociation was necessary in order to observe any binding. In the absence of heparin dissociation, we observed a first fast initial burst of binding, but the RU returned quickly to the baseline levels. There was no difference in ECD binding after a 10-min or 30-min heparin dissociation phase. These data suggest that heparin interferes and competes with ECD for binding to fibronectin, possibly because the ECD-binding sites on fibronectin overlap with one of the heparin-binding sites. On the contrary, the heparin presence

ASBMB *J. Biol. Chem.* (2021) 296 100584 **9**

99

had no effect on VEGF binding to fibronectin, suggesting that despite the similarities in VEGF and ECD binding to fibronectin, the sites for the two ligands are not identical. It is interesting to notice that the 40 kDa domain of fibronectin, which contains the VEGF-binding sites, can also bind a multitude of other growth factors and cytokines, suggesting the existence of mechanisms that regulate the availability of such a great number of binding sites within a limited domain and orchestrate the binding events (13). If the ECD-binding sites are also located in this domain, the presence of heparin chains (and not only their catalytic action) may be part of such a regulatory mechanism, determining which binding events take place. In future studies utilizing fibronectin fragments and mutants, we plan to map precisely the VEGF and ECD-binding sites on fibronectin.

The model that described best the SPR experimental data revealed the presence of two populations of fibronectin molecules (site A and site B) that can bind VEGF and ECD with different affinities (Fig. 5). Although the two-sites model described the data better than the one-site model, there were still discrepancies between the experimental data and the fitted values, especially for VEGF. Statistical analysis suggests that these discrepancies could be explained by the levels of experimental error (Table 2). However, it is possible that they reflect aspects of the interaction not captured adequately by a simple two-sites model, such as rebinding events as have been reported for one-site models (41, 43, 44). We did not incorporate this term in the fitting model to avoid overparameterization, especially since the system of differential equations describing the two-sites interaction does not have an analytical solution. We are currently developing a mathematical model to describe this phenomenon for two-site interactions, which will be presented in a future study.

According to the model, site A, which is the minority of the total population (20–30%), is characterized by high association and dissociation rates, whereas site B (70–80% of the total population) has association and dissociation rates lower than those for site A by one or more orders of magnitude (Table 3). Since the binding of VEGF and ECD to fibronectin was negligible in the absence of heparin treatment, this heterogeneity cannot be explained by the presence of fibronectin molecules on which the binding sites have not yet been opened by heparin. Furthermore, the action of heparin is very fast and even if the time of contact with the immobilized fibronectin was increased, the levels of VEGF and ECD binding remained the same. Therefore, it is also unlikely that the two binding populations reflect an incomplete action of heparin. Instead, these results suggest that not all fibronectin molecules respond equally to the action of heparin. Indeed, previous studies by atomic force microscopy (AFM) have identified structural heterogeneity on single fibronectin molecules, with approximately 70% of the visualized molecules adopting a similar configuration (7). The origin of this heterogeneity is not known, but may be related to the inherent variability in the amino acid sequence of the two fibronectin chains generated by alternative splicing (45) and/or the presence of diverse covalently bound glycans (GlyGen database: P02751–15). Irrespectively of the source of this structural heterogeneity, it is possible that when these molecules

respond to the heparin action generate binding site B, whereas the rest will generate site A. According to our model, site A is more accessible than site B for ligand binding, leading to higher association rates, but it can also be freed more quickly (higher dissociation rates). The actual values for the kinetic rates result
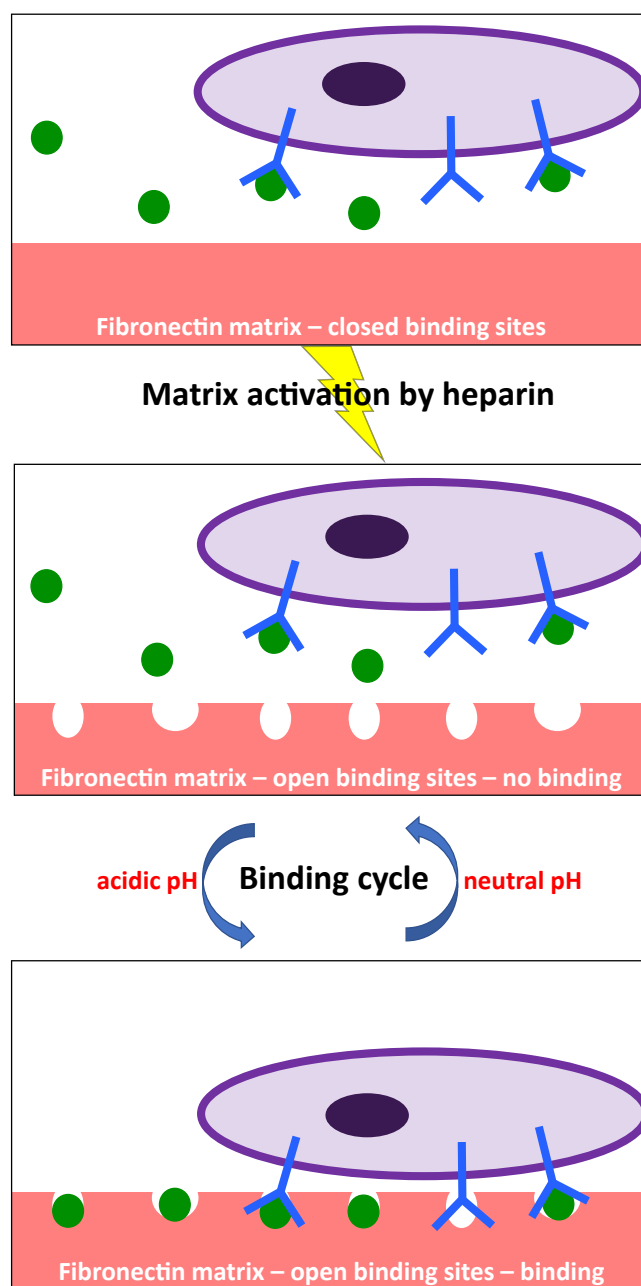
Figure 7. Schematic representation of interactions between VEGF, VEGFR2, and fibronectin in the extracellular matrix. Binding of VEGF (*green*) and VEGFR2 (*blue*) at the cell surface (*purple*) to fibronectin within the extracellular matrix (*red*) requires first the action of heparin, which alters the conformation of fibronectin and exposes the binding sites. One set of sites (site A) is characterized by fast association and dissociation rates, leading to a fast turnover (represented by the wider circles in the fibronectin matrix). On the other hand, binding of VEGF and VEGFR2 on the second set of sites (site B) occurs with lower association and dissociation rates, resulting in more stable binding (represented by the narrower circles in the fibronectin matrix). However, binding of either VEGF or VEGFR2 to fibronectin cannot occur unless the pH of the cell microenvironment becomes acidic. When pH returns back to neutral, VEGF and VEGFR2 dissociate from fibronectin, completing the binding cycle.

in site A having higher affinity for VEGF, and site B exhibiting higher affinity for ECD, and since site B represents the majority of binding sites, the overall affinity of ECD for the fibronectin matrix would be higher than that of VEGF, which is consistent with the results of the equilibrium studies. Consequently, high affinity binding of VEGF to fibronectin would be characterized by a high turnover rate, whereas ECD binding would be more stable. Moreover, VEGF binding would occur mostly on a small number of sites, whereas ECD could more readily interact with the majority of fibronectin sites within the extracellular matrix. These differences may have an impact on the dynamics of the interactions between the three molecules and fine-tune their functionalities. A model describing VEGF/VEGFR2/fibronectin interactions occurring *in vivo*, extrapolated from our *in vitro* observations, is shown in Figure 7.

The enhanced binding of VEGF and ECD on fibronectin at acidic pH may have significant consequences for angiogenesis. It is known that hypoxia, signalizing the need for angiogenesis, leads to anaerobic metabolism and consequently, decreases locally the extracellular pH (46). In tumors, which also require angiogenesis to sustain their growth and metastasize, there are additional mechanisms stimulating glycolysis, even under normoxic conditions, contributing to the low levels of extracellular pH. There have been cases of tumors with extracellular pH as low as 5.8 (47). Thus, fibronectin would bind the angiogenic factor VEGF and its receptor primarily in areas requiring active angiogenic signaling. Such sequestration of VEGF within the matrix may increase its bioavailability and help create gradients to guide the growth of new vessels. On the other hand, fibronectin-bound VEGF can alter VEGFR2 signaling (48). It is possible that VEGFR2 binding to fibronectin may alter its residence time on the cell membrane, altering its signaling output. Finally, such interactions may facilitate the formation of higher-order complexes, including integrins and neuropilins, fine-tuning the cell response to an angiogenic stimulus. It is interesting that upon switching the pH back to neutral, both fibronectin-bound VEGF and ECD can be quickly released (Fig. 3). This behavior would act as a regulatory mechanism that can potentially terminate VEGF/VEGFR2 angiogenic signaling when the conditions in the extracellular microenvironment cease to be acidic.

CD spectra of VEGF and ECD acquired at neutral (pH 7.5) and acidic (pH 5.5) pH revealed that the pH alteration did not cause major conformational changes on either molecule (Fig. 4). Therefore, the pH dependency of the interactions might rely completely on pH-sensitive amino acids within the binding sites. Using structure-based algorithms to calculate pKa values of individual amino acids, we could identify several residues, especially His residues, on both VEGF and ECD that could act as pH sensors (Table 1). Control experiments with nontagged VEGF or His-tagged VEGF isoforms that do not interact with fibronectin suggest that the His residues of the tag used for recombinant protein production are not involved in the enhanced binding observed at acidic pH. In ECD, most of the candidate residues were found on domains 3, 4, and 5, and their side chains were not involved in interactions with VEGF in the VEGF-VEGFR2 complex, or in stabilizing the secondary and tertiary structure of the protein. In VEGF, on the other hand, most of the candidate residues were involved in interactions either with VEGFR2 or with the second monomer in the biologically active dimeric form of VEGF, except for one His residue in the C-terminal domain of VEGF (His125), which is free from interactions and could participate in interactions with fibronectin. However, this residue is missing in VEGF$_{121}$, another VEGF isoform that can also bind to fibronectin in a pH-dependent manner (12). Therefore, His125 cannot be the only pH-sensitive residue involved in VEGF–fibronectin interactions. It is known that pKa values are very sensitive to the microenvironment of the residue, and electrostatics, conformational fluctuations, and solvent thermodynamics can cause pKa shifts (49). Moreover, structural information is fragmentary for both VEGF and ECD. High-resolution structures exist only for individual domains and not for the full-length proteins. Therefore, the prediction of the pKa values of individual residues based on the known structures should be interpreted with caution. Nonetheless, His residues often act as pH sensors, modulating protein structure and protein–protein interactions (36, 37).

Decreasing the pH may also affect the binding sites on fibronectin. Several studies have shown that fibronectin undergoes conformational changes in response to pH changes (50). It is possible that these conformational changes also affect the VEGF and ECD-binding sites on fibronectin. We did calculate pKa values on surface-exposed residues in the FNIII 12–14 domains of fibronectin, which contains the VEGF and possibly the ECD-binding sites, based on two alternative conformations that have been reported. Interestingly, we identified a large number of basic (pKa > 10) and acidic (pKa < 4), but none that could act as pH sensors (5.5 < pKa < 7.5). This suggests an elegant mechanism whereby the action of heparin regulates fibronectin conformation to expose VEGF/ECD-binding sites, whereas the local pH regulates ligand binding. However, given the size and flexibility of fibronectin, we cannot exclude the possibility that in the full-length protein different amino acid residues are exposed in the FNIII 12–14 domains or that they have different pKa values. Furthermore, as already discussed, additional regions of fibronectin may be involved in ECD binding.

Understanding VEGF/VEGFR2 interactions with fibronectin within the extracellular matrix may have implications for cancer therapy. Interestingly, some of the His residues in ECD that may be involved in the interactions with fibronectin are found mutated in several cancer cases (unpublished data). Understanding how fibronectin may affect the angiogenic potential of VEGF may help design novel drugs that are more specific, increase their efficacy, and decrease their side effects. Future studies identifying the exact binding sites on all molecular partners, and exploring the consequences of fibronectin binding to the structure and angiogenic signaling of VEGF/VEGFR2 complexes, can open up possibilities for novel therapeutic approaches.

Experimental procedures

Materials

The pFastBac vector (cat. no 10360–014) and the CellFectin transfection reagent were purchased from Invitrogen.

VEGFR2 binding to fibronectin

Ampicillin, kanamycin, chloramphenicol, tetracyclin, and X-Gal were purchased from VWR. Gentamicin and IPTG were purchased from Sigma. The Sf21 TiterHigh AC free cell line (European Collection of Authenticated Cell Culture, cat. no 05030202) was obtained from Sigma. The High Five (BTI-Tn-5B1-4; Hi5) cell line was kindly provided by prof. Ballmer-Hofer at the Paul Scherrer Institute, Switzerland. The insect cell culture medium SF-4 Baculo Express (cat. no 9–00F38-K) was purchased from BioConcept. The 100x Gibco Antibiotic/Antimycotic supplement (containing 10,000 units/ml penicillin, 10,000 μg/ml streptomycin, and 25 μg/ml amphotericin B) was purchased from Thermo Fisher Scientific (cat. no 15240062). The HisTrap Excel, Hi Trap G HP, and S200 10/30 Superdex chromatography columns were from GE Healthcare. Sephadex PD10 MiniTrap G-25 1-ml columns were purchased from Sigma. Glass-bottom 96-well plates were obtained from Life Systems Design (cat. no 324001), and hydrophobic polystyrene F-bottom 96-well plates were from Greiner (cat. no 655 101). The 1-step Turbo TMB substrate was from VWR, and the Clarity ECL chemiluminescence substrate was from BioRad. TGX (4–20% gradient) Stain-Free electrophoresis gels were purchased from BioRad. The Cy3-NHS ester used for protein fluorescence labeling was obtained from Lumiprobe (cat. no 11020). Heparin sodium salt from porcine intestinal mucosa was purchased from Sigma (cat. no H3393). The mouse anti-His (cat. no H1029-2 Ml) and anti-VEGFR (V3003-2 Ml) antibodies were purchased from Sigma. The HRP-conjugated goat anti-mouse secondary antibody (from Jackson Immunolabs) was purchased from MILAN Analytica (cat. no 115–035–003). Human plasma fibronectin was obtained from Millipore (cat. no FC010). The recombinant VEGF$_{165}$ protein, the ECD cDNA, and the DH10beta Embac YFP cells were kindly provided by prof. Ballmer-Hofer at the Paul Scherrer Institute, Switzerland. All other reagents were obtained from Sigma.

Cell culture

The Sf21 *Spodoptera frugipedra* and High Five (Hi5) *Trichoplusia ni* insect cell lines were cultured at 27 °C in the serum-free SF-4 Baculo Express medium, supplemented with 1000 units/ml penicillin, 1000 μg/ml streptomycin, and 0.25 μg/ml amphotericin B. The cultures were maintained in suspension at a density of no more than $2.0 * 10^6$ cells/ml.

Recombinant protein expression and purification

ECD, encompassing the seven domains of the extracellular part of human VEGFR2 and carrying a 6x His Tag at the C-terminus, was cloned in the pFastBac plasmid. DH10beta Embac YFP electrocompetent bacteria were transformed with the ECD/pFastBac plasmid by electroporation and positive colonies were isolated after ampicillin, kanamycin, chloramphenicol, tetracycline, gentamicin, IPTG, and X-Gal selection for bacmid generation. Sf21 cells grown in 6-well plates at a density of $0.5 * 10^6$ cells/ml were transfected with the ECD bacmid using CellFectin according to the manufacturer's instructions, and the secreted virus was harvested from the medium after 48 h incubation at 27 °C (V$_0$). The virus was amplified by infection of suspension Sf21 cell cultures (3 ml of

V$_0$ in a 500-ml culture) at a density of $0.5 * 10^6$ cells/ml. The V$_1$ viral stock ($1.5 * 10^7$ pfu/ml) was harvested 9 days after infection, when 90% of the cells exhibited YFP fluorescence. The virus was amplified a second time by infection of suspension Sf21 cell cultures (10 ml of V$_1$ in a 1-L culture) at a density of $1.0 * 10^6$ cells/ml. The V$_1$ viral stock ($2.2 * 10^8$ pfu/ml) was harvested 4 days after infection, when more than 90% of the cells exhibited YFP fluorescence. Aliquots of the viral stocks were stored at −80 °C.

The V$_2$ viral stock was used for protein production. Suspension Hi5 cultures ($4 * 1$ L) were infected with 10 ml/L of the V$_2$ viral stock at a density of $1.0 * 10^6$ cells/ml. The culture was monitored daily for cell viability and infection (by fluorescence). When more than 90% of the cell population exhibited YFP fluorescence (usually 4 days post infection), the culture medium was collected by centrifugation (5000 x *g* for 15 min at 10 °C), filtered, and loaded on 4-ml HisTrap Excel columns. The His-tagged protein was eluted by applying a linear 0–100% buffer B gradient in 20-column volumes (buffer A: 50 mM Tris, 300 mM NaCl, 10 mM imidazole pH 8.0; buffer B: 50 mM Tris, 300 mM NaCl, 500 mM imidazole pH 8.0). The fractions of the peak were collected, dialyzed against 20 mM Tris, pH 8.0, and loaded on an ion exchange 1-ml HiTrap Q HP column. The proteins bound to the column were eluted applying a linear 0–100% buffer B gradient in 20-column volumes (buffer A: 20 mM Tris, pH 8.0; buffer B: 20 mM Tris, 300 mM NaCl, pH 8.0). The fractions corresponding to the ECD (based on molecular weight by SDS-PAGE analysis) were collected, dialyzed against SEC buffer (50 mM Hepes, 150 mM NaCl, 5% glycerol, pH 7.5), concentrated to 0.5 ml, and loaded on an S200 10/30 Superdex size exclusion column. The proteins were eluted with one-column volume SEC buffer and 0.5 ml fractions were collected. The fractions corresponding to monomeric ECD were pooled, concentrated, and stored at −80°C. Protein storage at 4 °C for 15 days led to slight fragmentation. Protein yields ranged from 10 to 30 μg/L of culture. Protein purity during the sequential chromatographic steps was monitored by SDS-PAGE (Fig. S20).

VEGF$_{165}$ containing an N-terminal 6x His tag, expressed in *Pichia Pastoris*, and purified by immobilized metal affinity and size-exclusion chromatography, was kindly provided by prof. Ballmer-Hofer (Paul Scherrer Institute, Switzerland). Human plasma fibronectin was purchased from EMD Millipore. The purity of both VEGF and fibronectin was assessed by SDS-PAGE (Fig. S20).

ELISA-based binding assay

Fibronectin was added on glass-bottom or hydrophobic polystyrene 96-well plates (20 μg/ml in PBS; 50 μl/well) and was allowed to adsorb overnight at 4 °C. Subsequently, the plate was placed on ice, the solution was aspirated, the adsorbed layer was washed with phosphate-based saline (PBS) (three times; 50 μl/well each time), and was allowed to interact with VEGF or ECD in binding buffer (150 mM NaCl, 25 mM Hepes) at pH 7.5 or 5.5, for 1 h at 4 °C. The solution was then aspirated, the plate was washed with binding buffer (three

times; 50 μl/well each time), and the bound ligand was released with the appropriate extraction buffer. After incubation in the extraction buffer (1 min–1 h), the solution was transferred into a second 96-well polystyrene plate. To ensure complete transfer, an additional 50 μl of the extraction buffer was added to the original wells, pipetted twice up and down, and mixed with the material from the first extraction. The extracted ligand was allowed to adsorb on a new plate for 1 h on ice. Then, the solution was aspirated, the plate was washed with assay buffer (three times; 50 μl/well each time), and was incubated with an anti-His or an anti-VEGFR2 primary antibody for 1 h on ice. The solution was aspirated, the plate was washed with assay buffer (three times; 50 μl/well each time), and was incubated with an HRP-labeled secondary antibody for 1 h on ice. The solution was aspirated, the plate was washed with assay buffer (three times; 50 μl/well each time), and the signal was developed accordingly, for absorbance or chemiluminescence measurements. For absorbance, 50 μl of TMB substrate was added on the plate and incubated for 10 min at room temperature. The reaction was stopped by adding 50 μl 1 M H_2SO_4 and absorbance was measured at 450 nm and 570 nm using a Microplate reader Infinite 200 PRO (Tecan Group AG, Switzerland). The signal at 570 nm, corresponding to light scattering, was subtracted from the signal at 450 nm, corresponding to TMB absorbance, in order to correct for any features from the well bottom interfering with the measurement. For chemiluminescence, 100 μl of ECL substrate was added on the plate, and the luminescence signal was measured after 10 min, applying 1000 ms integration time and automatic gain using a Microplate reader Infinite 200 PRO. The luminescence signal was corrected by subtracting the sum of the signal from the surrounding eight wells multiplied by the correction factor 0.0454, which was determined by repeated measurements of the blanc in different wells, surrounded by samples of different luminescence values (Fig. S6).

Determination of fibronectin desorption

Fibronectin was fluorescently labeled with Cy3 according to standard amine chemistry procedures. Briefly, fibronectin (0.5 mg in 0.1 M NaHCO₃, pH 8.4) was mixed with 20x molar excess of Cy3-NHS dye and was incubated for 1.5 h on ice protected from light. The labeled protein was separated from free dye by size-exclusion column chromatography using 1-ml Sephadex G-25 columns. The protein was eluted in PBS and its concentration and labeling ratio were determined by measuring the absorbance at 280 nm and 550 nm (NanoDrop). Cy3-labeled fibronectin in PBS was added on black polystyrene or glass-bottom 96-well plates and was allowed to adsorb overnight at 4 °C. After the total fluorescence was measured using a Microplate reader Infinite 200 PRO (excitation wavelength = 550 nm; emission wavelength = 595 nm), the solution was aspirated, the adsorbed layer was washed three times with PBS, and then was subjected to a series of incubations (1 h each, on ice) with different buffers (PBS containing 1 mg/ml BSA and 0.05% Tween20 or 5 M NaCl, 25 mM Hepes, pH 7.5). After each incubation, the solution was aspirated,

the protein layer was washed three times with PBS, and fluorescence was measured as above to determine how much fibronectin remained adsorbed on the well surface.

Surface plasmon resonance (SPR) measurements

SPR measurements were performed with a BiaCore X instrument (GE Healthcare) using low-density carboxymethyldextran hydrogel (500 nm) biosensor chips with two flow cells (CDM500 L, Xantec bioanalytics GmbH, Germany). Fibronectin was immobilized on flow cell 2 according to the manufacturer's instructions, while flow cell 1 was used as a reference. Briefly, the chip surface in both flow cells was activated by injecting 70 μl of a 1:1 mixture of 100 mM NHS and 400 mM N-ethyl-N'(dimethylaminopropyl)carbodiimide hydrochloride (EDC) at a flow rate of 5 μl/min. Within 3 min after the surface activation, 70 μl fibronectin was injected on flow cell 2 only (0.2, 2, or 20 μg/ml in 10 mM sodium acetate buffer, pH 5.0) at a flow rate of 5 μl/min. The remaining free carboxyl groups on the surface of both flow cells were inactivated by injecting 70 μl 1 M ethanolamine, pH 8.0 at a flow rate of 5 μl/min. The interaction between immobilized fibronectin and VEGF or ECD was studied in running buffer (150 mM NaCl, 25 mM Hepes, pH 5.5) that had been autoclaved, filtered, and degassed. Different injection volumes (30 or 60 μl) and flow rates (10, 25, 50, and 100 μl/min) were tested, and the final measurements were performed with 60 μl VEGF or ECD (20 nM, 50 nM, 100 nM, 200 nM, 500 nM, and 1000 nM) at 50 μl/min. For assay optimization, only the association part of the sensogram was recorded. For complete analysis of the interaction and model fitting, the dissociation phase was monitored for a total of 720 s. A pretreatment step of the immobilized fibronectin with 1 μg/ml heparin in running buffer (50 μl at 50 μl/min) was included immediately before the VEGF or ECD injections. After each VEGF or ECD injection, the surface was regenerated with 2 M NaCl and 0.05 N NaOH (50 μl each at 50 ml/min). All measurements were performed at room temperature.

Kinetic modeling

The SPR data were analyzed with multiple models to extract kinetic parameters for the interactions between fibronectin and VEGF or ECD. Interestingly, we observed a drop in RU values prior to the nominal end of the association phase (59 ± 12 s for VEGF and 65 ± 10 s for ECD instead of 72 s), which, however, showed no correlation with VEGF/ECD concentration (Fig. S19). Although we cannot exclude the possibility that this may reflect some aspect of the binding interactions, we believe that it is caused by experimental error. Strengthening this conclusion is the fact that such time discrepancies were observed for both flow cells and were seemingly random. In the absence of any solid mechanistic justification for ligand dissociation during the association phase, the kinetic parameters reported here have been extracted using variable dissociation time in all cases. Before describing the individual models, we outline the mass conservation equations on which all further considerations are based. We assume that all VEGF or ECD molecules introduced

in the system either remain in the flow phase or bind to fibronectin that is immobilized on the surface; as a consequence, neglecting all other possible interactions, the total number of VEGF or ECD molecules is conserved.

The mass conservation equations that we used are derived from a two-compartment model developed previously (51), based on the complete description of the kinetic/mass transfer phenomena in an SPR experiment through partial differential equations (PDE). This model, although simpler than the original PDEs, is able to recapitulate accurately the key parameters describing the time evolution of the system. Briefly, the model takes into consideration two compartments: a flowing bulk phase with a time-invariant concentration of ligands (C_T) and a narrow volume slit (V_i) in the proximity of the surface (S) where receptors have been immobilized at an initial concentration R_T (Fig. 6). Ligand molecule exchange occurs between the flowing bulk phase and V_i (mass transfer), as well as between V_i and S (binding/unbinding events). Owing to these phenomena, the ligand concentration in the volume V_i (C), as well as the amount of free (R) and receptor-bound (B) ligand molecules at S, varies with time. Applying the principle of mass conservation to the volume V_i and to the surface S, we obtain the following system of equations:

$$\begin{cases} V_i\dfrac{dC}{dt} = \dot{R}_{in,V_i} - \dot{R}_{out,V_i} + k_m S(C_T - C) \\ S\dfrac{dB}{dt} = \dot{R}_{in,S} - \dot{R}_{out,S} \\ C(t=0) = 0 \\ B(t=0) = 0 \end{cases}$$

In the system above, $\dot{R}_{in,V_i}$ and $\dot{R}_{out,V_i}$ are, respectively, the rates of ligand molecule gain and loss in the volume V_i, as a consequence of binding/unbinding reactions. $\dot{R}_{in,S}$ and $\dot{R}_{out,S}$ refer to the same quantities with respect to the surface S. k_m is the convective mass-transfer coefficient for the exchange of ligand molecules between the flowing bulk and the volume V_i.

It is possible to express the quantities $\dot{R}_{in,V_i}$, $\dot{R}_{out,V_i}$, $\dot{R}_{in,S}$ and $\dot{R}_{out,S}$ in a way that is specific for the surface S:

$$\dot{R}_{in,V_i} = S\widehat{R}_{in,V_i} \; ; \; \dot{R}_{out,V_i} = S\widehat{R}_{out,V_i} \; ; \; \dot{R}_{in,S} = S\widehat{R}_{in,S} \; ; \; \dot{R}_{out,S} = S\widehat{R}_{out,S}$$

The newly defined quantities $\widehat{R}_{in,V_i}$, $\widehat{R}_{out,V_i}$, $\widehat{R}_{in,S}$ and $\widehat{R}_{out,S}$ have molar flux units. Consequently, the system of equations transforms as follows:

$$\begin{cases} V_i\dfrac{dC}{dt} = S\left[\widehat{R}_{in,V_i} - \widehat{R}_{out,V_i} + k_m(C_T - C)\right] \\ S\dfrac{dB}{dt} = S\left[\widehat{R}_{in,S} - \widehat{R}_{out,S}\right] \\ C(t=0) = 0 \\ B(t=0) = 0 \end{cases}$$

It is possible to divide the first equation by V_i and the second by S. The ratio between S and V_i is the reciprocal of the characteristic height (h_i) of the volume slit, where it is assumed that the mass transfer and binding/unbinding phenomena occur. Accordingly, the system of equation is transformed as follows:

$$\begin{cases} \dfrac{dC}{dt} = \dfrac{1}{h_i}\left[\widehat{R}_{in,V_i} - \widehat{R}_{out,V_i} + k_m(C_T - C)\right] \\ \dfrac{dB}{dt} = \widehat{R}_{in,S} - \widehat{R}_{out,S} \\ C(t=0) = 0 \\ B(t=0) = 0 \end{cases}$$

In the case of multiple-site reactions, the second expression in the system can be split into multiple equations, each describing the behavior of a specific reaction site.

Below, we present in detail the different models that have been used for fitting the experimental data (Fig. 6). In all models, the term receptor corresponds to the monomeric chain of each fibronectin dimer and the term ligand to VEGF or ECD.

One-site model

This is the simplest model, assuming one population of receptor molecules, with each receptor molecule possessing one ligand-binding site. We keep the same nomenclature outlined before for the binding sites of the free (R) and ligand-bound (B) receptor molecules, and we describe the ligand–receptor interactions using single association (k_a) and dissociation (k_d) kinetic constants. Consequently:

$$\widehat{R}_{in,V_i} = \widehat{R}_{out,S} = k_d B$$

$$\widehat{R}_{in,S} = \widehat{R}_{out,V_i} = k_a C R = k_a C(R_T - B)$$

The system of equation becomes:

$$\begin{cases} \dfrac{dC}{dt} = \dfrac{1}{h_i}\left[-k_a C(R_T - B) + k_d B + k_m(C_T - C)\right] \\ \dfrac{dB}{dt} = +k_a C(R_T - B) - k_d B \\ C(t=0) = 0 \\ B(t=0) = 0 \end{cases}$$

Two-sites model

This model assumes two populations of receptor molecules with surface concentrations $R_{T,1} = \alpha R_T$ and $R_{T,2} = (1 - \alpha)R_T$, respectively, with α ranging from 0 to 1. Each receptor molecule possesses a single ligand-binding site, as in the one-site model, but with distinct association ($k_{a,1}$ and $k_{a,2}$) and

dissociation ($k_{d,1}$ and $k_{d,2}$) rates. Ligand binding to receptor molecules belonging to either of the two populations (R_1 and R_2) occurs independently, generating molecular species B_1 and B_2. Thus, the second equation of the system that describes the evolution of the ligand-bound receptors is split into two different equations, one for each receptor population. The kinetic terms can be described as follows:

$$\dot{R}_{in,V_i} = k_{d,1}B_1 + k_{d,2}B_2$$

$$\dot{R}_{out,V_i} = k_{a,1}CR_1 + k_{a,2}CR_2 = k_{a,1}C(R_{T,1} - B_1) + k_{a,2}C(R_{T,2} - B_2)$$

$$\dot{R}_{in,S,1} = k_{a,1}CR_1 = k_{a,1}C(R_{T,1} - B_1)$$

$$\dot{R}_{in,S,2} = k_{a,2}CR_2 = k_{a,2}C(R_{T,2} - B_2)$$

$$\dot{R}_{out,S,1} = k_{d,1}B_1$$

$$\dot{R}_{out,S,2} = k_{d,2}B_2$$

Therefore, the system of equations becomes:

$$
\begin{cases}
\dfrac{dC}{dt} = \dfrac{1}{h_i}\big[-k_{a,1}C(R_{T,1}-B_1) - k_{a,2}C(R_{T,2}-B_2) \\
\qquad\qquad + k_{d,1}B_1 + k_{d,2}B_2 + k_m(C_T - C)\big] \\
\dfrac{dB_1}{dt} = k_{a,1}C(R_{T,1}-B_1) - k_{d,1}B_1 \\
\dfrac{dB_2}{dt} = k_{a,2}C(R_{T,2}-B_2) - k_{d,2}B_2 \\
C(t=0) = 0 \\
B_1(t=0) = 0 \\
B_2(t=0) = 0
\end{cases}
$$

Parallel reactions model

This model assumes that each receptor molecule possesses two ligand-binding sites that act independently. From a modeling perspective, this scenario can be treated as a special case of the two-sites model, where $R_{T,1} = R_{T,2} = R_T/2$ and $\alpha = 0.5$. Therefore, we used the same system of equations as for the two-sites model under these restrictions.

Consecutive reactions model

This model also assumes that each receptor molecule possesses two ligand-binding sites, but in contrast to the parallel reactions model, the binding sites do not act independently; instead, the first binding event is required before the second binding can occur. In this case, we do not consider the concentration of binding sites (B_1 and B_2) as was done in the other cases, but instead, the concentration of the various molecular species of the receptor: free (R), bound to the first ligand (R_A), and bound to the second ligand (R_{2A}), with $R_T = R + R_A + R_{2A}$. We consider the most general case, whereby the two

binding events occur with distinct association and dissociation rates: $k_{a,R}$ and k_{d,R_A} for the first reaction (R to R_A), and k_{a,R_A} and $k_{d,R_{2A}}$ for the second (R_A to R_{2A}). As for the two-sites model, the second equation of the system has to be split in multiple equations to describe the behavior of each molecular species. Then, the kinetic terms can be computed as follows:

$$\dot{R}_{in,V_i} = k_{d,R_A}R_A + k_{d,R_{2A}}R_{2A}$$

$$\dot{R}_{out,V_i} = k_{a,R}CR + k_{a,R_A}CR_A$$

$$\dot{R}_{in,S,R} = k_{d,R_A}R_A$$

$$\dot{R}_{out,S,R} = k_{a,R}CR$$

$$\dot{R}_{in,S,R_A} = k_{a,R}CR + k_{d,R_{2A}}R_{2A}$$

$$\dot{R}_{out,S,R_A} = k_{a,R_A}CR_A + k_{d,R_A}R_A$$

$$\dot{R}_{in,S,R_{2A}} = k_{a,R_A}CR_A$$

$$\dot{R}_{out,S,R_{2A}} = k_{d,R_{2A}}R_{2A}$$

Accordingly, the final system of equations becomes:

$$
\begin{cases}
\dfrac{dC}{dt} = \dfrac{1}{h_i}\big[k_{d,R_A}R_A + k_{d,R_{2A}}R_{2A} - k_{a,R}CR - k_{a,R_A}CR_A + k_m(C_T - C)\big] \\
\dfrac{dR}{dt} = -k_{a,R}CR + k_{d,R_A}R_A \\
\dfrac{dR_A}{dt} = k_{a,R}CR + k_{d,R_{2A}}R_{2A} - k_{a,R_A}CR_A - k_{d,R_A}R_A \\
\dfrac{dR_{2A}}{dt} = k_{a,R_A}CR_A - k_{d,R_{2A}}R_{2A} \\
C(t=0) = 0 \\
R(t=0) = R_T \\
R_A(t=0) = 0 \\
R_{2A}(t=0) = 0
\end{cases}
$$

Solution of the system of ordinary differential equations (ODEs) and optimization of the parameter values

The free parameters to be determined for each model are shown in Table 4. For the parameter h_i, we used a fixed value of 10^{-5} m, which is a reasonable approximation based on the characteristic size of the SPR microfluidics chip. Moreover, results from a previous study (51) show that the solutions of the equations describing an SPR experiment are insensitive to the value of h_i, which was also true here (data not shown). The values of the free parameters were determined by fitting the experimental data. To avoid overfitting, the experimental curves collected at different values of C_T were fitted simultaneously (global fitting). During the association phase, the values of C_T were considered equal to the experimental ones,

VEGFR2 binding to fibronectin

whereas at the beginning of the dissociation phase was set to zero. The units of the experimental data (RU) were converted to mol/m^2, based on previously reported assumptions (51), using the following equation:

$$L(RU) = L\left(\frac{mol}{m^2}\right) \cdot 10^{-4} \left(\frac{m^2}{cm^2}\right) \cdot MW \left(\frac{g}{mol}\right) \cdot 10^{10} \frac{RU}{g/cm^2}$$

MW represents the molecular weight of the ligand and is equal to 45 or 83 g/mol for VEGF or ECD, respectively. L represents the total ligand surface concentration and is calculated for the different models as follows:

$$L = B \ (One-site \ model)$$

$$L = B_1 + B_2 \ (Two-sites \ model; \ Parallel \ reactions \ model)$$

$$L = R_A + 2R_{2A} \ (Consecutive \ reactions \ model)$$

The ordinary differential equations were discretized and solved using the explicit Euler method, with a time interval of $dt = 10^{-2} \ s$. Given an initial set of parameter estimates, the ordinary differential equations system was solved and the output was compared with the experimental results. Unconstrained fitting was performed in Matlab using the function *lsqcurvefit*, which minimizes the following quantity:

$$F = \sum_{C_T} \sum_t \left(L_{exp}(C_T, t) - L_{mod}(C_T, t)\right)^2$$

L_{exp} and L_{mod} represent the total ligand surface concentration as derived from the experimental data or the fitted model, respectively. The summation is performed over the time points of a single data set (inner sum) and over different data sets collected at different values of C_T (outer sum).

The solution of the system can be performed according to two different scenarios. The first scenario consists in considering mass transfer limitations. In such a case, the systems of equations are identical with the ones explained above. The second scenario assumes mass transfer not to be limiting (rapid mixing): ligand exchange between the flowing bulk and the volume V_i is faster that the characteristic binding/unbinding timescales. Under such an assumption, $C = C_T$ replaces the first equation in all the systems discussed in the previous paragraphs.

Statistical analysis of curve fitting

The experimental data were fitted with all four models (one-site, two-sites, parallel reactions, and consecutive reactions model), under conditions of rapid mixing or mass transfer. The beginning of the dissociation phase was set to the maximum RU value achieved during the association phase (variable dissociation time). To ensure as much as possible that the solution did not represent a local minimum, the following strategy was adopted for all cases: the fitting was repeated multiple times, with sets of initial values for the free parameters that differed by several orders of magnitude. Considering all curves in the data set (with different C_T values), the residual sum of squares (RMS) was calculated for each solution as the sum of the squared residuals (difference between experimental and fitted value), and the solution with the lowest RMS value was selected. Confidence intervals were then calculated for each of the estimated parameters based on the residual values and the Jacobian matrix, using the *nlparci* Matlab function. Solutions for which the confidence intervals for one or more of the parameters were as large as to include negative values were rejected, indicating overfitting, and that the corresponding model could not be used to fit the data. For each model that gave a solution with well-defined confidence intervals for all estimated free parameters (Table S2), the following equations were used to calculate various goodness-of-fit indices, where Δ denotes the value of the residuals, n the number of experimental points, and p the number of model parameters:

1. Residual sum of squares: $RMS = \sum \Delta^2$

2. Residual variance: $\sigma^2 = \frac{\sum \Delta^2}{n-2}$

3. Akaike's Information Criterion: $AIC = n \cdot \log(\sigma^2) + 2 \cdot p \cdot \frac{n}{n-p-1}$

To assess the fitting, the absolute and relative values of these indices were examined (Table 2). Traditionally, the residual variance (corresponding to what is often termed as Chi square in the SPR literature) is used to assess the goodness of fit in SPR experiments. However, it is difficult to define absolute cutoff values, primarily because the residual variance depends on the level of the average signal. Usually, the fit can be considered acceptable when the square root of the residual variance is comparable to the level of experimental noise (52). To estimate the levels of experimental noise, the dose–response experiments were repeated three times using the same chip and injecting the different VEGF/ECD concentrations in a random order to ensure that the data were free of any systematic errors. The patterns were very similar in replicate experiments, but the absolute values were associated with an experimental error of 6–39% (corresponding to 3–24 RU) for ECD and 15–49% (corresponding to 7–18 RU) for VEGF (Fig. S18). This level of experimental error, significantly higher than that of the baseline fluctuations (4%), might have originated from pipetting errors during dilution and injection, as well as stochastic events during binding in both flow cells. Considering this level of noise, all fits, despite their discrepancies with the experimental data, could be acceptable based

on the residual variance values. However, not all fits could be considered equivalent. According to information theory, the Akaike's information criterion (AIC) can be used for model selection among different models that can fit a certain data set, combining absolute fit with model parsimony (53). In other words, it penalizes for the addition of parameters to the model in order to improve absolute fit. The model with the lower AIC is considered the best describing the data in question (53). According to this criterion, the models generating the best overall fit for the data were the consecutive reactions model for VEGF and the two-sites model for ECD. However, the two-sites model generated curves that resembled more closely the shape of the experimental curves for VEGF (Fig. S15); therefore, the two-sites model was also chosen to describe VEGF binding to fibronectin, even though, according to AIC, it was the second best model regarding overall fit.

Circular dichroism spectroscopy

CD spectra of VEGF, ECD, and complexes between VEGF and ECD were acquired with a J-815 spectrometer (JASCO) with a quartz cuvette and with a path length of 10 mm. Data were collected at 4 °C in the 250–205 nm wavelength range with a 0.2 nm data pitch, standard sensitivity (100 mdeg), 1 s digital integration time (D.I.T.), 1 nm bandwidth, and 20 nm/min scanning speed under a continuous scanning mode. The average spectrum of five sequential measurements (accumulation = 5) was used for processing. The baseline of each buffer was acquired using the same measurement parameters and was subtracted from each spectrum. The data were converted from mdeg to mean residue ellipticity using the molecular weight of each protein or protein complex: 45 kDa for VEGF, 83 kDa for ECD, and 211 kDa for the ECD/VEGF complex. CD measurements were performed in 150 mM NaCl, 25 mM Hepes, pH 7.5 or 5.5 (binding buffer) or in 10 mM sodium phosphate buffer, pH 7.4 or 5.8 (low ionic strength buffer).

Bioinformatics analysis

Structure predictions of pKa values of individual amino acid residues at the surface of VEGF, ECD, and the FNIII 12–14 domains of fibronectin were performed with the DelPhiPKa web server, using the known high-resolution structures of VEGF, ECD, and FNIII 12–14 fragments (pdb codes: 2VPF and 2VGH for VEGF, 3V2A, 2X1W, 2X1X, 3S35, 3S36, 3S37, 5OYJ, and 3KVQ for ECD, and 1FNH and 3R8Q for the FNIII 12–14 fibronectin domains). The parameters used for the prediction were those that gave the best results on a benchmark study against an extensive database of experimentally determined pKa values: $\sigma = 0.70$, $\varepsilon_{ref} = 8$, $\varepsilon_{ext} = 80$. Three different force fields were tested: AMBER, CHARMM, and PARSE, yielding very similar results (data not shown). The pKa values reported were calculated using the AMBER force field. According to the calculated pKa values, titration simulations were performed to calculate the probability of ionization of each residue at pH 7.5 and 5.5 assuming two microstates: protonated and deprotonated.

Data availability

All data used for this study are presented in this article in the form of graphs or tables. Raw data, as well as the Matlab source code used for fitting the various models on the SPR data, will be available upon request to the corresponding author: Maria Mitsi, maria.mitsi@alumni.ethz.ch, current affiliation: Ectica Technologies, Switzerland.

References

1. Singh, P., Carraher, C., and Schwarzbauer, J. E. (2010) Assembly of fibronectin extracellular matrix. *Annu. Rev. Cell Dev. Biol.* **26**, 397–419
2. Mezzenga, R., and Mitsi, M. (2019) The molecular dance of fibronectin: Conformational flexibility leads to functional versatility. *Biomacromolecules* **20**, 55–72
3. George, E. L., Baldwin, H. S., and Hynes, R. O. (1997) Fibronectins are essential for heart and blood vessel morphogenesis but are dispensable for initial specification of precursor cells. *Blood* **90**, 3073–3081
4. Stenzel, D., Lundkvist, A., Sauvaget, D., Busse, M., Graupera, M., van der Flier, A., Wijelath, E. S., Murray, J., Sobel, M., Costell, M., Takahashi, S., Fassler, R., Yamaguchi, Y., Gutmann, D. H., Hynes, R. O., *et al.* (2011) Integrin-dependent and -independent functions of astrocytic fibronectin in retinal angiogenesis. *Development* **138**, 4451–4463
5. Chiu, C.-H., Chou, C.-W., Takada, S., and Liu, Y.-W. (2012) Development and fibronectin signaling requirements of the zebrafish interrenal vessel. *PLoS One* **7**, e43040

6. Childs, S., Chen, J.-N., Garrity, D. M., and Fishman, M. C. (2002) Patterning of angiogenesis in the zebrafish embryo. *Development* **129**, 973–982

7. Mitsi, M., Hong, Z., Costello, C. E. E., and Nugent, M. A. (2006) Heparin-mediated conformational changes in fibronectin expose vascular endothelial growth factor binding sites. *Biochemistry* **45**, 10319–10328

8. Wijelath, E. S., Rahman, S., Namekata, M., Murray, J., Nishimura, T., Mostafavi-Pour, Z., Patel, Y., Suda, Y., Humphries, M. J., and Sobel, M. (2006) Heparin-II domain of fibronectin is a vascular endothelial growth factor-binding domain: Enhancement of VEGF biological activity by a singular growth factor/matrix protein synergism. *Circ. Res.* **99**, 853–860

9. Derricks, K. E., Trinkaus-Randall, V., and Nugent, M. A. (2015) Extracellular matrix stiffness modulates VEGF calcium signaling in endothelial cells; individual cell and population analysis. *Integr. Biol.* **7**, 1011–1025

10. Holmes, D. I. R., and Zachary, I. (2005) The vascular endothelial growth factor (VEGF) family: Angiogenic factors in health and disease. *Genome Biol.* **6**, 209

11. Grunstein, J., Masbad, J. J., Hickey, R., Giordano, F., and Johnson, R. S. (2000) Isoforms of vascular endothelial growth factor act in a coordinate fashion to recruit and expand tumor vasculature. *Mol. Cell. Biol.* **20**, 7282–7291

12. Goerges, A. L., and Nugent, M. A. (2004) pH regulates vascular endothelial growth factor binding to fibronectin: A mechanism for control of extracellular matrix storage and release. *J. Biol. Chem.* **279**, 2307–2315

13. Martino, M. M., and Hubbell, J. A. (2010) The 12th-14th type III repeats of fibronectin function as a highly promiscuous growth factor-binding domain. *Faseb J.* **24**, 4711–4721

14. Mitsi, M., Forsten-Williams, K., Gopalakrishnan, M., and Nugent, M. A. (2008) A catalytic role of heparin within the extracellular matrix. *J. Biol. Chem.* **283**, 34796–34807

15. Akerman, S., Fisher, M., Daniel, R. A., Lefley, D., Reyes-Aldasoro, C. C., Lunt, S. J., Harris, S., Bjorndahl, M., Williams, L. J., Evans, H., Barber, P. R., Prise, V. E., Vojnovic, B., Kanthou, C., and Tozer, G. M. (2013) Influence of soluble or matrix-bound isoforms of vascular endothelial growth factor-A on tumor response to vascular-targeted strategies. *Int. J. Cancer.* **133**, 2563–2576

16. Park, J. E., Keller, G., and Ferrara, N. (1993) The vascular endothelial growth factor (VEGF) Isoforms: Differential deposition into the subepithelial extracellular matrix and bioactivity of extracellular matrixbound VEGF. *Mol. Biol. Cell.* **4**, 1317–1326

17. Saint-Geniez, M., Kurihara, T., and D'Amore, P. A. (2009) Role of cell and matrix-bound VEGF isoforms in lens development. *Invest. Ophthalmol. Vis. Sci.* **50**, 311–321

18. Small, A. R., Neagu, A., Amyot, F., Sackett, D., Chernomordik, V., and Gandjbakhche, A. (2008) Spatial distribution of VEGF isoforms and chemotactic signals in the vicinity of a tumor. *J. Theor. Biol.* **252**, 593–607

19. Ruhrberg, C., Gerhardt, H., Golding, M., Watson, R., Ioannidou, S., Fujisawa, H., Betsholtz, C., and Shima, D. T. (2002) Spatially restricted patterning cues provided by heparin-binding VEGF-A control blood vessel branching morphogenesis. *Genes Dev.* **16**, 2684–2698

20. Chen, T. T., Luque, A., Lee, S., Anderson, S. M., Segura, T., and Iruela-Arispe, M. L. (2010) Anchorage of VEGF to the extracellular matrix conveys differential signaling responses to endothelial cells. *J. Cell Biol.* **188**, 595–609

21. Sack, K. D., Teran, M., and Nugent, M. A. (2016) Extracellular matrix stiffness controls VEGF signaling and processing in endothelial cells. *J. Cell. Physiol.* **231**, 2026–2039

22. Stuttfeld, E., and Ballmer-Hofer, K. (2009) Structure and function of VEGF receptors. *IUBMB Life* **61**, 915–922

23. Roskoski, R., Jr. (2008) VEGF receptor protein-tyrosine kinases: Structure and regulation. *Biochem. Biophys. Res. Commun.* **375**, 287–291

24. Ferrara, N. (2009) VEGF-A: A critical regulator of blood vessel growth. *Eur. Cytokine Netw.* **20**, 158–163

25. Grünewald, F. S., Prota, A. E., Giese, A., and Ballmer-Hofer, K. (2010) Structure-function analysis of VEGF receptor activation and the role of coreceptors in angiogenic signaling. *Biochim. Biophys. Acta - Proteins Proteomics* **1804**, 567–580

26. Ballmer-Hofer, K., Andersson, A. E., Ratcliffe, L. E., and Berger, P. (2011) Neuropilin-1 promotes VEGFR-2 trafficking through Rab11 vesicles thereby specifying signal output. *Blood* **118**, 816–826

27. Gitay-Goren, H., Soker, S., Vlodavsky, I., and Neufeld, G. (1992) The binding of vascular endothelial growth factor to its receptors is dependent on cell surface-associated heparin-like molecules. *J. Biol. Chem.* **267**, 6093–6098

28. Soldi, R., Mitola, S., Strasly, M., Defilippi, P., Tarone, G., and Bussolino, F. (1999) Role of alphavbeta3 integrin in the activation of vascular endothelial growth factor receptor-2. *Embo J.* **18**, 882–892

29. Byzova, T. V., Goldman, C. K., Pampori, N., Thomas, K. A., Bett, A., Shattil, S. J., and Plow, E. F. (2000) A mechanism for modulation of cellular responses to VEGF: Activation of the integrins. *Mol. Cell* **6**, 851–860

30. Carmeliet, P., and Jain, R. K. (2000) Angiogenesis in cancer and other diseases. *Nature* **407**, 249–257

31. Teleanu, R. I., Chircov, C., Grumezescu, A. M., and Teleanu, D. M. (2019) Tumor angiogenesis and anti-angiogenic strategies for cancer treatment. *J. Clin. Med.* **9**, 84

32. Lupo, G., Caporarello, N., Olivieri, M., Cristaldi, M., Motta, C., Bramanti, V., Avola, R., Salmeri, M., Nicoletti, F., and Anfuso, C. D. (2017) Anti-angiogenic therapy in cancer: Downsides and new pivots for precision medicine. *Front. Pharmacol.* **7**, 519

33. Finley, S. D., and Popel, A. S. (2012) Predicting the effects of anti-angiogenic agents targeting specific VEGF isoforms. *AAPS J.* **14**, 500–509

34. Micsonai, A., Wien, F., Kernya, L., Lee, Y. H., Goto, Y., Réfrégiers, M., and Kardos, J. (2015) Accurate secondary structure prediction and fold recognition for circular dichroism spectroscopy. *Proc. Natl. Acad. Sci. U. S. A.* **112**, E3095–E3103

35. Wang, L., Zhang, M., and Alexov, E. (2016) DelPhiPKa web server: Predicting pKa of proteins, RNAs and DNAs. *Bioinformatics* **32**, 614–615

36. Watanabe, H., Yoshida, C., Ooishi, A., Nakai, Y., Ueda, M., Isobe, Y., and Honda, S. (2019) Histidine-mediated intramolecular electrostatic repulsion for controlling pH-dependent protein–protein interaction. *ACS Chem. Biol.* **14**, 2729–2736

37. Charafeddine, R. A., Cortopassi, W. A., Lak, P., Tan, R., McKenney, R. J., Jacobson, M. P., Barber, D. L., and Wittmann, T. (2019) Tau repeat regions contain conserved histidine residues that modulate microtubule-binding in response to pH. *J. Biol. Chem.* **294**, 8779–8790

38. Watanabe, H., Matsumaru, H., Ooishi, A., Feng, Y., Odahara, T., and Suto, K. (2009) Optimizing pH response of affinity between protein G and IgG Fc: How electrostatic modulations affect protein-protein interactions. *J. Biol. Chem.* **284**, 12373–12383

39. Di Russo, N. V., Estrin, D. A., Martí, M. A., and Roitberg, A. E. (2012) pH-dependent conformational changes in proteins and their effect on experimental pK(a)s: The case of Nitrophorin 4. *PLoS Comput. Biol.* **8**, e1002761

40. Peng, Y., and Alexov, E. (2017) Computational investigation of proton transfer, pKa shifts and pH-optimum of protein–DNA and protein–RNA complexes. *Proteins* **85**, 282–295

41. Gopalakrishnan, M., Forsten-Williams, K., Cassino, T. R., Padro, L., Ryan, T. E., and Täuber, U. C. (2005) Ligand rebinding: Self-consistent mean-field theory and numerical simulations applied to surface plasmon resonance studies. *Eur. Biophys. J.* **34**, 943–958

42. Cébe-Suarez, S., Zehnder-Fjällman, A., and Ballmer-Hofer, K. (2006) The role of VEGF receptors in angiogenesis; complex partnerships. *Cell. Mol. Life Sci.* **63**, 601–615

43. Lagerholm, B. C., and Thompson, N. L. (1998) Theory for ligand rebinding at cell membrane surfaces. *Biophys. J.* **74**, 1215–1228

ASBMB

44. Berg, H. C., and Purcell, E. M. (1977) Physics of Chemoreception. *Biophys. J.* **20**, 193–219

45. Schwarzbauer, J. E. (1991) Alternative splicing of fibronectin: Three variants, three functions. *BioEssays* **13**, 527–533

46. Airley, R. E., and Mobasheri, A. (2007) Hypoxic regulation of glucose transport, anaerobic metabolism and angiogenesis in cancer: Novel pathways and targets for anticancer therapeutics. *Chemotherapy* **53**, 233–256

47. Wike-Hooley, J. L., Haveman, J., and Reinhold, H. S. (1984) The relevance of tumour pH to the treatment of malignant disease. *Radiother. Oncol.* **2**, 343–366

48. Buczek-Thomas, J. A., Rich, C. B., and Nugent, M. A. (2019) Hypoxia induced heparan sulfate primes the extracellular matrix for endothelial cell recruitment by facilitating VEGF-fibronectin interactions. *Int. J. Mol. Sci.* **20**, 5065

49. Pahari, S., Sun, L., and Alexov, E. (2019) Surface-free protocol for computing PKA's (DelPhiPKa): Applications to protein-protein interactions. *Biophys. J.* **116**, 166a

50. Williams, E. C., Janmey, P. A., Ferry, J. D., and Mosher, D. F. (1982) Conformational states of fibronectin. Effects of pH, ionic strength, and collagen binding. J. Biol. Chem. **257**, 14973–14978

51. Myszka, D. G., He, X., Dembo, M., Morton, T. A., and Goldstein, B. (1998) Extending the range of rate constants available from BIACORE: Interpreting mass transport-influenced binding data. *Biophys. J.* **75**, 583–594

52. Onell, A., and Andersson, K. (2005) Kinetic determinations of molecular interactions using Biacore - minimum data requirements for efficient experimental design. *J. Mol. Recognit.* **18**, 307–317

53. Maydeu-Olivares, A., and Garcia-Forero, C. (2010) Goodness-of-Fit testing. *Int. Encycl. Educ.* **7**, 190–196

VEGF and VEGFR2 bind to similar pH-sensitive sites on fibronectin, exposed by heparin-mediated conformational changes

Mattia Usuelli[1], Timmy Meyer[1], Raffaele Mezzenga[1#], Maria Mitsi[1*]

[1]Laboratory of Food and Soft Materials, Department of Health Sciences and Technology, ETH Zurich, Zurich, Switzerland

*Corresponding author: Maria Mitsi
E-mail: maria.mitsi@alumni.ethz.ch

#Co-corresponding author: Raffaele Mezzenga
E-mail: raffaele.mezzenga@hest.ethz.ch

Running title: VEGFR2 binding to fibronectin

I.   Development and optimization of an ELISA-based binding assay (Figures S1-S6; Table S1)

Initially, we attempted to detect the fibronectin-bound ligand directly, using an appropriate primary antibody and an HRP-labeled secondary antibody. We found that the addition of both BSA (1 mg/ml) and Tween20 (0.05%) was necessary and sufficient to suppress the non-specific binding of the antibodies on the plate surface and the adsorbed protein layers (Fig. S1). However, successive incubations with these blocking agents led to significant fibronectin desorption from the polystyrene plate surface (Fig. S2). On the contrary, fibronectin adsorption was much more stable on glass plates, where successive incubations with the BSA and Tween20 containing buffer had no effect (Fig. S2). Thus, we performed the binding assays on glass plates.

To recapitulate earlier observations (ref. 7 in the main text), VEGF binding was tested at two different pH values (pH 7.5 and 5.5) with or without pre-treatment of the adsorbed fibronectin with heparin. However, the non-specific binding of VEGF on the plate surface was very high under all conditions. The amount of adsorbed VEGF on the naked glass substrate was almost the same as that on fibronectin or a number of blocking proteins, including bovine serum albumin (BSA), egg-white albumin, and beta-lactoglobulin (Fig. S3). High concentrations of gelatin reduced VEGF non-specific binding by approximately 50% but this was still not sufficient to uncover the specific VEGF-fibronectin interactions, especially when higher VEGF concentrations were tested (Fig. S3). We attempted to reduce VEGF adsorption on non-specific binding sites by adding blocking proteins (BSA or milk) and detergents (Tween20) in the buffer during binding. The combination of milk and Tween20 worked very well at neutral pH (pH 7.5), but at acidic pH (pH 5.5) had a limited effect (Fig. S4). In a final attempt, we combined the blocking properties of gelatin as a substrate and milk as an additive in the binding buffer. We performed the assay on fibronectin adsorbed on a gelatin gel (several mm in thickness) polymerized inside the plate wells using 20% gelatin in water. However, the gelatin gel itself gave high background values, resulting in negative results and very large errors, preventing its further use (data not shown).

Since we were unable to reduce the non-specific binding of VEGF on the plate, we followed an indirect approach in order to detect the specifically-bound VEGF to surface-immobilized fibronectin. According to a previous study (ref. 7 in the main text), incubation with a high ionic strength solution (5 M NaCl)

1

could release fibronectin-bound VEGF. Thus, we added to the assay an additional extraction step with 5 M NaCl, followed by re-adsorption of the released VEGF on a second plate and detection by ELISA. Since in this assay format the adsorbed fibronectin does not come in contact with the ELISA blocking buffers containing BSA and Tween20, which would lead to its desorption from polystyrene plates, there was no further need to use glass plates for the assay. Instead, we used hydrophobic polystyrene plates, on which, as reported earlier (ref. 7 in the main text), adsorbed fibronectin adopts a compact conformation, and is amenable to structural regulation by heparin. We confirmed that the 5 M NaCl extraction did not lead to any fibronectin desorption from the polystyrene plate (Fig. S5). Additionally, we switched the detection method to luminescence, which exhibited a larger linear range for VEGF detection (Fig. S6).
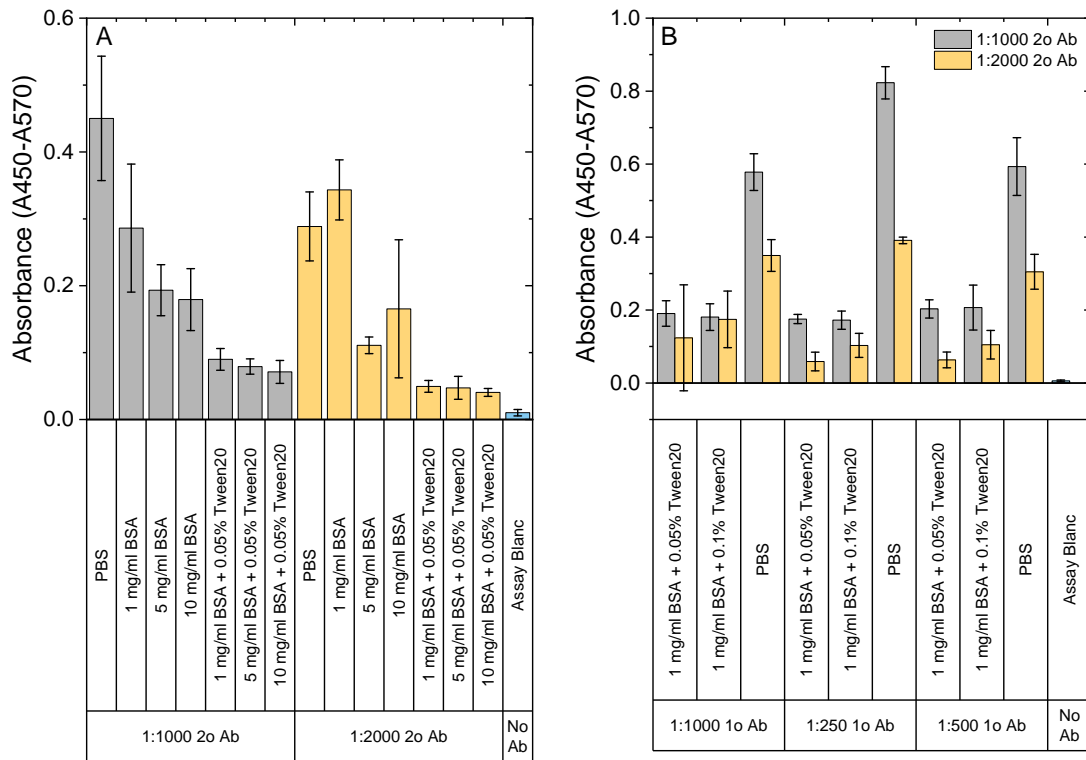
Figure S1. The combination of BSA and Tween20 is necessary and sufficient to suppress antibody non-specific binding. Fibronectin (20 µg/ml; 50 µl/well) was adsorbed on glass-bottom 96-well plates overnight at 4 °C, and was incubated for 1 h with the HRP-labeled anti-mouse secondary antibody (2o Ab) alone (A) or after a 1-h incubation with the anti-His mouse primary antibody (1o Ab) (B). The antibodies were diluted in PBS without any blocking agent or in PBS containing BSA (1, 5, or 10 mg/ml) in the absence or presence of Tween20 (0.05%). The dilution ratios tested were 1:1000 (gray bars) and 1:2000 (ochre bars) for the secondary antibody, and 1:250, 1:500, and 1:1000 for the primary antibody. Quadruplicate samples were measured, and the data are presented as mean values +/- standard deviation. The blanc value of the assay (adsorbed fibronectin with no antibody added) is also shown for comparison (light blue bar). The addition of Tween20 significantly decreased the non-specific binding of the secondary antibody at both dilutions tested, and had a more pronounced effect than increasing the amount of BSA, even by 10 fold (A). Furthermore, the combination of 1 mg/ml BSA and 0.05% Tween20 was able to suppress the non-specific binding of the primary antibody as well, even at the lowest dilution tested (B). Consequently, all ELISA assays were performed in this buffer (1 mg/ml BSA + 0.05% Tween20 in PBS).

3
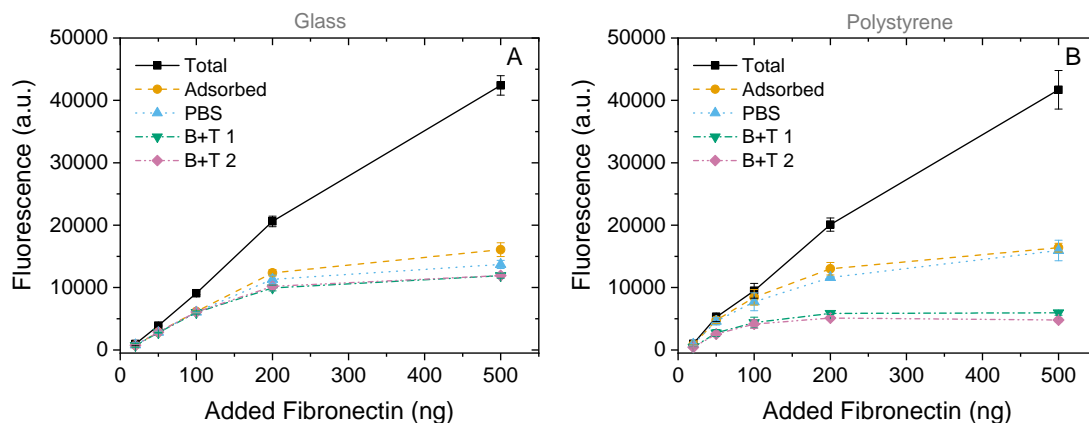
Figure S2. The ELISA blocking buffer containing 1 mg/ml BSA and 0.05% Tween20 (B + T) leads to fibronectin desorption from polystyrene but not from glass. Cy3-labeled fibronectin (20 - 500 ng) was adsorbed on glass-bottom (50 µl/well; A) or half-area black polystyrene (25 µl/well; B) 96-well plates overnight at 4 °C. Fluorescence was measured with a microplate reader (excitation wavelength = 550 nm; emission wavelength = 595 nm) following adsorption (total; black squares), after aspirating the solution and washing the protein layer 3 times with PBS (adsorbed; ochre circles), after 1-h incubation with PBS (PBS, light blue triangles), after 1 h incubation with the ELISA blocking buffer (B + T 1; green inverted triangles), and after a second 1-h incubation with the ELISA blocking buffer (B + T 2; pink rhombuses). Samples were measured in triplicate, and the data are presented as mean values +/- standard deviation.
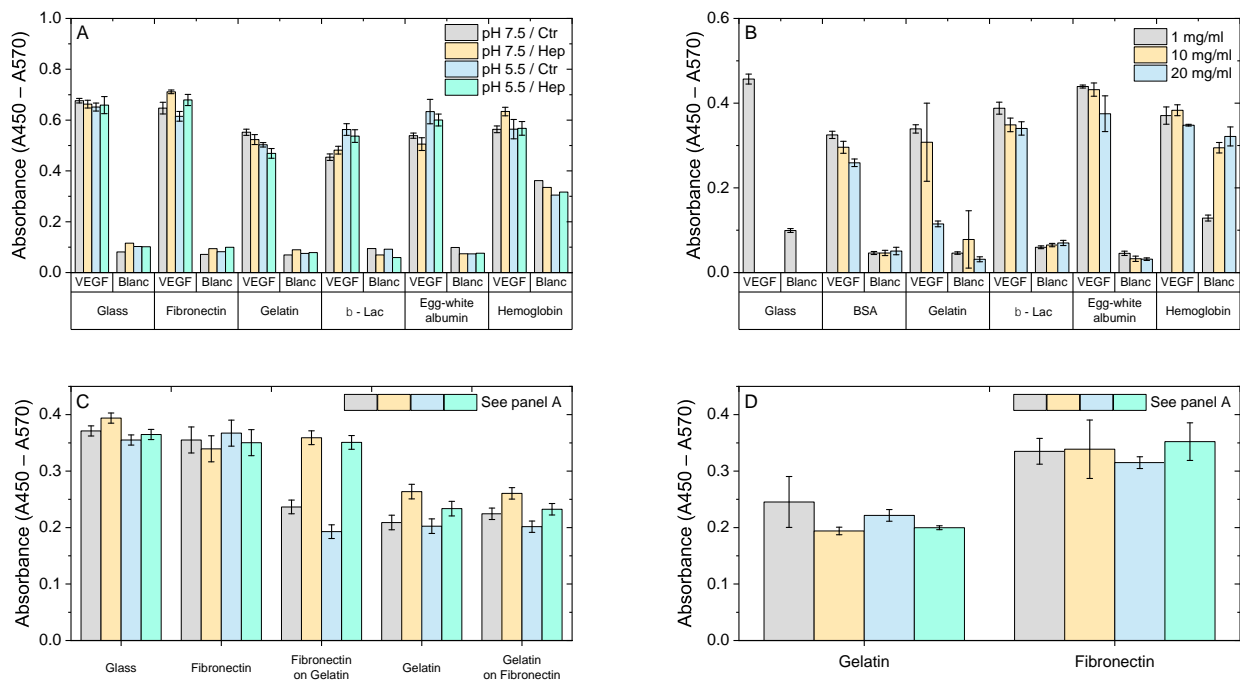
Figure S3. Adsorption of blocking proteins on the assay plate does not reduce non-specific VEGF binding. (A) Fibronectin (20 µg/ml; 50 µl/well) or a series of blocking proteins (1 mg/ml; 50 µl/well) were adsorbed on glass-bottom 96-well plates overnight at 4 °C. Gelatin, beta-lactoglobulin (β-Lac), egg-white albumin, and hemoglobin were tested. The plate was incubated with VEGF (5 µg/ml) in binding buffer (150 mM NaCl, 25 mM Hepes) at pH 7.5 (grey and ochre bars) or 5.5 (light blue and light green bars), in the presence (ochre and light green bars) or absence (grey and light blue bars) of pre-treatment of the adsorbed proteins with 100 µg/ml heparin in PBS. Bound VEGF was detected by ELISA with an anti-His primary antibody (1:1000) and an HRP-labeled secondary antibody (1:2000). Both antibody incubations were performed in ELISA blocking buffer (1 mg/ml BSA + 0.05% Tween20 in PBS). Samples were measured in triplicate, and the data are presented as mean values +/- standard deviation. VEGF adsorption on naked glass, as well as the blanc value of the assay (no antibody added) for each adsorbed protein are shown for comparison. (B) Increasing concentrations (1 mg/ml, grey bars; 10 mg/ml, ochre bars; and 20 mg/ml, light blue bars) of all the blocking proteins used in (A) plus bovine serum albumin (BSA) were adsorbed on glass-bottom 96-well plates (50 µl/well) overnight at 4 °C. VEGF binding was performed as in (A) but only at pH 7.5 in the absence of heparin treatment. Bound VEGF was detected by ELISA as in (A). Samples were measured in triplicate, and the data are presented as mean values +/- standard deviation. VEGF adsorption on naked glass, as well as the blanc value of the assay (no antibody added) for each adsorbed protein are shown for comparison. (C) Fibronectin (20 µg/ml; 50 µl/well) or gelatin (20 mg/ml; 50 µl/well) were adsorbed on glass-bottom 96-well pates overnight at 4 °C (conditions labeled as 'Fibronectin' and 'Gelatin', respectively). In a second step, aimed at testing the ability of gelatin to reduce non-specific binding in the presence of fibronectin without blocking the specific binding sites, fibronectin (20 µg/ml; 50 µl/well) was added on top of the adsorbed gelatin (condition labeled as 'Fibronectin on Gelatin'), and gelatin (20 mg/ml; 50 µl/well) was added on top of the adsorbed fibronectin (condition labeled as 'Gelatin on Fibronectin'). The proteins were allowed to adsorb for 1 h on ice. The plate was incubated with VEGF (5 µg/ml) in binding buffer (150 mM NaCl, 25 mM Hepes) at pH 7.5 or 5.5, in the presence or absence of pre-treatment of the adsorbed proteins with 100 µg/ml heparin in PBS. The color code used in the same as in (A). Bound VEGF was detected by ELISA as in (A). Samples were measured in triplicate, and the data are presented as mean values +/- standard deviation. The data presented have been corrected by subtracting from the raw data the value of the blanc (no added antibodies), for each corresponding condition. (D) Same as in (C) but with 10 µg/ml VEGF and including conditions

5

'Fibronectin' and 'Gelatin' only, without the second protein adsorption step. The color code used is the same as in (A).

The data presented here demonstrate the high levels of non-specific VEGF binding on the assay substrate and the failure of a series of blocking proteins to reduce it to levels comparable to the assay blanc values. The only promising protein to block VEGF non-specific binding was gelatin, especially when used at high concentrations (20 mg/ml). However, the blocking effects of gelatin varied between experiments, and were not as pronounced when higher VEGF concentrations (10 μg/ml) were tested.
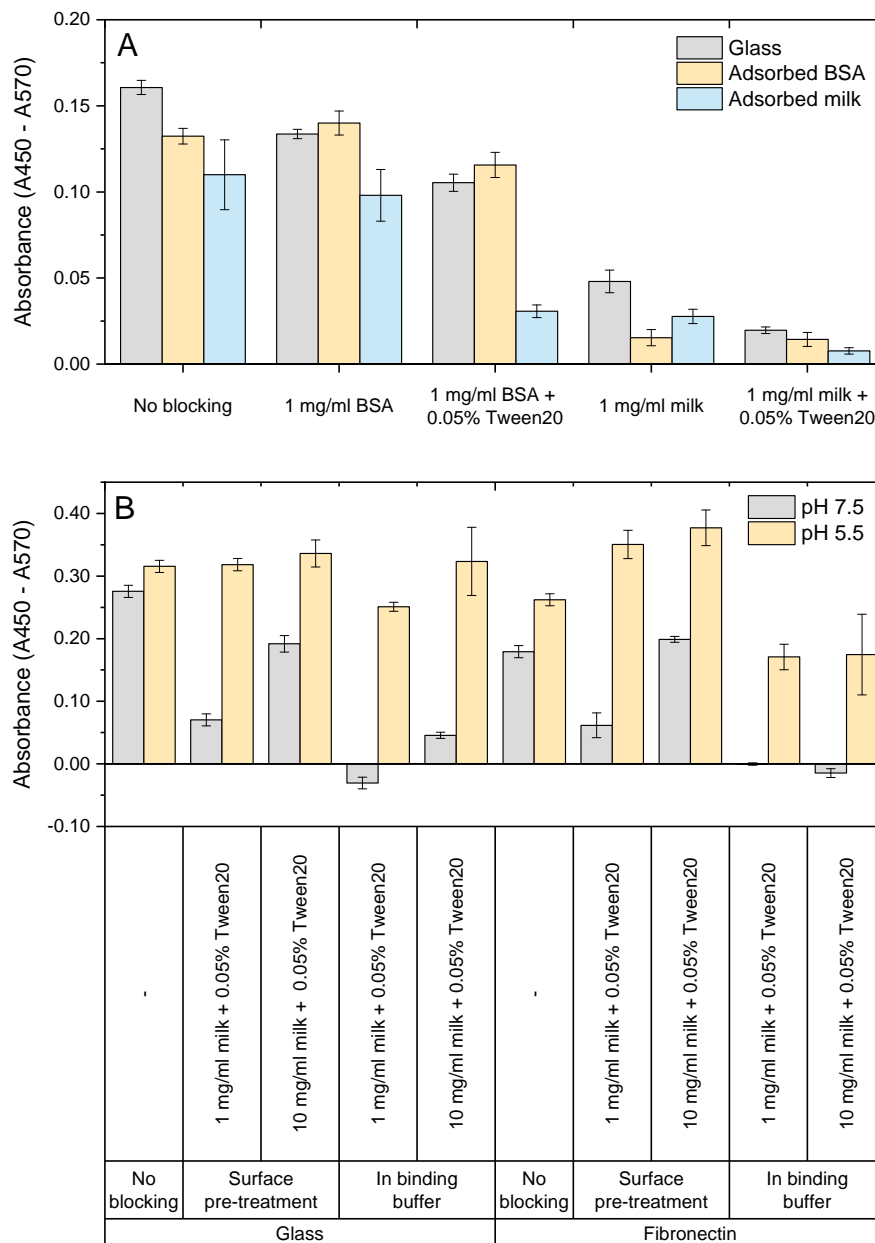
Figure S4. Milk reduces the non-specific binding of VEGF at pH 7.5 but not at pH 5.5. (A) BSA or milk (2 mg/ml; 50 µl/well) were adsorbed on glass-bottom 96-well plates for 1 h on ice. The surface (naked glass, grey bars; adsorbed BSA, ochre bars; adsorbed milk, light blue bars) was incubated for 1 h with binding buffer (150 mM NaCl, 25 mM Hepes, pH 7.5) in the absence (no blocking) or presence of 1 mg/ml BSA +/- 0.05% Tween20 or 1 mg/ml milk +/- 0.05% Tween20 as blocking agents. The plate was then incubated with VEGF (0.5 µg/ml) in the corresponding buffer for 1 h on ice, and bound VEGF was detected by ELISA with an anti-His primary antibody (1:1000) and an HRP-labeled secondary antibody (1:2000). Both antibody incubations were performed in ELISA blocking buffer (1 mg/ml BSA + 0.05% Tween20 in PBS). Samples were measured in triplicate, and the data are presented as mean values +/- standard deviation. The data presented have been corrected by subtracting from the raw data the value of the blanc (no added antibodies), for each corresponding condition. The data demonstrate the great effect of 1 mg/ml milk + 0.05% Tween20 at pH 7.5 to reduce VEGF non-specific binding to near blanc values, when added to the binding buffer. (B) Fibronectin (2 µg/ml; 50 µl/well) was adsorbed on glass-bottom 96-well plates overnight at 4 °C. The effect of 1 mg/ml milk + 0.05% Tween20 or 10

7

mg/ml milk + 0.05% Tween20 to suppress VEGF non-specific binding was tested at both pH 7.5 (grey bars) and pH 5.5 (ochre bars), by either surface pre-treatment prior to VEGF binding or by adding the blocking agents during VEGF binding. VEGF binding was performed with 0.5 µg/ml VEGF in binding buffer (150 mM NaCl, 25 mM Hepes, pH 7.5 or 5.5) in the absence (no blocking and in the conditions of surface pre-treatment) or presence of the blocking agents. Bound VEGF was detected by ELISA as in (A). Samples were measured in triplicate, and the data are presented as mean values +/- standard deviation. The data presented have been corrected by subtracting from the raw data the value of the blanc (no added antibodies), for each corresponding condition. Although the presence of milk and Tween20 during VEGF binding at pH 7.5 completely eliminated non-specific binding, its effect at pH 5.5 was limited.
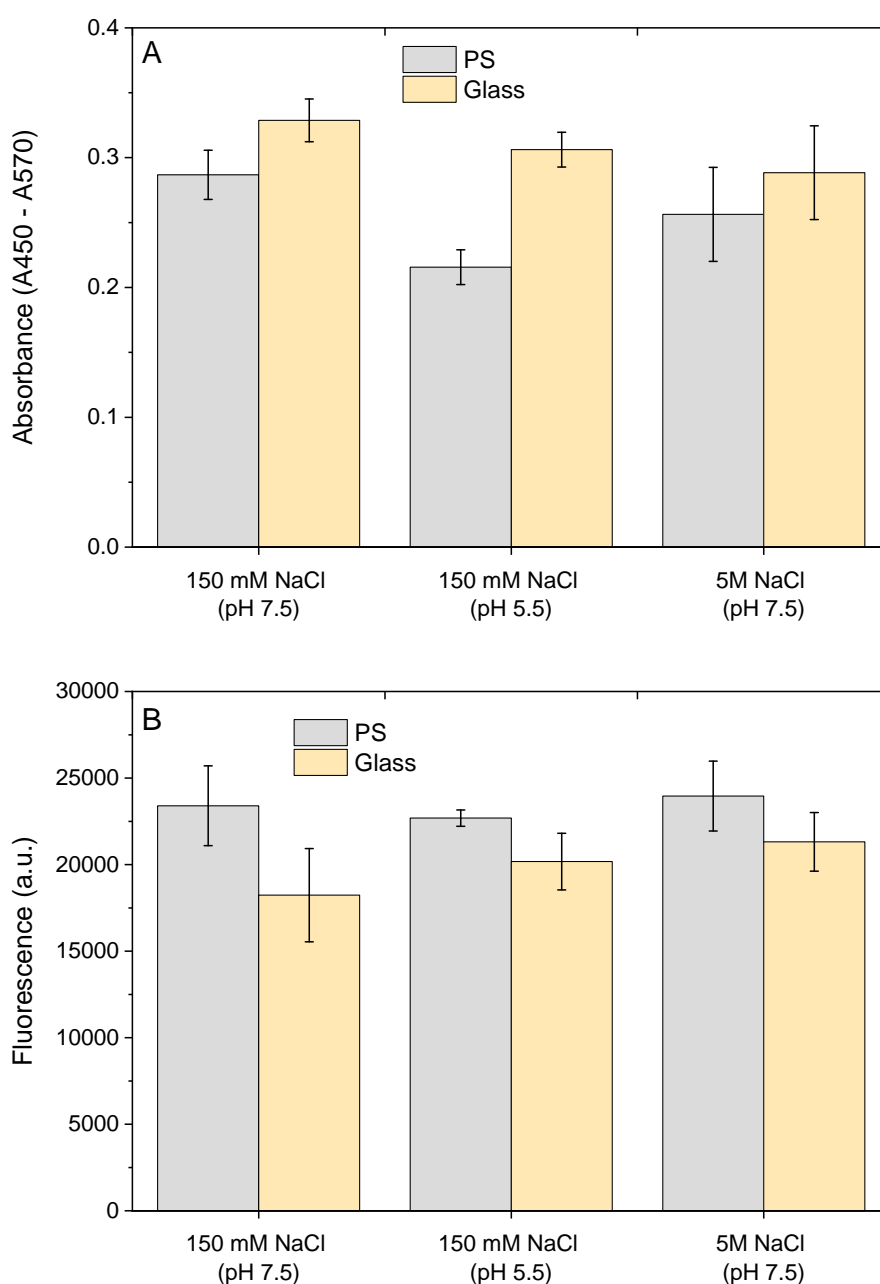
Figure S5. Buffers of different ionic strength and pH do not affect VEGF adsorption to or fibronectin desorption from glass and polystyrene. (A) VEGF was diluted in 3 different buffers (150 mM NaCl, 25 mM Hepes, pH 7.5; 150 mM NaCl, 25 mM Hepes, pH 5.5; 5 M NaCl, 25 mM Hepes, pH 7.5) at a final concentration of 0.5 µg/ml and was adsorbed on polystyrene (grey bars) or glass-bottom (ochre bars) 96-well plates for 1 h on ice (50 µl/well). Adsorbed VEGF was detected by ELISA with an anti-His primary antibody (1:1000) and an HRP-labeled secondary antibody (1:2000), with both antibody incubations performed in ELISA blocking buffer (1 mg/ml BSA + 0.05% Tween20 in PBS). Samples were measured in triplicate, and the data are presented as mean values +/- standard deviation. The data presented have been corrected by subtracting from the raw data the value of the blanc (no added antibodies), for each corresponding condition. The amount of VEGF adsorbed to the different substrates from the different buffers was very similar, with only a small decrease observed in VEGF adsorption to polystyrene at acidic pH. (B) Cy3-labeled fibronectin in PBS was adsorbed on half-area black polystyrene (25 ng; 25 µl/well; grey bars) or glass-bottom (50 ng; 50 µl/well; ochre bars) 96-well

plates overnight at 4 °C. The solution was aspirated, and the protein layer washed 3 times with PBS and treated with the corresponding buffer (150 mM NaCl, 25 mM Hepes, pH 7.5; 150 mM NaCl, 25 mM Hepes, pH 5.5; 5 M NaCl, 25 mM Hepes, pH 7.5) for 1 h on ice. The solution was aspirated, the plate was washed 3 times with PBS, and the amount of remaining protein was determined by fluorescence measurements with a microplate reader (excitation wavelength = 550 nm; emission wavelength = 595 nm). Samples were measured in triplicate, and the data are presented as mean values +/- standard deviation. The values for fibronectin desorption caused by the different buffers were similar. Since the binding buffers containing 150 mM NaCl have a similar ionic strength to that of PBS, which does not cause fibronectin desorption according to the data presented in Fig. S2, we can conclude that incubation with the solution of high ionic strength (5 M NaCl) did not lead to significant fibronectin desorption.
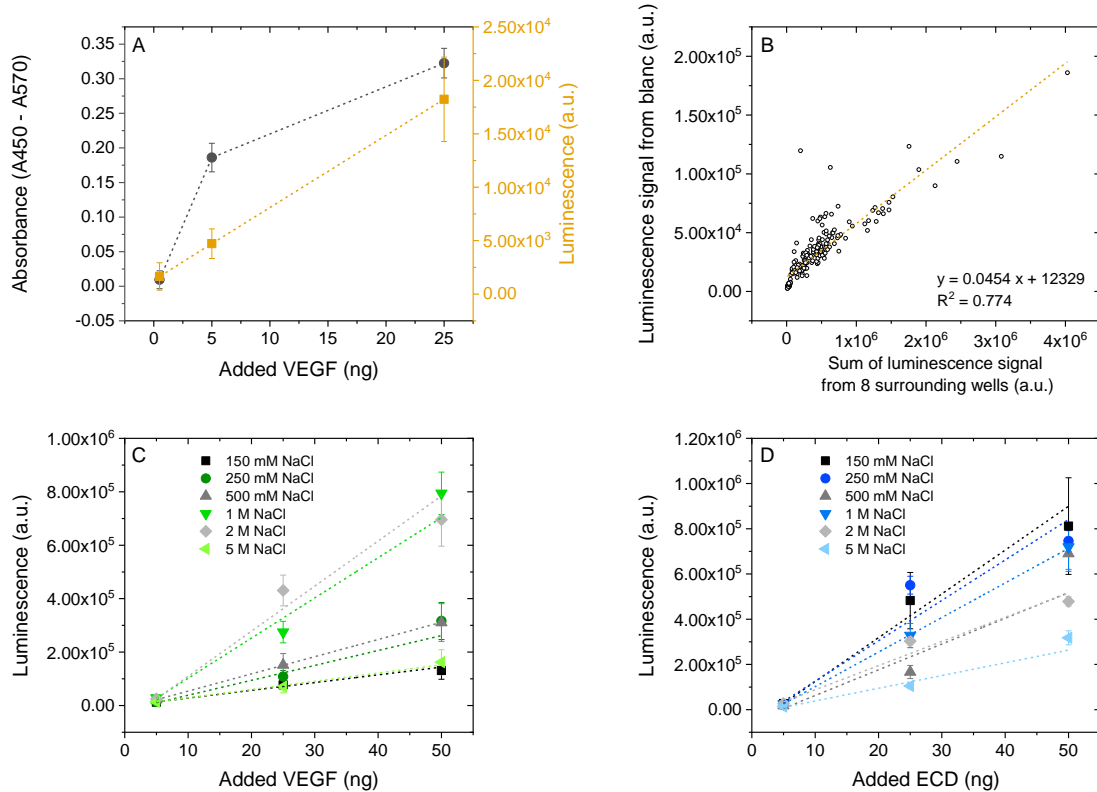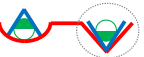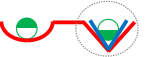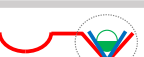
Figure S6. Detection of surface-bound VEGF by luminescence. (A) VEGF (0.5, 5, and 25 ng) was diluted in extraction buffer (5 M NaCl, 25 mM Hepes, pH 7.5) and adsorbed on polystyrene 96-well plates (50 µl/well) for 1 h on ice. Following solution aspiration and 3 washes with PBS, bound VEGF was detected by ELISA with an anti-His primary antibody (1:1000) and an HRP-labeled secondary antibody (1:2000). The signal was developed accordingly and either absorbance at 450 nm (grey circles) or chemiluminescence (ochre squares) was measured with a microplate reader. Samples were measured in triplicate (absorbance) or quadruplicate (luminescence), and the data are presented as mean values +/- standard deviation. The data presented have been corrected by subtracting from the raw data the value of the blanc (no added antibodies), for each corresponding condition. These results demonstrate the superior linear range of the luminescence-based detection method. Consequently, this technique was employed for all further experiments. (B) Since luminescence is emitted in all directions, we sought to determine the effect of the luminescence signal from neighboring wells on each measurement by comparing blanc values (no added antibody) measured in different wells surrounded by samples of varying luminescence intensity. A total of 219 blanc measurements from 7 independent experiments were collected, which show a strong positive linear correlation with the sum of luminescence signal from the 8 surrounding wells, with a slope of 0.0454 and an intercept of 12329 (R^2 = 0.7744). Accordingly, all luminescence measurements were corrected by subtracting the sum of the signal from the surrounding 8 wells multiplied by the correction factor 0.0454. (C, D) Increasing amounts (5, 25, and 50 ng) of VEGF (C) or ECD (D) were diluted in different buffers (150 mM NaCl, 25 mM Hepes, pH 7.5; 250 mM NaCl, 25 mM Hepes, pH 7.5; 500 mM NaCl, 25 mM Hepes, pH 7.5; 1 M NaCl, 150 mM Hepes, pH 7.5; 2 M NaCl, 25 mM Hepes, pH 7.5; 5 M NaCl, 25 mM Hepes, pH 7.5; color code explained in the figure) and adsorbed on polystyrene 96-well plates (50 µl/well) for 1 h on ice. Following solution aspiration and 3 washes with PBS, bound VEGF was detected by ELISA with an anti-His primary antibody (1:1000) and an HRP-labeled secondary antibody (1:2000). Both antibody incubations were performed in ELISA blocking buffer (1 mg/ml BSA + 0.05% Tween20 in PBS). Samples were measured in quadruplicate, and the data are presented as mean values +/- standard deviation. The blanc values (no added antibodies) for each corresponding condition have been subtracted from

the data presented. It is evident that the amount of VEGF/ECD adsorbed and/or detected by the anti-His antibody depends on the ionic strength of the solution. Accordingly, each data series was fit by a line and the slope was used to correct measurements performed in buffers of different ionic strength. The correction factors are shown in Table S1.

Equilibrium VEGF/ECD binding to surface-immobilized fibronectin (Figures S7-S8)

Figure S7. Prediction of molecular species following different VEGF and ECD binding scenarios to fibronectin. We distinguish between shared (red square) and distinct (red circle and triangle) binding sites for VEGF (green circle) and ECD (blue triangle) on fibronectin, which allow or not the formation of a VEGF/ECD complex after binding to fibronectin (complex permissive or non-permissive, respectively). Consequently, for each type of binding sites, we predict which molecular species would be generated by adding the preformed VEGF/ECD complex, VEGF followed by ECD, or ECD followed by VEGF. The complex permissive nature of the VEGF binding sites is depicted schematically by the filled part of the circle representing VEGF projecting away from the fibronectin binding site and being available to bind ECD. On the contrary, when the VEGF binding site of fibronectin is complex non-permissive, the filled part of the circle faces the fibronectin site and cannot interact with ECD. Similarly, the triangle representing ECD is positioned in such a way as to allow interactions with VEGF in the case of complex permissive binding sites, or to block VEGF binding in the case of complex non-permissive interactions. In the molecular species enclosed by the dashed circle (fibronectin-ECD-VEGF, complex permissive), ECD adopts a configuration that cannot be recognized by the anti-VEGFR2 antibody.
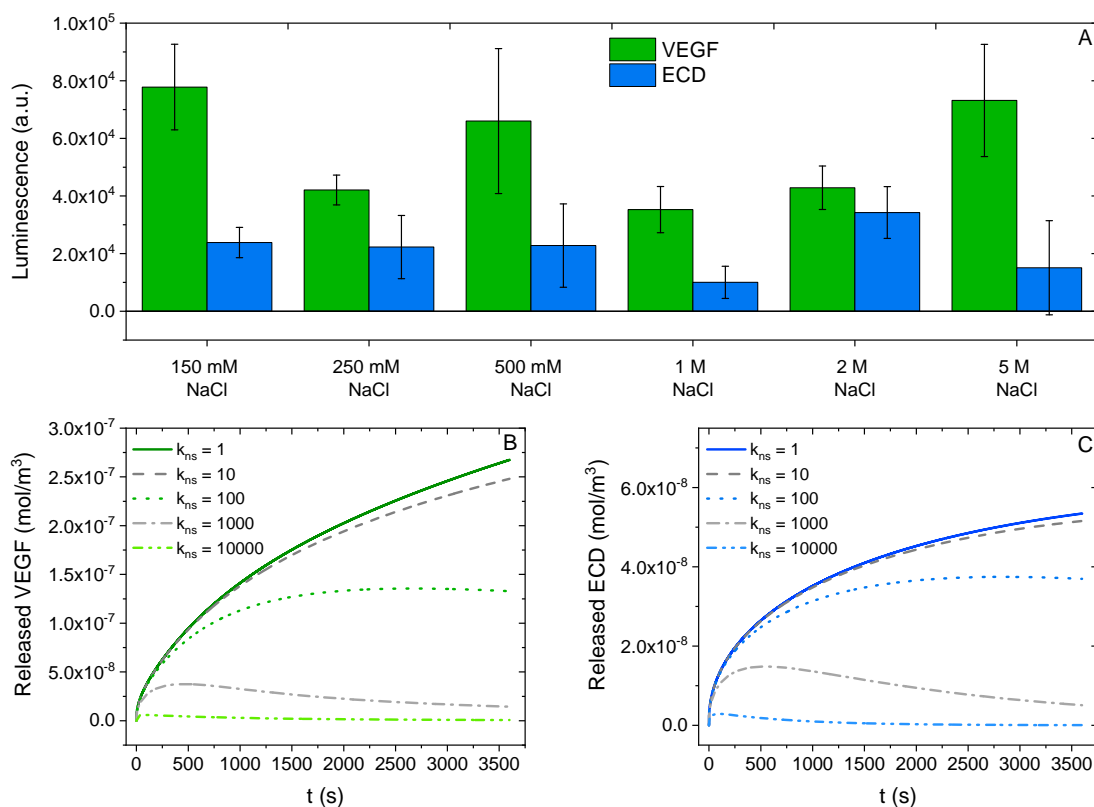
Figure S8. Change of pH is sufficient to release fibronectin-bound VEGF and ECD, but re-adsorption occurs over time. (A) Fibronectin was adsorbed on 96-well polystyrene plates (20 µg/ml; 50 µl/well) overnight at 4 °C. The plate was incubated for 1 h on ice with 50 µg/ml of VEGF (green bars) or ECD (blue bars) in binding buffer (150 mM NaCl, 25 mM Hepes) at pH 5.5 after pre-treatment of the adsorbed fibronectin with 100 µg/ml heparin in PBS (1 h on ice). Bound VEGF and ECD were extracted for 1 h on ice with buffers of increasing ionic strength: 150 mM NaCl, 25 mM Hepes, pH 7.5; 250 mM NaCl, 25 mM Hepes, pH 7.5; 500 mM NaCl, 25 mM Hepes, pH 7.5; 1 M NaCl, 25 mM Hepes, pH 7.5; 2 M NaCl, 25 mM Hepes, pH 7.5; 5 M NaCl, 25 mM Hepes, pH 7.5. The released ligand was re-adsorbed on a second plate, and detected by ELISA with an anti-His primary antibody (1:1000) and an HRP-labeled secondary antibody (1:2000). Both antibody incubations were performed in ELISA blocking buffer (1 mg/ml BSA + 0.05% Tween20 in PBS). Samples were measured in quadruplicate, and the data are presented as mean values +/- standard deviation. The data were corrected for differences in VEGF/ECD adsorption and detection from buffers of different ionic strength (Table S1). (B, C) Simulation of release experiments of VEGF (B) or ECD (C) from fibronectin using a two-sites model with the kinetic parameters shown in Table 3 and assuming an equal number of non-specific and specific (fibronectin) binding sites. Four different association rates for binding to the non-specific sites (k_{ns}) were considered: 1 (solid lines), 10 (dash lines), 100 (dot lines), 1000 (dash-dot lines) and 10000 (dash-double dot lines) $m^3 mol^{-1} s^{-1}$. For a given ratio of non-specific/specific binding sites, there exist a k_{ns} threshold that leads to a peak followed by a decrease in ligand release. The more abundant the non-specific binding sites in relation to the fibronectin binding sites, the lower the k_{ns} threshold.

III.   Structural determinants of VEGF/ECD-fibronectin interactions (Figure S9)
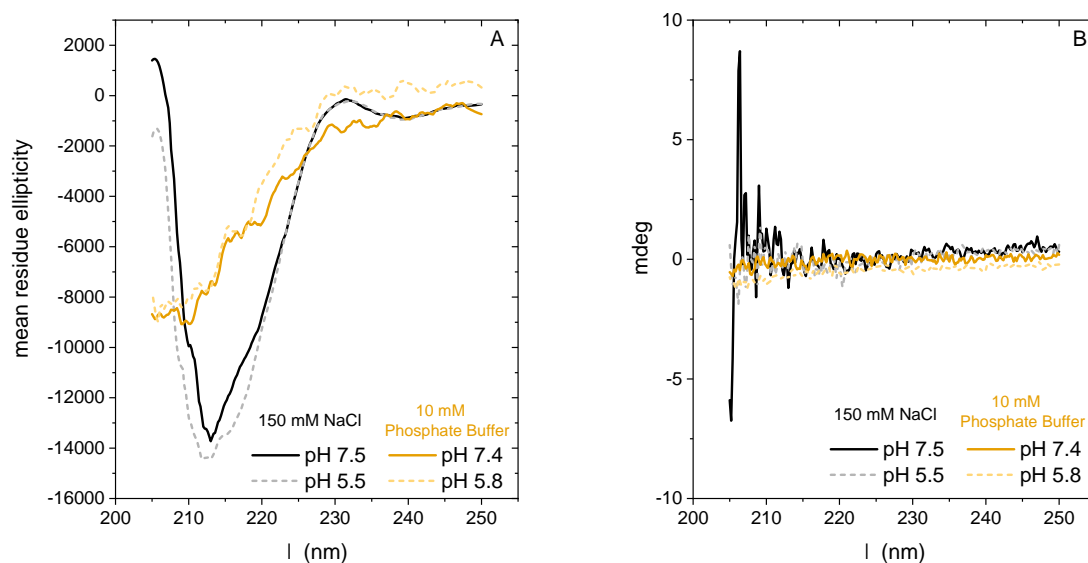
Figure S9. VEGF unfolding at low ionic strength. (A) VEGF was diluted in binding buffer (150 mM NaCl, 25 mM Hepes) at pH = 7.5 (black solid line) or pH = 5.5 (grey dashed line) at a concentration of 0.3 mg/ml or in 10 mM sodium phosphate buffer at pH 7.4 (ochre solid line) or pH = 5.8 (ochre dashed line) at a concentration of 0.05 mg/ml and CD spectra were acquired in the 250-205 nm wavelength range. The data are presented in units of mean residue ellipticity, following smoothing with a Savitzky-Golay filter with a 20-nm window. The data demonstrate that independent of pH, low ionic strength affects the β-sheet dominated structure of VEGF, shifting the negative peak at 215 nm to lower wavelengths, indicative of protein unfolding. Therefore, all CD measurements were performed in buffers containing 150 mM NaCl. (B) Buffer baselines (in mdeg) were collected using the same acquisition parameters as for the VEGF samples shown in (A). The same color code as in (A) applies. The data show that in the presence of 150 mM NaCl, measurements below 210 nm are associated with greater uncertainty, especially at pH 7.5.

Optimization of SPR assay to study and model the kinetics of VEGF/ECD-fibronectin interactions (Figures S10-S19; Table S2)
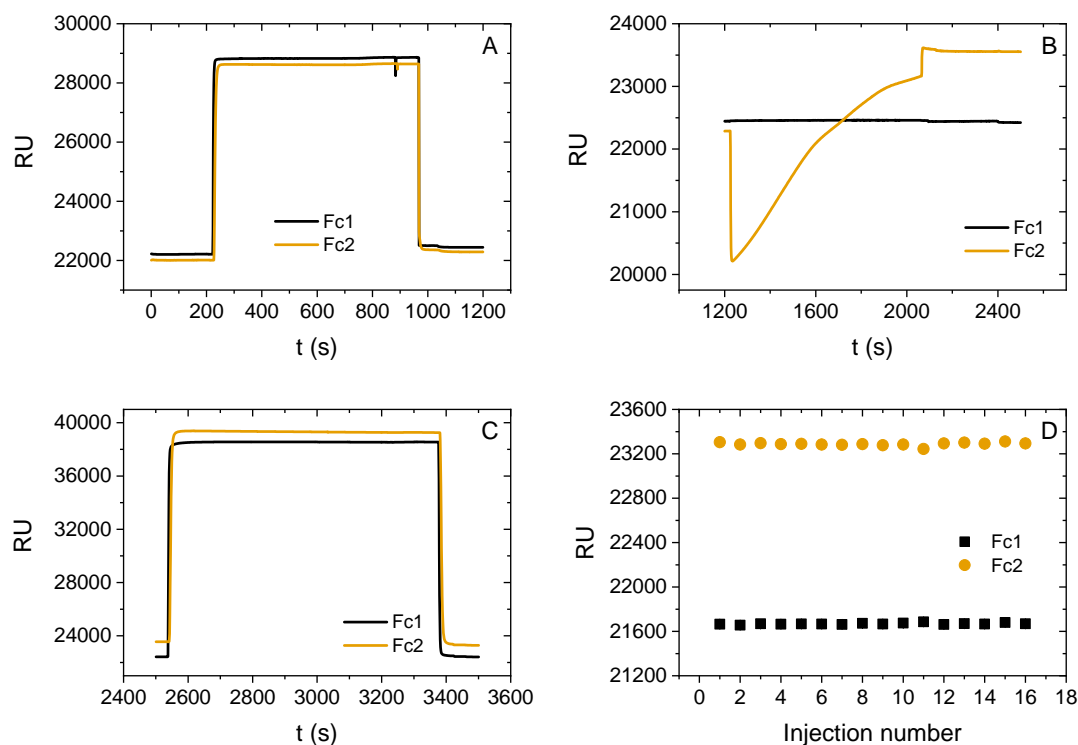
Figure S10. SPR chip functionalization. Fibronectin was immobilized on carboxymethyldextran hydrogel SPR chips based on standard amine chemistry. The first step was surface activation by the addition of NHS and EDC (A), followed by fibronectin (2 µg/ml) immobilization (B), and finally, surface quenching by ethanolamine (C). All steps were performed at a flow rate of 5 µl/min with an injection volume of 70 µl. Surface activation and quenching were performed in both flow cell 1 (Fc1; reference; black) and flow cell 2 (Fc2; sample; ochre), whereas fibronectin immobilization was performed only in flow cell 2. The difference in response units (RU) between flow cells 1 and 2 due to the mass of the immobilized fibronectin was very stable, and persisted after 16 sequential injections of different ligands, followed by 2 M NaCl/0.05 N NaOH regeneration cycles (D). Each point represents an average value from a part of the sensogram encompassing 50-100 values, and is associated with a standard deviation value less than or equal to 4% of the mean.
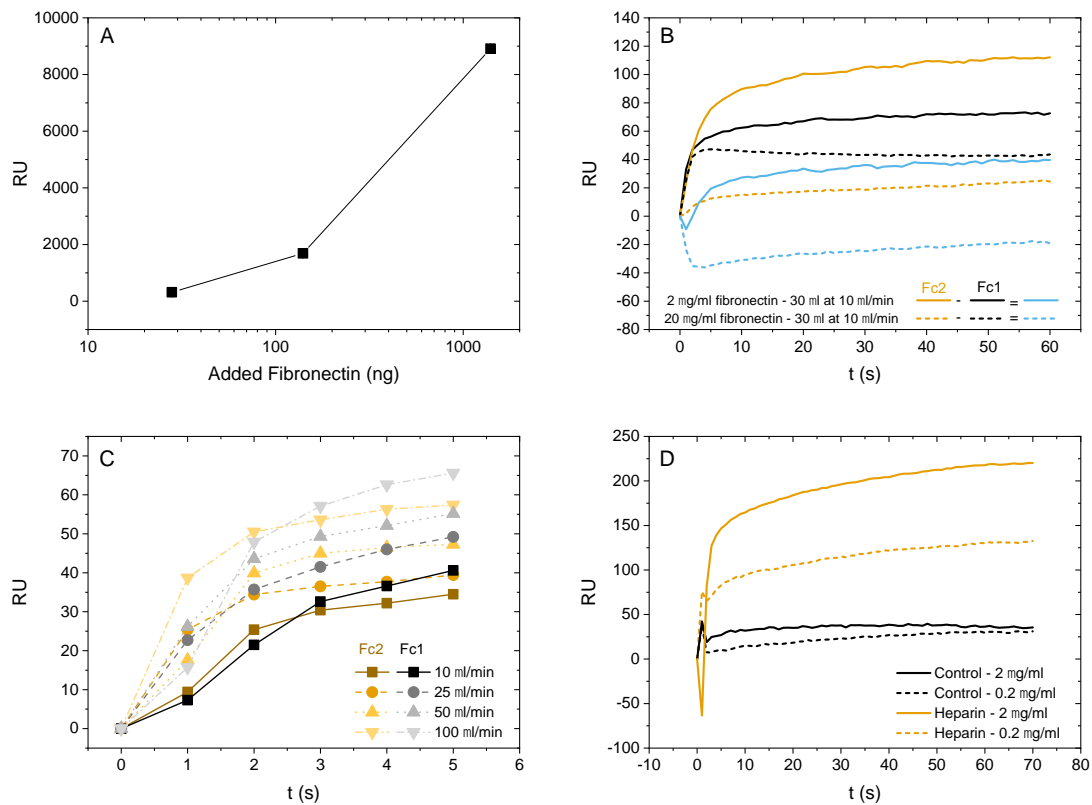
Figure S11. Optimization of fibronectin density and flow rates for SPR measurements. (A) Fibronectin was immobilized on the biosensor chip on flow cell 2 (Fc2) at 3 different densities (2 * 70 µl * 0.2 µg/ml = 28 ng; 70 µl * 2 µg/ml = 140 ng; 70 µl * 20 µg/ml = 1400 ng). Only the difference in RU between sample and reference flow cells (Fc2 – Fc1) is shown. Each point represents an average value from a part of the sensogram encompassing 50-100 values, and is associated with a standard deviation value less than or equal to 4% of the mean. (B) VEGF (30 µl of 1000 nM) was injected at a flow rate of 10 µl/min on chips with 140 ng (solid lines) or 1400 ng (dashed lines) immobilized fibronectin. Black lines correspond to the reference cell Fc1 and ochre lines to the sample cell Fc2. The difference signal (Fc2-Fc1), representing the specific binding events to fibronectin, is shown with the light blue lines. It is evident from the data that VEGF binding to fibronectin is minimal and does not increase by increasing the fibronectin density. On the contrary, at the highest fibronectin density, the value of Fc2 becomes lower than that of Fc1 (possibly because the higher surface coverage by fibronectin reduces VEGF non-specific binding), leading to negative difference curves. (C) Using the chip with the intermediate fibronectin density (140 ng), we tested VEGF binding at different flow rates: 10 µl/min (squares), 25 µl/min (circles), 50 µl/min (triangles), and 100 µl/min (inverted triangles). Only the first 5 s of association are shown for Fc1 (shades of black) and Fc2 (shades of ochre), demonstrating a tendency for faster association as the flow rate increases, which indicates the presence of mass transfer effects. Accordingly, subsequent measurements were performed at a flow rate of 50 µl/min. (D) VEGF (60 µl of 1000 nM) was injected at a flow rate of 50 µl/min on chips with 140 ng (solid lines) or 28 ng (dashed lines) immobilized fibronectin. Only the difference in RU between sample and reference flow cells (Fc2 – Fc1) is shown. VEGF association with fibronectin was recorded in the absence (black lines) or presence (ochre lines) of a pre-treatment step of the immobilized fibronectin with heparin (50 µl of 1 µg/ml at a flow rate of 50 µl/min). Heparin pre-treatment of the immobilized fibronectin significantly increased VEGF binding, and the effect was greater for the higher fibronectin density. Therefore, we chose to use this fibronectin density (70 µl * 2 µg/ml = 140 ng) for further experiments.

17
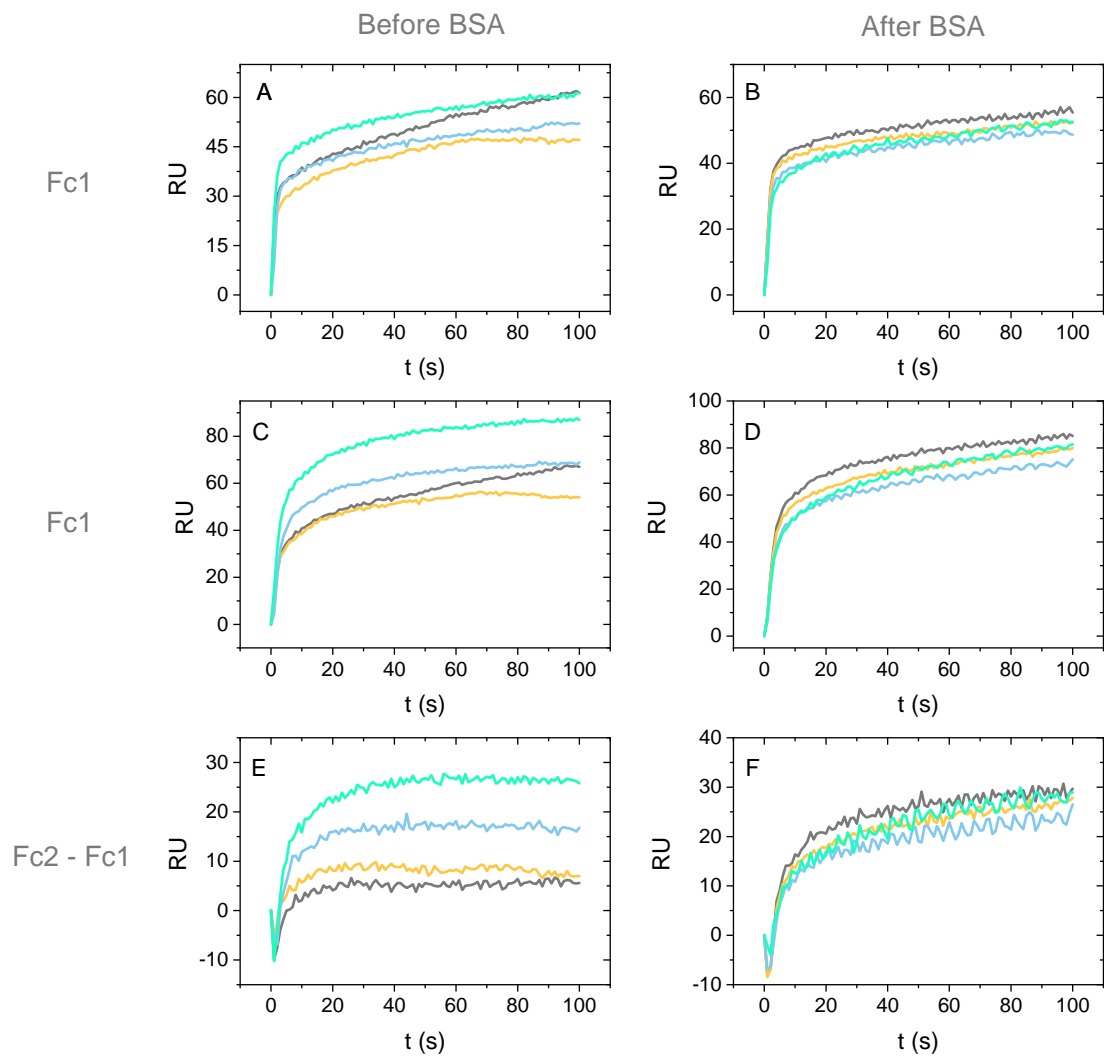
Figure S12. Stabilization of VEGF background binding to fibronectin by BSA injection. VEGF (60 µl of 1000 nM) was injected at a flow rate of 50 µl/min on a chip with 2 µg/ml immobilized fibronectin (140 ng) in the absence of any heparin pre-treatment step (control binding). Fc1 (A, B), Fc2 (C, D) and Fc2-Fc1 (E, F) signals are shown for four sequential injections (first injection: gray lines; second injection: ochre lines; third injection: light blue lines; fourth injection: green lines) performed before (A, C, E) and after (B, D, F) an injection with BSA (60 µl of 1 mg/ml) at a flow rate of 50 µl/min. Before BSA injection, the signal due to VEGF binding increased after each injection, an effect due to the higher values originating from the Fc2 cell. Following BSA injection, this trend disappeared, and the signal stabilized.

18
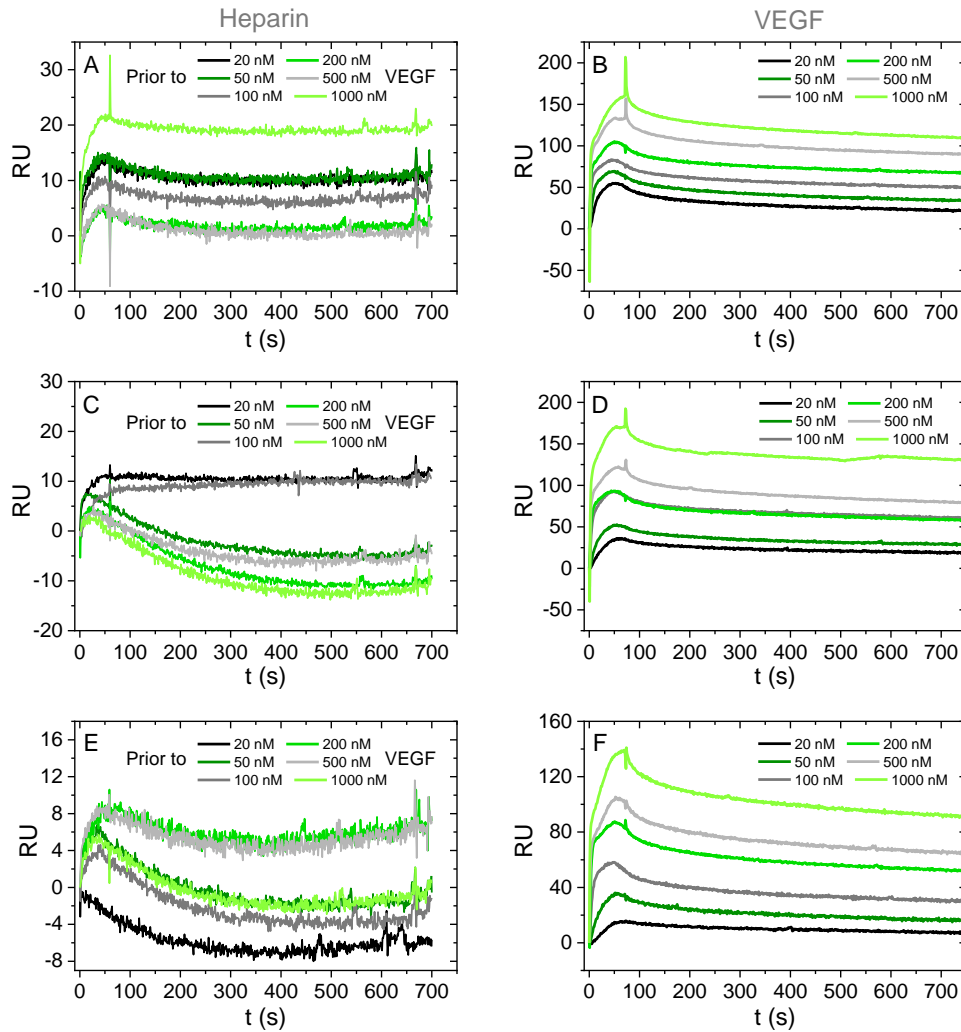
Figure S13. Heparin pre-treatment of immobilized fibronectin increases VEGF binding. Heparin (50 µl of 1 µg/ml) was injected at a flow rate of 50 µl/min on a chip with 2 µg/ml immobilized fibronectin (140 ng). Following association, heparin was allowed to dissociate for 10 min, and immediately afterwards, VEGF was injected (60 µl at 50 µl/min) at different concentrations: 20 nM, 50 nM, 100 nM, 200 nM, 500 nM, and 1000 nM (color code explained in the figure). Following association, VEGF was allowed to dissociate for 720 s. The different VEGF concentrations were injected following a random order in order to ensure that the measurements were free of systematic errors, and the progressive increase in VEGF binding with increasing concentration reflected the true binding. The surface was regenerated with 2 M NaCl and 0.05 N NaOH after every heparin/VEGF binding cycle. The heparin injections are shown in panels (A), (C), and (E), and the corresponding VEGF injections in panels (B), (D), and (F). The dose-response experiment was repeated three times using the same chip (run 1: (A), (B); run 2: (C), (D); run3: (E), (F)). Only Fc2-Fc1 traces are shown. Binding of heparin to fibronectin at this concentration did not result in a significant SPR signal (less than 25 RU for all injections). Occasionally, the sensogram line was not stable and drifted to negative values during the long dissociation phase following the heparin treatment. However, there was no correlation between the RU values following heparin treatment and VEGF binding. Mean and standard deviation values were calculated for VEGF binding from the triplicate experiments. The error associated with each data point was 15-49% (standard deviation normalized against the mean; see Fig. S18).
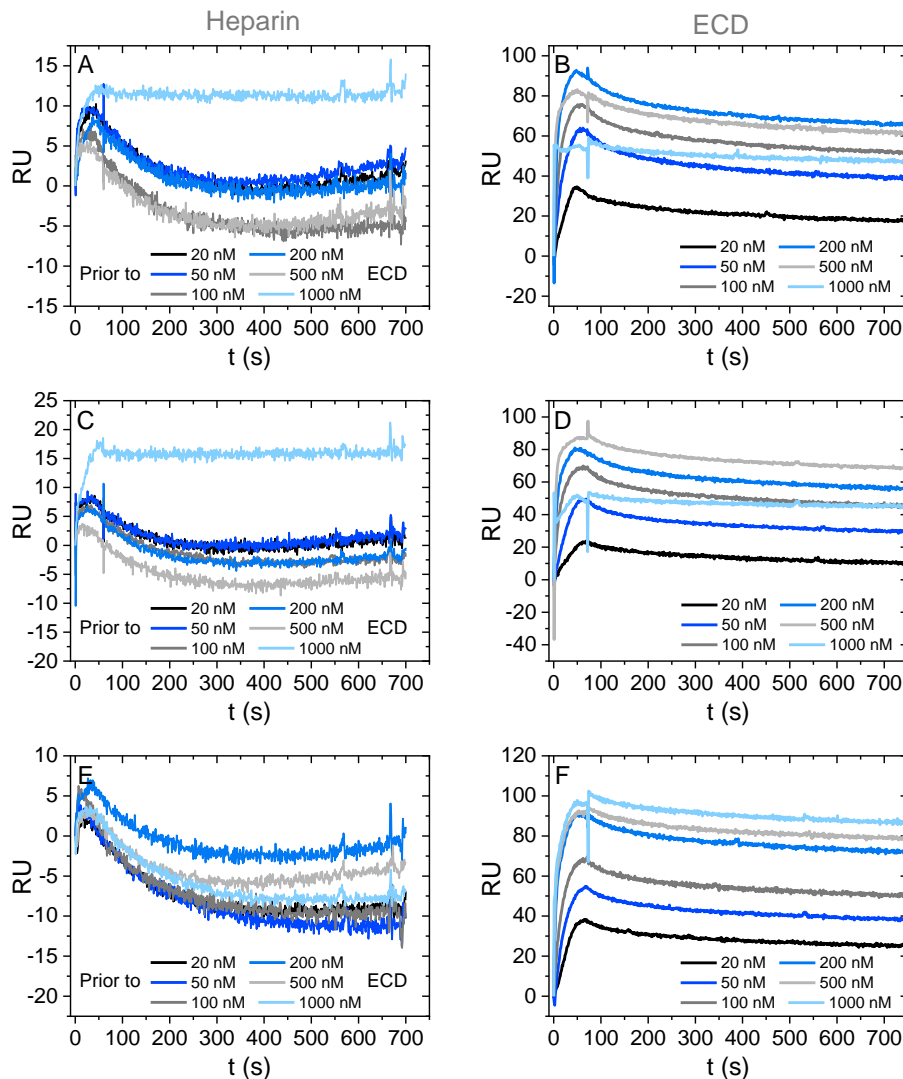
Figure S14. Heparin pre-treatment of immobilized fibronectin increases ECD binding. Heparin (50 µl of 1 µg/ml) was injected at a flow rate of 50 µl/min to a chip with 2 µg/ml immobilized fibronectin (140 ng). Following association, heparin was allowed to dissociate for 10 min, and immediately afterwards, ECD was injected (60 µl at 50 µl/min) at different concentrations: 20 nM, 50 nM, 100 nM, 200 nM, 500 nM, and 1000 nM (the color code is explained in the figure). Following association, ECD was allowed to dissociate for 720 s. The different ECD concentrations were injected following a random order to ensure that the measurements were free of systematic errors, and the progressive increase in ECD binding with increasing concentration reflected the true binding. The surface was regenerated with 2 M NaCl and 0.05 N NaOH after every heparin/ECD binding cycle. The heparin injections are shown in panels (A), (C), and (E), and the corresponding ECD injections in panels (B), (D), and (F). The dose-response experiment was repeated three times using the same chip (run 1: (A), (B); run 2: (C), (D); run3: (E), (F)). Only Fc2-Fc1 traces are shown. Binding of heparin to fibronectin at this concentration did not result in a significant SPR signal (less than 20 RU for all injections). Occasionally, the sensogram line was not stable and drifted to negative values during the long dissociation phase following the heparin treatment. However, there was no correlation between the RU values following heparin treatment and ECD binding. Mean and standard deviation values were calculated for ECD binding from the triplicate experiments. The error associated with each data point was 6-29% (standard deviation normalized against the mean; see Fig. S18).
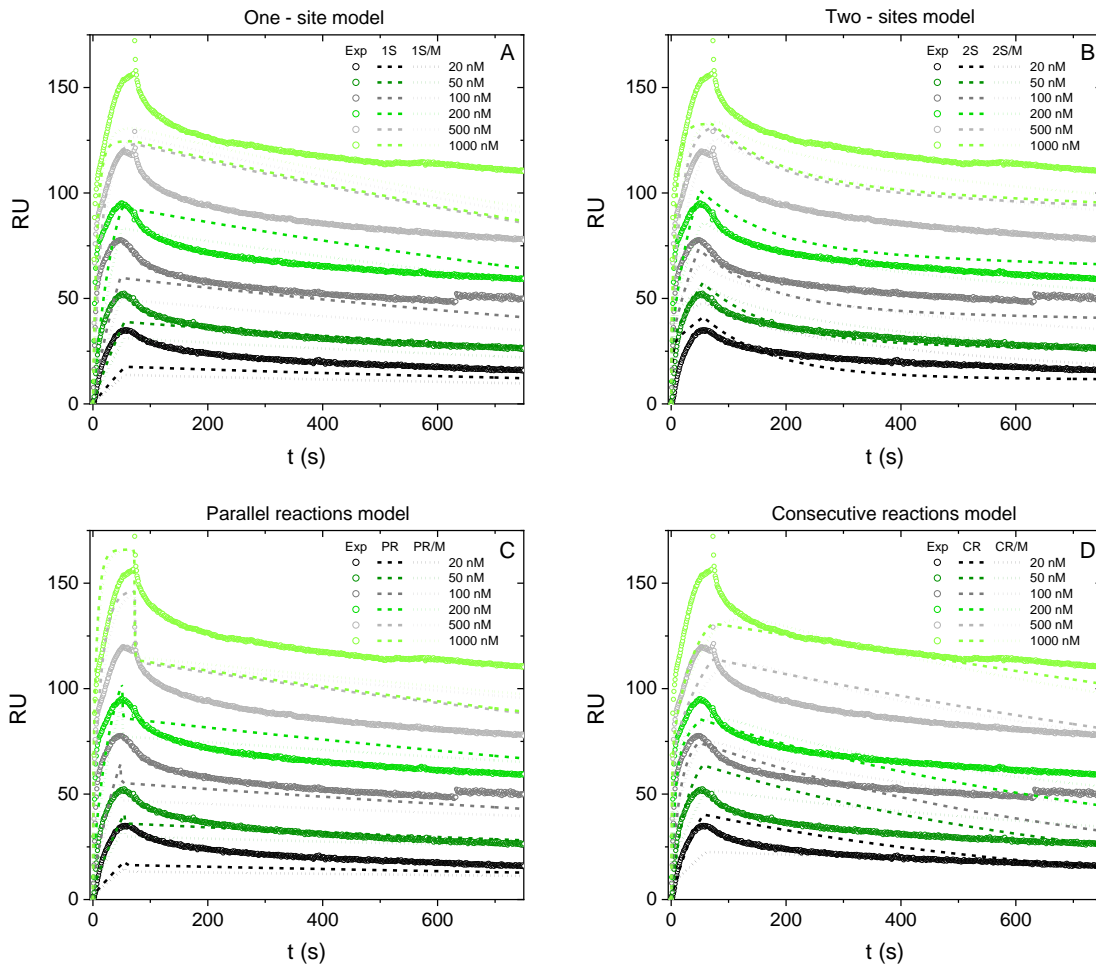
Figure S15. Model fitting of the association and dissociation data for VEGF binding to fibronectin. VEGF was injected (60 µl at 50 µl/min) at different concentrations (20 nM, 50 nM, 100 nM, 200 nM, 500 nM, and 1000 nM; color code explained in the figure) on a chip with 2 µg/ml immobilized fibronectin (140 ng) and pre-treated with heparin (50 µl of 1 µg/ml at 50 µl/min, followed by 10 min dissociation). The data represent mean values of triplicate experiments. The data were fitted with different models describing the association between VEGF and fibronectin (defined in Fig. 6): one-site (1S) (A), two-sites (2S) (B), parallel reactions (PR) (C), and consecutive reactions (CR) (D), considering rapid mixing (dashed lines) or mass transfer (dotted lines; M) phenomena. Model fitting was performed with the beginning of the dissociation time set to the time corresponding to the maximum RU value achieved during the association phase (variable dissociation time). The experimental data are represented by the empty symbols. Best fits were achieved with the two-sites model considering mass transfer. The same dataset and best fit are presented in Fig. 5C.
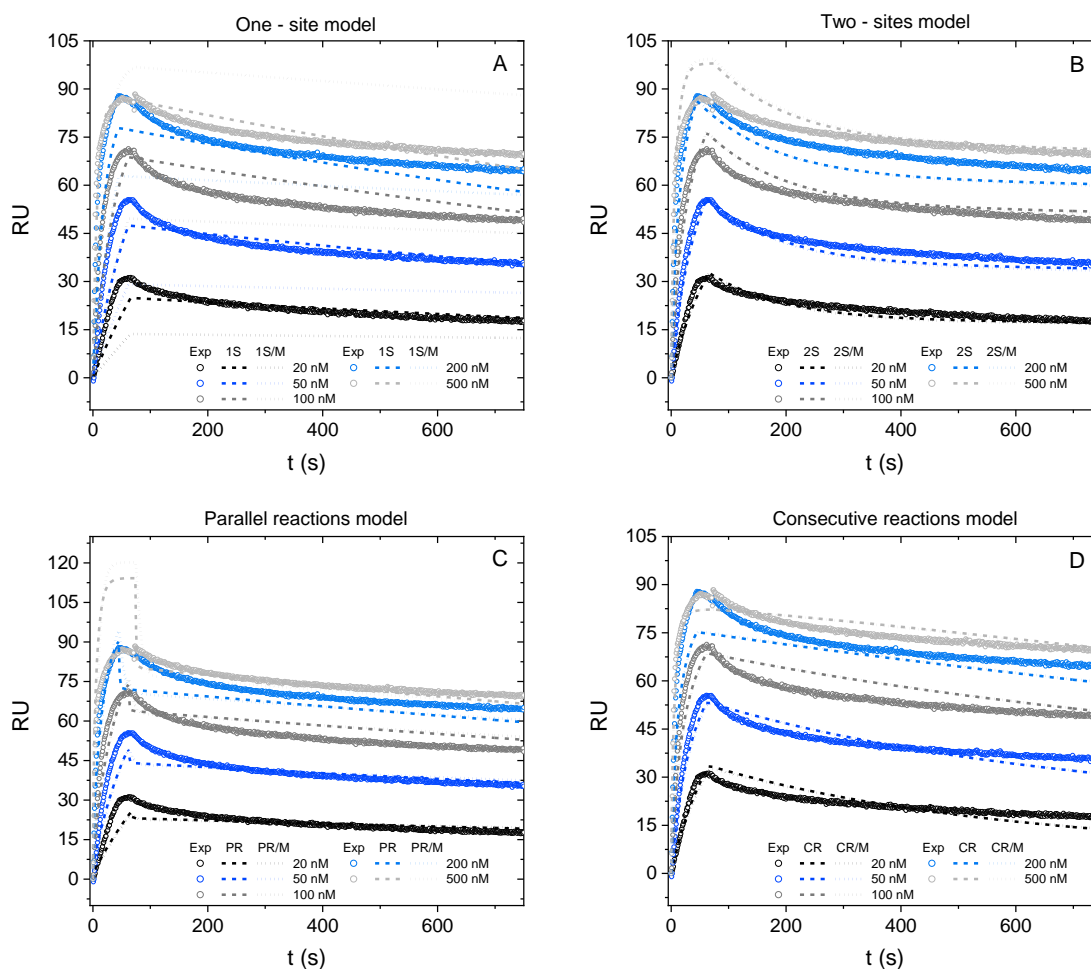
Figure S16. Model fitting of the association and dissociation data for ECD binding to fibronectin. ECD was injected (60 µl at 50 µl/min) at different concentrations (20 nM, 50 nM, 100 nM, 200 nM, and 500 nM; color code explained in the figure) on a chip with 2 µg/ml immobilized fibronectin (140 ng) and pre-treated with heparin (50 µl of 1 µg/ml at 50 µl/min, followed by 10 min dissociation). The data represent mean values of triplicate experiments. The data were fitted with different models describing the association between ECD and fibronectin (defined in Fig. 6): one-site (1S) (A), two-sites (2S) (B), parallel reactions (PR) (C), and consecutive reactions (CR) (D), considering rapid mixing (dashed lines) or mass transfer (dotted lines; M) phenomena. Model fitting was performed with the beginning of the dissociation time set to the time corresponding to the maximum RU value achieved during the association phase (variable dissociation time). The experimental data are represented by the empty symbols. Best fits were achieved with the two-sites model considering rapid mixing. The same dataset and best fit are presented in Fig. 5D.
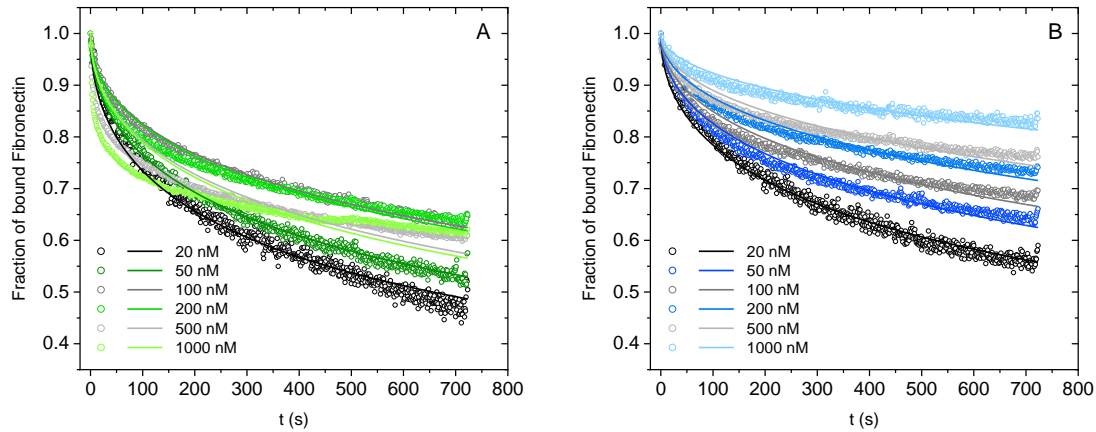
Figure S17. Model fitting of the dissociation data only for VEGF or ECD binding to fibronectin considering rebinding. VEGF (A) or ECD (B) were injected (60 µl at 50 µl/min) at different concentrations (20 nM, 50 nM, 100 nM, 200 nM, 500 nM, and 1000 nM; color code explained in the figure) on a chip with 2 µg/ml immobilized fibronectin (140 ng) and pre-treated with heparin (50 µl of 1 µg/ml at 50 µl/min, followed by 10 min dissociation). Only the dissociation curves were considered. The data represent mean values of triplicate experiments. The RU values were converted to values of the fraction of bound fibronectin (ρ) by normalizing against the initial value at the beginning of dissociation (72 s), which was considered equal to 1. The dissociation data (circles) were fitted to a one-site model taking into account rebinding effects (solid lines), according to the following equation:

$$\rho(t) = \rho(0) * e^{c*t} * erfc(\sqrt{c*t})$$

where:

$$erfc(z) = \frac{2}{\sqrt{\pi}} * \int_{z}^{\infty} e^{-x^2} dx$$

However, the curves showed a clear dependence of $\rho(t)$ on VEGF or ECD concentration. Therefore, the data cannot be fit with a single c parameter. Moreover, several of the individual curves could not be fit at all by this model, especially for high VEGF concentrations. These results further confirm the inability of a one-site model to describe the interactions even if rebinding phenomena are taken into account.
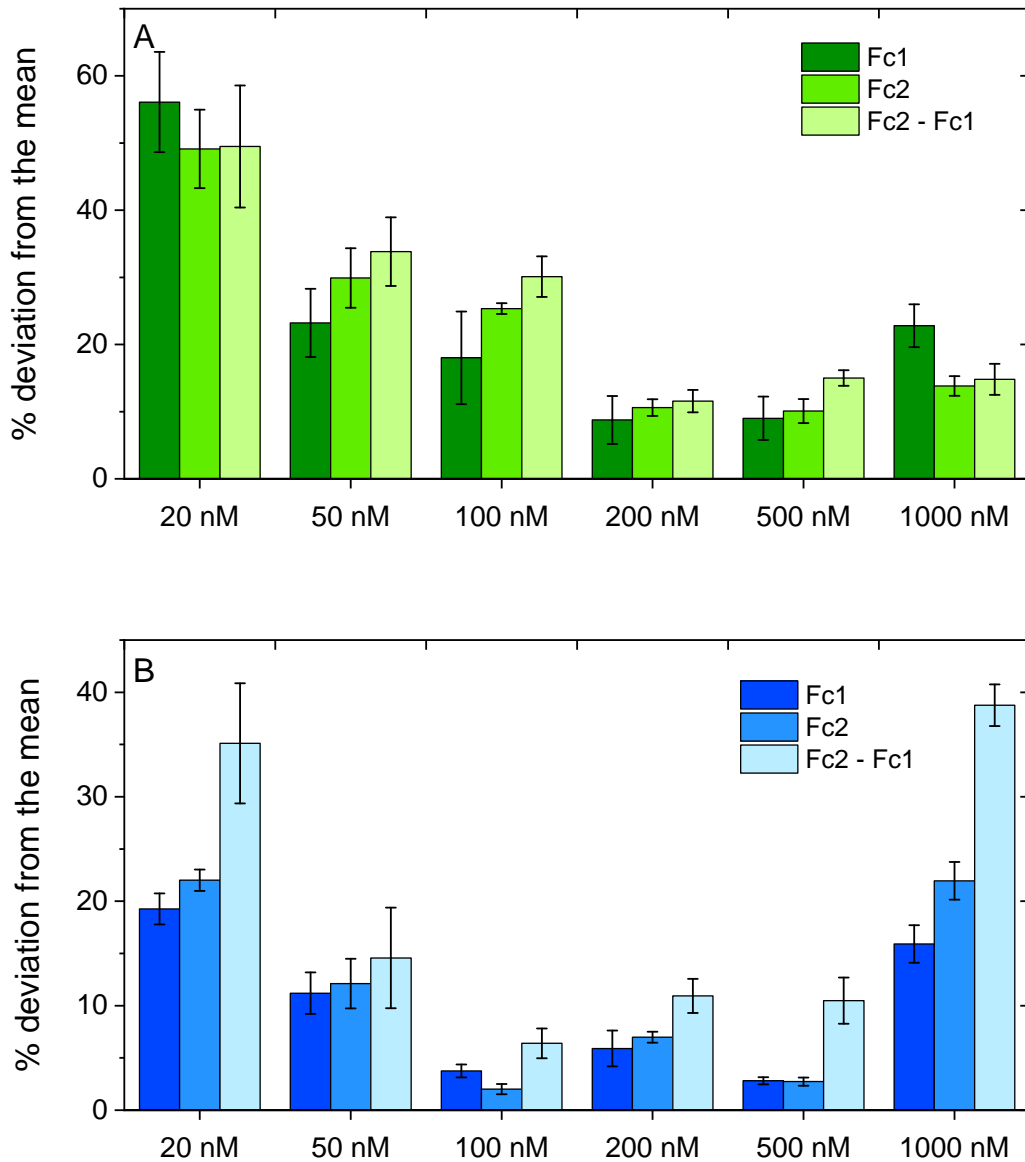
Figure S18. Experimental error associated with SPR dose-response curves. VEGF (A) or ECD (B) were injected (60 μl at 50 μl/min) at different concentrations (20 nM, 50 nM, 100 nM, 200 nM, 500 nM, and 1000 nM) on a chip with 2 μg/ml immobilized fibronectin (140 ng) and pre-treated with heparin (50 μl of 1 μg/ml at 50 μl/min, followed by 10 min dissociation). Each concentration was measured three times on the same chip. Mean and standard deviation values were calculated from the triplicate experiments. For each curve point, the standard deviation was divided by the corresponding mean value to calculate percent errors. A mean percent error value was then calculated from all points of each concentration curve, and are shown for Fc1, Fc2, and Fc2-Fc1.
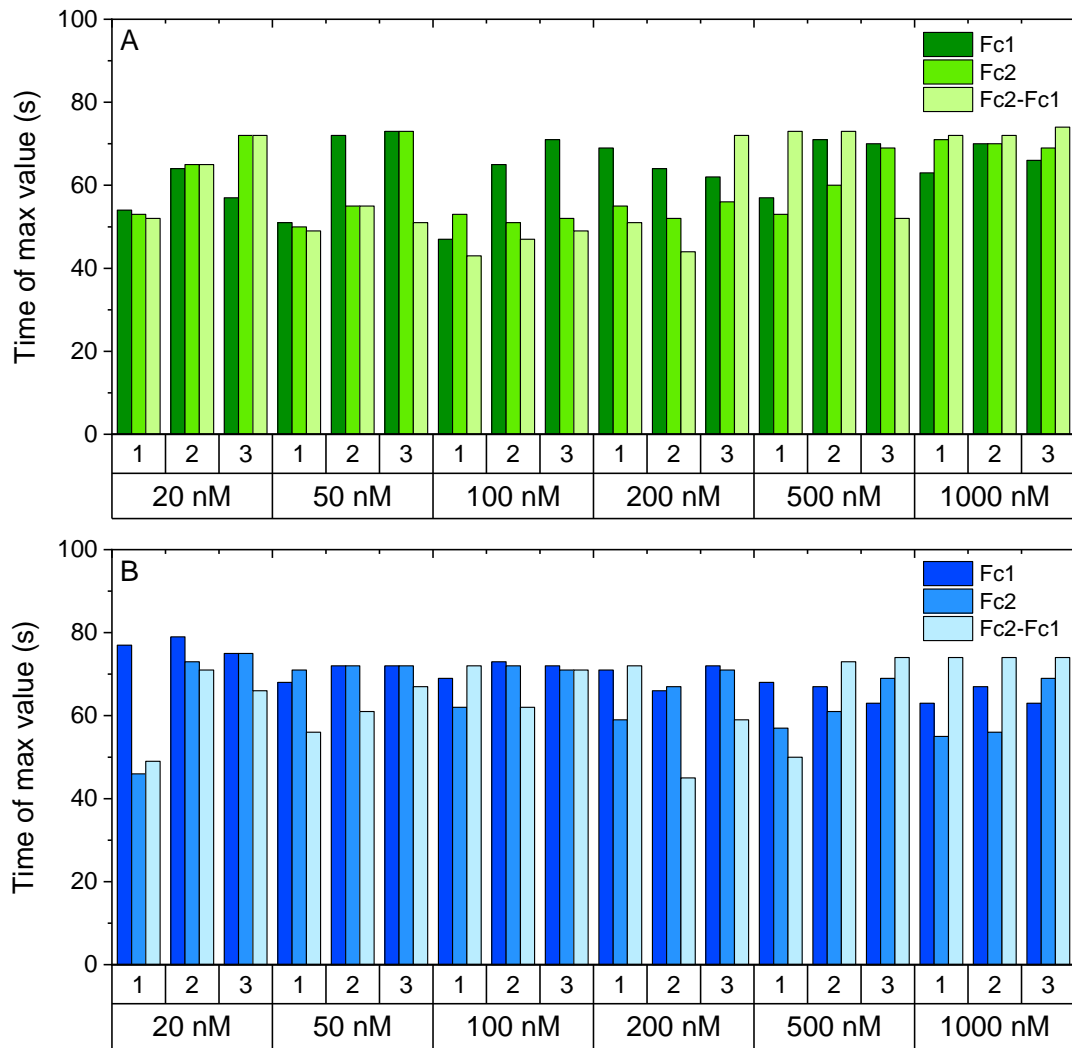
Figure S19. Variation in the time point at which the SPR signal decreases prior to the beginning of the dissociation phase. VEGF (A) or ECD (B) were injected (60 µl at 50 µl/min) at different concentrations (20 nM, 50 nM, 100 nM, 200 nM, 500 nM, and 1000 nM) on a chip with 2 µg/ml immobilized fibronectin (140 ng) and pre-treated with heparin (50 µl of 1 µg/ml at 50 µl/min, followed by 10 min dissociation). Each concentration was measured three times on the same chip. We observed that the RU values started decreasing slightly prior to the nominal beginning of the dissociation phase (72 s). The time point at which RU reached its maximum value during the association phase was calculated and is shown for Fc1, Fc2, and Fc2-Fc1 (color code explained in the figure), for each VEGF and ECD concentration and experimental run (1, 2, 3). The time of maximum RU did not show any obvious correlation with VEGF or ECD concentration, and showed significant variability across replicate experiments, as well as between Fc1 and Fc2 cells. These observations suggest that this variability is likely linked to experimental errors and does not reflect a true aspect of the interaction between fibronectin and VEGF or ECD.
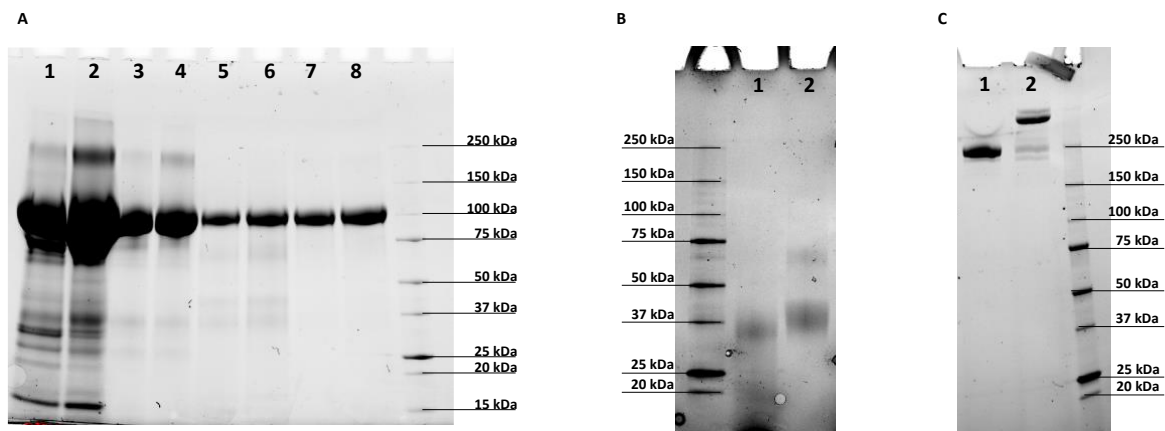
Figure S20. SDS-PAGE analysis of ECD, VEGF, and fibronectin. (A) Recombinant human ECD containing a C-terminal 6x His-tag and expressed in the Sf21 cell line was purified sequentially by immobilized ion affinity chromatography (lanes 1, 2), ion exchange chromatography (lanes 3, 4), and size exclusion chromatography (lanes 5-8). The protein eluted from the final chromatographic step (size exclusion chromatography) was stable after storage at -80 °C (lanes 7, 8), whereas it exhibited slight fragmentation after a 15-day storage period at 4 °C (lanes 5, 6). Two different fractions were collected after immobilized ion affinity chromatography and were processed independently (fraction 1: lanes 1, 3, 5, 7; fraction 2: lanes 2, 4, 6, 8) but resulted in samples indistinguishable by SDS-PAGE. (B) VEGF containing an N-terminal 6x His tag, expressed in *Pichia Pastoris*, and purified by immobilized metal affinity and size exclusion chromatography was analyzed by SDS-PAGE under reducing (lane 1) and non-reducing (lane 2) conditions to ensure sufficient purity and an intact dimeric form. (C). Human plasma fibronectin obtained from Millipore was analyzed by SDS-PAGE under reducing (lane 1) and non-reducing (lane 2) conditions to ensure sufficient purity and an intact dimeric form.

Table S1. Correction factors for adsorption of VEGF and ECD on polystyrene plates from buffers of different ionic strength. Correction factors were calculated from the slopes of the calibration curves shown in Fig. S6 C and D for VEGF and ECD respectively, in order to normalize release data from different extraction buffers to the values corresponding to 150 mM NaCl.

	VEGF	ECD
150 mM NaCl	1.00	1.00
250 mM NaCl	0.46	1.03
500 mM NaCl	0.44	1.36
1 M NaCl	0.18	1.19
2 M NaCl	0.19	1.67
5 M NaCl	0.86	2.84

Table S2. Free parameter estimation for all models used to fit the association and dissociation data for VEGF and ECD binding to fibronectin. The experimental data (mean values of triplicate measurements) presented on Fig. 5 C, D (as well as Figs. S13-14) were fitted with all possible models shown in Fig. 6, under conditions of rapid mixing or mass transfer, with the beginning of the dissociation phase set to the time corresponding to the maximum RU reached during the association phase (variable t). For each model, the fitting was repeated multiple times with a different set of estimates for the free parameters (different by several orders of magnitude) to reduce as much as possible the danger of the fitting algorithm being trapped in a local minimum. Only solutions where all parameter estimates had a well-defined confidence interval (i.e. confidence intervals that did not contain negative values) were accepted. The solution with the lowest residual sum of squares (RMS) was selected, and the parameter estimates together with their confidence intervals (lower and upper bound) are presented here.

		parameter estimate		lower bound		upper bound	
		rapid mixing	mass transfer	rapid mixing	mass transfer	rapid mixing	mass transfer
VEGF One-site	k_a (M^{-1}s^{-1})	1.38E+05	1.00E+05	1.34E+05	9.63E+04	1.41E+05	1.04E+05
	R_T (mol^{1}m^{-2})	2.78E-09	2.92E-09	2.75E-09	2.90E-09	2.81E-09	2.94E-09
	k_d (s^{-1})	5.34E-04	5.00E-04	5.10E-04	4.79E-04	5.57E-04	5.20E-04
	k_m (m^{1}s^{-1})		2.00E-03		1.80E-03		2.19E-03
ECD One-site	k_a (M^{-1}s^{-1})	2.61E+05	1.14E+05	2.57E+05	1.11E+05	2.65E+05	1.17E+05
	R_T (mol^{1}m^{-2})	1.04E-09	1.19E-09	1.04E-09	1.17E-09	1.05E-09	1.21E-09
	k_d (s^{-1})	4.19E-04	1.40E-04	4.07E-04	1.06E-04	4.31E-04	1.75E-04
	k_m (m^{1}s^{-1})		2.00E-03		9.37E-04		3.06E-03
VEGF Two-sites	k_{a1} (M^{-1}s^{-1})	2.00E+07	2.00E+07	5.07E+06	9.05E+06	3.49E+07	3.10E+07
	k_{a2} (M^{-1}s^{-1})	1.17E+05	6.50E+04	1.14E+05	6.28E+04	1.20E+05	6.72E+04
	R_T (mol^{1}m^{-2})	2.95E-09	3.00E-09	2.92E-09	2.97E-09	2.98E-09	3.03E-09
	α	2.19E-01	3.30E-01	2.09E-01	3.18E-01	2.30E-01	3.42E-01
	k_{d1} (s^{-1})	8.29E-03	6.43E-03	7.43E-03	2.87E-03	9.16E-03	9.99E-03
	k_{d2} (s^{-1})	1.23E-04	1.20E-04	8.67E-05	5.28E-05	1.59E-04	1.87E-04
	k_m (m^{1}s^{-1})		2.95E-06		2.18E-06		3.72E-06
ECD Two-sites	k_{a1} (M^{-1}s^{-1})	1.00E+06	1.00E+06	8.77E+05	8.82E+05	1.12E+06	1.12E+06
	k_{a2} (M^{-1}s^{-1})	2.10E+05	2.04E+05	2.07E+05	2.02E+05	2.13E+05	2.07E+05
	R_T (mol^{1}m^{-2})	1.19E-09	1.20E-09	1.18E-09	1.20E-09	1.19E-09	1.21E-09
	α	2.48E-01	2.48E-01	2.34E-01	2.34E-01	2.61E-01	2.62E-01
	k_{d1} (s^{-1})	7.60E-03	7.82E-03	7.02E-03	7.19E-03	8.19E-03	8.44E-03

	k_{d2} (s^{-1})	5.99E-05	7.82E-05	2.80E-05	4.50E-05	9.18E-05	1.11E-04
	k_m (m^{1}s^{-1})		1.99E-03		6.06E-04		3.38E-03
VEGF Parallel reactions	k_{a1} (M^{-1}s^{-1})	1.00E+06	1.00E+06	3.09E+05	1.53E+05	1.69E+06	1.85E+06
	k_{a2} (M^{-1}s^{-1})	1.40E+05	1.10E+05	1.36E+05	1.07E+05	1.44E+05	1.13E+05
	R_T (mol^{1}m^{-2})	5.07E-09	5.13E-09	5.00E-09	5.10E-09	5.13E-09	5.15E-09
	k_{d1} (s^{-1})	1.18E+00	1.29E+00	3.58E-01	1.89E-01	2.00E+00	2.39E+00
	k_{d2} (s^{-1})	3.59E-04	2.46E-04	3.35E-04	2.26E-04	3.84E-04	2.66E-04
	k_m (m^{1}s^{-1})		1.99E-03		1.83E-03		2.15E-03
ECD Parallel reactions	k_{a1} (M^{-1}s^{-1})	1.00E+06	1.00E+06	6.56E+05	2.76E+05	1.34E+06	1.72E+06
	k_{a2} (M^{-1}s^{-1})	2.60E+05	2.90E+05	2.55E+05	2.83E+05	2.65E+05	2.97E+05
	R_T (mol^{1}m^{-2})	1.94E-09	1.86E-09	1.92E-09	1.85E-09	1.96E-09	1.88E-09
	k_{d1} (s^{-1})	6.82E-01	3.97E-01	4.44E-01	1.29E-01	9.19E-01	6.65E-01
	k_{d2} (s^{-1})	2.75E-04	2.30E-04	2.60E-04	2.11E-04	2.91E-04	2.48E-04
	k_m (m^{1}s^{-1})		2.35E-06		1.89E-06		2.82E-06
VEGF Consecutive reactions	k_{aR} (M^{-1}s^{-1})	7.73E+05	1.50E+06	7.10E+05	1.30E+06	8.37E+05	1.70E+06
	k_{aRA} (M^{-1}s^{-1})	2.78E+04	1.50E+04	2.60E+04	1.32E+04	2.96E+04	1.68E+04
	R_T (mol^{1}m^{-2})	1.57E-09	1.74E-09	1.54E-09	1.68E-09	1.61E-09	1.80E-09
	k_{dRA} (s^{-1})	1.46E-03	2.83E-03	1.36E-03	2.43E-03	1.55E-03	3.23E-03
	k_{dR2A} (s^{-1})	4.53E-04	8.12E-04	4.18E-04	7.47E-04	4.88E-04	8.77E-04
	k_m (m^{1}s^{-1})		3.57E-07		3.34E-07		3.80E-07
ECD Consecutive reactions	k_{aR} (M^{-1}s^{-1})	1.00E+06	1.00E+06	9.49E+05	9.38E+05	1.05E+06	1.07E+06
	k_{aRA} (M^{-1}s^{-1})	2.30E+05	2.30E+05	2.25E+05	2.24E+05	2.35E+05	2.36E+05
	R_T (mol^{1}m^{-2})	4.96E-10	4.96E-10	4.89E-10	4.94E-10	5.03E-10	4.98E-10
	k_{dRA} (s^{-1})	2.13E-03	2.15E-03	1.99E-03	1.98E-03	2.28E-03	2.32E-03
	k_{dR2A} (s^{-1})	3.24E-04	3.41E-04	3.08E-04	3.24E-04	3.41E-04	3.58E-04
	k_m (m^{1}s^{-1})		4.62E-06		1.01E-06		8.23E-06

6. Conclusions and perspectives

The work presented in this doctoral thesis allowed to add key pieces of information to the broad (and still mysterious) puzzles of two classes of bio-macromolecules: amyloid fibrils and fibronectin.

Regarding amyloid fibrils, we presented three separate works that cover three different aspects of the behaviour of amyloid gels: their formation dynamics, their structure, and the possibility of strengthening them through the inclusion of polysaccharide chains.

In chapter 2, «Unraveling amyloid fibril gelation by Photon Correlation Imaging: kinetics, microscopic dynamics, and temporal heterogeneity», we showed a study, aimed at unveiling key physical phenomena that underlie amyloid fibril gelation. We prepared amyloid gels at two different ionic strengths, by allowing Na^+ and Cl^- ions to move into the fibril dispersion through a semi-permeable membrane. The gelation front was found to advance with a linear-in-time behaviour; although this phenomenon had already been observed in the case of a Ca^{2+}-induced alginate gel, the physical explanation of the non-diffusive behaviour of the ion species is still lacking. While this will be the topic of a future publication, we share hints that suggest the observed phenomenon to be related to a combination of Donnan effect and electrostatic screening heterogeneity.
On the side of the peculiar behavior of the gelation front, we also found that the ionic strength of the gels affected the entity and the spatial propagation of stress-releasing rearrangement events.
Future perspectives of this study consist in a further analysis based on changing a wider range of parameters (concentration of amyloid fibrils and their contour length), and in optimising the diffusion setup so that the salt bath is in volumetric large excess compared to the protein solution. In fact, if the concentration of salt in the reservoir can be assumed to be constant over the entire gelation process, it is possible to better compute the driving force that makes the ions move; furthermore, changing the single-fibril properties and their entanglement state allows to better appreciate how the rise and the propagation of stress-releasing events change as a function of network connectivity.

In chapter 3, «Probing the Structure of Filamentous Nonergodic Gels by Dynamic Light Scattering», we showed that the theory of scattering from nonergodic media can be combined with the theory of scattering from semi-flexible polymers, to derive an analytical expression that allows to extract the mesh size (ξ_m) of semi-flexible polymer networks from the plateau value of their measured intermediate scattering function ($f(q, \tau)$). One surprising point that emerged in the mathematical derivation was that the value of the mesh size is experimentally correlated only with the plateau value of $f(q, \tau)$, without the persistence length (l_p) of the network-constituting units playing any role. This result was shown to be related to a subtle cancellation effect: it is true that an increase in l_p lowers the bending fluctuations of the constituting units, but it is also true that such an increase leads to a higher value of the entanglement length (L_m), with the two effects balancing each other.
The established approach allowed to extract the mesh size of semi-diluted βLG amyloid fibril gels, which was in quantitative agreement with estimates made through a modified version of the cubic lattice model. As pre-factors in polymer physics are notoriously delicate, future studies are encouraged to explore whether the derived equations can be fruitfully used with other classes of semi-flexible polymers, to quantitatively extract the mesh size of the networks they form. Moreover, further research is needed to clarify the scaling dependence of L_m on the concentration of semi-flexible polymers (c) and on l_p. In fact, this scaling dependence, which is still debated in the literature, is important for the mathematical derivation of how ξ_m and the plateau value of $f(q, \tau)$ are related.

In chapter 4, «Polysaccharide-reinforced amyloid fibril hydrogels and aerogels», we explored the possibility of employing polysaccharide chains (κ-carrageenan and low-acetylated Gellan Gum) to mechanically strengthen amyloid fibril networks, while keeping the surface functionality of the protein component intact. An AFM analysis of the network constituting units showed that the polysaccharide components can diffuse inside already-formed amyloid gels. Such a diffusion, which was confirmed by gravimetric analysis, generated reinforced hydrogels and aerogels with a high degree of protein surface functionality.

The performed study shows an interesting route for the synthesis of functional, eco-friendly materials. At the same time, we believe that further steps would enable a more efficient transition of the established approach towards production up-scaling.

The first of these steps would make use a buffer system to shift the pH of the formed amyloid gels towards neutral values. In fact, in the performed study, the pH of the formed amyloid gels (initially equal to 2) was brought toward close-to-neutral values upon immersion in Milli-Q alkaline baths. Therefore, the final pH fluctuated considerably, with consequent inhibition of an optimal tuning of the diffusion of the polysaccharide components.

The second step would involve a better elucidation of how the polysaccharides become embedded in the already-formed amyloid fibril gels. Although SEM imaging on the aerogels gave precious hints on the microstructure of the synthesized hybrid materials, shrinkage during solvent exchange to ethanol and supercritical CO_2 drying probably led to differences between the microstructure of the aerogels and the one of the pristine hydrogels. We encourage therefore alternative ways ways to better unveil the mechanisms by which the polysaccharide units strengthen the gels, while leaving a close-to-intact surface reactivity of the amyloids.

The third step, the exploration of which we encourage, is related to the embedding mechanism of the polysaccharide component. In our study, we let the sugar units diffuse inside amyloid gels, the pH of which was close to neutrality: this was done to avoid electrostatic complexation. It would be beneficial to enrich the protocol with ways to directly mix the protein and the polysaccharide fractions, while avoiding charge-induced complexation phenomena. This last point would, in fact, allow to scale up the production of hybrid gels, closing in this way the gap between a lab-scale analysis and a pilot-plant production.

Regarding fibronectin, we showed in chapter 5 that heparin-mediated conformational changes of the macromolecule allow not only interactions with VEGF (as already known in the scientific community), but also with the extra-cellular domain of VEGFR2, the major cell-surface cognate receptor of this GF. The interactions of both VEGF and VEGFR2 with fibronectin were shown to be favoured at acidic pH, not due to structural changes in the ligands (as confirmed by CD experiments), but potentially due to changes in the protonation state of their binding sites (as suggested by a pKa analysis of surface-exposed amino acid residues). The importance of this observation becomes evident if we consider that acidic extracellular pH is a hallmark of hypoxia, which signals the need for angiogenesis. Moreover, the binding of the two ligands was shown to not be mutually exclusive: the assays we performed confirmed the possibility of forming a VEGF/VEGFR2/fibronectin triple complex. This discovery can pave new routes for better understanding the angiogenic signaling pathways led by the considered species.

The main contribution of the author of this doctoral thesis in this work, was to build the models and develop the codes for describing and interpreting SPR measurements in order to calculate the affinity and binding kinetics of VEGF and VEGFR2 towards fibronectin. The interactions did not follow a simple one binding site model and we explored several alternative models that could fit the experimental data. The model that better described the binding behavior assumed that the entire fibronectin population consisted of two classes of binding sites (A and B), which had different affinities and binding kinetics towards the ligands. The presence of two different populations was not ascribed to an incomplete action of heparin, but instead hypothesized to be related to structural heterogeneity of the fibronectin molecules, that might arise from alternative splicing or the presence of bound glycans. The performed study clarifies some important aspects of fibronectin/VEGF/VEGFR2 interactions, which could influence VEGF signaling and therefore, be of physiological significance. At the same time, it leaves some open questions for future study. A first important point to be clarified, is

where VEGF and VEGFR2 binding sites on fibronectin are located. We showed that the presence of heparin inhibited the binding of VEGFR2, but not the one of VEGF, suggesting that the two ligands do not share exactly the same binding sites. Therefore, future studies (based one the use of fibronectin fragments and mutants) are encouraged to map more precisely the location of the VEGF and VEGFR2 binding sites on fibronectin. Moreover, the modelling of the SPR data would benefit from the possibility of simultaneously considering rebinding phenomena with different substrate populations. We did not attempt this in the current study, in order to avoid over-parametrization in the used system of differential equations; however, we encourage a future exploration of mathematical studies in this direction.

To conclude, the studies presented in this doctoral thesis unveiled the gelation dynamics of βLG amyloid fibril solutions upon diffusion of ions, and showed paths to structurally characterize and reinforce already-formed amyloid fibril gels. We also presented a work that widens the understanding of key phenomena that underlie the binding mechanisms of fibronectin.

The sum of collected evidence sets a solid ground, on which future discoveries and applications can lay. The broader understanding on the gelation mechanism of amyloid fibrils, together with the double possibility of probing the structure and mechanically reinforcing amyloid gels, set routes to better design solid amyloid materials, which can be used in a broad ensemble of diverse fields. One can think, for instance, about the possibility of tuning the properties of gels and aerogels designed for drug delivery, wound healing or sensing purposes.

The presented study on fibronectin, VEGF and VEGFR2, on the side of widening our understanding about the fascinating mechanisms that Nature employs, adds to current literature key pieces of information, that can lead to a better design of drugs that target angiogenesis.

The author of this thesis hopes that the results and considerations shared herein will inspire new studies and discoveries.

Appendix

A. Investigating the Mechanism of Cyclodextrins in the Treatment of Niemann-Pick Disease Type C Using Crosslinked 2-Hydroxypropyl-β-cyclodextrin

Dario Carradori, Hsintsung Chen, Beat Werner, Aagam S. Shah, Chiara Leonardi, <u>Mattia Usuelli</u>, Raffaele Mezzenga, Frances Platt, and Jean-Christophe Leroux*

Investigating the Mechanism of Cyclodextrins in the Treatment of Niemann-Pick Disease Type C Using Crosslinked 2-Hydroxypropyl-β-cyclodextrin

Dario Carradori, Hsintsung Chen, Beat Werner, Aagam S. Shah, Chiara Leonardi,
Mattia Usuelli, Raffaele Mezzenga, Frances Platt, and Jean-Christophe Leroux*

Niemann-Pick disease type C (NPC) is a severe disorder that is characterized by intracellular transport abnormalities leading to cytoplasmic accumulation of lipids such as cholesterol and sphingolipids. The compound 2-hydroxypropyl-β-cyclodextrin (HPβCD) has high cholesterol complexation capacity and is currently under clinical investigation for the NPC treatment. However, due to its short blood half-life, high doses are required to produce a therapeutic effect. In this work, stable polymerized HPβCD is generated to investigate their in vitro mechanisms of action and in vivo effects. Crosslinked CDs (8–312 kDa) display a ninefold greater cholesterol complexation capacity than monomeric HPβCD but are taken up to a lower extent, resulting in an overall comparable in vitro effect. In vivo, the 19.3 kDa HPβCD exhibits a longer half-life than the monomeric HPβCD but it does not increase the life span of *Npc1* mice, possibly due to reduced brain penetration. This is circumvented by the application of magnetic resonance imaging-guided low intensity-pulsed focused ultrasound (MRIg-FUS), which increases the brain penetration of the CD. In conclusion, stable polymerized HPβCDs can elucidate CDs' mechanism of action while the use of MRIg-FUS warrants further investigation, as it may be key to harnessing CDs full therapeutic potential in the NPC treatment.

1. Introduction

Niemann-Pick disease type C (NPC) is a rare (estimated incidence of 1:120000 live births), inherited and prematurely fatal neurovisceral disorder attributed to the mutation of *Npc1* or *Npc2* genes (95% and 5% of the cases, respectively), which causes unique intracellular transport abnormalities of lipids and, subsequently, their accumulation in late endosomes/lysosomes (LE/LY).[1–4] The clinical course of this lipid storage disorder is heterogeneous and depends on the age of onset.[5–7] In most cases, motor impairment and cognitive decline lead to premature death due to pneumonia and respiratory failure, or therapy-resistant epilepsy. At present, miglustat (Zavesca) is the only drug approved for NPC treatment (in Europe, Brazil, South Korea, Canada and Japan). This iminosugar acts as a competitive inhibitor of the enzyme glucosylceramide synthase, which catalyzes the first step in glycosphingolipid synthesis (i.e., the glycosylation of ceramide). The oral availability and the capacity to cross the blood-brain barrier (BBB) are the main advantages of this drug but the clinical benefits on NPC patients, such as symptoms' stabilization and neurological improvement, remain limited to a short period of time.[8–11]

Different types of pharmacological approaches for NPC treatment are currently under investigation,[12–17] and many of them focus on the regulation of lipid storage in the LE/LY.[3] The cyclic oligosaccharide 2-hydroxypropyl-β-cyclodextrin (HPβCD) is a well-established pharmaceutical excipient that has generated much interest as a potential treatment for NPC due to its high affinity for cholesterol and other NPC-relevant lipids.[18–21] The cyclodextrin (CD) drives a redistribution of the cholesterol from the LE/LY to the extracellular space but the mechanism behind it is not fully understood. In vitro, HPβCD has been shown to trigger the exocytosis of LE/LY content via a pathway that depends on the calcium channel MCOLN1,[22] and to promote lysosomal cholesterol exchange from the cellular plasma membrane to the serum lipoproteins,[23] suggesting a dual action inside and outside the cell. HPβCD is in phase I/II [NCT03893071] and phase II/III [NCT03893071] clinical trials for NPC treatment under the name of Trappsol Cyclo and

Dr. D. Carradori, C. Leonardi, Prof. J.-C. Leroux
Institute of Pharmaceutical Sciences
Department of Chemistry and Applied Biosciences
ETH Zürich
Zürich 8049, Switzerland
E-mail: jleroux@ethz.ch

H. Chen, Prof. F. Platt
Department of Pharmacology
University of Oxford
Oxford OX1 3QT, UK

B. Werner
Center for MR-Research
University Children's Hospital
Zürich 8032, Switzerland

A. S. Shah
Institute of Neuroinformatics
ETH Zürich and University of Zürich
Zürich 8057, Switzerland

M. Usuelli, Prof. R. Mezzenga
Department of Health Sciences and Technology
ETH Zürich
Zürich 8092, Switzerland

The ORCID identification number(s) for the author(s) of this article can be found under https://doi.org/10.1002/smll.202004735.

**ADVANCED
SCIENCE NEWS**
www.advancedsciencenews.com

**NANO · MICRO
small**
www.small-journal.com

VTS-270, respectively. It is intravenously (i.v.) administered at high doses (1500 mg kg^{-1} or 2500 mg kg^{-1} over 8–9 h every 2 weeks) due to it short biological half-life (1.7 h[24]) and its low propensity to cross the BBB.[18] According to recent animal studies, the fraction of injected dose reaching the brain is very small,[25] and relatively low levels (30–450 µg mL^{-1}) have been detected in human cerebrospinal fluids 4 h after the beginning of the i.v. infusion. Consequently, strategies to increase HPβCD deposition in the brain are needed to enhance the efficacy of this treatment.

Recently, linear βCD-prodrugs with high molecular weight (i.e., an acid-labile βCD-based polyrotaxane with a molar mass of ≈30 kDa[26] and a linear pH-degradable βCD-based polymer of ≈33 kDa[27]) were shown to significantly increase the mean life span of NPC mice, while exhibiting a prolonged circulation time versus HPβCD. These preliminary studies suggested that CD's efficacy could be increased by reducing its systemic clearance. However, several mechanistic questions remain unanswered as neither of these studies investigated the impact of CD size on cholesterol complexation capacity, in vitro activity, and cellular uptake in a systematic way. Moreover, the contribution of the CD units (progressively released after administration) to the pharmacokinetics and biodistribution profile of the linear prodrugs was not evaluated and the polymeric CDs were not directly compared to their monomeric counterparts having identical molecular structures.

The molecular weight of CDs can be increased by several methods (e.g., by threading CDs to polymeric networks or by self-assembling host–guest inclusion complexes[28]), albeit crosslinking is one of the most straightforward approaches.[29–32] Epichlorohydrin (EPI) is the preferred crosslinker in polysaccharide chemistry[33] and EPI-derived crosslinked CDs have been found to complex hydrophobic molecules more than their native counterparts due to the presence of interstitial domains in the crosslinked polymer network.[34] One of the advantages of this approach is that EPI crosslinks are not biodegradable, allowing to study the impact of the molecular weight on CD activity, pharmacokinetics, and biodistribution without the interference created by the release of the single units.

In this study, stable HPβCDs of high molecular weight (from 8 to 312 kDa) were synthetized via EPI crosslinking and characterized. Their cytotoxicity profile, in vitro activity (i.e., ability to decrease intracellular cholesterol accumulation) and cellular uptake were investigated on U18666A-induced NPC-fibroblasts.

Furthermore, the pharmacokinetic and biodistribution profiles of a selected HPβCD were determined in healthy rats, and its therapeutic efficacy was assessed in vivo in a NPC animal model (*Npc1*–/– mice) to gain insights on the mechanism of action of CDs in NPC. Finally, the use of magnetic resonance imaging-guided low intensity pulsed-focused ultrasound (MRIg-FUS) was explored as a mean to promote the brain penetration of CDs.

2. Results

2.1. Characterization of Crosslinked HPβCDs

High molecular weight HPβCDs were synthesized by EPI crosslinking under alkaline conditions.[35] The molecular weight was varied by adjusting the reaction times, which were sixfold shorter than those reported for βCD due to the higher reactivity of HPβCD. Five different crosslinked HPβCDs were prepared and characterized for their physicochemical properties (**Table 1**, Figures 1S and 2S, Supporting Information). The molar mass was found to increase rapidly when the reaction time exceeded 30 min, with the highest reproducibility obtained when the reaction time was set at 40 min, leading to the 19.3 kDa HPβCD. This crosslinked CD had a hydrodynamic diameter of ≈6.5 nm, which is slightly below the renal excretion threshold by filtration (i.e., 7 nm).[36]

2.2. Cholesterol Complexation Capacity

The complexation capacity of crosslinked HPβCDs was determined by dissolving the latter in water in the presence of excess cholesterol (i.e., 390×10^{-6} M). As shown in **Figure 1**, the crosslinking reaction substantially increased the ability of CDs to bind cholesterol (approximately ninefold), as previously reported for other lipophilic compounds.[34] The concentrations of solubilized cholesterol ranged between 2.7×10^{-6} and 7.5×10^{-6} M for the monomeric HPβCD and reached 20×10^{-6} to 65×10^{-6} M for crosslinked HPβCDs at an equivalent monomeric CD concentration. Differences were also observed among crosslinked HPβCDs, but they were small and did not follow a specific trend, possibly because of the relatively large polydispersity of the macromolecules (Table 1).

Table 1. Crosslinked HPβCD characteristics. Two-way ANOVA with multiple comparisons among the parameters of the CDs within each column (Tukey's post-hoc test). Mean ± SD ($n = 5$ of independent batches, except * where $n = 4$).

Time [min]	MW [kDa]	D_h [nm]	PDI	CD/EPI [%]	HP$_i$/HP$_f$ [%]	Yield [%]
0	1.4 ± 0.6 (A)	2.5 ± 0.5	0.18 (A)	100	100	/
15	8.6 ± 3.8 (A)	5.7 ± 0.7	0.28 (B)	106 ± 11	101 ± 5.4*	40.6 ± 17.8
30	9.3 ± 3.0 (A)	5.6 ± 1.2	0.29 (B)	86.0 ± 21.6	84.0 ± 16.3	41.9 ± 8.2
40	19.3 ± 4.4 (A)	6.6 ± 2.4	0.28 (B)	76.0 ± 17.3	77.0 ± 13.5	46.8 ± 10.3
45	46.0 ± 26.5 (B)	8.2 ± 2.4	0.35 (C)	75.0 ± 13.3	77.0 ± 26.8	47.6 ± 4.9
60	312 ± 216 (B)	21.0 ± 13.2	0.41 (D)	80.0 ± 8.3	81.0 ± 16.0	54.4 ± 16.0

MW: molecular weight; D_h: hydrodynamic diameter; PDI: polydispersity index and HP$_i$/HP$_f$, initial/final hydroxypropyl groups ratios; matching letters in superscript (A, B, C, D) indicate a statistically significant difference ($p < 0.05$).

ADVANCED
SCIENCE NEWS
www.advancedsciencenews.com

NANO · MICRO
small
www.small-journal.com
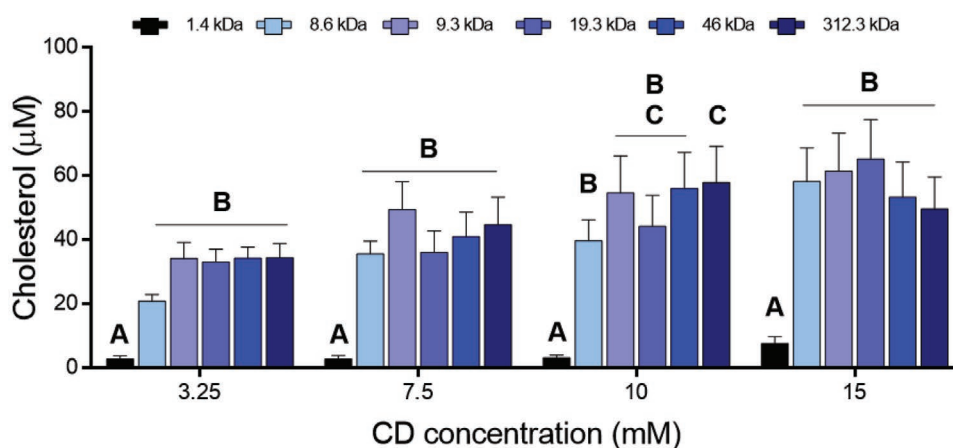
Figure 1. CD cholesterol complexation capacity at 3.25×10^{-3}, 7.5×10^{-3}, 10×10^{-3}, and 15×10^{-3} M. CD concentration is expressed in monomeric units. Two-way ANOVA with multiple comparisons among all CD at the same concentration (Tukey's post-hoc test). Mean + SD ($n = 4$). Different letters indicate a statistically significant difference ($p < 0.05$).

2.3. Impact on Intracellular Cholesterol Accumulation

The NPC-phenotype was induced in mice fibroblasts (L929 cells) with a cholesterol transport inhibitor (U18666A) that binds NPC1 and was confirmed microscopically by filipin staining.[37] NPC-induced fibroblasts were incubated for 48 h with increasing concentrations of CDs in U18666A-free complete medium in order to evaluate the cytotoxicity profile (i.e., lactate dehydrogenase (LDH) release and viability) as well as the CD in vitro activity (i.e., decrease in intracellular cholesterol). NPC-like fibroblasts treated with all tested CD concentrations showed ≥80% viability versus untreated cells, independently of CD molecular weight (**Figure 2**A, top panel). On the other hand, the LDH release progressively increased with CD concentrations (Figure 2A, bottom panel), likely due to the escalating deterioration of the plasma membrane integrity caused by CDs' cholesterol extraction.[38] NPC-like fibroblasts treated with ≤5 × 10^{-3} M HPβCDs released less than 10% of LDH compared to untreated cells while, at 10×10^{-3} M, the LDH release increased up to ≈10–20%. At 15×10^{-3} M, monomeric HPβCD had a significantly higher impact (61%) than the other CDs (up to 25%), which could be explained by the higher cellular uptake of the monomeric versus crosslinked HPβCDs (see Section 2.5). The cytotoxicity evaluation was also performed on normal fibroblasts with a similar outcome (Figure 3S, Supporting Information). Consequently, CD concentrations >10×10^{-3} M (i.e., 15 × 10^{-3} M) were excluded from subsequent cell experiments to avoid significant membrane damage during cellular incubation with the CDs.

Filipin staining revealed a progressive reduction of cytoplasmic and perinuclear cholesterol clusters with increasing CD concentrations (Figure 2B). More specifically, no significant effect was observed at 0.5×10^{-3} M while, above 1×10^{-3} M, all CDs decreased the intracellular cholesterol in a concentration-dependent fashion (Figure 2C), with a trend towards a slightly higher activity for the crosslinked ones. The strongest effect was observed for concentrations ≥5×10^{-3} M, where the intracellular cholesterol decreased down to the normal fibroblast's level (i.e., 67%). Moreover, the shape of the cells became slightly

rounded up when they were incubated for 48 h with 10×10^{-3} M CDs (Figure 3S, Supporting Information), suggesting a possible morphology change not necessarily related to lower cell viability.[39] However, the differences in the in vitro efficacy were not statistically significant among the various CDs at any of the concentrations (Figure 2C). The 5×10^{-3} M concentration was selected for subsequent experiments to ensure significant in vitro activity while excluding interferences due to cell morphology changes.

The impact of the CD size on the duration of the effect was investigated 24 and 48 h after CD treatment (Figure 2D). The reduction of intracellular cholesterol induced by the CDs remained essentially unchanged for 24 h independently of their molecular weight. However, the NPC-phenotype was no longer detectable 48 h after CD treatment since there was no significant difference between NPC-L929 and L929 values in the absence of CD treatment, probably due to cells' recovery from the U18666A inhibition. Therefore, the crosslinking did not increase the duration of the CD effect compared to the monomeric HPβCD.

2.4. Kinetics and Mechanism of CD Cellular Uptake

Monomeric (1.4 kDa), 19.3 and 312.3 kDa HPβCDs were selected to cover the small, medium, and large size ranges, respectively, and were fluorescently labeled with rhodamine B (RhB) to study their cellular uptake. NPC-like fibroblasts were incubated with fluorescent CDs during 48 h and analyzed at specific time points to correlate the CD cellular uptake with the intracellular cholesterol reduction. The incubations with the fluorescent CDs were also performed at low temperature (4 °C) or in absence of ATP in order to determine whether uptake/activity were influenced by membrane fluidity and/or were energy dependent.

The kinetic studies over 48 h showed that the progressive uptake of CDs in the cells (**Figure 3**A, right panel) was accompanied by a concomitant reduction of the intracellular cholesterol accumulation (Figure 3A, left panel). At incubation

**ADVANCED
SCIENCE NEWS**
www.advancedsciencenews.com

**NANO · MICRO
small**
www.small-journal.com
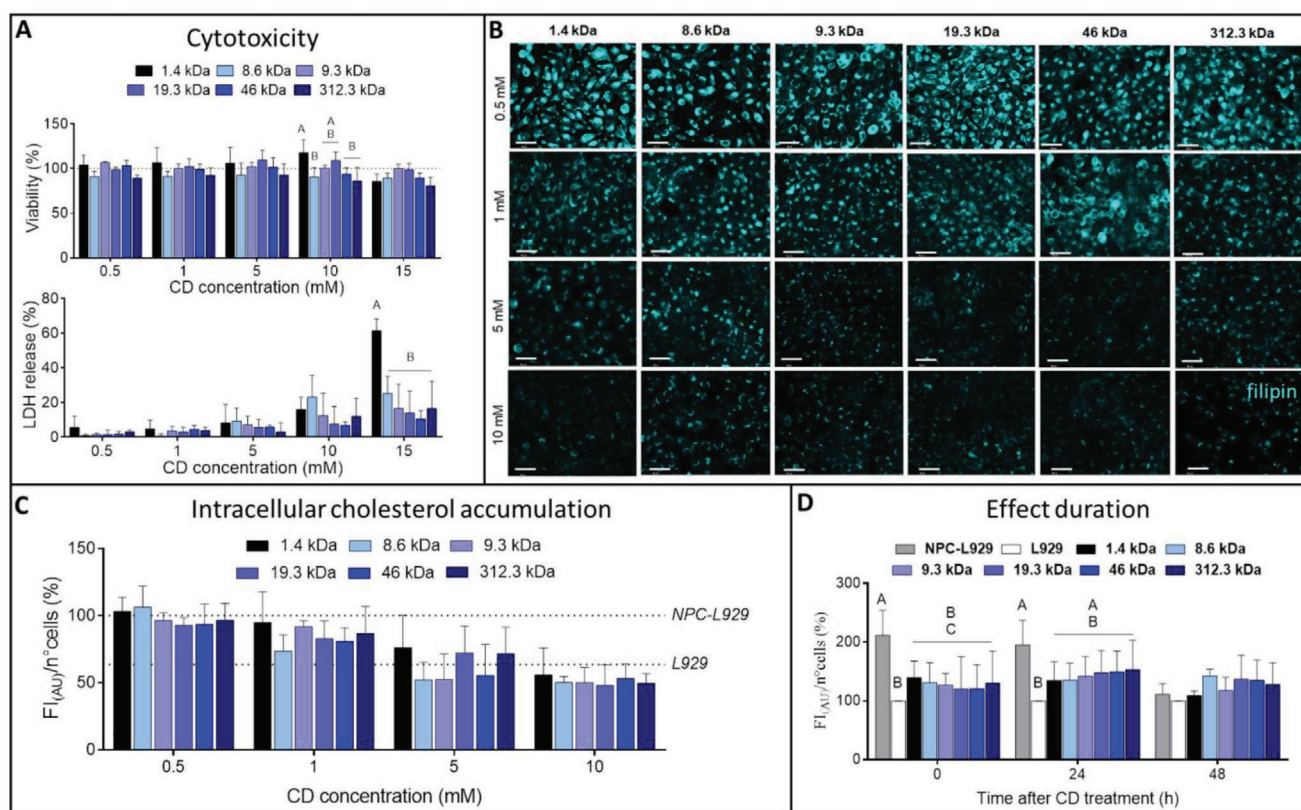
Figure 2. CD effect on intracellular cholesterol accumulation in NPC-like fibroblasts. NPC-L929 cells were treated with the different CDs (1.4–312.3 kDa) at increasing concentrations (0.5–15 × 10⁻³ M). CD concentration is expressed in monomeric units. A) LDH release and cell viability (by MTS) after CD-treatment. B) Representative epifluorescence microscopy images of NPC-L929 cells after CD-treatment. Cyan corresponds to filipin fluorescence (i.e., intracellular cholesterol accumulation). Scale bar: 50 µm. C) Intracellular cholesterol quantification after CD-treatment. D) Duration of CD effect. Two-way ANOVA with multiple comparisons among all CDs at the same concentration (Tukey's post-hoc test). Mean + SD ($n = 3$ for panel A, $n = 5$ for B and C, $n = 4$ for D). Different letters indicate a statistically significant difference ($p < 0.05$).

times ≤4 h, CD cellular uptake and impact on intracellular cholesterol were comparable for both crosslinked CDs. The monomeric HPβCD led to a comparable reduction of intracellular cholesterol, despite its uptake being sixfold higher than that of crosslinked HPβCDs. For longer incubation times (≥8 h), all CDs affected the intracellular cholesterol accumulation similarly, reducing it by -36% and -46% even though the monomeric HPβCD was taken up by cells 2- and 10-fold more than the 19.3 and 312.3 kDa HPβCDs, respectively. Representative images of the cells incubated with the CDs after different time-points are available in Figure 4S (Supporting Information). Furthermore, the intracellular localization of the fluorescent CDs was evaluated by scanning laser confocal microscopy. The orthogonal sectioning image analysis showed the progressive uptake of the CDs in the NPC-like fibroblasts over different time points (Figure 5S, Supporting Information), with a significant CD presence (monomeric and crosslinked) in the cytoplasm (Figure 3B, top panel) and at cholesterol accumulation sites after 48 h (Figure 3B, bottom panel).

The CD uptake was modulated by temperature and ATP levels (Figure 3C). At 4 °C, the uptake of all fluorescent CDs decreased (-75% for monomeric, -98% for 19.3 kDa HPβCD and

−95% for 312.3 kDa HPβCD), resulting in intracellular cholesterol levels 50–60% higher than those measured at 37 °C. On the other hand, the ATP depletion reduced the uptake of the crosslinked CDs exclusively (≈−80%), producing an intracellular cholesterol increase of 25% for 19.3 kDa HPβCD and 150% for 312.3 kDa HPβCD. The uptake of monomeric HPβCD was not impacted, though a small but significant increase (≈25%) of intracellular cholesterol was observed.

2.5. Modulation of the CD In Vitro Activity by the CD Inclusion Site

The importance of having free CD inclusion sites to achieve efficacious intracellular cholesterol complexation in NPC-like fibroblasts was investigated. Using CDs that were pre-complexed with cholesterol, the variation of intracellular cholesterol accumulation was quantified microscopically by filipin staining (**Figure 4**). Precomplexation with cholesterol significantly affected the monomeric HPβCD function, resulting in a 75% activity loss. Interestingly, when the exogenous cholesterol and the monomeric HPβCD were added separately, the

**ADVANCED
SCIENCE NEWS**

www.advancedsciencenews.com

NANO · MICRO

small

www.small-journal.com
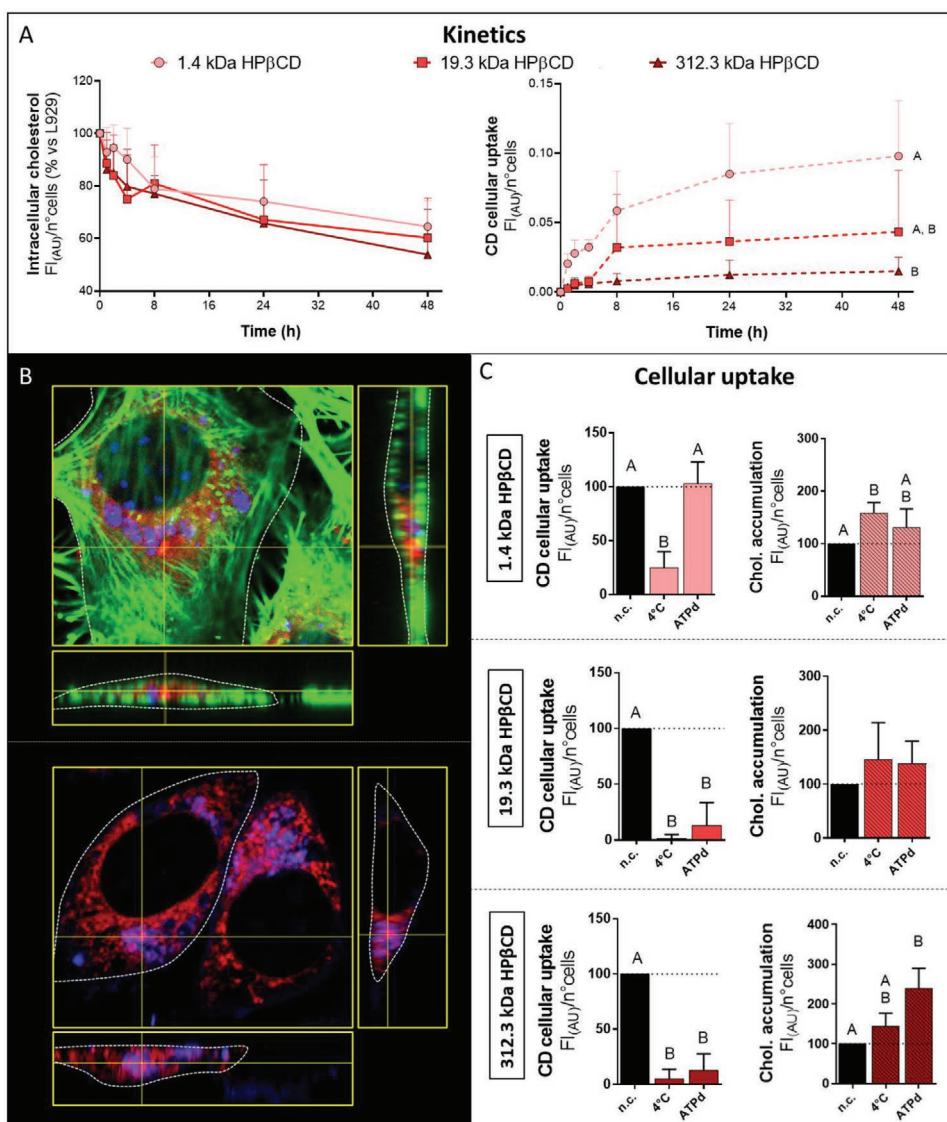
Figure 3. CD cellular uptake. A) Intracellular cholesterol (left panel) and CD cellular uptake (right panel) kinetics. Two-way ANOVA with multiple comparisons among all CDs at the same time point (Tukey's post-hoc test). Mean + SD ($n = 5$). B) Representative orthogonal sections of confocal microscopy images of CDs (monomeric HPβCD in this case) inside the cells (top panel) and colocalized with intracellular cholesterol (bottom panel). Blue corresponds to filipin (i.e., intracellular cholesterol), green corresponds to phalloidin (i.e., cytoskeleton), red corresponds to RhB (i.e., fluorescent CD), and violet corresponds to the colocalization between filipin and RhB. C) CD cellular uptake under normal conditions (n.c.), at low temperature (4 °C) or under ATP depletion (ATPd). One-way ANOVA with multiple comparisons among the different incubation conditions of each CD (Tukey's post-hoc test). Mean + SD ($n = 5$). Different letters indicate a statistically significant difference ($p < 0.05$).

effect on intracellular cholesterol complexation was preserved, indicating the importance of having a free inclusion site in the oligosaccharide structure. On the other hand, the activity of the crosslinked HPβCDs was not significantly reduced by the precomplexation in comparison to adding the CDs and cholesterol separately. Therefore, the crosslinking seemed to counteract the activity loss observed in the pre-complexed monomeric HPβCD. Monomeric HPβCD can only rely on the inclusion site of its cyclic structure while crosslinked CDs have binding sites in their polymeric network (i.e., the "extra" interstitial sites). Since the amount of cholesterol used for precomplexation is the same among all CDs, the remaining number of

available sites for cholesterol complexation in the presence of the cells is higher for crosslinked CDs. Therefore, most of their activity can be maintained as opposed to monomeric HPβCD, which are less active.

2.6. Pharmacokinetic Study

Despite having a similar in vitro activity to the other crosslinked CDs (Figures 1–4), the 19.3 kDa HPβCD was selected for the pharmacokinetics and efficacy experiments based on its favorable size, which should contribute to a longer half-life in
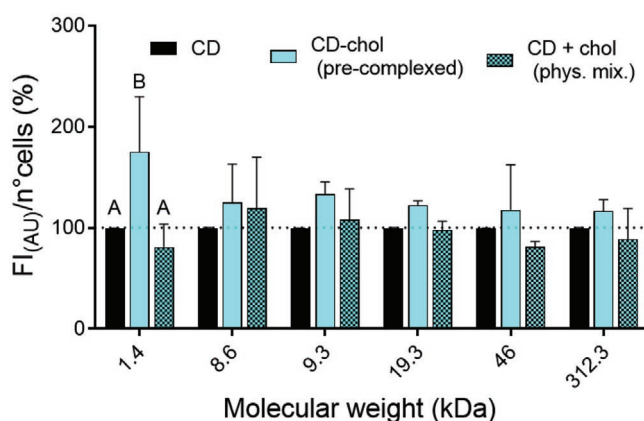
Figure 4. Role of CD inclusion site after precomplexation with cholesterol on in vitro activity. Two-way ANOVA with multiple comparisons among the different complex-related conditions of each CD (Tukey's post-hoc test). Mean + SD ($n = 3$). Different letters mean a statistically significant difference ($p < 0.05$).

vivo (i.e., 2.5 times larger than native HPβCD but close to the renal filtration threshold).

Following i.v. injection in wild-type rats, the 19.3 kDa HPβCD displayed a prolonged circulation time compared to the monomeric HPβCD (**Table 2**, **Figure 5**A). The terminal half-life ($t_{1/2}$) and mean residence time (MRT) increased from 2.6 to 3.8 h and 0.2 to 2.3 h, respectively, while the clearance (CL) was reduced by 40%, likely reflecting a slower elimination from the body. Moreover, the apparent volume of distribution (V_d) decreased from 0.086 to 0.076 L kg^{-1}, reflecting the increased retention in the blood pool.

Twelve hours after CD injection, 19.3 kDa HPβCD was mainly found in lung, liver and spleen ($\approx$10% of the injected dose per g of organ, ID g^{-1}), followed by the kidney and the pancreas ($\approx$5% ID g^{-1}), while the monomeric HPβCD could only be recovered in small amounts in the liver and spleen ($\approx$2% ID g^{-1}) (Figure 5B). The distribution in the central nervous system was generally extremely low ($\leq$0.5% ID g^{-1}) for both CDs. Traces of the 19.3 kDa HPβCD were found in the spinal cord (0.4% ID g^{-1}). Since the concentration of both types of CDs seemed similar in the brain, their penetration in the parenchyma was compared. The 19.3 kDa HPβCD was confined in small clusters while the 1.4 kDa HPβCD diffused widely and homogeneously in the tissue (Figure 5C).

Table 2. Pharmacokinetic parameters of i.v. injected monomeric and crosslinked CDs ($t_{1/2}$, terminal half-life; C_{max}, maximum serum concentration; AUC$_{0-t}$, area under the curve from 0 to t ($t = 12$ h for 1.4 kDa HPβCD and $t = 24$ h for 19.3 kDa HPβCD); CL: clearance; V_d: apparent volume of distribution, MRT: mean residence time).

Parameters	Unit	1.4 kDa HPβCD	19.3 kDa HPβCD
$t_{1/2}$	h	2.62	3.78
C_{max}	µg mL^{-1}	4160	4160
AUC$_{0-t}$	[µg mL^{-1}] h	2200	3550
CL	mg h^{-1}	0.023	0.014
V_d	L kg^{-1}	0.086	0.076
MRT	H	0.2	2.3

In order to test the in vivo activity, monomeric (1.4 kDa) and crosslinked (19.3 kDa) HPβCD were intraperitoneally (i.p.) injected in Npc1 mice at two different doses (1333 and 4000 mg kg^{-1}). The selected dose was based on previous reports[40–42] showing efficacy after single dosing. In the literature,[43] it was reported that in this model, mice with no treatment had a life span of about 11 weeks. The administration of the crosslinked HPβCD did not appear to increase survival, resulting in a lifespan of $\approx$11–12 weeks. Indeed, the therapeutic effect was significantly inferior compared to that of the monomeric HPβCD at the two tested doses, i.e., 13.8 and 15. 3 weeks at 1333 and 4000 mg kg^{-1}, respectively (Figure 5D).

2.7. Magnetic Resonance Imaging-Guided Low Intensity-Pulsed Focused Ultrasound

The limited in vivo therapeutic activity of the 19.3 kDa HPβCD was attributed to its increased retention in the blood pool (Table 2) and lower diffusion in the organs in comparison to the monomeric HPβCD (Figure 5B), in particular in the brain (Figure 5). In a pilot study in wild type rats, magnetic resonance imaging-guided low intensity-pulsed focused ultrasound (MRIg-FUS) was applied to transiently open the BBB and increase the accumulation and diffusion of the monomeric and 19.3 kDa HPβCD in the brain parenchyma.

Extravasation of gadolinium (**Figure 6**A) and Evan's blue (Figure 6B) indicated an increased BBB permeability in the site of MRIg-FUS application. Therefore, 19.3 kDa HPβCD was i.v. injected during the FUS sequence and its brain accumulation was evaluated 8 h after CD administration. The macromolecule showed a stronger and wider diffusion compared to the control regions (i.e., ultrasound-untreated areas) (Figure 6C). Furthermore, the CD was found in the proximity of astrocytes and oligodendrocytes (Figure 6D), suggesting a diffusion towards the neural cells rather than an accumulation on the epithelial cells of the blood vessels. The combination of i.v. injected monomeric CD with MRIg-FUS produced similar results, such as stronger and wider CD diffusion versus control regions and CD localization in proximity of astrocytes and oligodendrocytes (Figure 6S, Supporting Information).

3. Discussion

NPC is a devastating neurovisceral disorder with a profound impact on the patient's life, imposing tremendous limitations in basic physiological and social needs. The progression of the disease leads NPC patients to inexorably lose their autonomy, while financial costs, emotional stress, and logistical complexities increase.[1–7] To date, miglustat is the only approved NPC treatment but its clinical benefit is limited. Several pharmacological approaches are currently under clinical trial, including HPβCD, adrabetadex [NCT03643562], lithium carbonate [NCT03201627], N-acetyl-L-leucine [NCT03759639], arimoclomol [NCT02612129, NCT04316637], vorinostat [NCT02124083] and pluripotent stem cells [NCT03883750]).[17] HPβCD is one of the most studied molecules for NPC treatment and is being tested in several clinical trials, six of them are currently active (source:

**ADVANCED
SCIENCE NEWS**

www.advancedsciencenews.com

NANO · MICRO

small

www.small-journal.com
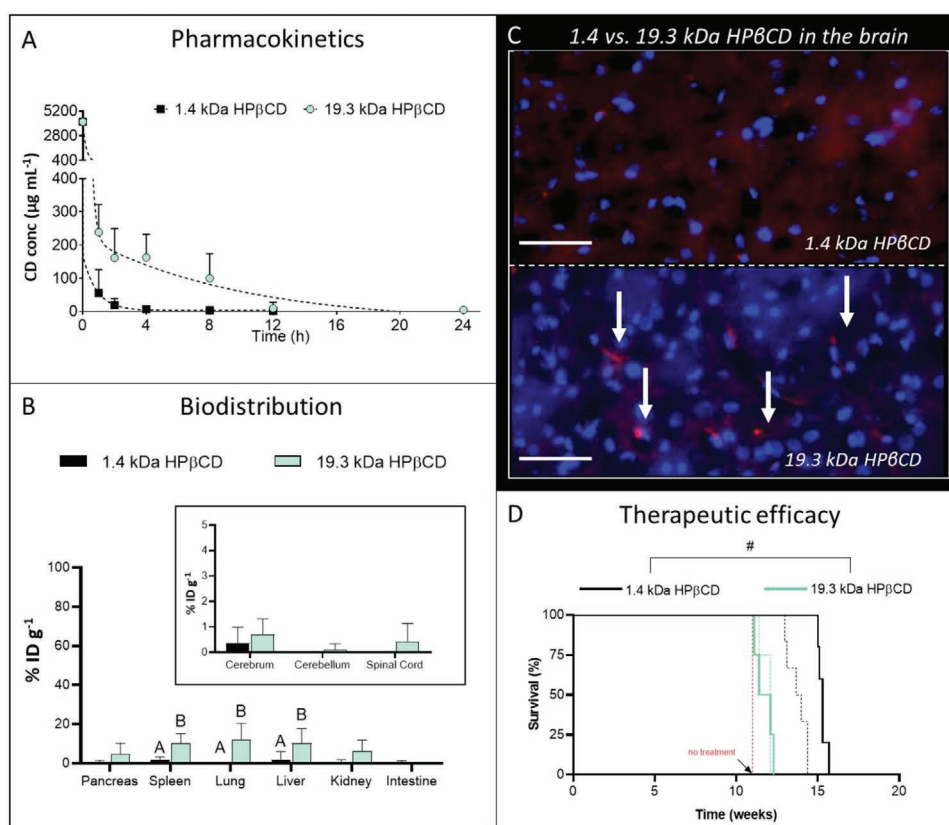
Figure 5. CD pharmacological properties. A) CD pharmacokinetics in rat plasma at different time-points. B) CD biodistribution in rat main organs 12 h after CD i.v. administration. Two-way ANOVA with multiple comparisons (Tukey's post-test). Mean + SD ($n = 6$ for cerebrum, cerebellum and spinal cord, $n = 7$ for the other organs). Different letters indicate a statistically significant difference ($p < 0.05$). C) Representative epifluorescence microscopy images of monomeric versus crosslinked CD diffusion in the brain parenchyma. Blue corresponds to Hoechst (i.e., cell nuclei), red corresponds to RhB (i.e., fluorescent CD), scale bar: 50 µm. D) CD therapeutic efficacy in P7 Npc1 mice after CD i.p. injection at 1333 mg kg^{-1} (dotted line) or 4000 mg kg^{-1} (continuous line). Kaplan-Meier survival plot with Log-rank test (Mantel-Cox) between the CDs ($n = 4$ for 19.3 kDa HPβCD at both doses, $n = 6$ for 1.4 kDa HPβCD at 1333 mg kg^{-1} and $n = 5$ for 1.4 HPβCD kDa at 4000 mg kg^{-1}). The symbol # indicates a statistically significant difference ($p < 0.05$).

clinicaltrials.gov). However, there is no consensus on its mechanism of action[44] nor on the need to cross the BBB to display efficacy.[45] Recent reports indicate that increasing the molecular weight of CDs could represent a useful approach to improve the therapeutic outcome by prolonging the circulation time of these drugs.[19] On the other hand, increasing the molecular weight can also decrease the amount of drug reaching the brain due to the BBB.[46] Previous studies relied on macromolecular CD systems,[26,27] which were designed to gradually release monomeric βCD. However, they did not distinguish between the released unit and the linear prodrug, complicating interpretations of the impact of the molecular weight on the efficacy. In this work, stable crosslinked HPβCD with non-biodegradable linkers were developed as a tool to gain insight into the mechanism of action of CDs.

The simple modulation of the reaction time during EPI crosslinking produced different molecular weight HPβCDs. The presence of interstitial ("extra") inclusion sites in the branched polymeric network made these compounds significantly more capable of cholesterol complexation in solution (up to ninefold) than the monomeric HPβCD. The higher complexation capacity, however, did not result in a higher in vitro

efficacy in NPC-phenotype fibroblasts. Crosslinked HPβCDs were taken up by the cells less efficiently (from 2- to 10-fold) than monomeric HPβCD. Consequently, it is possible that the lower cell uptake of the crosslinked HPβCDs counteracted their high cholesterol complexation capacity, thwarting its in vitro effect. Precomplexation with cholesterol had been previously characterized physicochemically[47,48] and used to reduce the toxicity of high CD concentrations by decreasing CD-induced cholesterol extraction from plasma membrane. However, its impact on the CD-mediated intracellular cholesterol accumulation had not been investigated in vitro.[49] By preloading the CDs with cholesterol at a ratio sufficient to saturate the cavities of the CD units (but not those created by the crosslinks), it was possible to establish that cholesterol complexation is crucial for the in vitro activity. This central role in the mechanism of action is in line with a recent publication where βCDs were less efficient in vitro when their inclusion site was stably occupied by a polymeric chain.[50] Indeed, our data showed that prefilling CD inclusion sites generally abolished the in vitro efficacy of monomeric HPβCD, whereas the effect was much less pronounced with the crosslinked CDs, which were still capable of capturing cholesterol in the void spaces created by the crosslinks.

**ADVANCED
SCIENCE NEWS**

www.advancedsciencenews.com

**NANO · MICRO
small**

www.small-journal.com
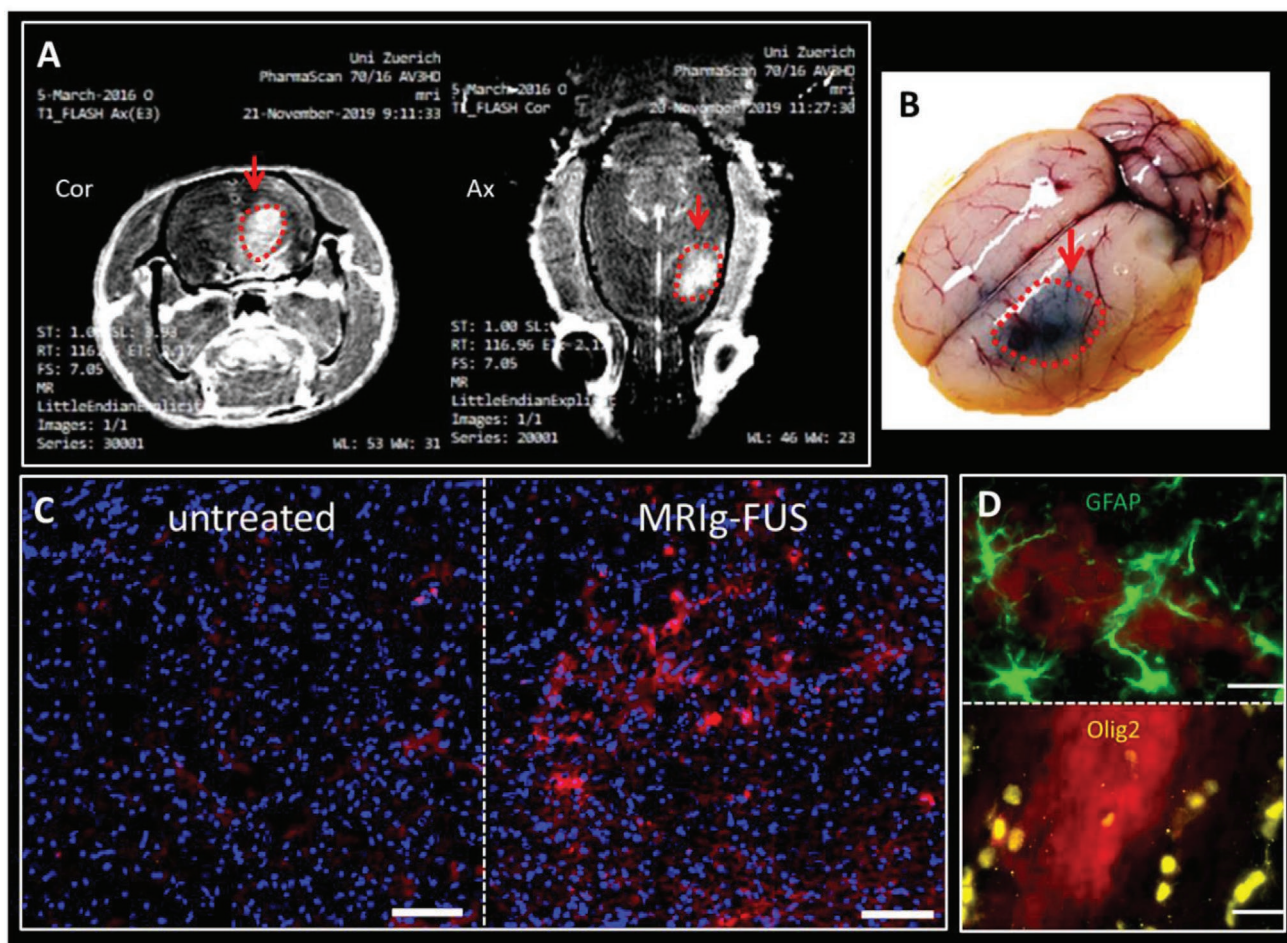
Figure 6. Brain diffusion of crosslinked CD after MRIg-FUS. A) T1-weighted MRI of gadolinium extravasation (clear grey) after MRIg-FUS. B) Full brain picture of Evan's blue extravasation (dark blue) after MRIg-FUS. C) Representative microscopy images showing the diffusion of 19.3 HPβCD in untreated (left) and MRIg-FUS treated (right) brain regions. Blue corresponds to Hoechst (i.e., cell nuclei), red corresponds to RhB (i.e., fluorescent CD), scale bar: 100 µm. D) Representative microscopy images showing the localization of 19.3 HPβCD compared to the astrocytes and oligodendrocytes. Green corresponds to GFAP (i.e., astrocytes), yellow corresponds to Olig2 (i.e., oligodendrocytes), red corresponds to RhB (i.e., fluorescent CD), scale bar: 20 µm.

Our data also indicated that the cellular uptake was key for the activity of either types of CDs. The crosslinked CDs were mainly taken up via an energy-dependent process (likely endocytosis), which could be expected considering that their large molecular weight would hamper their diffusion through the cell membrane.[51] In contrast, the fact that monomeric HPβCD uptake was only reduced at 4 °C and not under energy depleting conditions would support the theory that a diffusive process might be involved.[52] Indeed, it is known that the rigidity of the cell membrane increases at low temperature, which might impair interactions with the CDs as already observed with other compounds.[53] These findings confirm previous data from Vacca et al.[21] suggesting that cellular uptake is a prerequisite for CDs to significantly decrease intracellular cholesterol accumulation. The authors showed that an important part of the CD activity takes place inside the cell by interacting with a pathway dependent on the calcium channel MCOLN1.[21] Thus, the kinetics and mechanism of cellular internalization of the CD can dictate its efficacy.

The 19.3 kDa HPβCD was selected for the in vivo studies, mainly because its hydrodynamic diameter would make this polymer large enough to increase circulation time, while still allowing its glomerular filtration.[54] The pharmacokinetics profile obtained for the monomeric HPβCD was in line with previously published data,[26,27] showing rapid and nonlinear clearance. On the contrary, the 19.3 kDa HPβCD exhibited longer plasma half-life and decreased clearance, being completely cleared from the bloodstream 24 h after injection. This is in contrast with previous reports on macromolecular βCD-based systems with higher molecular weight (30 kDa[26] and 33 kDa[27]), which were still clearly detectable after 24 and 48 h, respectively. After 12 h, the crosslinked HPβCD was found in small amounts mainly in the organs of the mononuclear system (liver and spleen) and lungs, while monomeric HPβCD was mostly cleared from the body. The concentrations of CD detected in the brain (cerebrum and cerebellum) were extremely low and not significantly different between monomeric and crosslinked HPβCDs, as previously reported for the biodegradable 30 kDa

linear polymer.[26] The fact that after 12 h the monomeric HPβCD was still detectable in the brain is probably due to its slow brain clearance.[55] The prolonged blood circulation time did not lead to a high penetration of the crosslinked CD into the brain. Here, at the same % ID g^{-1}, the monomeric HPβCD showed a wider and more homogeneous diffusion compared to the crosslinked HPβCD that could be attributed to the size difference.

The in vivo activity of the crosslinked HPβCD was assessed in a Npc1$^{-/-}$ mouse model in which the single i.p. injection of an HPβCD dose in P7 old mice had been reported to result in a significant prolonged life span.[40–42] Despite having a comparable in vitro activity on NPC-like fibroblasts and longer circulation time, the crosslinked CD was significantly less effective than the monomeric counterpart at the tested doses, which was the opposite of previously reported findings with the other macromolecular βCD-based systems.[26,27] Aside from the fact that the animal model, dosing regimen, administration route and nature of the monomeric CD (e.g., HPβCD vs βCD) were not the same as in those previous studies, the discrepancy could be explained by the fact that in our system, monomeric CDs were not released from the macromolecular structure due to the non-biodegradability of the crosslinking.[34,35] It is possible that given the lower volume of distribution of the macromolecule and its limited diffusion into the organs' parenchyma, the 19.3 kDa HPβCD may not be able to diffuse deep enough in tissues to exert its activity. It is also conceivable that since crosslinked CDs are taken up by an active endocytotic process, any cells that are unable to passively internalize these larger structures in sufficient amounts would not contribute to the overall in vivo activity.

The limited brain delivery and penetration was addressed employing MRIg-FUS, which has been shown to enhance the deposition of different drugs in various organs[56–58] while being well tolerated by animals[59–63] and humans.[64,65] Moreover, MRIg-FUS showed therapeutic efficacy per se on phosphorylated Tau and amyloid plaques.[66,67] In our exploratory study, brain accumulation and diffusion of the 19.3 kDa HPβCD were appreciably improved after only one application of FUS. Therefore, the combination of MRIg-FUS with the i.v. administration of CDs may represent a new promising strategy for the treatment of NPC. Indeed, it would allow both monomeric and crosslinked HPβCDs to achieve higher doses in the brain, answering the critical question about the importance of brain penetration in the activity of CDs.

To conclude, stable crosslinked CDs proved to be valuable tools to study the mechanism of action of CDs, revealing that both cholesterol complexation and cellular uptake are important determinants of CDs' capacity to lower the intracellular accumulation of cholesterol. By increasing the hydrodynamic diameter of HPβCD, it was possible to increase its circulation time. However, the nonbiodegradable crosslinks impaired tissue penetration and reduced its activity. This could be partially overcome with MRIg-FUS, with which promising results were obtained promoting the penetration of high molecular weight CDs in the brain parenchyma. Considering the technology's increasing availability in hospitals worldwide, MRIg-FUS should be further investigated for its potential implementation in NPC patients receiving CDs or other treatments.[17] In view of previously published work, these data further suggest that

sustained release formulations of CDs, for instance in the form of a biodegradable CD-based implant, could potentially simplify the dosing regimen while potentially improving the treatment efficacy. On the other hand, MRIg-FUS promotes the penetration of high molecular weight CDs in the brain parenchyma and should be further investigated. Indeed, this technology is becoming more easily accessible in the hospitals worldwide and could therefore be implemented in the near future in NPC patients receiving CDs or other treatments.[17]

4. Experimental Section

Animals: Jugular vein-catheterized adult female Sprague Dawley rats were purchased from Janvier Labs (Le Genest Saint Isle, France). Rats were maintained on a constant 12:12 h light:dark cycle while water and food were provided ad libitum. Pharmacokinetic and biodistribution studies were performed in accordance with procedures and protocols approved by the cantonal veterinary authorities (Kantonales Veterinäramt Zürich, license ZH218/17). The animals were euthanized with an overdose of xylazine and ketamine.

The 9 females and 10 males Npc1 mice (BALBc/NPC^{nih}, BALB/cNctr-*Npc1*^{m1N}/J) were generated from heterozygous mice (*Npc1*$^{+/-}$) breeding stock obtained from The Jackson Laboratory (The Jackson Laboratory, Charles River, UK).[53] Mice were maintained on a constant 12:12 h light:dark cycle with food and water available ad libitum. The experiments with these mice were conducted using protocols approved by the United Kingdom home Office Animal Scientific Procedures Acts 1986 (P8088558D).

Rats were selected for the biodistribution and pharmacokinetic study to keep the number of used animals low (more blood can be sampled in rats than in mice) while providing a good model for investigating the impact of crosslinking on the circulation time of macromolecules.[68] However, since a rat model of NPC is not available, the efficacy study was performed on mutant mice, that are widely used for NPC investigations.[69] The type of injection was selected to directly compare the results with the existing literature.[26,27,40–42]

Materials: HPβCD was purchased from CycloLab (Budapest, Hungary). Sodium hydroxide 98.5–100% pellets (NaOH), 15 mm Ø No.1 coverslips and hydrochloric acid (HCl) 37% were purchased from VWR International (Radnor, PA). Filipin III complex *Streptomyces filipinensis* 75% (filipin), acetone 99%, maleic acid ≥ 99%, paraformaldehyde 95% (PFA), epichlorohydrin 99% (EPI), triphenylphosphine (Ph3P) ≥ 95%, sodium azide (NaN$_3$) ≥ 99.5%, sodium methoxide (NaOCH$_3$) ≥ 97%, dichloromethane anhydrous (DCM) ≥ 99.8%, palladium on carbon (PdC) 10 wt%, hydrazine hydrate 98%, rhodamine b isothiocyanate (RhB) mixed isomers, 2-deoxy-D-glucose ≥ 98%, and iodine (I$_2$) 99.9%, Evan's blue 75% were purchased from Merck KGaA (Darmstadt, Germany). Spectra/Por3 dialysis membranes MWCO 3500 were purchased from Spectrum Labs (Rancho Dominguez, CA). Syringe filter units Filtropur S 0.45 μm were purchased from Sarstedt (Nümbrecht, Germany). Pierce LDH Cytotoxicity Assay Kit and Amplex Red Cholesterol Assay Kit were purchased from Invitrogen (Waltham, MA). 96-well black microplates were purchased from Greiner bio-one (Kremsmünster, Austria). Deuterium oxide was obtained from Cambridge Isotope Laboratories (Tewksbury, MA). NCTC clone 929 cells (L929, mouse fibroblasts) were from the American Type Culture Collection (Manassas, VA). CellTiter 96 Aqueous One Solution Cell Proliferation Assay Kit was purchased from Promega AG (Dübendorf, Switzerland). Micro BCA Protein Assay Kit, Gibco fetal bovine serum, Hoechst, rabbit anti-Olig2 polyclonal antibody, rabbit anti-GFAP polyclonal antibody, Alexa goat anti-rabbit Alexa 488 secondary antibody, Gibco DMEM-high glucose-HEPES-no phenol red, Gibco Trypsin-EDTA-phenol red (0.25%), Gibco MEM-GlutaMAX and Gibco penicillin-streptomycin (10 000 U mL^{-1}) were from ThermoFisher Scientific (Waltham, MA). Dimethylformamide (DMF) extra pure was purchased from Fisher Chemical (Hampton, NH). Methanol (CH$_3$OH)

99.8% and pyridine 99.5% were purchased from Acros Organics (Geel, Belgium). 1,2-Distearoyl-sn-Glycero-3-Phosphocholine (DSPC) was from Avanti Polar Lipids (Alabaster, AL). DSPC-N-[methoxy(polyethylene glycol)-2000] (DSPE-PEG2000) and DSPC-N-[methoxy(polyethylene glycol)-5000] (DSPE-PEG5000) were purchased from Corden Pharma (Liestal, Switzerland). Syringes for the production of the microbubble were purchased from Tyco Healthcare (Mansfield, MA).

Synthesis of Crosslinked HPβCDs: Crosslinked HPβCDs were prepared adapting the protocol described by Renard et al.[35] Briefly, 3 g of HPβCD was dissolved in 7 mL of NaOH solution (35% w/w) at 25 °C. The solution was then heated up to 30 °C and 1.72 mL of EPI were added while stirring. After 15, 30, 40, 45, or 60 min, the reaction was stopped by adding 10 mL of acetone. The aqueous phase containing the CD was collected via separating funnel. The solution was neutralized using HCl and dialyzed against deionized water for 3 d using a 3.5 kDa cutoff membrane. The ratios EPI/HPβCD and initial/final hydroxypropyl groups in the crosslinked HPβCDs were obtained by an ^{1}H NMR AV400 400 MHz spectrometer (Bruker, Billerica, MA) (Figure 1S, Supporting Information).[70]

Fluorescently Labeled CDs: The fluorescent CDs were prepared following the method described in Malanga et al.[71] in three steps: azidation, amination, and rhodamine B isothiocyanate (RhB) labeling. Azidation was achieved by dissolving 16 mg of Ph3P (0.06 mmol) and 16 mg of I$_2$ (0.06 mmol) in 20 mL of extra pure DMF under stirring at a temperature below 40 °C. Then, 1.3 mmol of CD (monomeric, 19.3 kDa or 312.3 kDa HPβCD) were added to the solution and the temperature was increased up to 50 °C and stirred for 1 h. The temperature of the solution was decreased down to 30 °C, and 100 mL of CH$_3$OH with 0.1 g of NaOCH$_3$ (1.85 mmol) were added. The solution was kept under stirring for 30 min before removing CH$_3$OH with a rotary evaporator at 40 °C for 1 h at 2 kPa. Afterwards, 2 mL of DMF with 8 mg of NaN$_3$ (0.12 mmol) were added and the solution was heated up to 80 °C and stirred for 2 h. DMF was removed by rotary evaporation at 80 °C for 2 h at 2 kPa and by high vacuum overnight. Subsequently, 20 mL of water were added to the dry material and filtered by glass filtration. The filtrate was extracted by adding 40 mL of DCM. The aqueous phase was frozen overnight and lyophilized for 2 d (yield around 90%). Amination was achieved by dissolving the lyophilized compound in 15 mL of water. Then, 0.18 g of PdC, previously suspended in 2 mL of water, and 1 mL of hydrazine hydrate (0.02 mol) were added to the solution and heated to reflux (at 105 °C) for 1 h. The solution was cooled down and PdC was removed by glass filtration (three times) and centrifugation (4000 × g for 30 min). The supernatant was collected, and the pH was adjusted to 4–5. The solution was frozen overnight and lyophilized for 2 d (yield around 90%). RhB labeling was achieved by dissolving 1 g of the lyophilized compound and 6 mg of RhB in 10 mL of pyridine at 65 °C and stirred the mixture for 20 h. Pyridine was removed from the solution by rotary evaporator at 60 °C for ≈5 h at 2 kPa and by high vacuum overnight. Then, 50 mL of water were added to dissolve the powder that was extracted three times with DCM and then dialyzed with 2- and 3.5 kDa cutoff membranes, for monomeric and crosslinked CDs, respectively, during 24 h. The solution was frozen overnight and lyophilized for 2 d (yield around 94%).

Static and Dynamic Light Scattering Measurements: The molecular weight of crosslinked HPβCDs was measured using a 3D-LS Spectrometer (LS Instruments, Fribourg, Switzerland). The range of investigated concentrations was between 1 and 10 wt%. The refractive index increment of dn/dc = 1.26 × 10^{-4} mL mg^{-1} was empirically obtained with a RFM 340 refractometer (Bellingham & Stanley Ltd, Tunbridge Wells, United Kingdom) and data were analyzed by Debye Plot[72,73] (Figure 2S, Supporting Information) . The hydrodynamic diameter and polydispersity index were measured using a Malvern Zetasizer Nano ZS (Malvern Instruments, Herrenberg, Germany) with a crosslinked HPβCD concentration of 5 wt%. All samples were prepared in nanopure water and filtered through a 0.45 μm syringe filter.

Solubility Studies of Cholesterol–CD Complexes: The cholesterol complexation capacity of the crosslinked HPβCDs was measured following the method described by Dos Santos et al.[74] Briefly, a

10 mL aqueous solution containing excess amount of cholesterol (390 × 10^{-6} M) and increasing concentrations (0–15 × 10^{-3} M) of monomeric or crosslinked HPβCDs was stirred for 48 h at 55 °C. The samples were then centrifuged (4000 × g, 4 °C, 2 h) and the supernatants were collected and filtered through a 0.45 μm syringe filter. The concentration of solubilized cholesterol (i.e., the cholesterol complexed by the CDs) was measured in each sample with the Amplex Red Cholesterol Assay Kit following the provider's instructions. As reported by Dos Santos et al., the solubility of cholesterol alone at these conditions is low (i.e., 0.1 × 10^{-6} M). Consequently, it can be neglected for the quantification of the cholesterol solubilized by the CDs.

U18666A-Induced NPC-Like fibroblasts: L929 cells (i.e., mouse fibroblasts) were treated to develop the NPC-phenotype by following a protocol described by Lange et al.[37] Briefly, fibroblasts were cultured at 37 °C, 5% CO$_2$ in MEM GlutaMAX supplemented with 10% fetal bovine serum and 1% penicillin/streptomycin (complete medium). The cells were seeded at 2.5 × 10^4 mL^{-1} and incubated with 4 × 10^{-6} M U18666A cholesterol transport inhibitor for 72 h. The medium containing U18666A was removed and replaced by specific media depending on the experiment's aim.

Cytotoxicity Experiments: L929 cells were seeded at 2.5 × 10^4 mL^{-1} in a 96-well plate (200 μL per well) and treated to develop the NPC phenotype. The NPC-inducing medium was removed and replaced by complete medium with increasing concentrations of CDs (0.5 × 10^{-3}, 1 × 10^{-3}, 5 × 10^{-3}, 10 × 10^{-3} and 15 × 10^{-3} M) for 48 h. At the end of the treatment, the medium of each condition was collected to quantify lactic dehydrogenase (LDH) by Pierce LDH Cytotoxicity Assay Kit while the cells were analyzed by CellTiter 96 Aqueous One Solution Cell Proliferation Assay Kit (i.e., MTS), following each providers' instructions. The values obtained from CD-untreated cells were considered as 0% LDH release and 100% cell viability for LDH and MTS assays, respectively.

In Vitro Intracellular Cholesterol Modulation: L929 cells were seeded at 2.5 × 10^4 mL^{-1} on 15 mm Ø 24-well coverslips (500 μL per well) and treated to develop the NPC-phenotype. NPC-like fibroblasts were incubated with increasing concentrations of CDs (0.5 × 10^{-3}, 1 × 10^{-3}, 5 × 10^{-3}, and 10 × 10^{-3} M) for 48 h. At the end of the treatment, the medium was removed, and the cells were washed with PBS (once) and fixed with 4% PFA for 10 min. The fixing solution was removed, cells were washed with PBS (three times) and stained with filipin (0.05 mg mL^{-1} in PBS) for 2 h at room temperature in the dark. Cells were then rinsed with PBS (three times), mounted on glass slides and analyzed by DMI600 wide field fluorescence microscope (Leica microsystems, Wetzlar, Germany). Laser intensity and gain were first adjusted and kept fixed during the analysis of each independent experiment. Three images/condition were acquired (excitation 340–380 nm, emission 450–490 nm, 40× magnification). Filipin fluorescence intensity (FI) was obtained by LAS X software (Leica microsystems, Wetzlar, Germany) and divided by the number of cells/image. The value obtained from untreated NPC-fibroblasts was considered as 100%.

Duration of the In Vitro CD Effect: L929 cells were seeded at 2.5 × 10^4 mL^{-1} on 15 mm Ø 24-well coverslips (500 μL per well) and treated to develop the NPC-phenotype. NPC-like fibroblasts were incubated with the CDs (5 × 10^{-3} M) for 48 h. The medium was then removed and replaced with CD-free complete medium. At different time points (24 or 48 h after CD treatment) the cells were stained with filipin and analyzed by fluorescence microscopy as described above. The value obtained from untreated fibroblasts was considered as 100%.

CD Precomplexation Experiments: CD–cholesterol complexes were prepared by adjusting a protocol described in dos Santos et al.[74] Briefly, a 10 mL aqueous solution containing 390 × 10^{-6} M of cholesterol and 10 × 10^{-3} M of native or crosslinked HPβCDs was stirred for 5 d at 55 °C until complete cholesterol dissolution. The samples were collected and frozen overnight at -20 °C and then lyophilized for 2 d. L929 cells were seeded at 2.5 × 10^4 mL^{-1} on 15 mm Ø 24-well coverslips (500 μL per well) and treated to develop the NPC-phenotype. NPC-like fibroblasts were incubated with CD–cholesterol complexes (obtained from monomeric or crosslinked HPβCDs). At the end of the treatment, the cells were stained with filipin and analyzed by fluorescence microscopy as previously

ADVANCED
SCIENCE NEWS
www.advancedsciencenews.com

NANO · MICRO
small
www.small-journal.com

described. The % of cholesterol was obtained by the filipin FI divided by the number of cells and then normalized to CD-treated NPC-L929 cells (100%).

CD Uptake Kinetics: L929 cells were seeded at 2.5×10^4 mL^{-1} on 15 mm Ø 24-well coverslips (500 µL per well) and treated to develop the NPC-phenotype. NPC-like fibroblasts were incubated with 5×10^{-3} M (based on HPβCD units) of fluorescently labeled monomeric, 19.3 kDa or 312.3 kDa HPβCDs up to 48 h. At selected time points (1, 2, 4, 8, 24, and 48 h after incubation) the medium was removed, and the cells were stained with filipin and analyzed by fluorescence microscopy as described above. In addition to filipin, RhB signal was acquired at excitation 525–550 nm, emission 585–640 nm.

Inhibition of Active Processes: L929 cells were seeded at 2.5×10^4 mL^{-1} on 15 mm Ø 24-well coverslips (500 µL per well) and treated to develop the NPC-phenotype. The cells were washed with complete medium and kept at 37 °C, 5% CO$_2$ for 24 h. Then, NPC-like fibroblasts were either preincubated (30 min) at 4 °C or pretreated (1 h) with adenosine triphosphate depletion solution (ATPd, 10×10^{-3} M sodium azide and 6×10^{-3} M 2-deoxy-D-glucose) at 37 °C. Afterwards, the cells were washed with complete medium and incubated with 5×10^{-3} M of fluorescent monomeric, 19.3 kDa or 312.3 kDa HPβCDs for 8 h while keeping the temperature at 4 °C and 37 °C, respectively. At the end, the cells were stained with filipin and analyzed by fluorescence microscopy as described before.

Confocal Laser Scanning Microcopy: Samples from kinetics and inhibition of the active processes were analyzed by Fluoview 3000 (Olympus, Tokyo, Japan). One z-stack/condition was acquired (405, 488, and 594 nm lasers at 63× magnification using an oil-immersion objective) while the z-projections were elaborated using the ImageJ software (National Institute of Health, Bethesda, MD).

Biodistribution and Pharmacokinetics: Seven jugular vein-catheterized adult female Sprague Dawley rats were intravenously injected with 200 mg kg^{-1} of fluorescently labeled CD (either monomeric or 19.3 kDa HPβCD) and euthanized 12 h later. After overdose of xylazine and ketamine, animals were intracardially perfused with 4% PFA. Blood sampling was performed at 1, 2, 4, 8, and 12 h post CD injection, while main organs (cerebrum, cerebellum, spinal cord, lung, liver, kidney, spleen, pancreas, and intestine) were collected after animal perfusion (i.e., after 12 h). Plasma was isolated by centrifugation (5000 × g for 5 min at 4 °C) and stored at -80 °C until CD quantification while organs were prepared following a protocol described by Polomska et al.[75] Briefly, 0.1 g of tissue per 1 mL of PBS was homogenized with stainless steel beads of 5 mm (25–30 Hz for 5 min) by a Tissuelyser (Qiagen, Venlo, Netherlands). The homogenates were centrifuged at 10 000 × g for 10 min and the supernatant was collected and stored at −80 °C until CD quantification. All the samples were then analyzed by Infinite M200 (Tecan, Zürich, Switzerland) to quantify fluorescent CDs (543 nm excitation/580 nm emission, 100% gain, integration time 20 µs, number of flashes: 20). Calibration curves were obtained for both CDs in blood and organs of untreated rats. In order to evaluate the penetration of the CDs in the organs' parenchyma, small sections of all were collected before homogenization. These sections were sliced and stored at −80 °C until further manipulation. Immunofluorescence was performed on 10 µm lung, liver, kidney, and brain serial sections, treated with cold methanol for 10 min at −20 °C, washed three times in PBS, stained for nucleus with Hoechst (1:1000 in PBS) for 20 min at RT and then mounted on glass slides. At least three pictures/section were acquired at 10× (lung, liver, and kidney) and 40× (brain) magnification by DMI600 wide field fluorescence microscope (Leica microsystems, Wetzlar, Germany). Hoechst signal (cell nucleus) was acquired at excitation 340–380 and emission 450–490 channels and RhB (crosslinked CD) was acquired at excitation 542–582 and emission 604–644 channels. In the pharmacokinetic study, CD concentration in the plasma was expressed in µg mL^{-1} while $t_{1/2}$, C_{max}, AUC 0-t, CL, V_d, and MRT were calculated using the Excel-based function PK Solver 2.0 plugin (Microsoft Corporation, Redmond, WA) by setting a noncompartmental analysis after i.v. bolus input. CD concentration in the organs was expressed as % of injected dose (ID) per g of tissue. Additional four rats were injected with 200 mg kg^{-1} of fluorescent 19.3 kDa HPβCD and euthanized 24 h later. Blood samples were collected at 24 h post CD injection and treated as described above.

Therapeutic Efficacy In Vivo: The in vivo was performed in a blinded fashion. The person administering the CDs and following the life span of the animals did not know which groups were receiving the monomeric HPβCD and which groups were receiving the crosslinked HPβCD. There were four groups ($n = 6$ for the lower dose of monomeric HPβCD, $n = 5$ for the higher dose of monomeric HPβCD and $n = 4$ for both doses of crosslinked HPβCD). The Npc1 mice received intraperitoneal injection on postnatal day 7 (P7) with either crosslinked HPβCD or monomeric HPβCD at the dose of 1333 or 4000 mg kg^{-1}. The injections were performed with 7 or 20% (w/v) CD in phosphate buffered saline, respectively. Survival is expressed as % of the cumulative number of dead animals versus the initial number of animals per group.

Magnetic Resonance Imaging-Guided Low Intensity-Pulsed Focused Ultrasound: Microbubbles were prepared adapting the protocol developed by Feshitan et al.[76] Briefly, a lipid suspension of 90 mol% DSPE, 5 mol% DSPE, 5 mol% DSPE PEG 2 kDa, and 5 mol% DSPE PEG 5 kDa was prepared in chloroform at 2 mg mL^{-1} in 100 mL PBS. The chloroform was then evaporated under nitrogen and kept in vacuum overnight. The resultant films were then resuspended in PBS containing 10% glycerol and 10% propylene glycol. The suspension was preheated to 70 °C and then bath sonicated for 30 min. Perfluorobutane gas was introduced by flowing it over the surface of the solution and sonication was applied using a Branson SLPe (Marshall Scientific, Hampton, NH) at 70% power. The suspension was centrifuged three times (300 × g for 3 min) to collect all microbubbles into a cake. After of each centrifugation, the supernatant was discarded while the cake of microbubbles was resuspended in PBS. At the end, microbubbles were stored at 4 °C until their use (within 24 h). Size distribution of the microbubbles was measured using a Multisizer 4 (Beckman Coulter, Brea, CA). The median diameter of the microbubbles was 1.556 µm and the suspension was diluted (57 µL of microbubbles in 543 µL of PBS) before administration.

BBB Opening Setting: Four jugular vein-catheterized adult female Sprague Dawley rats were anesthetized with isoflurane (2.5% in a mixture 4:1 air:oxygen) and placed into the animal support of the rodent FUS system (IGT, Pessac, France). Their skull region was shaved, and the body temperature of the animals was kept constant (36–37 °C) using a hot water circuit integrated into the animal support. T1-weighted anatomical MR images were acquired on a Bruker BioSpec 470/30 small animal MR system (Bruker, Billerica, MA) operating at 7.0 T and used to set the position of the 1.5 MHz FUS transducer on the head of the animals. The rats were i.v. injected with 2.4 mL kg^{-1} of microbubbles (600 µL min^{-1} injection speed) 30 s before the beginning of the FUS sequence, which lasted for 3 min with fixed parameters during the whole session (length: 10 ms pulse; sequence: 1 Hz pulse repetition frequency; acoustic pressure emitted: 0.9 MPa; estimated pressure in situ: 0.4–0.5 MPa; duty cycle: 1%; mechanical index: 0.7; expected thermal index: ≈0) and was adapted from a protocol described by Papachristodoulou et al.[58] Twenty min after FUS sequence, rats were i.v. injected with 75 µL per animal of gadolinium-DOTA (Guerbet, Paris, France) and T1-weighted MR images were acquired to confirm BBB opening. Then, one rat was i.v. injected with Evan's blue and euthanized by an overdose of xylazine and ketamine, the brain was collected and analyzed to confirm BBB opening.

Combination of MRIg-FUS and CDs: Eight jugular vein-catheterized adult female Sprague Dawley rats were prepared as in BBB opening setting. The rats were first i.v. injected with 2.4 mL kg^{-1} of microbubbles (600 µL min^{-1}) 30 s before the beginning of the FUS sequence. The injection of the microbubbles lasted ≈60 s and had 30 s of overlap with the beginning of the FUS sequence, that lasted 3 min in total. Right after the injection of the microbubbles, 200 mg kg^{-1} of fluorescently labeled crosslinked CD were i.v. injected in less than 5 s. The FUS sequence was concluded ≈145 s after CD injection (i.e., 3 min in total). BBB opening confirmed with T1-weighted contrast-enhanced MRI. Animals were euthanized 8 h later with an overdose of xylazine and ketamine and intracardially perfused with 4% PFA. The brains were collected, stored at −80 °C and sliced to be further analyzed. Immunofluorescence was

performed on 15 µm brain serial sections, treated with cold methanol for 10 min at −20 °C, washed three times in PBS and incubated with BSA 1% and Triton 100 × 0.5% (both in PBS) for 30 min at RT. Sections were then incubated either with rabbit anti-Olig2 (1:100 in PBS) or with rabbit anti-GFAP (1:200 in PBS) primary antibodies overnight at 4 °C and stained for oligodendrocytes and astrocytes, respectively, with Alexa goat anti-rabbit Alexa 488 secondary antibody (1:250 in PBS) for 90 min at RT. Sections were ultimately stained for nucleus with Hoechst (1:1000 in PBS) for 20 min at RT and then mounted on glass slides. At least three pictures/section were acquired at 40× and 63× magnification by DMI600 wide field fluorescence microscope (Leica microsystems, Wetzlar, Germany). Hoechst signal (cell nucleus) was acquired at excitation 340–380 and emission 450–490, Alexa 488 channels (either astrocytes or oligodendrocytes) was acquired at excitation 460–500 and emission 512–542 channels, and RhB (crosslinked CD) was acquired at excitation 542–582 and emission 604–644 channels.

Data Analysis: Experiments were performed at least three times. n refers to the number of independent experiments. The statistical analysis (statistical significance $p < 0.05$) and the graphs were made by GraphPad Prism 8.0. Data are expressed as mean + standard deviation (SD). The type of statistical test and post-hoc multiple comparison is specified in the caption of each figure and was selected according to the number of replicates/groups and the type of comparison. and the suggestion of the software. Outliers were identified and excluded by GraphPad QuickCalcs.

Supporting Information

Supporting Information is available from the Wiley Online Library or from the author.

Conflict of Interest

The authors declare no conflict of interest.

Author Contributions

D.C. codesigned the study, performed the experiments, analyzed and interpreted the data, and wrote the original draft of the manuscript. H.C. and F.P. designed, performed, and assisted with the interpretation of the in vivo study on the NPC mouse model and funded this element of the project (NPUK and NPRF). B.W. and A.S.S. assisted with the FUS study on healthy rats. C.L. assisted with the in vitro mechanistic studies of HPβCDs. M.U. and R.M. assisted with the execution and interpretation of SLS measurements. J.C.L. codesigned the study, obtained funding, supervised the project, and guided experimental design, data interpretation and manuscript preparation. All authors reviewed the manuscript.

Data Availability Statement

Main data are reported in the article. Supporting information (i.e., representative ^{1}H NMR spectra, images and controls for all experiments) are provided in a separate file. Any other raw data are available upon request.

[1] E. D. Carstea, J. A. Morris, K. G. Coleman, S. K. Loftus, D. Zhang, C. Cummings, J. Gu, M. A. Rosenfeld, W. J. Pavan, D. B. Krizman, J. Nagle, M. H. Polymeropoulos, S. L. Sturley, Y. A. Ioannou, M. E. Higgins, M. Comly, A. Cooney, A. Brown, C. R. Kaneski, E. J. Blanchette-Mackie, N. K. Dwyer, E. B. Neufeld, T.-Y. Chang, L. Liscum, J. F. Strauss III, K. Ohno, M. Zeigler, R. Carmi, J. Sokol, D. Markie, R. R. O'Neill, O. P. van Diggelen, M. Elleder, M. C. Patterson, R. O. Brady, M. T. Vanier, P. G. Pentchev, D. A. Tagle, *Science* **1997**, *277*, 228.
[2] A. I. Rosenbaum, F. R. Maxfield, *J. Neurochem.* **2011**, *116*, 789.
[3] M. C. Patterson, S. U. Walkley, *Mol. Genet. Metab.* **2017**, *120*, 34.
[4] J. Newton, S. Milstien, S. Spiegel, *Adv. Biol. Regul.* **2018**, *70*, 82.
[5] S. Mukherjee, F. R. Maxfield, *Biochim. Biophys. Acta* **2004**, *1685*, 28.
[6] W. S. Garver, G. A. Francis, D. Jelinek, G. Shepherd, J. Flynn, G. Castro, C. W. Vockley, D. L. Coppock, K. M. Pettit, R. A. Heidenreich, F. J. Meaney, *Am. J. Med. Genet., Part A* **2007**, *143A*, 1204.
[7] E. Mengel, H. H. Klünemann, C. M. Lourenço, C. J. Hendriksz, F. Sedel, M. Walterfang, S. A. Kolb, *Orphanet J. Rare Dis.* **2013**, *8*, 166.
[8] A. Treiber, O. Morand, M. Clozel, *Xenobiotica* **2007**, *37*, 298.
[9] M. C. Patterson, D. Vecchio, H. Prady, L. Abel, J. E. Wraith, *Lancet Neurol.* **2007**, *6*, 765.
[10] S. Fecarotta, A. Romano, R. Della Casa, E. Del Giudice, D. Bruschini, G. Mansi, B. Bembi, A. Dardis, A. Fiumara, M. Di Rocco, G. Uziel, A. Ardissone, D. Roccatello, M. Alpa, E. Bertini, A. D'Amico, C. Dionisi-Vici, F. Deodato, S. Caviglia, A. Federico, S. Palmeri, O. Gabrielli, L. Santoro, A. Filla, C. Russo, G. Parenti, G. Andria, *Orphanet J. Rare Dis.* **2015**, *10*, 22.
[11] M. Pineda, K. Juríčková, P. Karimzadeh, M. Kolnikova, V. Malinova, J. L. Insua, C. Velten, S. A. Kolb, *Orphanet J. Rare Dis.* **2019**, *14*, 32.
[12] A. U. Tikkanen, K. Buxton, C. K. Ullrich, S. S.-D. Stone, D. L. Nimec, *Pediatrics* **2019**, *144*, e20191438.
[13] C. De Nuccio, A. Bernardo, A. Ferrante, R. Pepponi, A. Martire, M. Falchi, S. Visentin, P. Popoli, L. Minghetti, *Sci. Rep.* **2019**, *9*, 9782.

ADVANCED
SCIENCE NEWS

www.advancedsciencenews.com

NANO · MICRO

small

www.small-journal.com

[14] H. Yanagisawa, T. Ishii, K. Endo, E. Kawakami, K. Nagao, T. Miyashita, K. Akiyama, K. Watabe, M. Komatsu, D. Yamamoto, Y. Eto, *Sci. Rep.* **2017**, *7*, 1.

[15] J. Newton, N. C. Hait, M. Maceyka, A. Colaco, M. Maczis, C. A. Wassif, A. Cougnoux, F. D. Porter, S. Milstien, N. Platt, F. M. Platt, S. Spiegel, *FASEB J.* **2017**, *31*, 1719.

[16] T. Kirkegaard, J. Gray, D. A. Priestman, K.-L. Wallom, J. Atkins, O. D. Olsen, A. Klein, S. Drndarski, N. H. T. Petersen, L. Ingemann, D. A. Smith, L. Morris, C. Bornæs, S. H. Jørgensen, I. Williams, A. Hinsby, C. Arenz, D. Begley, M. Jäättelä, F. M. Platt, *Sci. Transl. Med.* **2016**, *8*, 355ra118.

[17] N. Hammond, A. B. Munkacsi, S. L. Sturley, *Biochim. Biophys. Acta, Mol. Cell. Biol. Lipids* **2019**, *1864*, 1109.

[18] P. Calias, *Curr. Pharm. Des.* **2017**, *23*, 6231.

[19] A. Puglisi, Y. Yagci, *Macromol. Rapid Commun.* **2019**, *40*, 1800557.

[20] A.-M. Neßlauer, A. Gläser, M. Gräler, R. Engelmann, B. Müller-Hilke, M. Frank, C. Burstein, A. Rolfs, J. Neidhardt, A. Wree, M. Witt, A. U. Bräuer, *Lipids Health Dis.* **2019**, *18*, 146.

[21] Y. Maeda, K. Motoyama, R. Nishiyama, T. Higashi, R. Onodera, H. Nakamura, T. Takeo, N. Nakagata, Y. Yamada, Y. Ishitsuka, Y. Kondo, T. Irie, H. Era, H. Arima, *Nanomaterials* **2019**, *9*, 802.

[22] F. Vacca, S. Vossio, V. Mercier, D. Moreau, S. Johnson, C. C. Scott, J. P. Montoya, M. Moniatte, J. Gruenberg, *J. Lipid Res.* **2019**, *60*, 832.

[23] M. Feltes, S. E. Gale, S. Moores, D. S. Ory, J. E. Schaffer, *J. Lipid Res.* **2020**, *61*, 403.

[24] T. Loftsson, M. D. Moya-Ortega, C. Alvarez-Lorenzo, A. Concheiro, *J. Pharm. Pharmacol.* **2016**, *68*, 544.

[25] I. Hajdu, J. Angyal, D. Szikra, I. Kertész, M. Malanga, E. Fenyvesi, L. Szente, M. Vecsernyés, I. Bacskay, J. Varadi, P. Fehér, Z. Ujhelyi, G. Vasvari, A. Rusznyak, G. Trencsényi, P. Fehér, *Eur. J. Pharm. Sci.* **2019**, *128*, 202.

[26] A. Tamura, N. Yui, *J. Controlled Release* **2018**, *269*, 148.

[27] A. Kulkarni, P. Caporali, A. Dolas, S. Johny, S. Goyal, J. Dragotto, A. Macone, R. Jayaraman, M. T. Fiorenza, *Sci. Rep.* **2018**, *8*, 9547.

[28] F. Van De Manakker, T. Vermonden, C. F. Van Nostrum, W. E. Hennink, *Biomacromolecules* **2009**, *10*, 3157.

[29] B. Martel, D. Ruffin, M. Weltrowski, Y. Lekhiri, M. Morcellet, *J. Appl. Polym.* **2005**, *97*, 433.

[30] R. Ananda, M. Malangab, I. Maneta, F. Manolia, K. Tuzab, A. Aykaçc, C. Ladavièred, E. Fenyvesib, A. Vargas-Berenguelc, R. Grefe, S. Monti, *Photochem. Photobiol. Sci.* **2013**, *12*, 1841.

[31] M. J. García-Fernándeza, N. Tabaryb, B. Martelb, F. Cazauxb, A. Olivac, P. Taboadad, A. Concheiroa, C. Alvarez-Lorenzo, *Carbohydr. Polym.* **2013**, *98*, 1343.

[32] J. Cheng, K. T. Khin, M. E. Davis, *Mol. Pharmaceutics* **2004**, *1*, 183.

[33] N. Morin-Crini, G. Crini, *Prog. Polym. Sci.* **2013**, *38*, 344.

[34] S. Nie, S. Zhang, W. Pan, Y. Liu, *Drug Dev. Ind. Pharm.* **2011**, *37*, 606.

[35] E. Renard, A. Deratani, G. Volet, B. Sebille, *Eur. Polym. J.* **1997**, *33*, 49.

[36] H. S. Choi, W. Liu, P. Misra, E. Tanaka, J. P. Zimmer, B. Itty Ipe, M. G. Bawendi, J. V. Frangioni, *Nat. Biotechnol.* **2007**, *25*, 1165.

[37] Y. Lange, J. Ye, M. Rigney, T. Steck, *J. Biol. Chem.* **2000**, *275*, 17468.

[38] A. Biswas, P. Kashyap, S. Datta, T. Sengupta, B. Sinha, *Biophys. J.* **2019**, *116*, 1456.

[39] R. Zidovetzki, I. Levitan, *Biochim. Biophys. Acta.* **2007**, *1768*, 1311.

[40] B. Liu, C. M. Ramirez, A. M. Miller, J. J. Repa, S. D. Turley, J. M. Dietschy, *J. Lipid Res.* **2010**, *51*, 933.

[41] C. M. Ramirez, B. Liu, A. M. Taylor, J. J. Repa, D. K. Burns, A. G. Weinberg, S. D. Turley, J. M. Dietschy, *Pediatr. Res.* **2010**, *68*, 309.

[42] S. Nusca, S. Canterini, G. Palladino, F. Bruno, F. Mangia, R. P. Erickson, M. T. Fiorenza, *Neurobiol. Dis.* **2014**, *70*, 117.

[43] J. B. Nietupski, J. J. Pacheco, W. L. Chuang, K. Maratea, L. Li, J. Foley, K. M. Ashe, C. G. Cooper, J. M. Aerts, D. P. Copeland, R. K. Scheule, S. H. Cheng, J. Marshall, *Mol. Genet. Metab.* **2012**, *105*, 621.

[44] J. E. Vanace, B. Karten, *J. Lipid Res.* **2014**, *55*, 1609.

[45] C. C. Pontikis, D. C. Davidson, S. U. Walkley, F. M. Platt, D. J. Begley, *J. Inherited Metab. Dis.* **2013**, *36*, 491.

[46] W. A. Banks, *BMC Neurol.* **2009**, *9*, S3.

[47] R. O. Williams, V. Mahaguna, M. Sriwongjanya, *Eur. J. Pharm. Biopharm.* **1998**, *46*, 355.

[48] H. W. Frijlink, A. C. Eissens, N. R. Hefting, K. Poelstra, C. F. Lerk, D. K. F. Meijer, *Pharm. Res.* **1991**, *08*, 9.

[49] L. Szente, A. Singhal, A. Domokos, B. Song, *Molecules* **2018**, *23*, 1228.

[50] A. Tamura, N. Yui, *Sci. Rep.* **2015**, *4*, 4356.

[51] J. Mosquera, I. García, L. M. Liz-Marzán, *Acc. Chem. Res.* **2018**, *51*, 2305.

[52] C. Coisne, S. Tilloy, E. Monflier, D. Wils, L. Fenart, F. Gosselet, *Molecules* **2016**, *21*, 1748.

[53] D. Carradori, A. G. Dos Santos, J. Masquelier, A. Paquot, P. Saulnier, J. Eyer, V. Préat, G. G. Muccioli, M.-P. Mingeot-Leclercq, A. des Rieux, *J. Controlled Release* **2018**, *292*, 248.

[54] M. E. Fox, F. Szoka, J. M. Fréchet, *Acc. Chem. Res.* **2009**, *42*, 1141.

[55] J. Pitha, A. Gerloczy, A. Olivi, *J. Pharm. Sci.* **1994**, *83*, 833.

[56] A. Burgess, K. Hynynen, *ACS Chem. Neurosci.* **2013**, *4*, 519.

[57] M. A. Stavarache, N. Petersen, E. M. Jurgens, E. R. Milstein, Z. B. Rosenfeld, D. J. Ballon, M. G. Kaplitt, *J. Neurosurg.* **2018**, *130*, 989.

[58] A. Papachristodoulou, R. D. Signorell, B. Werner, D. Brambilla, P. Luciani, M. Cavusoglu, J. Grandjean, M. Silginer, M. Rudin, E. Martin, M. Weller, P. Roth, J.-C. Leroux, *J. Controlled Release* **2019**, *295*, 130.

[59] V. Krishna, F. Sammartino, A. Rezai, *JAMA Neurol.* **2018**, *75*, 246.

[60] A. Burgess, S. Dubey, S. Yeung, O. Hough, N. Eterman, I. Aubert, K. Hynynen, *Radiology* **2014**, *273*, 736.

[61] K. Hynynen, N. McDannold, N. Vykhodtseva, F. A. Jolesz, *Acta Neurochir. Suppl.* **2003**, *86*, 555.

[62] M. Çavuşoğlu, J. Zhang, G. D. Ielacqua, G. Pellegrini, R. D. Signorell, A. Papachristodoulou, D. Brambilla, P. Roth, M. Weller, M. Rudin, E. Martin, J.-C. Leroux, B. Werner, *Phys. Med. Biol.* **2019**, *64*, 045012.

[63] B. P. Mead, C. T. Curley, N. Kim, K. Negron, W. J. Garrison, J. Song, D. Rao, G. W. Miller, J. W. Mandell, B. W. Purow, J. S. Suk, J. Hanes, R. J. Price, *Small* **2019**, *15*, 1903460.

[64] N. Lipsman, Y. Meng, A. J. Bethune, Y. Huang, B. Lam, M. Masellis, N. Herrmann, C. Heyn, I. Aubert, A. Boutet, G. S. Smith, K. Hynynen, S. E. Black, *Nat. Commun.* **2018**, *9*, 2336.

[65] A. R. Rezai, M. Ranjan, P.-F. D'Haese, M. W. Haut, J. Carpenter, U. Najib, R. I. Mehta, J. Levi Chazen, Z. Zibly, J. R. Yates, S. L. Hodder, M. Kaplitt, *Proc. Natl. Acad. Sci. USA* **2020**, *117*, 9180.

[66] M. E. Karakatsani, T. Kugelman, R. Ji, M. Murillo, S. Wang, Y. Niimi, S. A. Small, K. E. Duff, E. E. Konofagou, *Theranostics* **2019**, *9*, 5396.

[67] M. S. Bobola, L. Chen, C. K. Ezeokeke, T. A. Olmstead, C. Nguyen, A. Sahota, R. G. Williams, P. D. Mourad, *Brain Stimul.* **2020**, *13*, 1014.

[68] R. Mehvar, M. A. Robinson, J. M. Reynolds, *J. Pharm. Sci.* **1994**, *83*, 1495.

[69] C. K. Fog, T. Kirkegaard, *Expert Opin. Drug Discovery* **2019**, *14*, 499.

[70] G. Dufour, B. Evrard, P. De Tullio, *Eur. J. Pharm. Sci.* **2015**, *73*, 20.

[71] M. Malanga, L. Jicsinszky, E. Fenyvesi, *J. Drug Delivery Sci. Technol.* **2012**, *22*, 260.

[72] B. H. Zimm, *J. Chem. Phys.* **1948**, *16*, 1093.

[73] I. Puskás, A. Szemjonov, É. Fenyvesi, M. Malanga, L. Szente, *Carbohydr. Polym.* **2013**, *94*, 124.

[74] C. dos Santos, M. P. Buera, M. F. Mazzobre, *J. Sci. Food Agric.* **2011**, *91*, 2551.

[75] A. Polomska, M. A. Gauthier, J.-C. Leroux, *Small* **2017**, *13*, 1602066.

[76] J. A. Feshitan, F. Vlachos, S. R. Sirsi, E. E. Konofagou, M. A. Borden, *Biomaterials* **2012**, *33*, 247.

NANO ‖ MICRO

small

Supporting Information

Investigating the Mechanism of Cyclodextrins in the Treatment of Niemann-Pick Disease Type C Using Crosslinked 2-Hydroxypropyl-#-cyclodextrin

Dario Carradori, Hsintsung Chen, Beat Werner, Aagam S. Shah, Chiara Leonardi, Mattia Usuelli, Raffaele Mezzenga, Frances Platt, and Jean-Christophe Leroux*

Investigating the mechanism of cyclodextrins in the treatment of Niemann-Pick Disease Type C using crosslinked 2-hydroxypropyl-β-cyclodextrin

Dario Carradori, Hsintsung Chen, Beat Werner, Aagam S. Shah, Chiara Leonardi, Mattia Usuelli, Raffaele Mezzenga, Frances Platt, and Jean-Christophe Leroux

1. Representative ^{1}H NMR spectra of crosslinked HPβCDs.
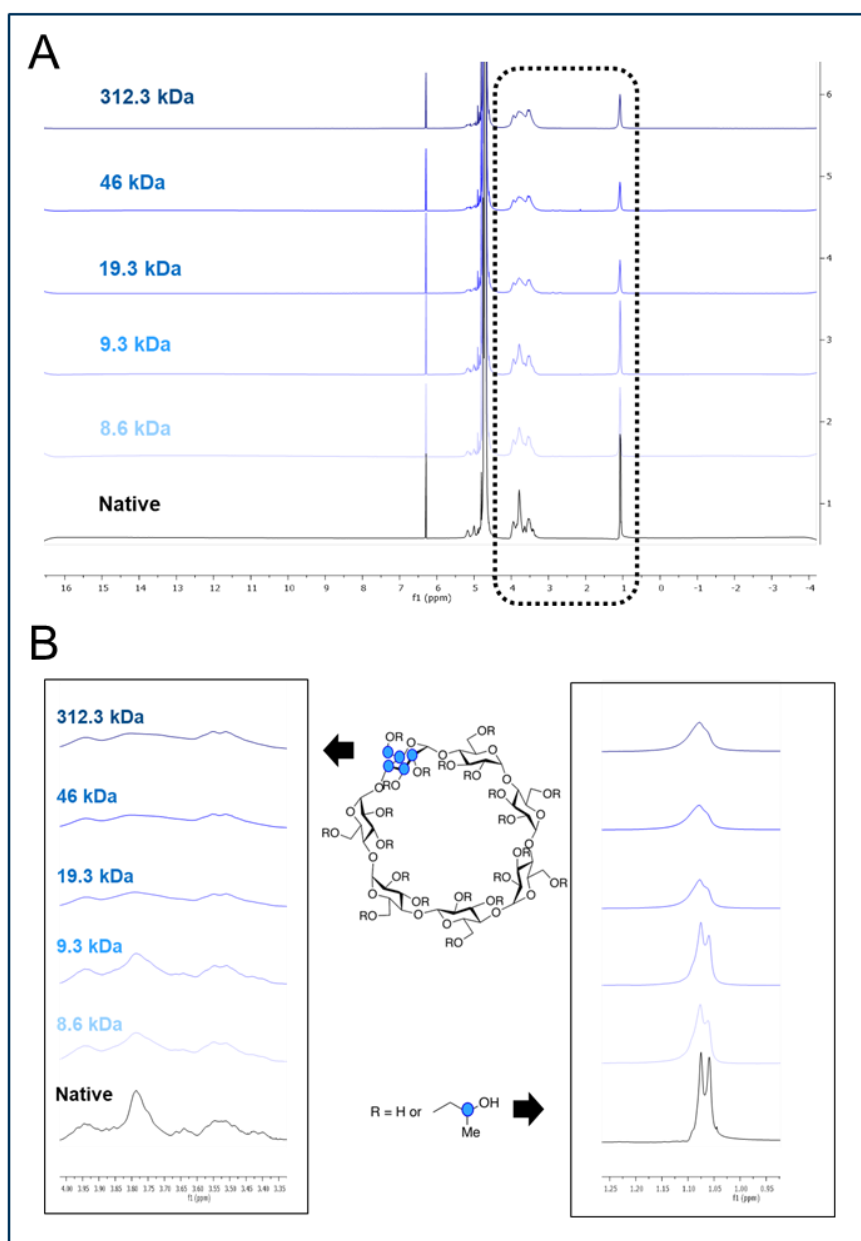
Figure 1S. ^{1}H NMR spectra of crosslinked HPβCDs. Ten mg of each CD were dissolved in 600 μL of deuterium oxide containing 35 mM of maleic acid (internal standard). Samples were analyzed with a ^{1}H NMR 400 MHz spectrometer. **A**, full spectra. **B**, details showing the modified regions after cross-linking.

2. Representative SLS analysis of crosslinked HPβCDs.
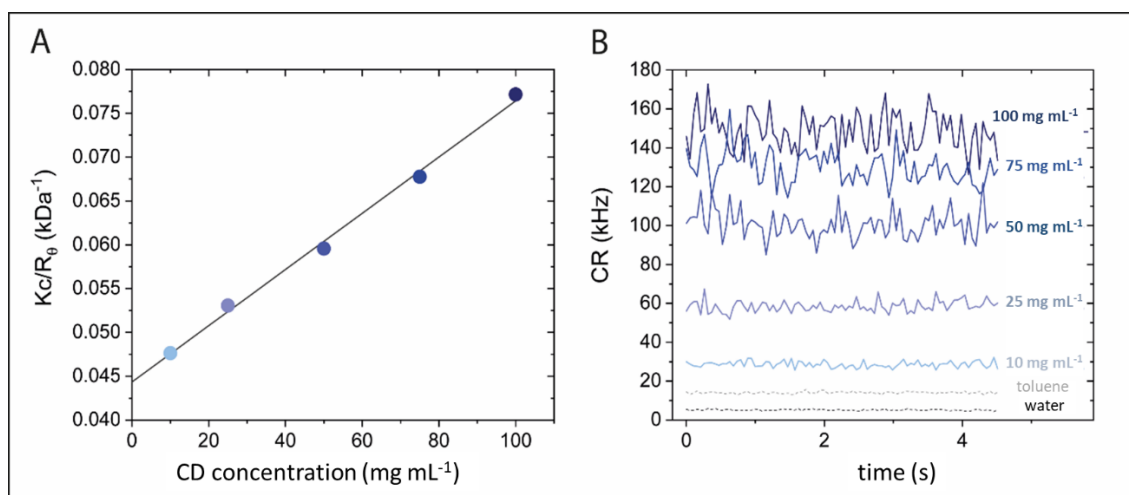
Figure 2S. SLS analysis of the 19.3 kDa crosslinked HPβCD. A) Debye Plot and **B**) raw count rate (CR) at different CD concentrations. Kc corresponds to the optical constant (obtained from the laser wavelength and the refractive index of solvent and sample) and R_θ is the Rayleigh ratio of the sample. Toluene and water were used as internal controls.

*3. Cytotoxic profile of normal fibroblasts (L929) after incubation with crosslinked HPβCDs.*
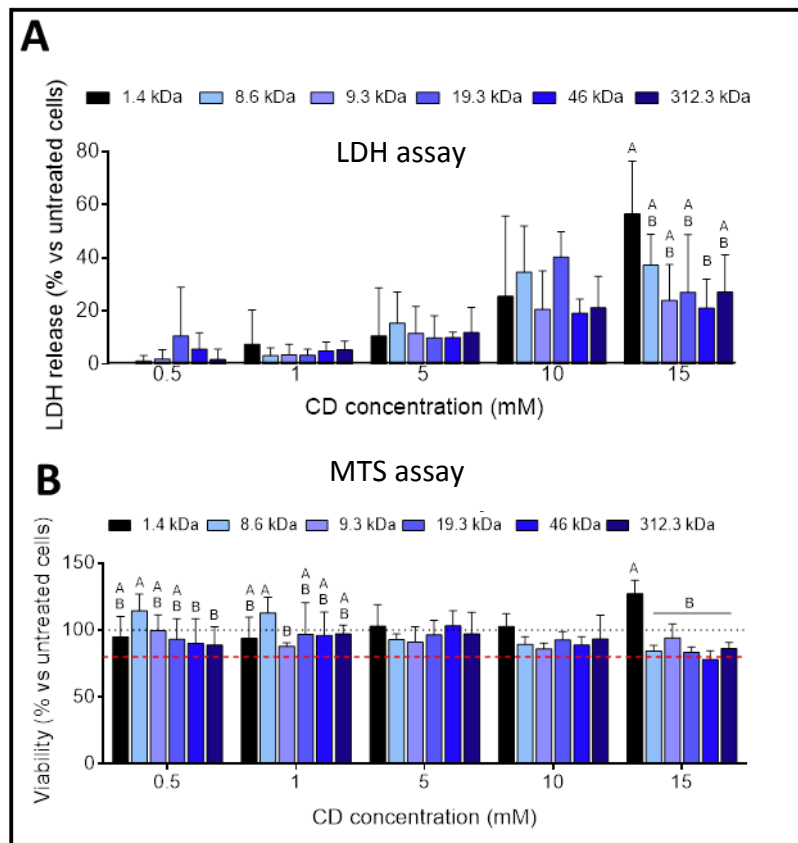
Figure 3S. CD effect on normal fibroblasts. CD treatment was performed at 37 °C in CO_2 5% for 48 h. **A**) LDH release and **B**) cell viability after CD-treatment. The % of LDH release and the % of cell viability were normalized to untreated NPC-L929 cells (100%). Two-way ANOVA with multiple comparisons (Tukey's post-hoc test). Mean + SD (*n*=3). Different letters indicate a statistically significant difference (p < 0.05).
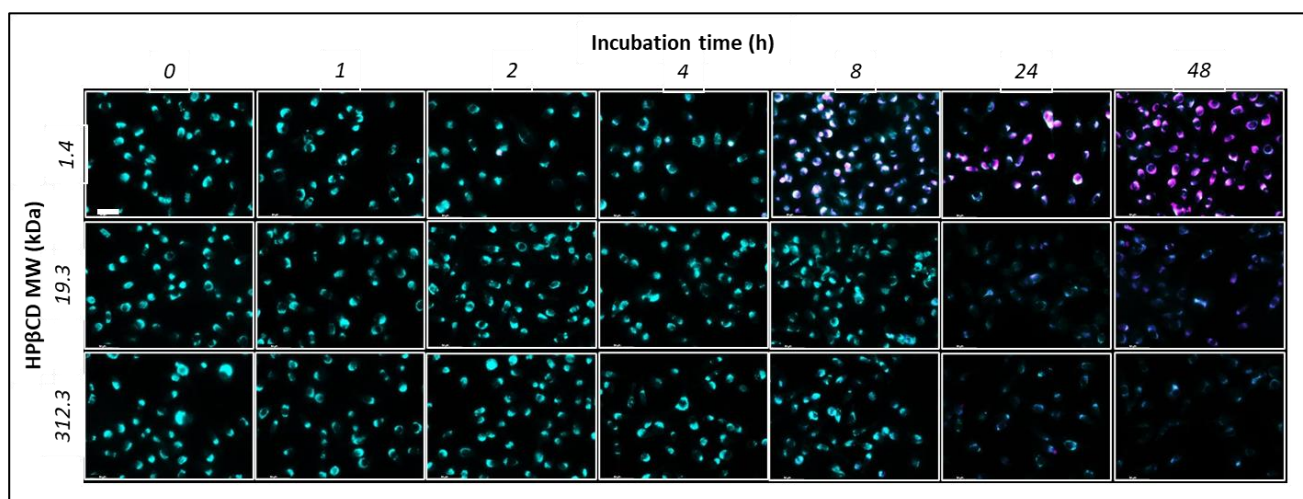
Figure 4S. CD cellular uptake at different time-points. Representative pictures of NPC-L929 cells incubated for different times (1, 2, 4, 8, 24, and 48 h) with 5 mM fluorescent CDs (monomeric, 19.3 or 312.3 kDa HPβCD). Cyan corresponds to filipin fluorescence (*i.e.,* intracellular cholesterol accumulation) and pink corresponds to RhB (*i.e.,* fluorescent CDs). Scale bar: 50 μm.
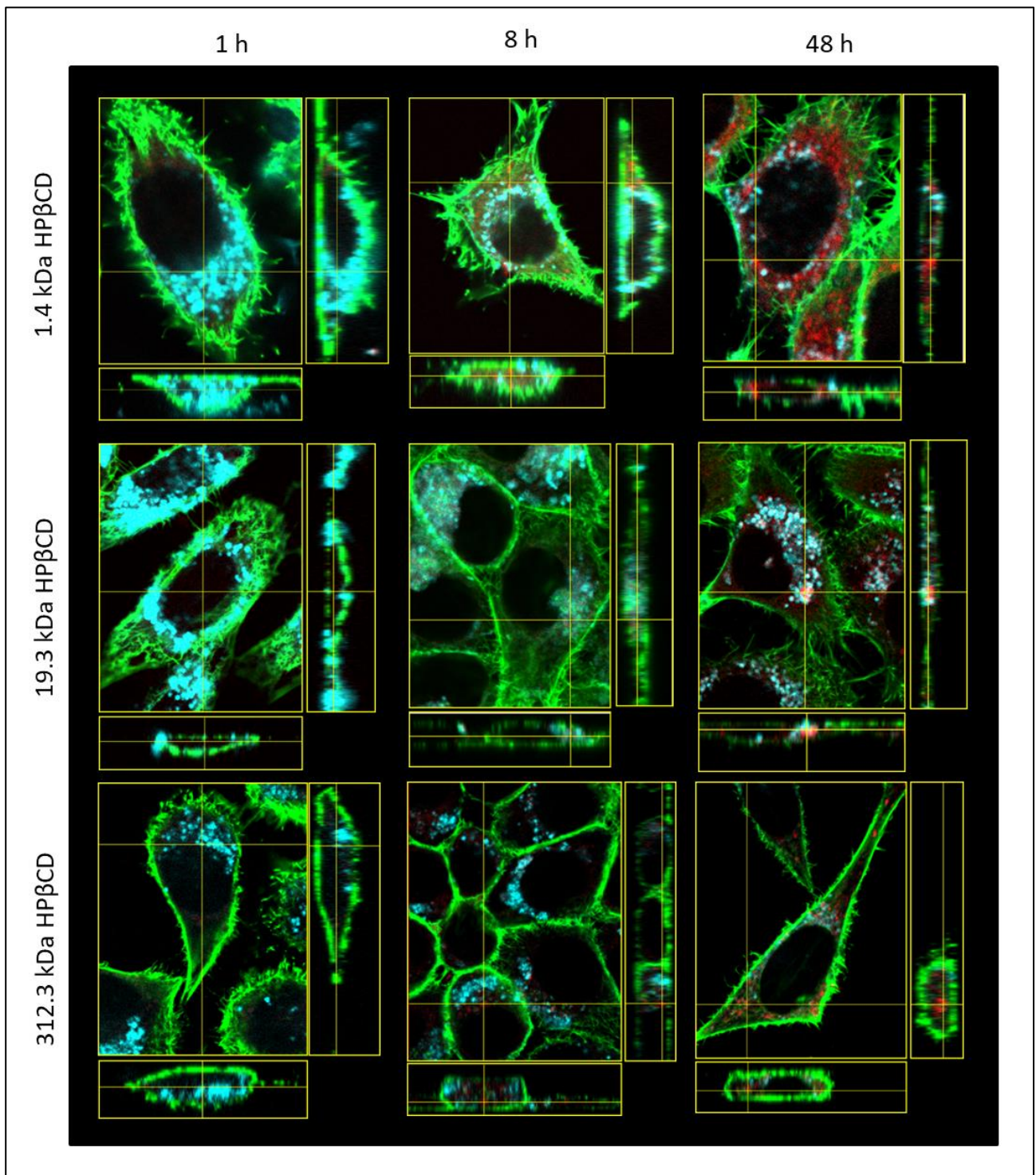
Figure 5S. CD localization at different time-points. Representative orthogonal section pictures of NPC-L929 cells incubated for different times (1, 8, and 48 h) with 5 mM fluorescent CDs (monomeric, 19.3 or 312.3 kDa HPβCD). Cyan corresponds to filipin fluorescence (*i.e.*, intracellular cholesterol accumulation), green is phalloidin-488 (*i.e.*, cytoskeleton) and red corresponds to RhB (*i.e.*, fluorescent CDs).
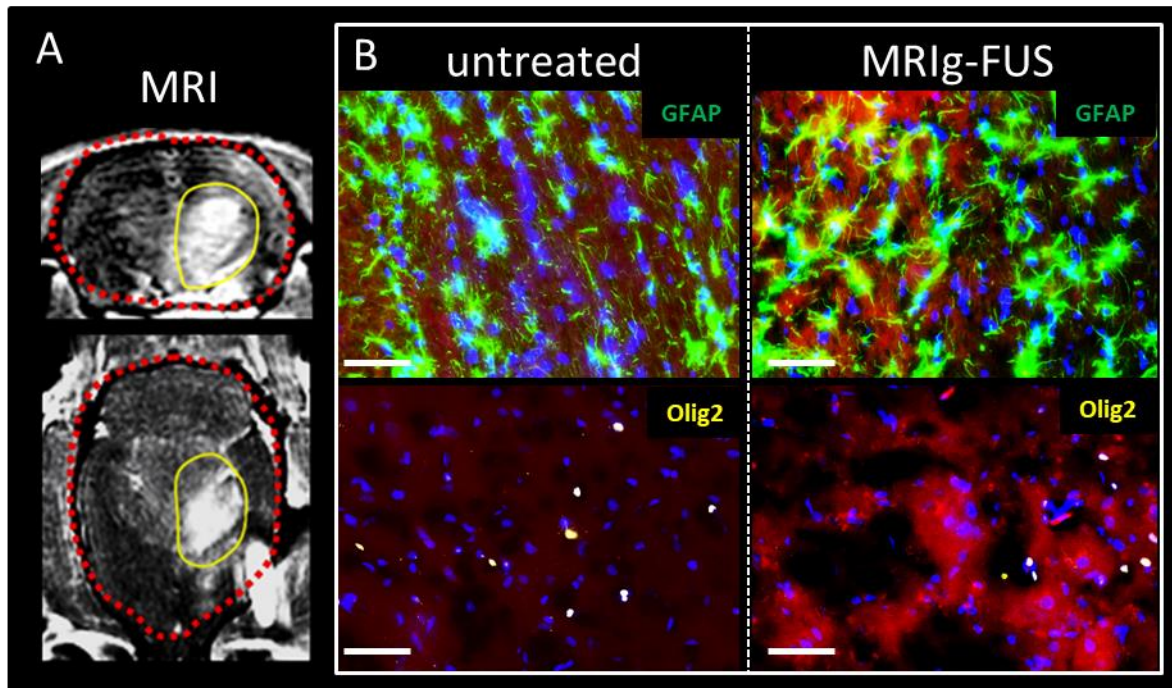
Figure 6S. Brain diffusion of monomeric CD after MRIg-FUS. A) T1-weighted MRI of gadolinium extravasation (clear grey) after MRIg-FUS. **B**) Representative pictures showing the localization of 1.4 kDa HPβCD compared to the astrocytes (green) and oligodendrocytes (yellow) with and without MRIg-FUS. Blue corresponds to Hoechst (*i.e.*, cell nuclei), green corresponds to GFAP (*i.e.*, astrocytes), yellow corresponds to Olig2 (*i.e.*, oligodendrocytes), red corresponds to RhB (*i.e.*, fluorescent CD), Scale bar: 50 µm.